Wind assisted ship propulsion: A rotating cylinder study

Design, realisation and characterisation of an aerodynamic rotating cylinder experiment

K.C. van Gaalen

Master of Science Thesis

TU Delft

Wind assisted ship propulsion: A rotating cylinder study

Design, realisation and characterisation of an aerodynamic rotating cylinder experiment

by

K.C. van Gaalen

Master of Science Thesis
Delft University of Technology
Department of Flow Physics and Technology
Low Speed Laboratory - Leeghwaterstraat 42, Delft

As partial fulfillment to obtain the degree of Master of Science within the field of Aerospace Engineering,

to be defended publicly on March 31st, 2025 at 10:00 PM till 14:00 AM.

Student number:	4442679	
Thesis committee:	Prof. Dr. Ir. M. Kotsonis,	TU Delft, chair
	Dr. Ir. T. Michelis	TU Delft, supervisor
	Prof. Dr. Ir. L.L.M. Veldhuis	TU Delft, examiner
	Dr. Ir. A.F. Rius Vidales	TU Delft, additional

An electronic version of this thesis is available athttp://repository.tudelft.nl/.

Cover image shot by Alan Jamieson (2015) is taken from: https://commons.wikimedia.org/wiki/File:E-Ship_1_(20037221244).jpg

TU Delft

Preface

The written pages in this report appear on the surface as the name suggests, solely as the work that has been performed for conducting this Master Thesis on experimental aerodynamic research of rotating cylinders. However, for the people who know, it is so much more than that. Although these few lines could never describe the full story, for me it has been an accumulation of an intense and demanding, but overall enjoyable and rewarding learning curve, that took place over the course of both my years as a bachelor and master Aerospace Engineering student at the Delft University of Technology, and my internship period spend abroad in Switzerland. On this journey I got the chance to unravel the seemingly mysterious topics surrounding the movement of air, only to reveal even bigger mysteries that sparked my curiosity, and occasional confusion, to a greater extent. The amount of incredibly talented and enthusiastic people I have gotten the chance to learn from, and discover alongside with, has been amazing and showed me the strength of what combined efforts can do. This period in my life provided me with experiences that I could have only dreamt of as a little kid, and reinsured me my interest in aerodynamics was not misplaced as it grew to something much larger than just an interest I once had.

This thesis will mark the end of my studies at the Delft University of Technology and will be the final deliverable to obtain the degree of Master of Science in Aerospace Engineering. For my final months as a master's student, I desired to delve deeper in the world of low speed experimental aerodynamics and I am glad to have spend it at the Low Speed Laboratory of the TU Delft. There is a plethora of people I would like to thank for their support throughout this thesis and during the entirety of my studies here in Delft.

First of all, I want to express my gratitude towards my daily supervisor Dr. Theo Michelis, who impressively manages his tight schedule while simultaneously being one of the most approachable and easy-going persons I have ever met. His inviting, having the door open at all times, style of supervision is more than appreciated and strikes a good balance by offering all the help needed when necessary, but leaving enough room for figuring things out on your own. His enthusiasm of not only the topics at hand but also the willingness to explain more than the necessary, which often involved humor with a sprinkle of sarcasm, made our interactions a pleasant experience. As such, I can only say that it has been a pleasure of having Theo as my supervisor and I thank him sincerely for his support.

For the realisation of the experimental setup, I would like to thank the technicians of the Low Speed Laboratory; Emiel I. Langedijk, Dipl.-Ing. Stefan Bernardy, Ir. Martijn Looman and Ing. Gert-Jan M.A. Berends for their technical advice and help on the logistics and operation of the experiment. In a similar trend, I would like to express my thanks to Dr. Tomas Sinnige and Ir. Martijn van Sluis for lending and explaining to me the electrical motor and control system as well as their technical advice on dealing with experiments involving rotating objects.

Further thanks goes to Prof. Marios Kotsonis for welcoming me to the research group at the Low Speed lab and his valuable advice during the initial phases of the thesis project. Similarly, I would like to thank Prof. Leo L.M. Veldhuis for bringing me into contact with the people from the Low Speed Laboratory and introducing me to the topic of wind assisted ship propulsion. On the topic of wind assisted ship propulsion, I would like to express my thanks to Dr. Alberto F. Rius Vidales, for sharing his knowledge on this field in particular.

Inside and outside of the Low Speed Laboratory walls, fellow students, family and friends have been non other than supportive, which has been appreciated greatly. Special thanks goes to everyone who I had the pleasure to work with during my multiple years spent at Formula Student Team Delft. Here our teamwork and combined passion for motorsport and engineering made us thrive to overcome numerous of challenges and I wish them all the best for the future to come.

My final thanks go to the people that are the dearest to me, whom have encouraged me to pursue my passions, provided me with unwavering support and believed in me throughout all these years. My appreciation for them goes well beyond to what is written down here. To my significant other, Lisa, who's honesty and genuine caring character I highly value and has encouraged me countless times to see things from another perspective and to try things differently at the moments I get stuck. To my brother, Donny, who's strength and resilience is unparalleled, which inspires me deeply every day, and to my sister in law, Maaike, for her continued interest in the work I do. Their combined efforts of always finding a way to cheer me up is highly appreciated. At last, to my parents, without whom, all things considered, I would not have been able to live these years as I did. Their love, support and encouragement to let us find and pursue the things we want most in our lives is beyond comprehension. I could not be more grateful and proud to be their son.

Kenny C. van Gaalen
March 17, 2025
Delft, The Netherlands

Abstract

An alarming rise in greenhouse gas emissions for the shipping industry has been ongoing for many years. In 2012, it was stated in the report from Anderson and Bows (2012), that without measures, emissions will rise at unprecedented rates. Over the last decade this proved to be an increase of 20% in total GHG emissions by the world fleet, while it is further projected that the maritime trade sector will continue to grow with roughly 3% over the period between 2024 and 2028 (United Nations Conference on Trade and Development, 2023).

To combat this alarming trend, the International Marine Organization and International Chamber of Shipping are pushing for a more sustainable shipping industry to reach net-zero GHG emissions by or around 2050 (International Maritime Organization, 2023). As a result, research in fuel efficient propulsion systems and sustainable fuels is actively being pursuit. Among such research, a proven concept of the past that yields great potential in the reduction of shipping GHG's, is wind assisted ship propulsion or for short WASP. In particular, the Magnus effect driven Flettner Rotor, a rotating cylinder concept placed upright on the deck of a ship, is on the forefront of promising candidates, mainly due to its substantial aerodynamic force producing capabilities and its relatively low power consumption compared to more conventional ship propulsion.

At the Low Speed Laboratory of the Delft University of Technology, investigations on such rotating cylinder devices is desired, where a particular focus on large scale wind assisted ship propulsion applications will be given in the future. To accommodate this research, the work presented in this report is aimed to fulfil the following main objectives;

1. Development, design and realisation of a suitable experimental setup that can be used as a basis for future research on rotating cylinders up to critical Reynolds numbers.
2. Aerodynamic characterisation of the experimental setup by conducting a series of experiments, from which reference curves will be generated and a general understanding of the setups capabilities established.

Additionally, as there are many unknowns regarding testing of rotating cylinders at high blockage ratios, and a large full scale is considered when looking into wind assisted ship propulsion applications, this project further aimed to investigate the effects of testing at a high blockage ratio. As a result, the viability of large blockage ratio testing of rotating cylinders is evaluated to enable higher critical Reynolds number testing in smaller scale wind tunnel facilities. As such, the research attempts to realise, test and validate an experimental setup for rotating cylinders by answering the following main research question:

Main research question

"What are the aerodynamic characteristics of a two-dimensional rotating cylinder in uniform subsonic flow at subcritical Reynolds numbers and high blockage ratio?"

The project has been conducted in the Low Speed Laboratory of the Delft University of Technology by making use of the newly configured open-return low turbulence SLT wind tunnel facility. The aerodynamic characteristics are obtained by the utilisation of force measurements, encoder rpm readouts and low speed planar particle image velocimetry flow visualisation. By comparison with available data in literature, the existence of known aerodynamic characteristics of a rotating cylinder were tested and discrepancies analysed. Proper orthogonal decomposition analysis enabled the visualisation of the flow fields dominant characteristics, where a particular focus was put on the identification of vortical structures.

During the course of the project and the initial experimental campaign, various inconveniences and unexpected delays were encountered that altered the quality and contents of the research performed. The outer surface of the cylinder model remained non-machined and resulted in an approximate 1 mm variation in external diameter at the centre section. Furthermore, a balancing procedure of the rotating model had been established and was performed in-house, which was cut short due to time constraints. Consequently, the experiment was conducted at lower subcritical Reynolds numbers following set maximum rpm restrictions to 3820 rpm, which in turn limits the obtainable spin ratio range at a given Reynolds number. Moreover, although lowered, the downstream centre spanwise beam of the support structure is believed to interfere with the tunnel jet in specific conditions, adding another factor of uncertainty. At last, due to the unavailability of delta pressure measurements for the determination of the free stream velocity, a pitot-static probe was used to determine the free stream velocity at the stationary cylinder case only, as it was found to be affected by the influence of the cylinder when rotation was added. For future experiments it is recommended to improve these aspects of the experimental setup.

The performed experiments concerned three cases at subcritical Re_D = 62500, 125000 and 250000 with spin ratio ranges equal to $0 \leq k \leq 8$, $0 \leq k \leq 4$ and $0 \leq k \leq 2$ respectively. The lower than anticipated Reynolds numbers meant the uncertainty in the instantaneous force measurements increased substantially due to force sensor sensitivities, whereas the presented mean force coefficient data remained to be accurate due to large sample sizes. Comparable to full scale wind assisted ship propulsion applications and existing literature, an aspect ratio of the cylinder model equal to 4.5 was chosen. As a result, the area blockage ratio deliberately reached an unconventional high 33%.

The open test section with side walls installed of the current setup, resulted in a force coefficient behaviour that resembles closest to the three-dimensional cylinder with stationary endplates at subcritical Reynolds numbers up to k = 2.5. Although the magnitudes of the force coefficients do not match with other similar experiments, owing to the large blockage ratio and variations in experimental setup, the experimental trends in the force coefficient curves are fully captured, with the exception for spin ratios beyond k > 2.5, where interference effects appear to become more dominant.

Between $0 \leq k \leq 0.8$, the aerodynamic characteristics are affected by both the Reynolds number and spin ratio, where differences in boundary layer transition, laminar separation bubble formation, boundary layer lengths and vortex shedding behaviour are the underlying mechanisms causing a change in the obtained force coefficients. Within this range and at these specific Reynolds numbers, reversal of the Magnus effect can occur. The reversal effect is stronger and occurs earlier at the larger Reynolds numbers tested. Beyond k > 0.8, advancing side boundary layer transition has taken place for all Re_D. The force coefficients and flow field topology showed great similarities between the different Reynolds numbers with a further increase of the spin ratio, for which both the lift and drag coefficient increases. Slight variations in turbulent kinetic energy production were observed in the retreating side boundary layer and shear layer behaviour, possibly owing to laminar to turbulent transition. For k > 2.0 the periodic shedding of vortical structures is no longer observed, which coincides with the formation of the highly turbulent rotating boundary layer, settling of the near-wake, and a knee in the force coefficient curves within the range of $2.2 \leq k \leq 2.6$. The remainder of the spin ratios, k > 2.6, showed to deviate substantially from literature. At these large spin ratios, the flow field has completely reversed and is pointed in opposite direction of the incoming free stream, where large negative mean drag coefficients are recorded. This is believed to be the result of unsteady nozzle-model gap interactions with the separated region of the cylinder as a cause of the large blockage ratio.

The large blockage ratio and close nozzle proximity seems to cause the stagnation region in-front of the cylinder to extend into the nozzle and appears to have an increased effect at the larger subcritical Reynolds numbers. At k = 0 it is speculated that the combination of increased nozzle and support beam interference causes the results for Re_D = 250000 to deviate from expectations to a larger extent. Additionally, with an increase of the spin ratio the ability of the cylinder to deflect the tunnel jet in its entirety increases. At the lower Reynolds numbers the cylinder appears to be more effective in working against the tunnel jet, where an increased blockage of the upper nozzle-model gap is the result. It is speculated that as a result the inflow conditions changes and an increasingly larger portion of the

tunnel jet is forced through the lower nozzle-model gap, increasing the velocity and tilting the flow field as a whole. This results in the recorded negative mean drag coefficients and lowering of the mean lift coefficient, where the unsteady nature of this phenomenon further results in large fluctuations in the instantaneous force coefficients. Consequently, discrepancies in the force coefficients behaviour between the different Reynolds numbers is believed to be a result of these interference effects, for which it is further expected that, dictated by the blockage ratio, similar interference effects occur for closed section testing at high spin ratios.

Depending on the contents of future research, it is either recommended to increase the model distance to the nozzle outlet and decrease the blockage ratio, or if interested, perform investigations into the sensitivity to the blockage ratio and nozzle proximity. These investigations can be extended to the effects of open and closed section testing. At high spin ratios, the region between the nozzle-model gap, when open, or wall-model gap, when closed, is worth investigating as in full scale operations such devices tend to run at these high spin ratios, resulting in potential large discrepancies between the results.

On the topic of fundamental research, the state of the retreating side boundary layer and the highly vortical rotating boundary layer could be other topics of interest following the presented work, as the associated mechanisms are not yet fully understood. Additional topics, such as the effects of compressibility, free-stream turbulence and interaction effects with the tunnel boundary layer or wall model junction could further provide valuable insights to improve comparisons of results between different experiments in the future.

Contents

List of Figures

List of Tables

Nomenclature

Abbreviations

BL	Boundary layer
CFD	Computational Fluid Dynamics
CPR	Cycles per Revolution
DNS	Direct Numerical Simulation
F.O.V.	Field of View
FS	Frequency Spectrum
GHG	Greenhouse gas
ICS	International Chamber of Shipping
IMO	International Marine Organization
L	Laminar state
LSB	Laminar Separation Bubble
PCA	Principal Component Analysis
PIV	Particle Image Velocimetry
POD	Proper Orthogonal Decomposition
RANS	Reynolds-Averaged Navier-Stokes
rms	Root mean square
sCMOS	scientific Complementary Metal Oxide Semiconductor
SLT	Slow Low Turbulence Tunnel
T	Fully turbulent state
TG	Taylor-Görtler vortices
TrBL	Transition in boundary layer state
TrSL	Transition in shear layer state
TrW	Transition in wake state
URANS	Unsteady Reynolds-Averaged Navier-Stokes
VT	Vortex tubes
WASP	Wind Assisted Ship Propulsion
WT	Wind Tunnel

Physics symbols

$\Delta\vec{v}$	Particle image velocity	$[m/s]$

$\Delta\vec{x}$	Particle image displacement	$[m]$
ν	Kinematic viscosity	$[m^2/s]$
ω_f	Angular frequency	$[1/s]$
ω_z	Vorticity on x - y plane	$[1/s]$
ϕ	Power spectral density	$[db/Hz]$
Φ^n	Spatial POD mode	$[-]$
ϕ_{uu}	Streamwise spectral densities of turbulence intensity	$[db/Hz]$
Ψ	Yaw angle	$[°]$
ρ	Air density	$[kg/m^3]$
ρ_∞	Freestream density of air	$[kg/m^3]$
σ	Standard deviation	$[-]$
θ	Angular position	$[°]$
θ_R	Angular position of resultant force w.r.t. incoming flow direction	$[°]$
θ_S	Angular position of separation point	$[°]$
ε	Surface roughness height	$[m]$
A	Aspect ratio	$[-]$
$Area_D$	Cylinder projected frontal area	$[m^2]$
$Area_s$	Cylinder surface area	$[m^2]$
$Area_W$	Wind tunnel cross-sectional area	$[m^2]$
B	Cylinder span	$[m]$
C	Coefficient of cross-correlation	$[-]$
$C_D^{'}$	Fluctuating coefficient of drag	$[-]$
$C_L^{'}$	Fluctuating coefficient of lift	$[-]$
C_{Df}	Coefficient of skin-friction drag	$[-]$
C_{Dp}	Coefficient of pressure drag	$[-]$
C_D	Coefficient of drag	$[-]$
C_f	Coefficient of skin friction	$[-]$
C_g	Center of gravity	$[m]$
C_L	Coefficient of lift	$[-]$
C_m	Coefficient of moment	$[-]$
$C_{p_{min}}$	Minimum pressure coefficient	$[-]$
$C_{p_{pow}}$	Coefficient of power	$[-]$
C_p	Coefficient of pressure	$[-]$
C_R	Coefficient of resulting force	$[-]$

C_T	Coefficient of torque	$[-]$
D	External cylinder diameter	$[m]$
D_e	Endplate diameter	$[m]$
E	Energy efficiency	$[-]$
E	Spatial POD mode relative energy	$[\%]$
e	eccentricity	$[-]$
F	Force	$[N]$
f	frequency	$[Hz]$
f_a	Sampling frequency	$[Hz]$
f_p	Pass frequency	$[Hz]$
f_s	Eddy-shedding frequency	$[Hz]$
F_x	Drag force	$[N]$
F_y	Lift force	$[N]$
I	Image intensity	$[-]$
k	Spin-ratio	$[-]$
k_{crit}	Critical spin-ratio	$[-]$
L_f	Length of eddy formation	$[m]$
L_w	Length of near-wake	$[m]$
M	Mach number	$[-]$
M_∞	Freestream Mach number	$[-]$
M_{crit}	Critical Mach number	$[-]$
m_C	Correction weight	$[kg]$
M_f	Optical magnification factor	$[-]$
m_{res}	Maximum residual weight	$[g]$
m_R	Cylinder weight	$[kg]$
m_{su}	Specific unbalance	$[gmm/kg]$
M_{tan}	Cylinder surface tangential Mach number	$[-]$
m_T	Trial weight	$[kg]$
N	Data samples	$[-]$
N_t	Number of time instances	$[-]$
N_x	Number of spatial locations in x	$[-]$
N_y	Number of spatial locations in y	$[-]$
P	Power consumption	$[W]$
Q	Peak ratio	$[-]$

Q_ω	Directional Q-criterion	$[1/s^2]$
Q_{crit}	Q-criterion	$[1/s^2]$
R	External cylinder radius	$[m]$
r_C	Correction radius	$[mm]$
Re	Reynolds Number	$[-]$
Re_D	Reynolds Number for flow past a cylinder	$[-]$
Re_{rel}	Relative Reynolds Number seen by the boundary layer of a rotating cylinder	$[-]$
St	Strouhal Number	$[-]$
St_D	Strouhal Number for flow past a cylinder	$[-]$
T	Temperature	$[K]$
t	time	$[s]$
t_a	acquisition time	$[s]$
T_i	Turbulence intensity	$[\%]$
T_s	Turbulence scale	$[m]$
t_s	t-score	$[-]$
t_w	Cylinder skin thickness	$[m]$
U	Velocity magnitude	$[m/s]$
u	x-component of the velocity vector	$[m/s]$
u_{95}	95% confindence expanded uncertainty	$[N]$
U_∞	Freestream velocity	$[m/s]$
u_{bias}	Standard bias uncertainty	$[N]$
u_m	Standard measurement uncertainty	$[N]$
U_{pitot}	Pitot-static probe measured velocity	$[m/s]$
U_r	Cylinder tangential velocity	$[m/s]$
v	y-component of the velocity vector	$[m/s]$
Δt	Pulse separation time	$[s]$
Λ	Diagonal matrix of eigenvalues	$[m^2/s^2]$
λ	Eigenvalue	$[m^2/s^2]$
TKE	Turbulent kinetic energy eigenvalues	$[m^2/s^2]$
a	Matrix of temporal eigenfunctions	$[-]$
R	Autocovariance matrix	$[m^2/s^2]$
S	Snapshot matrix	$[m/s]$

1 Introduction

The global transportation of goods is almost solely done through shipping, where it has been stated that around 90% of the world's trade is carried out by the international shipping industry (International Chamber of Shipping, 2014). As a consequence, a large 3% share of total global emissions in greenhouse gases, GHG's, owes to shipping alone. Over the period between 2012 and 2018 this share in global contribution remained at roughly 3%, however total GHG emissions by shipping grew with 9.3% (International Maritime Organization, 2020). Recently, the rise in total GHG emissions of the world fleet continued, as partially indicated by the increase of 20% in carbon dioxide emissions over the last decade, Figure 1.1. This, in combination with a more than 3% projected growth of the maritime trade sector over the period between 2024 and 2028 (United Nations Conference on Trade and Development, 2023), becomes an alarming prospect if no measures are taken in the near future.

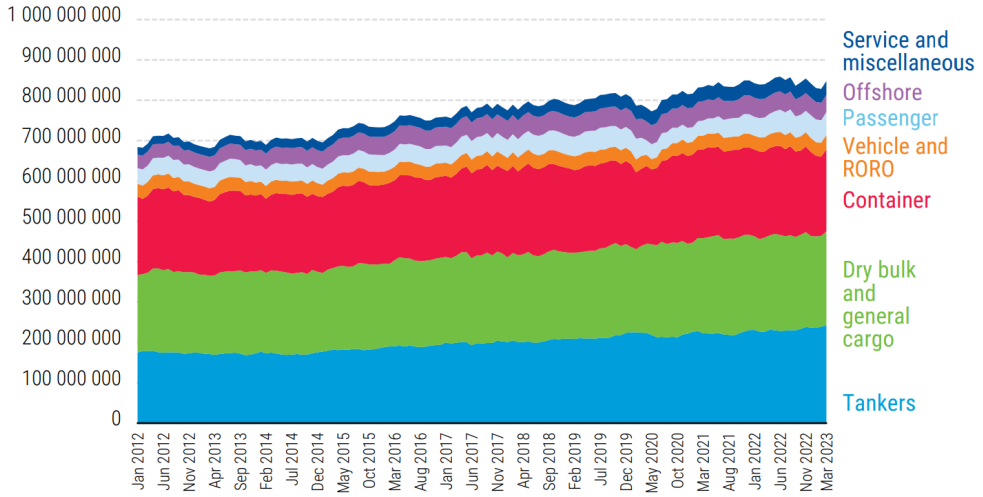

Figure 1.1: Carbon dioxide emissions by main vessel types in tons between January 2012 - March 2023 (United Nations Conference on Trade and Development, 2023).

Historically as the shipping industry is driven by its operational costs, low fuel prices makes it unattractive for the more convenient fossil fuel propeller driven ships to make way for sustainable innovations. Only in a short period after the oil crisis of the seventies, a push was made for introducing more sustainable means of transport. Unfortunately, following plummeting oil prices in the years after, and the lesser emphasis put on environmental aspects at the time, efforts were put aside.

In today's world, the need for sustainable innovations has made a resurgence. Now on the grounds of not only an economical basis, but also the environmental aspects are considered extensively. Strict regulations on greenhouse gas emissions have been set out by the International Marine Organization, IMO, the regulator of international shipping, back in 2018. In 2023, a revised version has been released

to further cement the sustainable future of international shipping, with the goal to reach net-zero GHG emissions by or around 2050 (International Maritime Organization, 2023).

This vision of a sustainable future is shared by the largest trade association for shipping, the International Chamber of Shipping, ICS. Recently, the ICS is proposing pricing mechanisms on emissions to accelerate the transition to a more sustainable industry, and hence making it more attractive for ship owners to make the switch to alternative ship propulsion and more sustainable fuels (International Chamber of Shipping, 2024a, 2024b).

As a result of the global need in cutting GHG emissions, and the combined efforts of governing parties on realising such a feat, research surrounding sustainable shipping has spiked again. A particular active area that saw a resurgence in interest has been on the development of wind assisted ship propulsion or for short WASP. Over a span of a hundred years, especially during specific periods of interest, e.g. the seventies oil crisis, many different devices have been extensively investigated.

Bergeson and Greenwald (1985) summarized various devices and it was shown that one of such devices, the rotating cylinder or Flettner Rotor placed upright on a deck of ship, could provide substantially large forces for a given surface area compared to other types, e.g. wingsails or soft sails, see Figure 1.2. It was further stated that besides its promising force producing capabilities, the Flettner rotor possesses additional benefits due to it being a storm proof and relatively simple system. Therefore, it could be used for an extensive range of weather conditions and ship types, hence yielding large potential in the reduction of shipping GHG's.

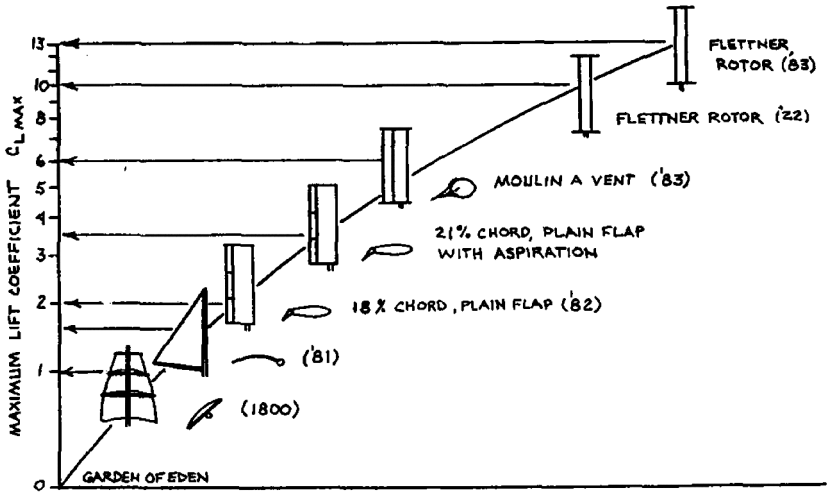

Figure 1.2: Comparison of maximum lift coefficient for various lift generating devices (Bergeson & Greenwald, 1985).

The implementation of such rotors on new or existing ships and its potential benefits are however affected by many factors. Under the right circumstances, e.g. taxation rates, shipping routes and wind directions, it has been shown that as of now a reduction of fuel consumption of up to 20% may be achieved, resulting in reductions of GHG's as well as increased economic benefits for the ship owners (Talluri et al., 2018).

Largely because of this and aforementioned reasons, the Flettner Rotor has been on the forefront of wind assisted ship propulsion ever since its introduction dating back to the 1920s. The Flettner rotor was named after its inventor Anton Flettner, who successfully implemented multiple instances of the device on ships as their main propulsive source. First on the modified ship *Buckau*, which was equipped with two Flettner rotors and made its maiden voyage across the Atlantic Ocean in 1926, Figure 1.3a. And later, the larger and purposely built Flettner rotor ship *Barbara* with three installed Flettner rotors, which served as a freighter between 1926 and 1929 across the Mediterranean Sea, Figure 1.3b. Unfortunately, as mentioned before, the more convenient diesel powered propeller ships quickly took over after these early successes.

To reach the goal of net-zero GHG emissions by 2050 as layed out by the IMO in the battle against global warming, research on the improvement of the Flettner Rotor's performance is ongoing and needed. In particular the aerodynamic performance, as it is the cause of the propulsive capabilities, has been an active field of research. Therefore, this master thesis project concerns the aerodynamic performance of a rotating cylinder used as a propulsive device for wind assisted ship propulsion.

The structure of the report is as follows. Chapter 2 presents the state-of-the-art in rotating cylinder research with a specific focus on thrust producing applications. Firstly, the fundamentals of isolated non-rotating cylinder flow are discussed, such that a basis on the aerodynamic principles involved are established. From these general principles the rotating case is extensively covered in the subsequent sections, covering both numerical and experimental findings on fundamental and applied topics. The findings are then used to formulate the research problem which is presented at the end of the chapter. The experimental setup used to achieve the outcomes of the presented research is then in detail described in chapter 3, where model design, experimental techniques, listing of equipment used and constraints are covered. Measurement and post-processing methodologies are explained in chapter 4, followed by the presentation, analysis and discussion of the results in chapter 5. The conclusions drawn out of this research are presented in chapter 6. At last, chapter 7 shares an evaluation of the performed research yielding recommendations for future research and use of the experimental setup.

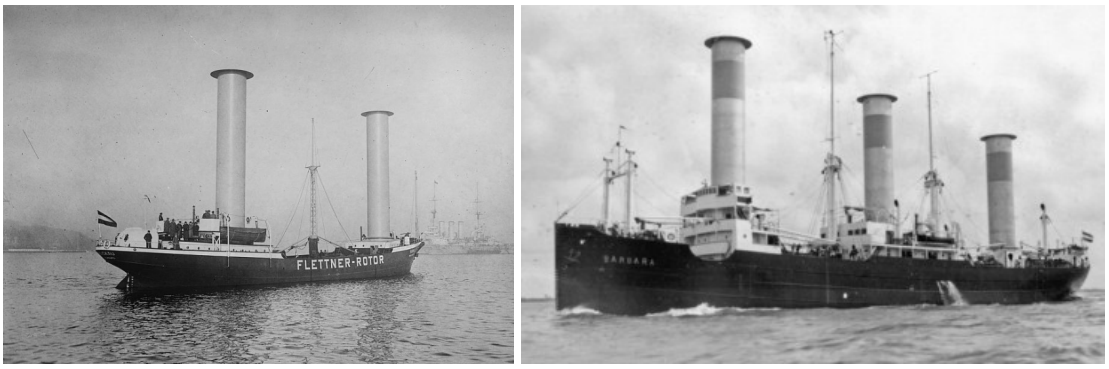

(a) *Buckau (Bain News Service, n.d.)* (b) *Barbara (Seifert, 2012)*

Figure 1.3: Flettner Rotor ships; (a) *Buckau*, (b) *Barbara*.

2

Theoretical background

This chapter summarises the findings in literature on rotating cylinder research and presents the formulation of the established project. Section 2.1 first lays down important theories and concepts applicable to both stationary and rotating cylinders placed in a flow. Then, section 2.2 and section 2.3 present a comprehensive summary of the state-of-the-art in aerodynamic rotating cylinder research, covering fundamental and applied topics using both numerical and experimental results. Finally, section 2.4 concludes this chapter by presenting the formulation of the established research objectives, questions and limitations based on the discoveries made in literature.

2.1. Introduction to the fundamentals of a stationary cylinder in subsonic flow

Although not the focus of the research, some important aspects of non-rotating cylinder flow are covered in this section. Mainly, to explain the flow regimes present when varying the Reynolds number, to be covered in subsection 2.1.1, such that the terminology used is clear when rotation is added in section 2.2 and the rest of the report. These Reynolds number regimes are of importance as it allows to explain flow phenomena that would also occur on the rotating cylinder case and helps in separating the effects due to rotation and scaling when comparing model scale to full scale applications. The non-rotating cylinder flow has been extensively researched. Mainly, this has been due to the combination of its simple geometry and the highly complex flow phenomena present that varies with changing Reynolds numbers. For many of the studies performed the non-rotating cylinder has served as an primary case for fundamental aerodynamic research, as well as an excellent test case for numerical algorithm bench marking, of which Schäfer et al. (1996) for laminar flow and Ye and Wan (2017) for turbulent flow are merely two examples. As this section will only cover some aspects on the fundamentals of non-rotating cylinders in subsonic flow, it is advised to consult the books from Zdravkovich (1997, 2003) as they are often considered to be the most comprehensive and complete set of literature on cylinder flow at the time.

2.1.1. Reynolds number regimes for disturbance-free flow

The circular cylinder is considered to be a *bluff body*. Bluff bodies are characterized by a large and often unsteady wake that is left behind by the body when placed in a flow. In case of a circular cylinder, the absence of sharp edges on its surface results in the ability of the separation points to move. This movement is initiated by changes in flow conditions within the disturbed flow regions surrounding the cylinder, and flow structures present in the wake region (Zdravkovich, 1997). This makes circular cylinder flow a highly dynamic problem, which will be further influenced by the addition of rotation, see section 2.2.

The state of the disturbed flow regions around a circular cylinder in a disturbance-free flow is governed by the Reynolds number, Re. The Reynolds number was named after Oswald Reynolds due to the discoveries he made through his experiments on flow transition in a smooth pipe (Reynolds, 1883).

The Reynolds number is the non-dimensional ratio of the inertial forces to viscous forces, which determines, without the presence of large disturbances, the transition of flow from laminar to the turbulent state after a critical value is reached. Importantly, it is useful to note that in case of incompressible flow, dynamic flow similarity can be achieved between two different flows having the same Reynolds number. Hence wind tunnel model testing often aims for achieving the same or close to the same Reynolds number of the full scale applications, and if not possible an effort on understanding the scaling effects are being made.

The Reynolds number based on circular cylinder flow, Re_D, was first established by Rayleigh (1896) through the application of dimensional analysis. The Reynolds number is calculated using Equation 2.1, with U_∞, the freestream velocity, D, the characteristic length taken as the external cylinder diameter, and ν, the kinematic viscosity.

$$Re_D = \frac{U_\infty D}{\nu} \tag{2.1}$$

Depending on the value of Re_D, the disturbance-free flow around a circular cylinder is behaving in certain ways, where transitions occur in succession within the various affected flow regions. Based on this observation, distinct regimes of flow states are established and hence denoted as the Reynolds regimes. The main states are in the order of increasing Re_D, (fully) laminar, L, transition in wake, TrW, transition in shear layers, TrSL, transition in boundary layers, TrBL, and (fully) turbulent, T. Within these states many flow regimes exists based on the flow phenomena present. An complete overview of the Reynolds regimes for disturbance-free flow, recreated from the table in Zdravkovich (1997), can be found in Table 2.1, where L_w is the length of the near-wake, L_f, the length of the eddy formation, and C_D, the coefficient of drag. The + and - indicate increasing or decreasing behaviour of the quantity in question, with multiple instances indicating the severity of the effect. Complementing the table, a representation of the given flow regimes for a non-rotating circular cylinder in subsonic flow can be viewed in Figure 2.1.

Table 2.1: Disturbance-free flow regimes for non-rotating cylinders (Recreated from (Zdravkovich, 1997)).

STATE		REGIME		Re_D RANGES	L_w/L_f	C_D
L	LAMINAR	1	NO-SEPARATION	0 to 4-5	NONE	-
		2	CLOSED WAKE	4-5 to 30-48	+	-
		3	PERIODIC WAKE	30-48 to 180-200	-	+
TrW	TRANSITION IN WAKE	1	FAR-WAKE	180-200 to 220-250	-	+
		2	NEAR-WAKE	220-250 to 350-400	+	-
TrSL	TRANSITION IN SHEAR LAYER	1	LOWER	350-400 to 1k-2k	+	-
		2	INTERMEDIATE	1k-2k to 20k-40k	-	+
		3	UPPER	20k-40k to 100k-200k	SAME	SAME
TrBL	TRANSITION IN BOUNDARY LAYER	0	PRECRITICAL	100k-200k to 300k-340k	+	-
		1	SINGLE BUBBLE	300k-340k to 380k-400k	?	--
		2	TWO-BUBBLE	380k-400k to 500k-1M	?	--
		3	SUPERCRITICAL	500k-1M to 3.5M-6M	NONE	+
		4	POSTCRITICAL	3.5M-6M to (?)	?	SAME
T	FULLY TURBULENT	1	INVARIABLE	(?) to ∞	?	SAME
		2	ULTIMATE	(?) to ∞	?	?

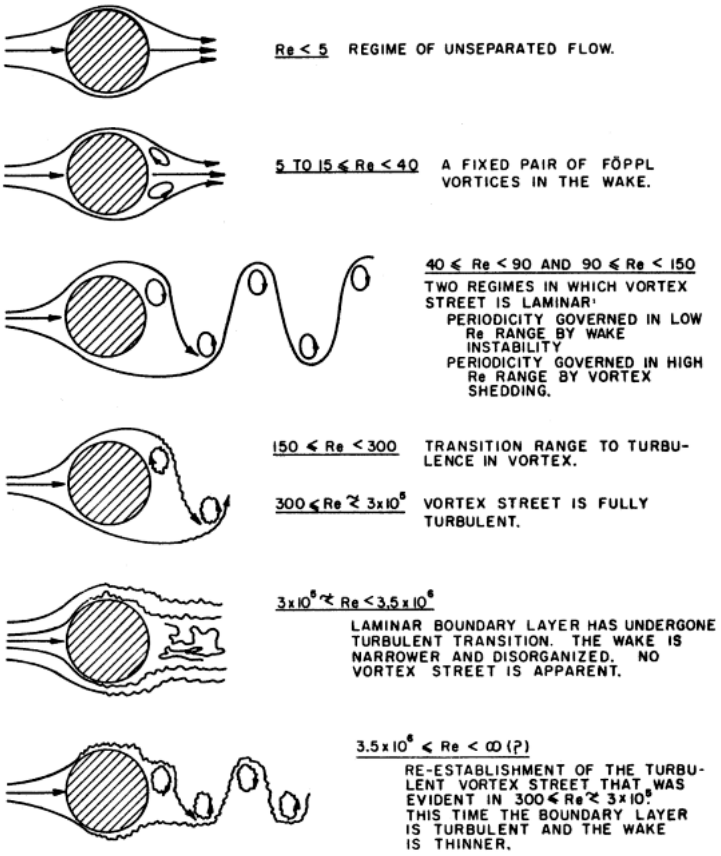

Figure 2.1: Regimes of fluid flow across circular cylinders (Lienhard, 1966).

Applying these findings to the applications of thrust producing devices located on the deck of ships, the state of the flow around is predominantly within the upper TrBL and T regimes, where Reynolds numbers are in the order of a few millions. This has to do with the large scale of the characteristic external diameter reaching several meters, as is the case for current commercially available Flettner rotor devices.

As these large sizes and corresponding large Reynolds numbers bring many impracticality's for both numerical and experimental investigations, it often leads to lower Reynolds number being tested. In case of wind tunnel testing the limitations are often due to the maximum size of the test section and maximum achievable freestream velocities, and will be covered in more detail in section 3.1. While in numerical testing, the spatial and temporal resolutions needed increases significantly with increasing Reynolds number, as well as an increased risk of solver instabilities due to the lesser influence of the stabilizing effects due to viscosity.

Concerning these limitations, investigations on marine scale Flettner rotor applications are more likely to fall within the upper TrSL and lower TrBL regimes. Only limited literature is available at the larger Re regimes which will follow in section 2.2. The L and TrW regimes are therefore not further covered in detail, but for the interested reader the early works from Bérnard (1908a, 1908b), Von Kármán (1911) and Von Kármán and Rubach (1912) on the laminar regime and Roshko (1954) on the TrW regime as well as the overview given by Zdravkovich (1997) are a recommended start.

The transition in shear layers regime, often denoted as the subcritical regime, is characterised by its fully laminar boundary layer before the separation points, resulting in all transitions taking place along the shear layer created between the freestream and wake region, Figure 2.2. The shear layers start of as laminar and become turbulent in the following three phases with increasing Re_D.

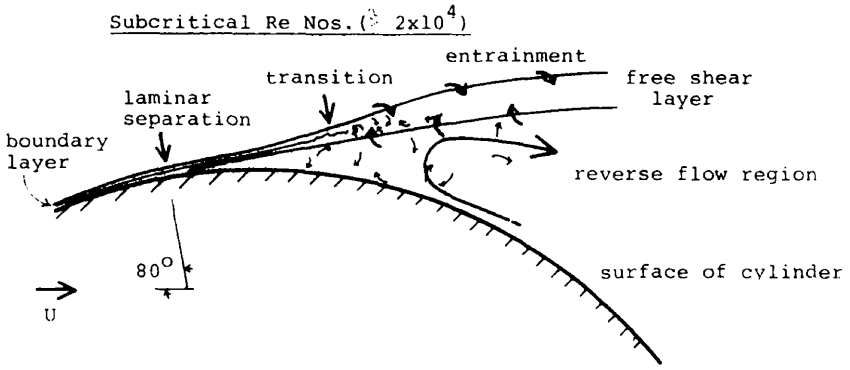

Figure 2.2: Representation of the transition in shear layer regimes near the separation point (Basu, 1985).

At the lower TrSL1 regime, transition waves are formed along the shear layer and a stabilized near-wake is present. These waves are then rolling up into transition eddies in the intermediate TrSL2 regime, which are formed closer and closer towards the separation points. Then in the final upper TrSL3 regime the transition to turbulence is immediate and close to the separation points accompanied by a small near-wake with the formation of eddies close to the rear surface of the cylinder (Zdravkovich, 1997).

The transition in boundary layers regime is often denoted as the critical regime. It is initiated by the precritical regime TrBL0, where the transition of the shear layers is first occurring along the separation lines in a three-dimensional fashion. This three-dimensionality results in the eddy formation to be delayed and a decrease in C_D is observed as a result of the vortices greater distance to the cylinder surface (Zdravkovich, 1997).

At a particular point the TrBL1 or one-bubble regime is initiated. On one side of the cylinder the transition of the shear layer is sufficient to form a separation bubble on the surface of the cylinder accompanied with turbulent reattachment (Bearman, 1969). The result is an asymmetric pressure distribution, a sudden jump to lower C_D due to a significantly delayed turbulent separation of the boundary layer, and increased eddy shedding frequency.

A further drop in C_D is observed when the same phenomena occurs on the other side of the cylinder in the TrBL2 or two-bubble regime, where eddy shedding frequency increases and the pressure distribution is restored to a more symmetric behavior (Zdravkovich, 1997). A closeup of the state of the boundary layer at the one-bubble and two-bubble transition in boundary layers regimes are depicted in Figure 2.3.

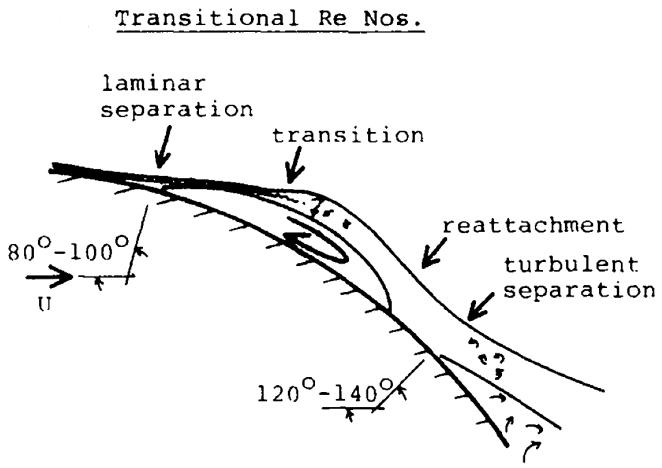

Figure 2.3: Representation of transition in the critical boundary layer regimes near the separation point (Basu, 1985).

The TrBL3 or supercritical regime is characterised by the transition of the boundary layer on the primary separation line in a fragmented manner, where the separation bubbles are destroyed and transition to turbulence occurs on the surface of the cylinder. The disappearance of separation bubbles in an irregular manner results in the ceasing of the periodic eddy shedding, which is another main feature of the TrBL3 regime. For visualisation and more detail on the TrBL0, TrBL1, TrBL2 and TrBL3 regimes the works from Naumann et al. (1966) and Bozhkov et al. (1980) can be consulted.

The final transition in boundary layers regimes is the TrBL4 or postcritical regime, where the formation of separation bubbles are no longer occurring along the span of the cylinder. The transition of the boundary layers to a turbulent state is therefore between the stagnation and separation lines of the cylinder and moves closer to the stagnation line with increasing Re_D in an asymptotical fashion (Zdravkovich, 1997). Additionally, at this state the regular shedding of eddies is reinstated (Roshko, 1961). A representation of the TrBL4 regime is depicted in Figure 2.4.

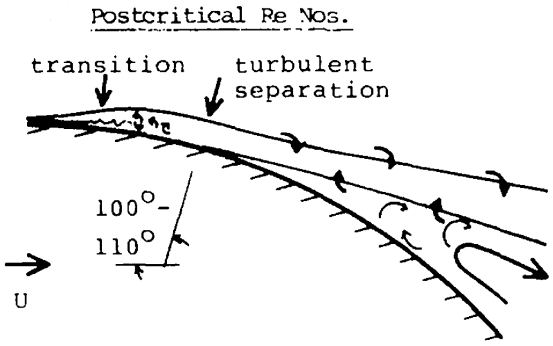

Figure 2.4: Representation of transition in the postcritical boundary layer regimes near the separation point (Basu, 1985).

When all the disturbed flow regions around the cylinder are transitioned to a turbulent state, the final regime is initiated. Within this final fully turbulent state the drag coefficient and eddy shedding are expected to be invariant with further increasing Re_D only when the Reynolds numbers remains as the governing parameter. In reality, at these very high Reynolds numbers, the Reynolds number is almost never the sole governing parameter as compressibility effects or cavitation, depending on the medium, will take over the governing role.

Finally, a summary of the variation in force coefficients across the different Reynolds regimes is given in Figure 2.5, where both the time-averaged and fluctuating coefficient of lift, C_L and C'_L, and the coefficient of drag, C_D and C'_D respectively are shown. The latter is further decomposed in the coefficients of skin-friction drag, C_{Df}, and pressure drag, C_{Dp}. From the figure it becomes apparent that the aerodynamics is of an unsteady nature at the TrSL2 regime and beyond as shown by the random fluctuations in the force coefficients. This is due to the shedding of the vortices and wake fluctuations present around the symmetrical cross-sectional shape as stated earlier within the various regimes.

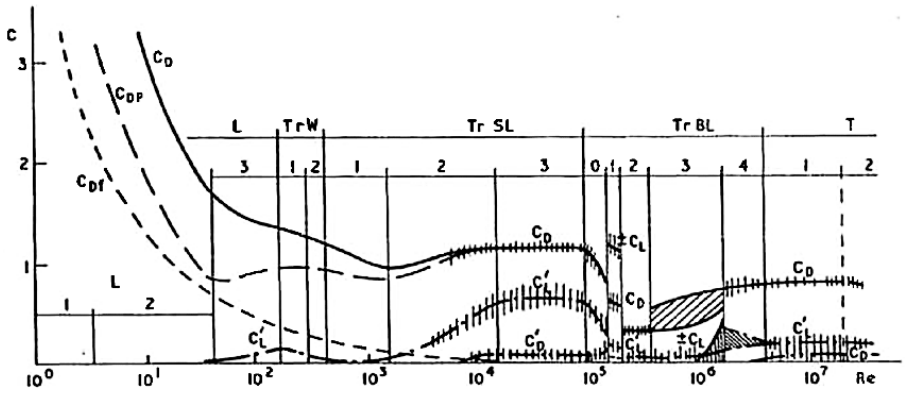

Figure 2.5: Force coefficients versus Reynolds number on a stationary cylinder in disturbance-free flow (Zdravkovich, 1997).

2.1.2. Strouhal number

When considering non-rotating and rotating cylinder flow, the Strouhal number, St_D, among the Reynolds number is another important parameter to address. The Strouhal number was established by Vincenc Strouhal following his experiments on vortex shedding and acoustics of wires (Strouhal, 1878). This non-dimensional number is the ratio between the inertial forces due to the local acceleration, to the inertial forces due to the convective acceleration of the flow, or in other words the measure of unsteadiness, Equation 2.2. It changes with the Reynolds number as well as the surface roughness, where f_s is the frequency of eddy shedding, D the diameter of the cylinder taken as the characteristic length, and U_∞ the freestream velocity.

$$St_D = \frac{f_s D}{U_\infty} \tag{2.2}$$

In case of a finite Strouhal number the variations of the force coefficient can change drastically due to the effects of the periodic vortex shedding. It has been observed that, for both the non-rotating and rotating cylinder, the magnitude of the random fluctuations in the lift direction, with a smaller effect on the drag, can be of the same order as the mean value of the net force acting on the cylinder (Swanson, 1961). Besides the unsteady aerodynamic behaviour, these fluctuations can lead to various practical difficulties on the full scale marine application, such as vortex induced vibrations, e.g. in offshore wind turbines (Yin et al., 2022).

For the non-rotating case, Lienhard (1966) established from published experimental data, available at that point of time, an overview on the effects of the Strouhal number for rigid cylinder flow. It included the relationship of the Strouhal number with the Reynolds number as depicted in Figure 2.6. Lienhard mentioned that especially the values within the critical regimes and fully turbulent state were not fully understood at the time and was therefore uncertain about the validity of the data within that regime.

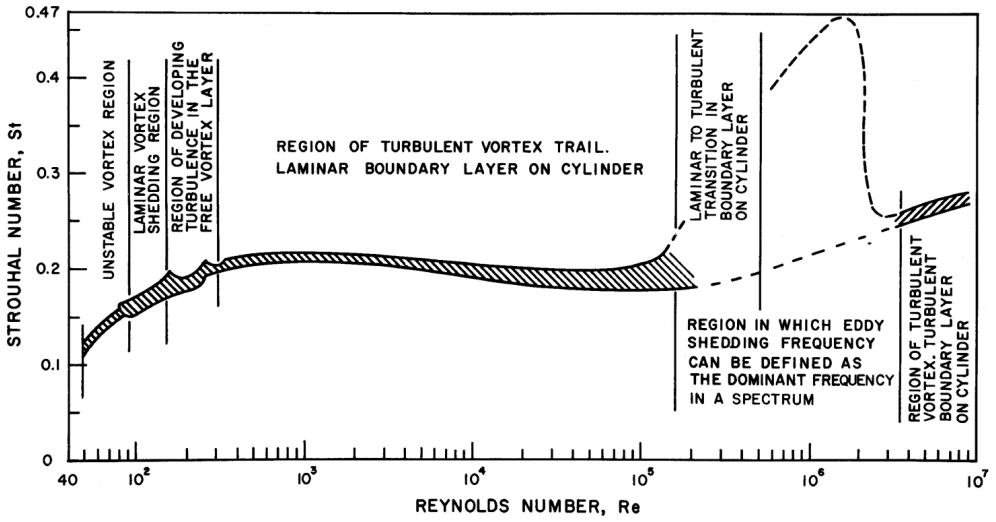

Figure 2.6: The Strouhal-Reynolds number relationship for circular cylinders (Lienhard, 1966).

In a more recent study from Yin et al. (2022), the established Strouhal-Reynolds relation from Lienhard was overlaid with a collection of modern day data from various sources, see Figure 2.7. The data proofs the predicted differences within the critical regimes as mentioned by Leinhard, however in general good agreement in the other states was found.

The Strouhal-Reynolds relation for the rotating cylinder case is influenced by the addition of rotation and will therefore no longer follow the same behaviour as shown in the figures above. The influence of rotation will be covered in the subsection 2.2.6.

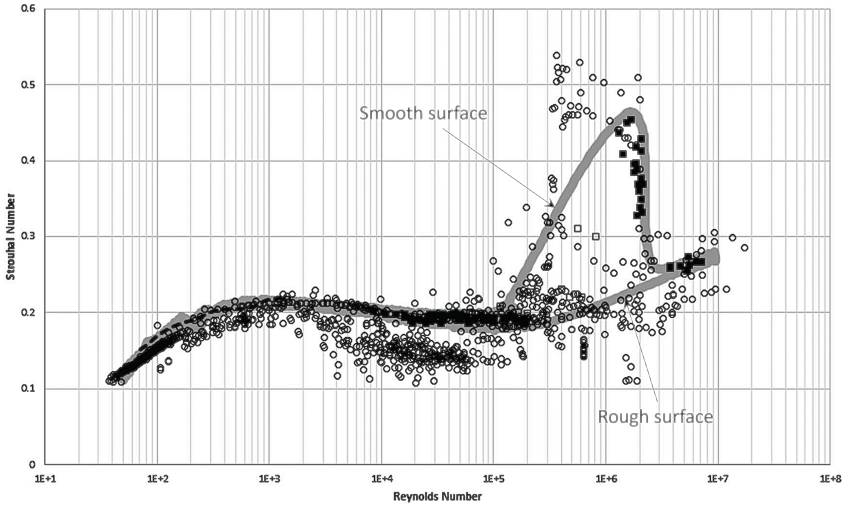

Figure 2.7: Strouhal-Reynolds relation based on the original figure from Lienhard added with modern day data (Yin et al., 2022).

2.1.3. Disturbances and influential parameters

Now that the importance of the Reynolds number and strouhal number are explained for near to ideal flow conditions, it must be stated that the flow around real-life applications of cylinders is often subjected to many more influencing parameters each affecting the state of the flow. These parameters, when sufficiently large, can be become the governing parameter and in turn initiate, skip or alter the Reynolds regimes discussed in the previous section (Zdravkovich, 1997). The same influencing parameters will hold for the rotating case and hence it is important to be aware of the most typical disturbances.

Without going into too much depth as each disturbance can be a complete field of research on its own, and following the statements made by Zdravkovich (1997) on disturbances, the typical disturbances found in freestream or controlled wind tunnel testing environments are: freestream turbulence, surface roughness, wall blockage, wall proximity, aspect ratio, free end conditions, and both longitudinal and lateral oscillations. An overview of the disturbances is given in Figure 2.8.

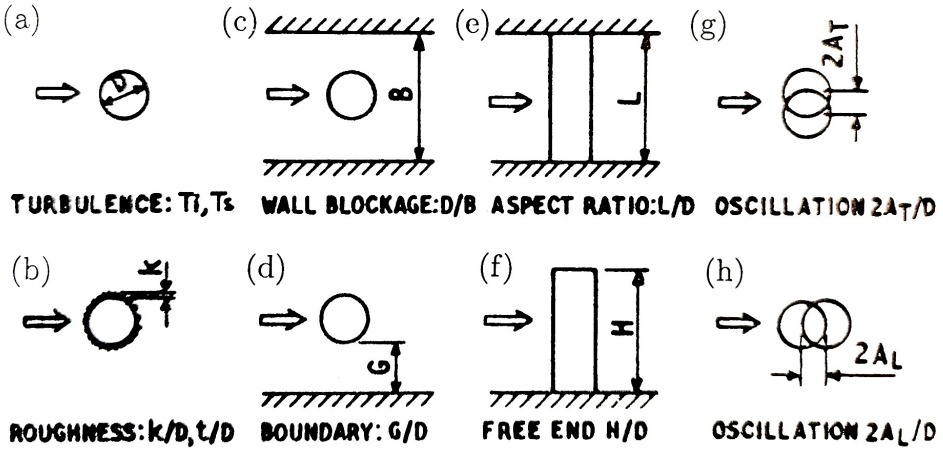

Figure 2.8: Typical disturbances; (a) freestream turbulence, (b) surface roughness, (c) wall blockage, (d) wall proximity, (e) end effect, (f) free end, (g) transverse oscillation, (h) streamwise oscillation (Zdravkovich, 1997).

Freestream turbulence affects strongly all of the transition states and depending on the setup a large scatter of data between different experiments can be the result of it. The freestream turbulence is quantified by three parameters, namely the turbulence intensity, or the ratio of the rms streamwise

fluctuating velocity and the time averaged velocity, T_i, the turbulence scale, or integral length scale, T_s, and the frequency spectrum of the random fluctuations in the three-dimensional components of the velocity, FS. If there is a sufficiently large T_i and T_s smaller than the cylinder diameter, D, the freestream turbulence will become a governing parameter as a consequence of the imposed pressure gradients of which transition is particular susceptible (Zdravkovich, 1997).

The effects of the freestream turbulence have been well documented for a non-rotating cylinder. Thangadurai et al. (2017) performed experiments for a non-rotating cylinder at laminar and subcritical Reynolds numbers, 500 < Re_D 32000, for varying levels of freestream turbulence. It has been noted that freestream turbulence is mainly promoting boundary layer transition, due to its energizing effects, and hence causing delayed separation, thinning of the wake, a reduction of the drag coefficient and increased eddy shedding frequency.

The underlying process of promoting the boundary layer transition is due to the interaction of amplified eddies in the freestream with the boundary layer. The scales of turbulence in the freestream are amplified due to vortex stretching in close proximity to the stagnation point, and are of the same order as the thickness of the boundary layer (Kwok, 1986). Hence, it may be expected that for the rotating case the one-bubble and two-bubble regimes will occur at lower subcritical Reynolds numbers with an increase of the freestream turbulence, but is for now unconfirmed.

Hence for proper comparison of data, these parameters should be known and noted beforehand with any setup to arrive at correct conclusions of the effects observed. For further details on the effects of freestream turbulence in general, the comprehensive review from Bearman and Morel (1983) is advised. Unfortunately for the rotating cylinder it is believed no such studies have been performed as of now.

The effectiveness of surface roughness is determined by the relative size of the roughness elements compared to the cylinder diameter, as well as the general texture and shape. The surface roughness is especially important on the state and behaviour of the boundary layer due to its application on the surface of the cylinder. The effects of roughness on the rotating cylinder will be addressed shortly in subsection 2.3.4.

For wind tunnel testing the addition of walls for closed test sections will impose additional pressure gradients on the flow. These pressure gradients may influence both the free shear layers and boundary layers at high wall blockage ratios. The ratio is measured as the ratio between the model projected frontal area and test section cross-sectional area, $Area_D/AreaW$. In a similar but asymmetric manner, a single wall placed in close proximity to the cylinder will result in additional pressure gradients on one side. In this case the gap size to cylinder diameter is the influencing parameter. Typically for wind tunnel testing, correction methods are in place to address these effects, however for the case of rotating cylinder flow this is less trivial and will be further elaborated upon in section 3.2.

The aspect ratio, A, is the ratio of the cylinder span, B, over the cylinder diameter, D, which has a pronounced effect on the aerodynamic efficiency similarly to airplane wings. In case of a cylinder with a free end, the introduction of tip effects will have significant influences for both the non-rotating and in particular rotating cylinder. Formation of tip vortices and pressure equalisation at the free end result in changes of the pressure distribution along the span of the cylinder, which in case of a small aspect ratio will become governing. For the rotating cylinder these effects are amplified and will be covered in more detail in subsection 2.2.12 as well as the effects of the aspect ratio in subsection 2.2.4.

At last, the effects due to vibrations are especially detrimental on affecting the Reynolds regimes when high enough amplitudes and or frequencies are reached. Hence a stiff and well-balanced system is particularly important for the aerodynamic behaviour of the cylinder.

2.2. Fundamental rotating cylinder aerodynamics in subsonic flow

Following the important fundamental aerodynamic concepts of a stationary cylinder placed in a subsonic flow, the effects of rotation will be covered extensively in this section. The section will start with a brief history on the discovery of the driving principle behind the rotating cylinder, now better known as the ”Magnus effect”, which preceded the works from Anton Flettner. Then the Magnus effect will be covered in more depth, where the influencing parameters and their effects are explained, the varying flow phenomena and regimes due to rotation are shown, and boundary layer behaviour is explained. Force characteristics within the various Reynolds number regimes will be covered throughout the chapter. Additional topics such as the power consumption, compressibility effects and the three-dimensional case of the rotating cylinder, will be covered at the end of this chapter.

2.2.1. Brief history on the discovery of the Magnus effect and its marine application

The first in history recorded observations of the Magnus effect and an attempted explanation is said to have come from Isaac Newton in an letter to Oldenberg in 1671. Here, he described the observations he made on the curved trajectory of a tennis ball after being struck by an oblique racket. In his explanation, he correctly used his observation that the ball received both a circulatory and progressive motion and that where the motions conspire a proportionally larger reaction of the air close to the ball shall occur (Seifert, 2012).

Many years later, the same phenomenon was found to be a problem in gunnery, where the deflection of projectiles, e.g. bullets and shells, was investigated first by Robins (1805). Robins described that bullets travel with both a progressive and a whirling motion and concluded that in the region where the whirling motion acts with the progressive one, the air resistance is increased and hence causes the bullet to deflect.

The proof of the existence, and subsequent naming, of the Magnus effect followed from the qualitative experiments performed by Gustav Magnus (1853). The experimental setup consisted out of a brass cylinder constrained between two bearings, which was then in its entirety supported on a freely rotating frame through two connecting arms. The freestream flow was provided by a blower and the cylinder rotation was initiated by the use of a string. It was shown that the cylinder was deflected to the side where the rotation was acting in the same direction as the wind direction immediately after rotation was applied.

The first attempt on numerically explaining the curved trajectory of a tennis ball affected by the now discovered Magnus effect was made by Rayleigh (1877). Within the research paper, Rayleigh tried to calculate the force as a result of the Magnus effect from the pressure distribution around a rotating body by setting up the potential flow solution of a cylinder with circulation. However, due to the lack of mathematical methods explaining the influence of friction between the fluid and the cylinder surface and how this would then result in the production of circulation, meant Rayleigh was sceptical on the validity of the results.

Lafay (1912a) was the first on records to perform quantitative experiments on rotating cylinders. In his work, Lafay showed that a rotating cylinder was able to produce a force much larger compared to a plane surface with the same projected area. He further showed the distribution of pressures around the cylinder surface as well as on how the streamlines are behaving in close proximity to the cylinder.

Shortly after, the invention of the Flettner rotor was a result from the works by Anton Flettner in the 1920s. Together with the Göttingen Research Group, he conducted many experiments on rotating cylinders. From these experiments, it was concluded that the thrust produced by the rotor was many times greater than the equivalent area of a sail and that the power necessary to rotate the rotor was much smaller than that of more conventional screw propulsion. From this point on it was clear that the Flettner rotor could be used as an attractive alternative for ship propulsion, sparking the interest of many researchers for years to come of which a selection will be presented in the rest of this chapter.

For further reading into the history, fundamentals and applications of the Magnus effect, the review paper from Seifert (2012) gives a detailed summary that serves as an excellent introductory read on the topic.

2.2.2. The Magnus effect

The incomplete and simplified explanation of the Magnus effect is often described from the frictionless and irrotational potential flow solution and Bernoulli's principle. The potential flow is represented by a doublet flow superimposed with a uniform freestream and a bound vortex, Figure 2.9. From Bernoulli, the accelerated flow on one side of the doublet, due to the addition of the vortex, is paired with a decrease in static pressure, while the reverse occurs on the opposite site. The resultant force due to the pressure difference is then the Magnus effect or force and acts perpendicular to the incoming flow direction.

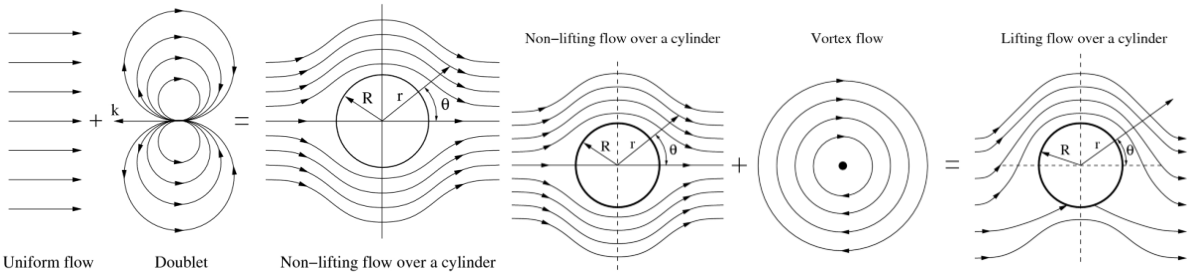

(a) *Non-rotating cylinder* (b) *Rotating cylinder*

Figure 2.9: Potential flow representation of a non-rotating and rotating cylinder by superposition of fundamental flow solutions (Kaushik, 2019).

The real-life cause of the Magnus effect is a much more complex viscous interaction of the boundary layers surrounding the cylinder surface and the formed flow topology. Swanson (1961) describes the cause of the Magnus effect to be a consequence of the differences in boundary layer transition, re-attachment and separation between the upper and lower surface and the resultant asymmetric and unsteady flow patterns. The difference in the length of boundary layers and resultant pressure distribution between the two sides are then the cause of the Magnus effect. This phenomenon of boundary layer behaviour was later described by Ericsson (1988) as the *moving wall effect*. Through his own investigations he added that the boundary layer behaviour can influence the unsteady aerodynamics of various rotating body shapes significantly even when no separation is present.

The extent of the Magnus effect and in particular the limit of the lift coefficient generated by a rotating cylinder through this effect have had the attention of many researchers over the years. Prandtl (1925) hypothesised that the maximum achievable lift coefficient is reached when the stagnation points on both sides of the cylinder meet, after which no more vorticity can be generated and the circulation remains constant. The maximum lift coefficient will then be equal to a value of 4π, which he had based on the similarities of his experimental flow visualisations at Re_D = 4000 and the ideal flow situation obtained from potential flow theory at which this value is reached.

Experimental investigations by Busemann (1932), Thom (1934) and Swanson (1961), with the latter explaining restrictions in the apparatus from Prandtl that consequently resulted in false deductions of the maximum lift coefficient, showed there was no such limit for a purely two-dimensional cylinder even at larger Reynolds numbers. With an increase of the spin ratio, covered in the subsection 2.2.3, the lift coefficient was found to keep increasing in an almost linear fashion, with the drag coefficient converging to a value lower than the maximum observed, Figure 2.10.

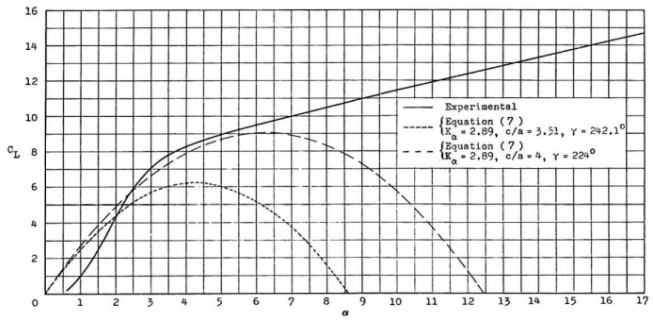

(a) *Lift coefficient versus spin ratio (here α)*

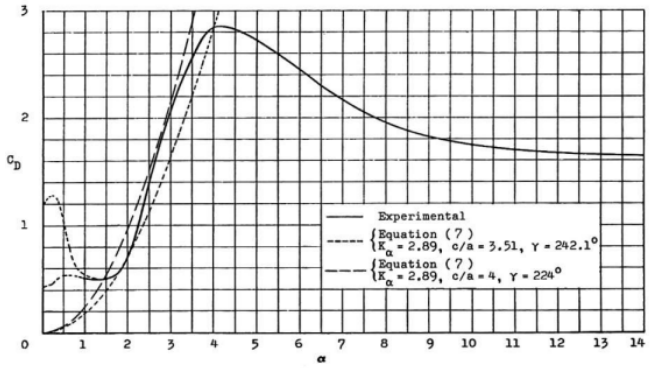

(b) *Drag coefficient versus spin ratio (here α)*

Figure 2.10: Lift and drag coefficients versus spin ratio (here α) for a close to pure two-dimensional rotating cylinder and comparison to theoretical approximations (Swanson, 1961).

A definitive limit as of now has not been found in both numerical and experimental investigations, where numerical simulations at low Reynolds numbers have even reported values exceeding thirty, C_L > 30 (Mittal & Kumar, 2003). It is however expected that at very high Reynolds numbers and or spin ratios compressibility effects will become large enough to become potentially a limiting factor, but little on this in literature is shown. The effects of compressibility will be covered later in subsection 2.2.11.

The maximum lift coefficient of a particular Magnus effect device, much like the aerodynamic characteristics of a non-rotating cylinder, is influenced by a variety of parameters and disturbances, e.g. Reynolds number and spin ratio. In literature, depending on the magnitude of each parameter, the differences observed in the force coefficients and their limits can therefore possibly be explained between the different studies.

2.2.3. Governing parameter: spin ratio

In section 2.1 on non-rotating cylinder flow the Reynolds number is deemed as the sole governing parameter for disturbance-free flow, while a variety of disturbances and secondary parameters of influence are influential to the resultant flow regime and forces in real flow applications. For the rotating cylinder flow case the same list of parameters are influential, with the Reynolds number remaining to play a governing role. However, it is not a surprise the rotation is adding another parameter to the problem and has been briefly introduced in the previous section. To cover the effects due to rotation the non-dimensionalised spin ratio or velocity-ratio, k, has been established in Equation 2.3. The spin ratio is the ratio of the cylinder tangential surface velocity, U_r, to the incoming freestream flow velocity, U_∞.

$$k = \frac{U_r}{U_\infty} = \frac{2\pi R \omega_f}{U_\infty} \tag{2.3}$$

Recent experimental studies within the subcritical, critical and supercritical Reynolds regimes have addressed the importance of the spin ratio for rotating cylinder flow. Badalamenti (2010) conducted experiments on a three-dimensional isolated rotating cylinder, with subcritical Reynolds numbers between 15000 < Re_D < 95000 and for high spin ratios of k < 8, in which the effects of a selection of the

aforementioned influencing parameters were addressed. The effects due to changing Reynolds number and spin ratios on the aerodynamic force coefficients, C_L and C_D, for the plain three-dimensional cylinder indicated that only within a small range, at the lower spin ratios, the Reynolds number has an effect, see Figure 2.11. Based on this among his other experiments, he concluded that out of all the parameters the spin ratio is of primary importance.

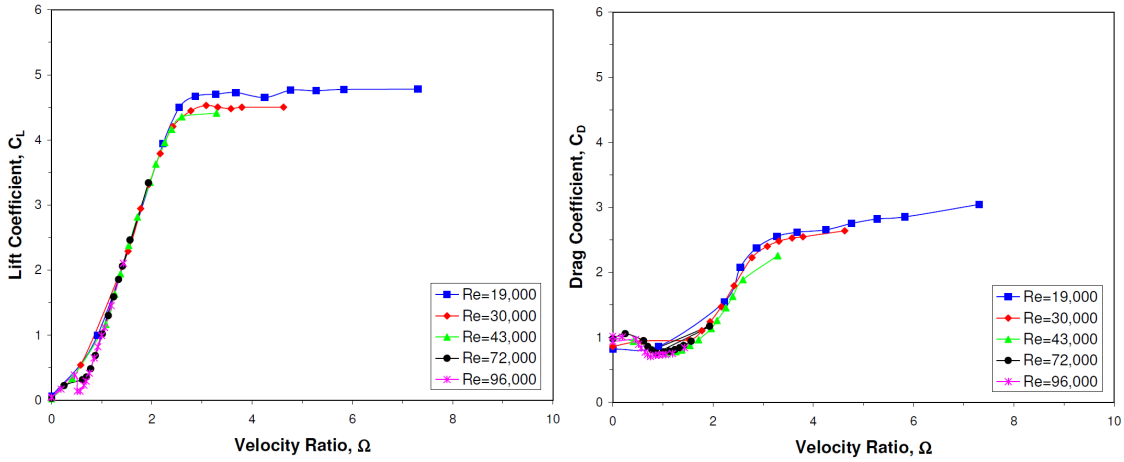

(a) *Lift coefficient* (b) *Drag coefficient*

Figure 2.11: The effects of subcritical Reynolds numbers on the lift and drag coefficients versus spin ratio (here Ω) of a three-dimensional cylinder without endplates (Badalamenti, 2010).

Chen and Rheem (2019) investigated the hydrodynamics of non-rotating and rotating cylinder at higher subcritical and critical Reynolds numbers, Re_D = 95700, 159000, 223000, and similarly high spin ratios, k < 8, with varying aspect ratios. From the investigations, it was similarly found that at these larger Reynolds numbers the force coefficients were strongly dependent on the spin ratio and only weakly dependent on the Reynolds number at low spin ratios as is shown in Figure 2.12.

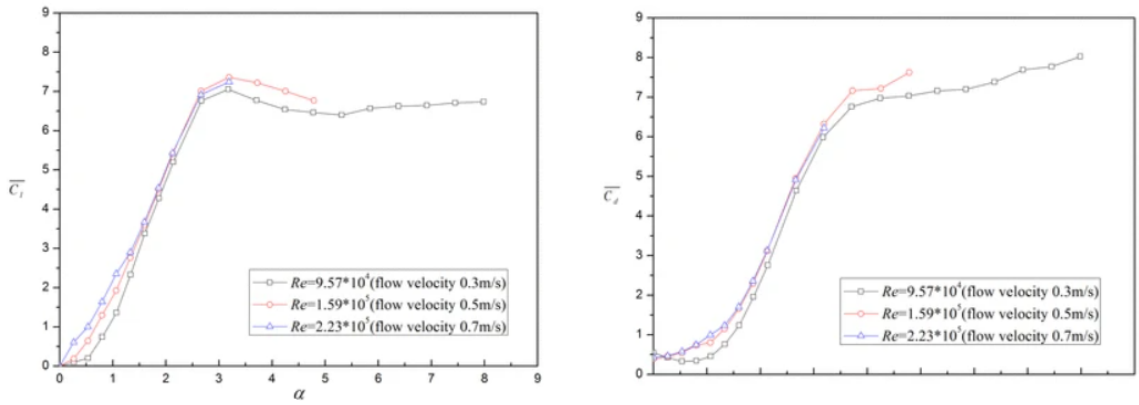

(a) *Lift coefficient* (b) *Drag coefficient*

Figure 2.12: Lift and drag coefficient versus spin ratio at high subcritical and critical Reynolds numbers (Chen & Rheem, 2019).

At last, due to difficulties of high Reynolds number testing, see section 3.1 for more details, as of now only Bordogna et al. (2019a) performed experiments on a large scale two-dimensional Flettner rotor within the higher critical and supercritical regimes with Reynolds numbers ranging between 180000 < Re_D < 1000000 and at moderately high spin ratios k < 5. Within these Reynolds regimes valuable insights were obtained on the aerodynamic characteristics of such a rotor closer to the full scale marine applications. From the data shown in Figure 2.13, Bordogna et al. concluded that the lift coefficient was only affected by the Reynolds number within the critical regime up to a certain spin ratio, k < 2.5, which after inspection agrees well with the data from Badalamenti (2010) and Chen and Rheem

(2019), while in the supercritical regime it is no longer varying. The drag coefficient however remains to be dependent on the Reynolds number also for the supercritical regime.

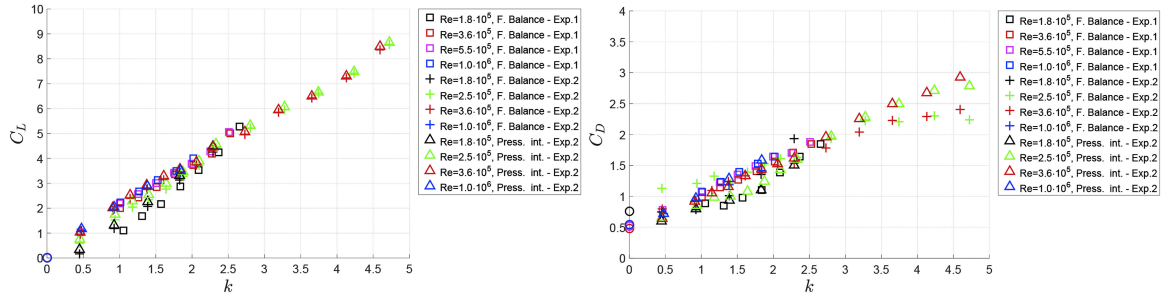

(a) *Lift coefficient* (b) *Drag coefficient*

Figure 2.13: Lift and drag coefficient versus spin ratio at critical and supercritical Reynolds numbers (Bordogna et al., 2019a).

From this it has been shown that the spin ratio is the main governing parameter for rotating cylinder flow by drastically influencing the aerodynamic characteristics, where the Reynolds number being a secondary governing parameter only within a certain range of Reynolds number and spin ratios. The larger influence of the Reynolds number at the subcritical and critical regimes at moderately low spin ratios is mainly influenced by the transitional state of the boundary layers and will be covered in more depth in subsection 2.2.7 and subsection 2.2.8.

The effects due to changes in the other influencing parameters will be covered in more detail later in the report, e.g. aspect ratio in subsection 2.2.4, free-end effects in subsection 2.3.4, surface roughness in subsection 2.3.4 and blockage effects in section 3.2.

2.2.4. Aspect ratio

Earlier, a short introduction on the aspect ratio has been in given subsection 2.1.3. The aspect ratio, A, is a geometrical parameter which describes the slenderness of a given object, and has a pronounced effect on the generation of aerodynamic forces of a given thrust producing device. In case of a cylinder the aspect ratio is determined as the ratio of the cylinder span over the external cylinder diameter, B/D. Many studies, for both stationary and rotating cylinders, have been performed at different Reynolds number regimes to determine its effect. For this section the focus will be on the higher more Reynolds regimes as they would be more fitting for marine scale applications.

Badalamenti and Prince (2008a) and Badalamenti (2010) summarised the results of many experimental investigations, including his own, with various levels of aspect ratio. From the results it appears that the aspect ratio only has an effect on the lift coefficient for $k > 1.5$, except for the lowest $A = 1.7$, where a distinct difference in its behaviour was found. In general, an increase of aspect ratio results in an increase of the maximum lift coefficient and delays the reduction of the lift coefficient to higher spin ratios. The cause of this behaviour is linked to the trailing vortex system, which is further discussed in subsection 2.2.12, as it impacts the span-wise lift distribution on the cylinder, where a shorter cylinder brings the vortices closer together and a larger extend of the span is affected by their influence.

Badalamenti (2010) further explained that the drag coefficient appeared to be more sensitive to variation in the experimental setups, as has been discussed before, and therefore a connection to changes in the aspect ratio is more difficult to establish. However, a larger aspect ratio does suggest a reduction of the drag coefficient at higher spin ratio. Another observation is the lower drag coefficient for low aspect ratio cylinders at low spin ratios, $k < 0.3$. This has been the cause of the pronounced inflow from the sides of the cylinder, which results in a relatively large pressure equalisation and narrowing of the wake in comparison to the span of the cylinder, and hence a reduction of the drag coefficient is realised.

The numerical parametric study from Kwon et al. (2022) investigated, among other effects, the results of changing aspect ratio with the use of three-dimensional steady RANS simulations at supercritical $Re_D = 766000$ by keeping the rotor height the same and varying the cylinder diameter. The results

showed a reduction of the absolute lift, drag and torques with an increase of aspect ratio. However, it must be noted that this might also be due to the change of area and perhaps Reynolds number, which has not been mentioned to remain the same eventhough the cylinder diameter varies. A more indicative measure was the effect of increasing aspect ratio on the non-dimensional, where both showed improvements, see Figure 2.14a,b. More details on the lift-to-drag ratio and energy efficiency of a rotating cylinder will be covered in subsection 2.3.1 and subsection 2.3.2 respectively.

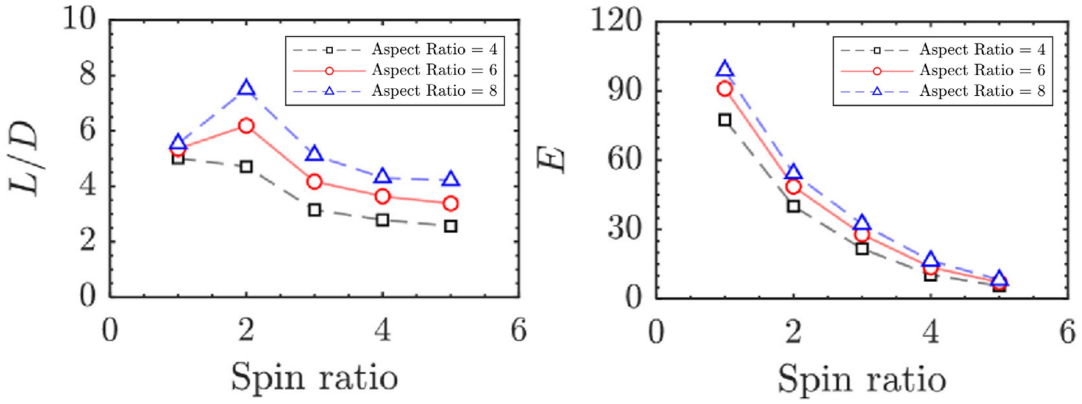

(a) *Lift-to-drag ratio (here L/D)* (b) *Energy efficiency*

Figure 2.14: Aspect ratio effect on lift-to-drag ratio (here L/D) and energy efficiency with varying spin ratio (Kwon et al., 2022).

Chen et al. (2023) performed three-dimensional experiments on a Flettner rotor with one free-end and no endplate with varying aspect ratio for subcritical Re_D = 233000 and k < 4.5, Figure 2.15. Similar to the findings from Badalamenti (2010), but now for k < 1, little variation in the C_L, C_D and C_L/C_D is found with a change of aspect ratio, except for the lowest aspect ratio tested. For k > 1, the maximum lift coefficient increases and the point of reduction is delayed. The drag coefficient further showed, between the two lowest A, and the two highest A, a difference at high k, which has not been explained. In either case, the lift-to-drag ratio increases with an increase in B/D and the maximum is achieved in the range of 1.5 < k < 2. This is in good agreement with the results from Badalamenti (2010) and Kwon et al. (2022).

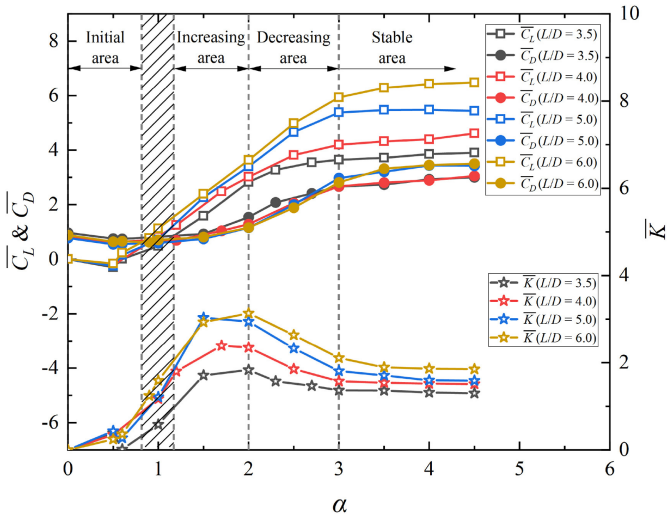

Figure 2.15: Aspect ratio effect (here L/D) on the mean lift coefficient (here $\overline{C_L}$), mean drag coefficient (here $\overline{C_D}$), and lift-to-drag ratio (here $\overline{K}$) at Re_D = 233000 (Chen et al., 2023).

2.2.5. Flow regimes for rotating cylinders

Unlike non-rotating cylinders placed in a flow, classification of flow regimes around a rotating cylinder are more difficult to define as it depends on both the Reynolds number and spin ratio, while also secondary influencing parameters, e.g. aspect ratio and blockage ratio, can cause scatter in the results obtained and phenomenon observed. Although differences due to variations in the influencing parameters can occur, some general trends in the flow patterns are observed.

Prandtl and Tietjens (1934) were among the first to provide an extensive set of flow visualisations of rotating cylinders at a Re_D = 4000. A selection of which are shown in Figure 2.16. At small spin ratios, 0 < k < 1, the wake of a rotating cylinder is similar to that of the non-rotating case, where at this particular Reynolds number, periodic eddy shedding and a relatively thick bluff body wake is observed, Figure 2.16a,b. By increasing the spin ratio from standstill to k = 1, asymmetries in the flow patterns are introduced. The size and strength of the shed eddies will vary, where in case of eddies coming of the advancing side, a growth in both size and strength occurs, while for the retreating side the opposite will hold. The formation length of the eddies is also shortened considerably and the size of the wake is reduced.

At k = 2, periodic eddy shedding cease to exist and a quasi-steady state of the flow is reached, Figure 2.16c. The wake of the cylinder is now reduced significantly in its size and is deflected more towards the advancing side of the cylinder. This process continues with increasing spin ratio to k = 4 and 6, Figure 2.16d,e. At this point the flow patterns are showing more similarity to the potential flow solution at its ideal spin ratio of k = 2, where the formation of closed streamlines around the surface are observed. This led Prandtl to assume the theoretical maximum obtainable lift coefficient to be equal to 4π as was explained in the earlier subsection 2.2.2.

Swanson (1961) mentioned when the closed streamlines are formed around the cylinder surface, a further increase of the spin ratio will mean that the velocity of the cylinder surface will be traveling faster than what can be observed anywhere in the external flow. From this point on, the lift coefficient is shown to keep increasing, although with a slower rate, Figure 2.10a. The drag coefficient on the other hand rises first to a greater value, due to the prolonged boundary layer attachment on the rear side of the cylinder, similarly as for a stationary cylinder, and its associated greater suction, while eventually decreasing and converging to a set value due to the movement of the near-wake to the front of the cylinder, Figure 2.10b. Betz (1925) further made the comment that the formation of the closed streamline, or rotating boundary layer formed around the surface of the cylinder, effectively makes a change of the cross-section of the cylinder. While Badalamenti (2010) further mentioned, based on experimental and computational results, that the size of the rotating boundary layer grows with increasing spin ratio and decreases with an increase of the Reynolds number.

The final flow visualisation was performed with a rotating cylinder in still flow conditions, which corresponds to a theoretical infinite value of the spin ratio, Figure 2.16f. The flow pattern observed is a single large eddy with its influence extending far from the surface of the cylinder in the form of concentric circles.

Another general observation in the flow patterns is the gradual movement of the stagnation point in the direction opposite of the rotation, while the separation point on the retreating side is considerably delayed, Figure 2.16a,b,c,d,e. At high spin ratios this results in the coming together of both the stagnation and separation points. At high enough spin ratios the two will coincide and with an even further increase in spin ratio lifting off from the surface follows.

From the flow visualisations, two distinct regimes in the flow patterns can be observed. A regime of periodic eddy shedding and one where the shedding ceases. The spin ratio at which this occurs is deemed the critical spin ratio, k_{crit}, and was found to be equal to a value of 2 in the experiments from Prandtl and Tietjens (1934). However, the value of the critical spin ratio seems to be a discussion on its own where in various numerical and experimental studies different values were found, e.g. in the studies from Badalamenti (2010) and Ma et al. (2022). Especially, in the lower Reynolds number regimes, large differences in critical spin ratios are observed, Figure 2.17.

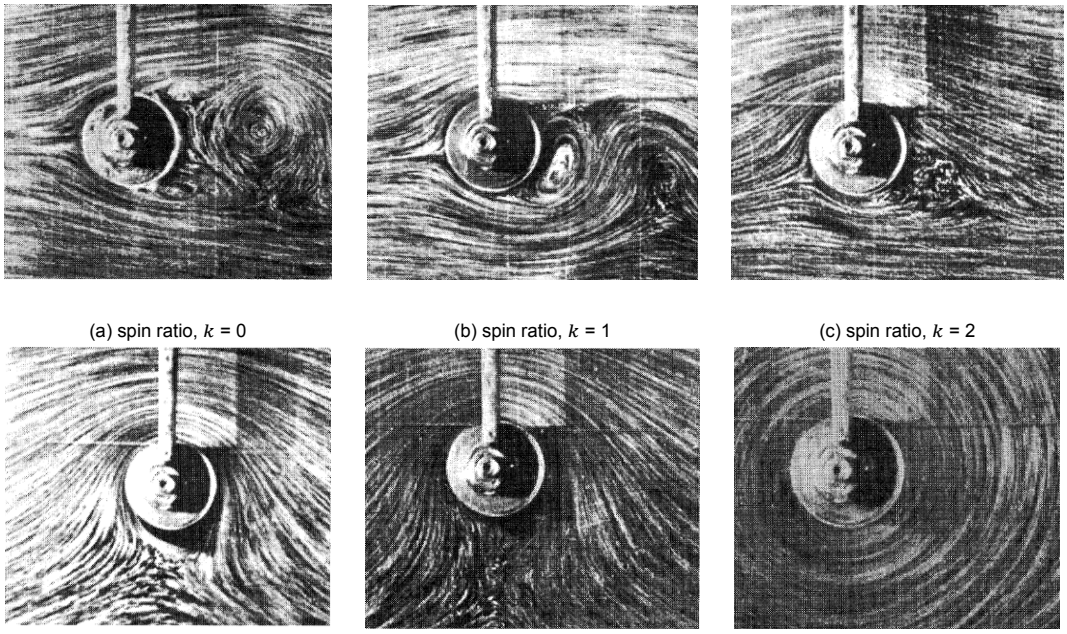

(a) spin ratio, k = 0 (b) spin ratio, k = 1 (c) spin ratio, k = 2

(d) spin ratio, k = 4 (e) spin ratio, k = 6 (f) spin ratio, k = ∞

Figure 2.16: Water surface flow visualisation around a rotating cylinder for Re_D = 4000 and varying spin ratios (Prandtl & Tietjens, 1934).

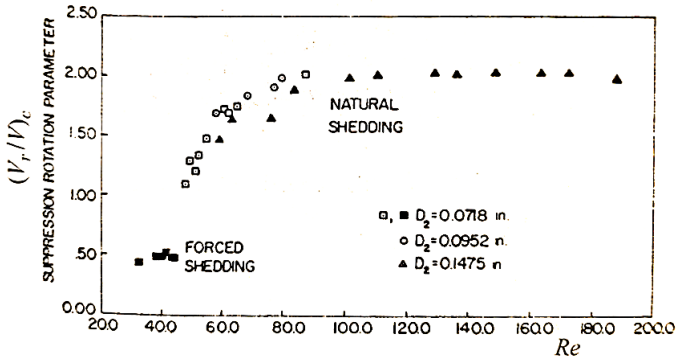

Figure 2.17: Variation in critical spin ratio for eddy shedding suppression at low Reynolds numbers (Jaminet & Van Atta, 1969).

Based on the extensive experiments on the nature of rotating cylinder wake flow, Diaz et al. (1983, 1985) made a different distinction between the flow regimes. It was stated that after a spin ratio of k > 1 a fundamental change in the formation of periodic eddies is observed. This was said to be due to the asymmetric velocity distribution on the surface of the cylinder and the growing of the rotating boundary layer close to the surface.

Further flow visualisations in the studies from Prandtl and Tietjens (1934) were on impulsively started cylinders, this subject of fundamental research on rotating cylinders will however not be covered as it is of little importance to the main of topic of this review on thrust producing applications of the rotating cylinder. For a particular interest in this topic the works form Prandtl and Tietjens (1934) and Coutanceau and Menard (1981) can serve as a good starting point. It is however worth noting that from the numerical work of Mittal and Kumar (2003) it is stated that it takes a considerable amount of time for the flow to reach the final solution after an impulsive start. This in turn can result in scatter of results obtained when not enough time is given for the flow to develop fully before measurements are taken.

Swanson (1961), among others, was skeptical on the flow visualisation results obtained by Prandtl. Swanson claimed that the flow patterns obtained were on a free surface with uniform pressure and at only one particular Reynolds number, e.g. Re_D = 4000, and therefore the actual flow patterns in the wake are expected to be different. Based on results from other experiments in that time, differences were observed compared to Prandtl's results, especially in the movement of the forward stagnation point. However many future studies, e.g. Coutanceau and Menard (1981), Diaz et al. (1983, 1985) showed good agreement with the general behaviour of the wake and eddy shedding, and therefore differences might be explained by the extend of other influencing parameters or disturbances present.

The extensive numerical investigation from Mittal and Kumar (2003) based on solving the incompressible Navier-Stokes equations in its primitive variable form at Re_D = 200 and k < 5, showed good agreement with the earlier observations. However, the existence of a second vortex mode was found to be present for a small band of spin ratios in the range of 4.4 < k < 4.8. This second vortex mode was found to consist out of vortices only shed from the advancing side of the cylinder at a reduced rate and with a single orientation, e.g. clockwise or counterclockwise, compared to the periodic eddy shedding mode found at the lower spin ratios. During the same time, also the numerical investigation from Stojković et al. (2003) using a different method at similar Reynolds numbers, 60 < Re_D < 200, showed the occurrence of the second eddy shedding mode at spin ratios, 4.35 < k < 5.45. The occurrence of the second vortex mode was said to be highly dependent on the Reynolds number, where an increase would result in the appearance of the mode at lower spin ratios and lasting for longer. Additionally, it was found that the second shedding mode has a particular strong influence on the fluctuating force coefficients compared to the first range of periodicity, Figure 2.18.

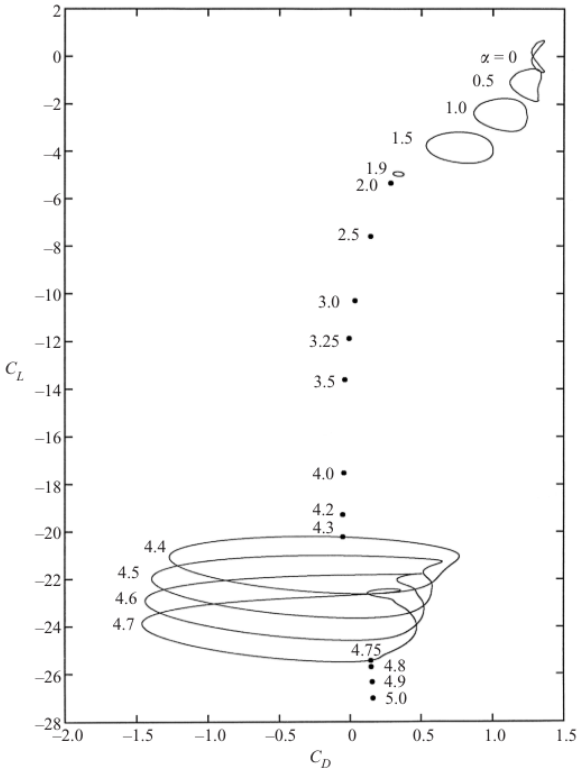

Figure 2.18: Lift coefficient versus drag coefficient of a rotating cylinder at Re_D = 200 for various spin ratios (here α) (Mittal & Kumar, 2003).

The experimental proof of the second shedding mode came from Kumar et al. (2011) with the use of PIV measurements. For the Reynolds numbers, Re_D = 200, 300, 400, and spin ratios, k < 5, it was found that the second shedding mode existed at k = 4.45, showing good agreement with the numerical results obtained before, Figure 2.19.

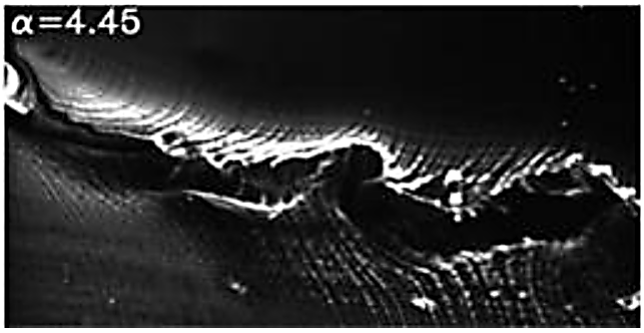

Figure 2.19: Flow visualisation of second vortex mode using PIV at Re_D = 200 and k = 4.45 (here α) (Kumar et al., 2011).

Aljure et al. (2015) performed direct numerical simulations, DNS, at the lower subcritical Reynolds regimes, Re_D = 5000 and k < 5. Figure 2.20 shows the mean velocity profiles. The results are in good agreement with the aforementioned flows, e.g. Prandtl and Tietjens (1934) and Coutanceau and Menard (1981), in terms of wake and stagnation point behaviour. It was similarly mentioned that eddy shedding ceases for k > 2, with the appearance of the rotating boundary layer, named here as the highly vorticial circumvolving layer, occurring for k > 3. At k = 5, a second regime of unsteadiness was found, as was mentioned by Mittal and Kumar (2003), with large fluctuations in the instantaneous lift coefficient as a result, Figure 2.21.

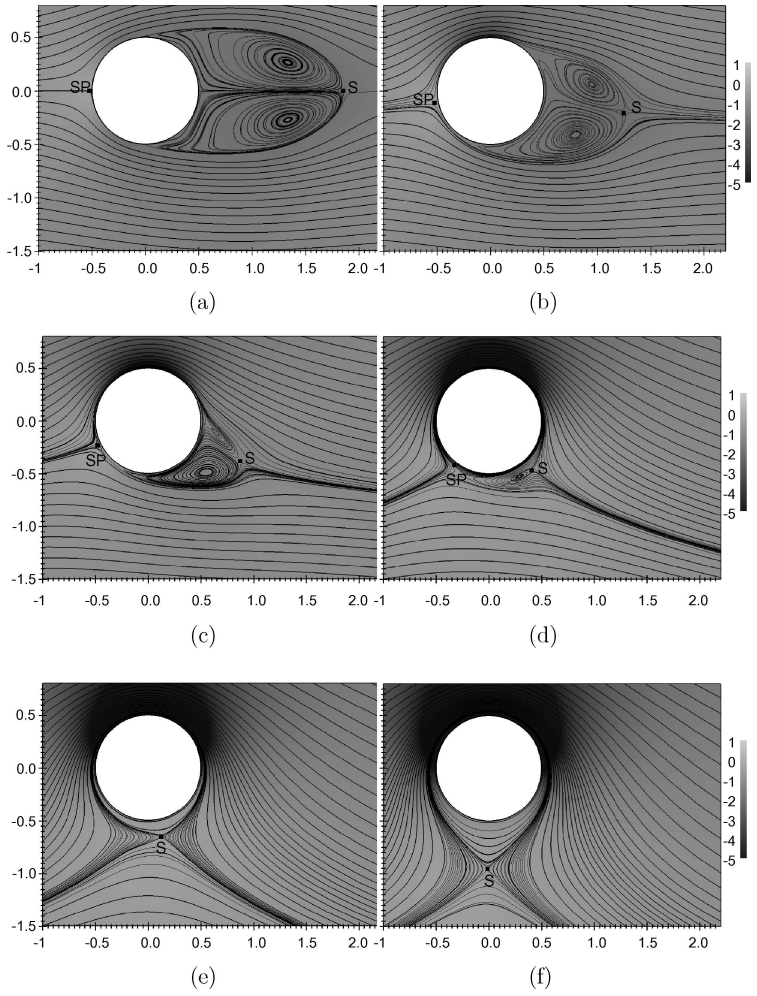

Figure 2.20: Mean streamlines and pressure fields at Re_D = 5000 and various spin ratios; (a) k = 0, (b) k = 1, (c) k = 2, (d) k = 3, (e) k = 4, (f) k = 5 and location of the stagnation points, SP, and saddle points, S. (Aljure et al., 2015).

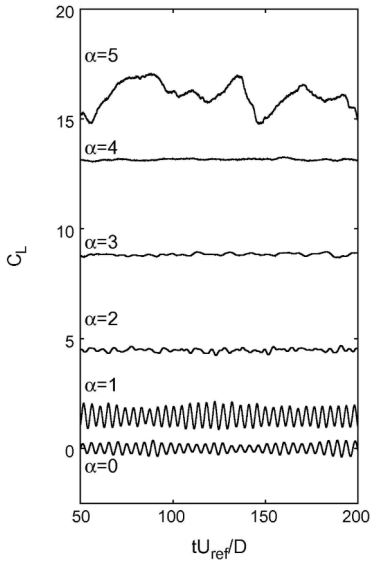

Figure 2.21: Variation in the instantaneous lift coefficient at various spin ratios (here α) (Aljure et al., 2015).

The visualisation of instantaneous coherent structures in spanwise direction, which are inherently three-dimensional, using the second invariant of the velocity gradient tensor, Q-criterion, provided more insight in the intricate processes present with an increase of the spin ratio, especially for the two regimes of unsteadiness, Figure 2.22.

The general wake structure at low spin ratio remains mostly the same. For low k <1, wake is deflected in the direction of the tangential velocity and the shear layers shrink, where vortex shedding will persist if present. With k approaching 1, the recirculation zone in the mean velocity profile reduces, Figure 2.20b, and spanwise vortex tubes become more coherent due to the coming together of the shear layers and the elimination of some three-dimensional effects, Figure 2.22a,b. The more coherent vortex tubes, indicated by VT, are inflicting larger variations in the instantaneous lift coefficient, Figure 2.21.

When the critical k, here k = 2, is reached, eddy formation ceases and lift coefficient variations reduces again, Figure 2.21. The interaction between the shear layers is no longer present and the wake is fully turbulent, which is now composed out of small vortices that are shed in an irregular manner, Figure 2.22c. Additionally, the shear layers roll over further around the cylinder and the onset of Taylor-Görtler, TG, vortices, is observed. Taneda (1980) was among the first to demonstrate the appearance of these toriodal shaped vortices around an impulsively started cylinder. Matsui (1981) linked the appearance of the Taylor-Görtler vortices with the suppression of the periodic eddy shedding.

At k = 3, the bottom shear layer is no longer formed, while the top layer is almost fully wrapped around the cylinder circumference. This wrapping process continues until the stagnation points coincide at the bottom, Figure 2.20e. At this point the circumvolving layer is formed around the cylinder and TG vortices start to grow, Figure 2.22d,e,f.

At k = 4, the circumvolving layer forces the stagnation point from the surface, Figure 2.20e, which had been shown by the early observations from Prandtl and Tietjens (1934) and in potential flow theory. The drag coefficient increases again after this point, while the lift coefficient keeps increasing beyond Prandtl limit but at a slower rate than before k < 3, as was also mentioned by Swanson (1961).

At higher k = 5, the wake thickens again due to the build up of vorticity in the zone near the stagnation point. This allows for the formation and shedding of vortices at a reduced rate in the same sense of the rotation, different to the periodic shedding at lower k. This phenomenon had previously been mentioned by Mittal and Kumar (2003) at lower Reynolds numbers. The shedding of the vortices feeds the wake and increases its width. This process is also associated with the formation and growth of Taylor–Görtler vortices on the cylinder surface (Aljure et al., 2015). The Taylor-Görtler vortices cluster

up and detach in an irregular manner from the circumvolving layer if sufficient size is reached, resulting in the second shedding mode and large fluctuations in the force coefficients. Matsui (1981) showed experimentally, at 59 < Re_D < 1600, the existence of the rotating boundary layer and the separating layer off this boundary that is fed by the vortices emerging from the circumvolving layer.

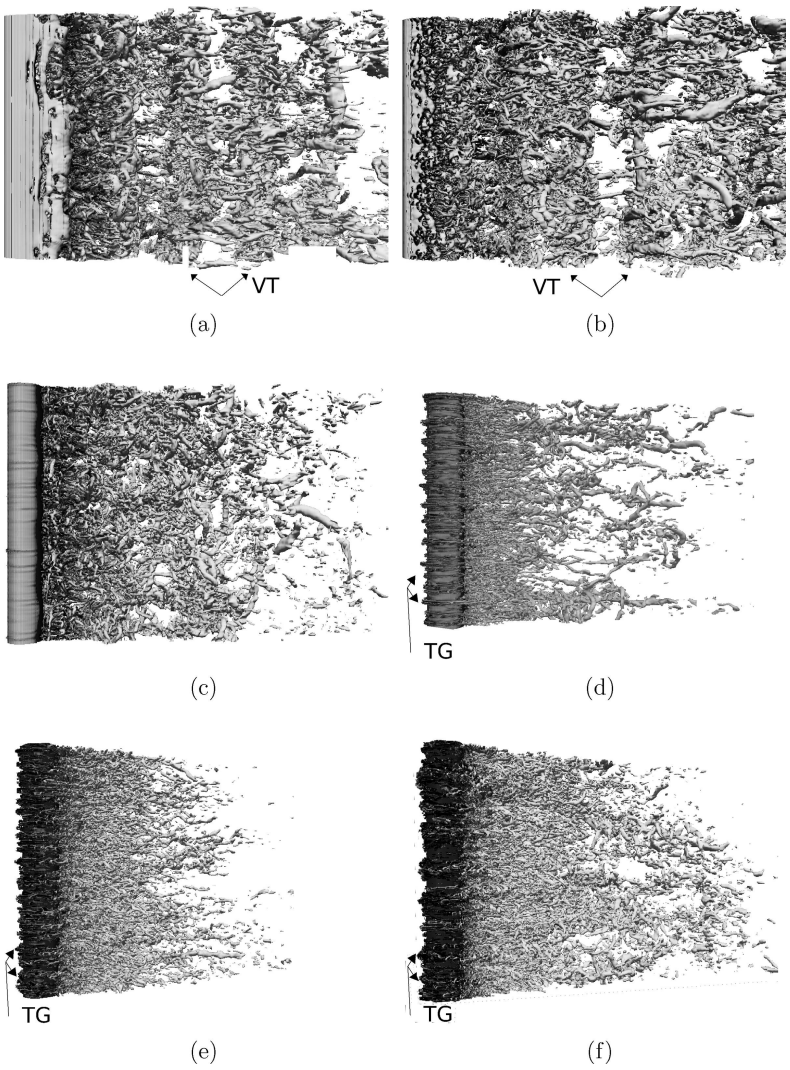

Figure 2.22: Instantaneous coherent structures using Q-criterion isosurfaces, viewed from the retreating side, at Re_D = 5000 and various spin ratios; (a) k = 0, (b) k = 1, (c) k = 2, (d) k = 3, (e) k = 4, (f) k = 5. Vortex tubes, VT, and Taylor-Görtler vortices, TG, are indicated. (Aljure et al., 2015).

Karabelas et al. (2012) performed flow visualisations at high critical and supercritical Reynolds numbers, 500000 < Re_D < 5000000, and various spin ratios, 0 < k < 8, using numerical RANS and URANS simulations. The simulations showed a different behaviour between the laminar flow states shown before and the turbulent flow states at high Reynolds numbers, Figure 2.23. At supercritical Reynolds numbers the coming together of the stagnation point is also present, which slightly lifts of the surface with increasing k, but at approximately same azimuthal position and does not vary much after k > 4. For the laminar case the lifting off the surface is increasing continuously with increasing spin ratio and is moved closer to the center line of the cylinder. The circumvolving layer is also present at the higher Reynolds regimes, described as an intensely swirling velocity flow field, that influences the external flow field. However, the second shedding mode previously found in lower Reynolds number flows is not mentioned here, even at the same lower Reynolds numbers. It can be speculated that this may be an indication of the second vortex mode being an highly complex three-dimensional effect, which the simpler RANS simulations potentially fails to predict.

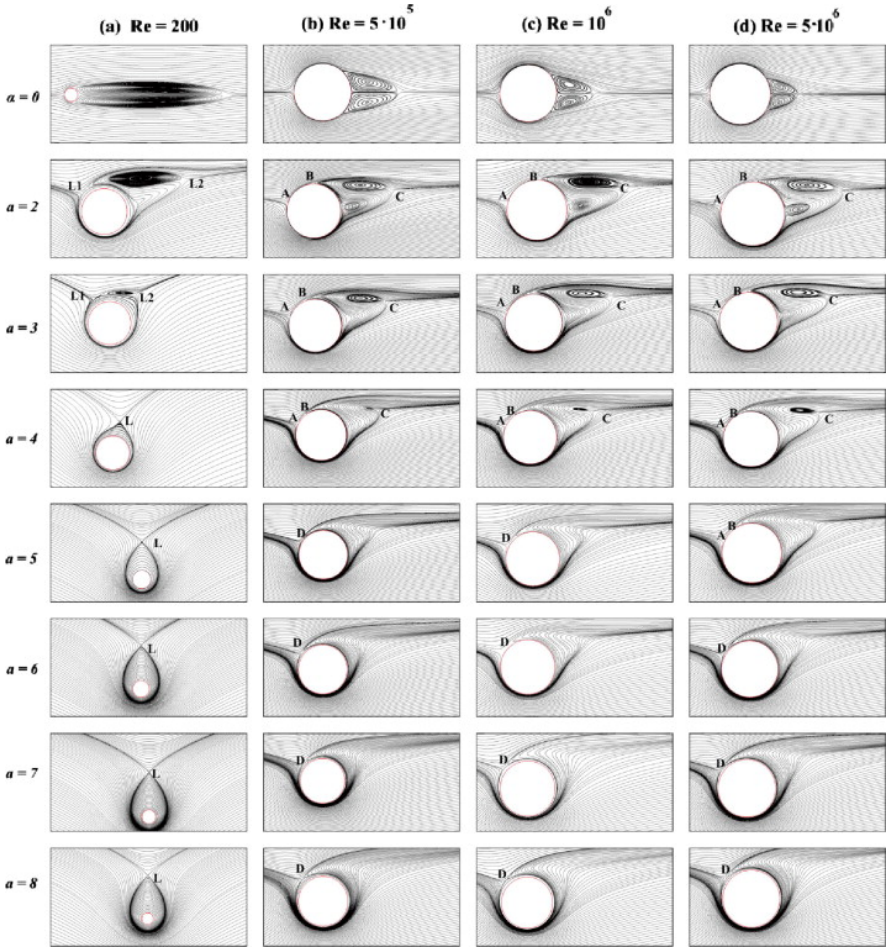

Figure 2.23: Mean streamline patterns at varying Reynolds numbers and spin ratios. Stagnation point locations are indicated by L1, L2 for the laminar state and A, B, C, D for the turbulent states (Karabelas et al., 2012).

Recent numerical and experimental studies were conducted by Ma et al. (2022) and Liu et al. (2023), where the former indicated variations in vortex shedding behaviour when transitioning between the subcritical and one-bubble regimes. Liu et al. (2023) showed that during the transition at the advancing side, small vortices with similar frequencies as the dominant vortices appear, where a shift in energy towards the smaller vortices is gradually taking place with increasing spin ratio, Figure 2.24. After transition the dominant vortex has disappeared and now the wake composes solely out of the smaller vortices. On the retreating side it was mentioned that observing small vortices of such kind was more difficult.

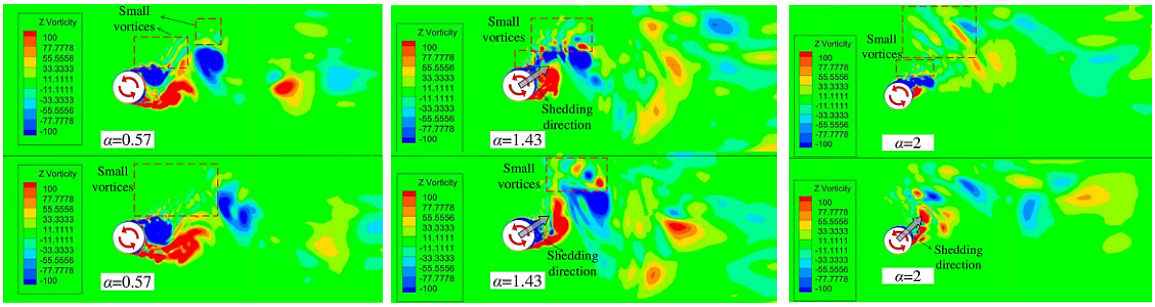

(a) spin ratio, k = 0 (b) spin ratio, k = 1 (c) spin ratio, k = 2

Figure 2.24: Vorticity isosurfaces at Re_D = 81000 and varying spin ratios (here α) (Liu et al., 2023).

Further experimental investigations on the nature of wake within various flow regimes around a rotating cylinder were performed by Radi et al. (2013), providing evidence of new vortex modes present within very specific bands of Reynolds number in the lower laminar states, and Badalamenti and Prince (2008b) at 41000 < Re_D < 98000 showing a second regime of periodicity at high spin ratio, k > 2.7, different than the second shedding mode discussed before.

2.2.6. Strouhal number behaviour

The Strouhal number is determined by using the dominant frequency that appears in the energy spectrum of a wake as the eddy shedding frequency and its value is dependent on both the spin ratio and Reynolds number for a smooth rotating cylinder in a disturbance-free flow.

Badalamenti (2010) mentioned that although the general trend in experimental studies is always an increase of the Strouhal number with increasing spin ratio up until shedding ceases, numerical studies are divided in either showing the same experimental trend, or a slight decrease in St with the increase of spin ratio, even when different numerical methods are applied at the same Reynolds numbers. Jaminet and Van Atta (1969) gave an explanation and argued that the coming together of the separation points, moves the vortices that are being shed from the two sides closer together, this in turn results in a decrease of the characteristic length scale of the shedding, a larger frequency as it is inversely proportional, and thus a larger Strouhal number. This is in favour of the experimental trend and as it was also shown in their own experiments at very low Reynolds numbers, Figure 2.25.

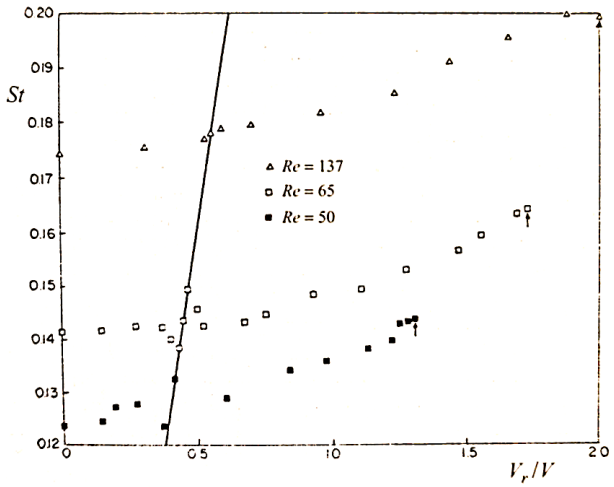

Figure 2.25: Strouhal number variation with spin ratio (here V_r/V) at various Reynolds numbers in the laminar regime with the solid line indicating the St of the rotational frequency (Jaminet & Van Atta, 1969).

Another phenomenon associated with eddy shedding on a rotating cylinder is shown in Figure 2.25. The solid line indicates the Strouhal number associated with the rotation frequency of the cylinder. It was observed that when the rotation frequency of the cylinder approaches the eddy shedding frequency, disturbances will be observed in the shedding characteristics, while at slightly higher spin ratios the shedding lock-on phenomenon occurs. In the presence of this phenomenon the eddy shedding frequency synchronises with the rotation frequency and shedding becomes very stable, regular and occurs at an increased amplitude. Large vibrations of the cylinder can be the result. With a further increase of the spin ratio, the synchronisation is broken and eddy shedding returns to its expected behaviour.

Within the subcritical and critical Reynolds number regimes, Tanaka and Nagano (1973) showed that the Strouhal number initially remained nearly constant at low spin ratios, Figure 2.26. At higher spin ratios, the lower Reynolds number tested, Re_D = 45000, showed an increase in St similar to the results from Jaminet and Van Atta (1969). The larger Reynolds numbers tested experienced a rapid rise of Strouhal number to a somewhat higher value, before eddy shedding disappears completely when the critical spin ratio is reached. The critical spin ratio at which the eddy shedding does no longer occur

was significantly lower in their tests and occurs at higher spin ratios with larger Reynolds numbers compared to what has been found in many other studies as shown before within the subcritical and critical regimes. Zdravkovich (2003) gave as an possible explanation the low aspect ratio used as well as the distant location of the hot-wire from which their measurements were based.

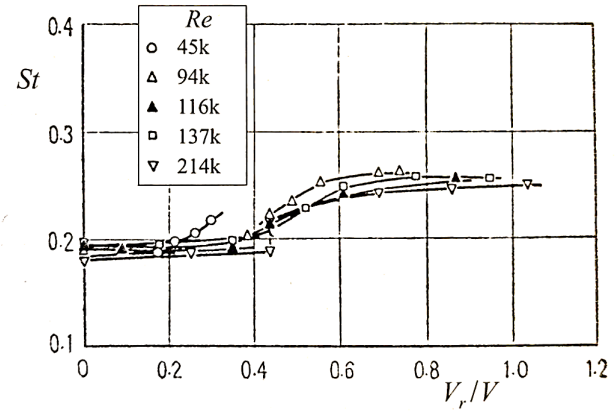

Figure 2.26: Strouhal number variation with spin ratio (here V_r/V) at various Reynolds numbers in the subcritical and critical regimes (Tanaka & Nagano, 1973).

Ma et al. (2022) investigated vortex shedding behaviour between the subcritical and one-bubble Reynolds number regimes. The wake and shedding characteristics were determined with the use of a pressure probe rake consisting out of 6 Cobra probes at different locations. The results showed a similar trend to the results obtained from Tanaka and Nagano (1973), however the two earlier explained differences can be observed. Firstly, the critical spin ratio was now found to go to a value of k = 1.5, and secondly, a lower critical spin ratio with an increase of Reynolds number is observed, Figure 2.35. Figure 2.27 further shows that the Strouhal number is not affected by deviations of the wake flow as the provided Cobra probe data in different locations show similar results. Furthermore, it was shown that the discontinuity grows with the increase of Reynolds number and is assumed to be the cause of variations in the formation of the laminar separation bubble, LSB, at different Reynolds numbers. The same variation in the Strouhal number with an increase of spin ratio and similar Reynolds numbers have been found by Liu et al. (2023).

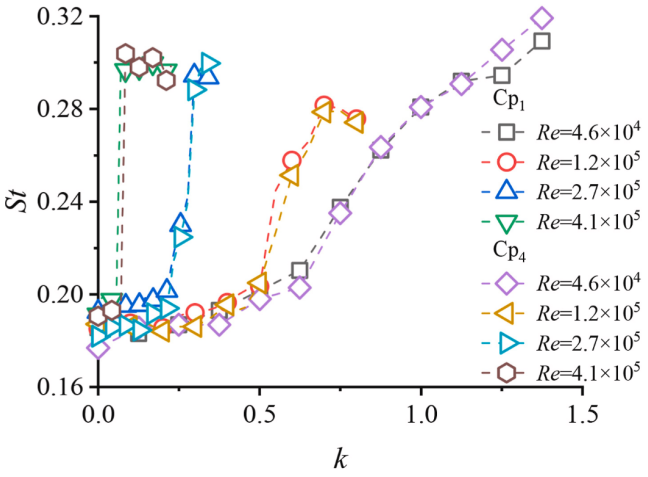

Figure 2.27: Strouhal number variation with spin ratio, k, at various Reynolds numbers in the subcritical and critical regimes, measured at two different Cobra probes (Ma et al., 2022).

Chen and Rheem (2019) investigated three dimensional cylinders at different aspect ratios and subcritical Reynolds numbers, 30600 < Re_D < 223000, in a water tunnel. They made further distinctions in the behaviour of the Strouhal number with an increase of the spin ratio. The area of vortex shed-

ding occurred at $k \approx < 1$, since only one distinct peak in the frequency domain of the hydrodynamic lift coefficient was observed, such that a single Strouhal number is determined that increases with the increase of spin ratio. For 1 < k < 3, an area of weak vortex shedding is present. A main peak still exist, which decreases in strength with increase of the spin ratio and corresponds to the dominant vortex shedding. The Strouhal number of the dominant peak does however not disappear up to k = 3 and now decreases with the increase of spin ratio. Additionally, peaks appear of growing strength with increase of spin ratio, corresponding to smaller weaker vortices. This appearance of and shift in strength to smaller vortices was later confirmed by Liu et al. (2023) as explained in the previous section. Then for k > 3, dominant peaks are no longer visible in the frequency spectrum, but rather the fluctuations are spread out over a band of frequencies. This behaviour had been associated with unsteady wake fluctuations which is different to the vortex shedding behaviour explained above.

The second eddy shedding mode, discovered in the numerical studies from Mittal and Kumar (2003) and Stojković et al. (2003) at low laminar Reynolds numbers, showed vastly different shedding characteristics compared to the mode present at the lower spin ratios as explained before. The Strouhal number has been found to be much smaller, due to the slow build up of vorticity in the circumvolving layer before being shed in the flow, and it is highly dependent on the spin ratio, Figure 2.28. The experimental proof of the second shedding mode by Kumar et al. (2011) showed good agreement with the numerical results in both Strouhal number behaviour and flow topology.

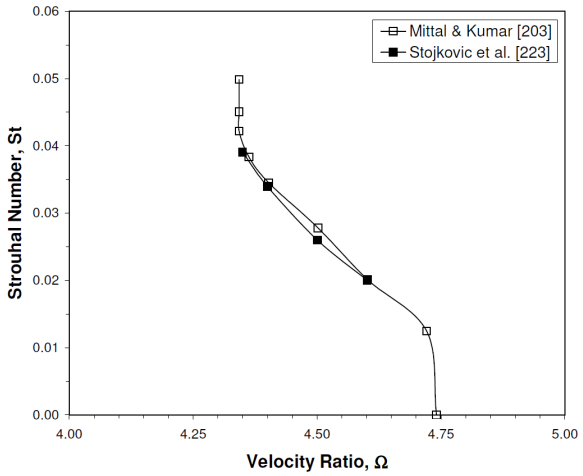

Figure 2.28: Strouhal number variation with spin ratio (here Ω) at Re_D = 200 for the second eddy shedding mode based on the results from Mittal and Kumar (2003) and Stojković et al. (2003). Figure by (Badalamenti, 2010).

2.2.7. Boundary layer behaviour

Thom (1931) was one of the first to perform measurements of the boundary layers around the surface of a rotating cylinder. He managed, albeit with questionable accuracy, to capture with the use of small pitot and static probes velocity profiles of the boundary layer across separated runs.

Years later Swanson (1961) in his review paper introduced two concepts, based on his own boundary layer experiments and existing literature, to describe the behaviour of the boundary layers on both sides of the rotating cylinder. The first of which stemmed from Krahn (1956) hypothesis's on boundary layer behaviour who introduced the concept of *relative Reynolds number*, Re_{rel}, where due to the spin ratio, the boundary layers on either side of the cylinder will experience a different effective Reynolds number, Equation 2.4. Based on this Krahn and Swanson concluded that for the retreating side, which acts with the free stream flow, the relative Reynolds number is decreased and hence a delay in transition is expected, while similarly for the advancing side the opposite can be said. The relative Reynolds number can therefore be used to qualitatively estimate the position of boundary layer transition as well as the total length of the boundary layer on each side.

$$Re_{rel} = Re_D(1 \pm k) \tag{2.4}$$

Swanson (1961) did mention however that it is expected that both boundary layers will reach the turbulent state at a large enough velocity ratio in favour of the idea of an completely laminar state of the retreating side boundary layer, eventhough Re_{rel} and hence its relative velocity is small. He argued boundary layer instabilities and transition are in general a function of absolute velocity, which is considerably larger at the retreating side of the cylinder for large spin ratios due to the acceleration of the freestream by the moving wall. Hence the concept of a relative Reynolds number appears to be somewhat limited.

He further introduced the concept of *boundary layer origin*. Swanson (1961) described that for a non-rotating body, e.g. an airfoil, the boundary layer origin coincides with the forward stagnation point based on the idea of a boundary layer being a shear layer and that after its origin the shear is in opposite direction on both sides of the body. In case of a rotating body, the stagnation point is not stationary and will move in opposite direction of the rotation, while it also can no longer be a point of zero velocity located on the surface. The result is that the boundary layer origin lays at the point of zero relative velocity between the freestream flow and the tangential surface velocity and moves with the rotation, opposite to the stagnation point, Figure 2.29.

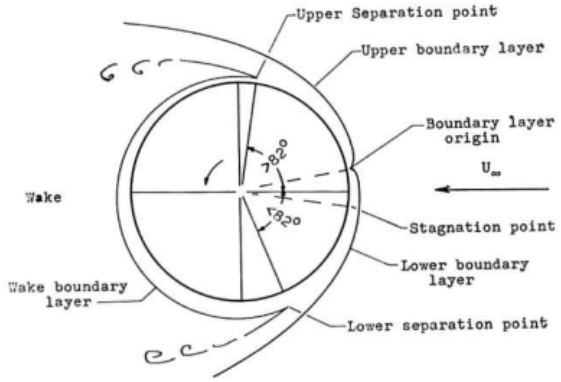

Figure 2.29: Boundary layer, boundary layer origin, separation point and stagnation point representation around a rotating cylinder at k = 0.2 and Re_D = 4000 (Swanson, 1961).

Peller (1986) performed boundary layer measurements on a low aspect ratio cylinder with high blockage ratios at a Reynolds number of 48000 using Laser Doppler Velocimetry, LDV. He concluded that the radial component of the velocity is negligible for the boundary layer velocity profile in non-separated regions and therefore only the tangential velocity has to be measured. In doing so the following boundary layer mean velocity profiles were measured, where the thin line close to the surface indicates the tangential surface velocity of the cylinder, Figure 2.30a,b,c. From these figures a clear momentum increase is visible on the retreating side of the cylinder, further confirming the prolonged attachment of the boundary layer on the retreating side of the cylinder.

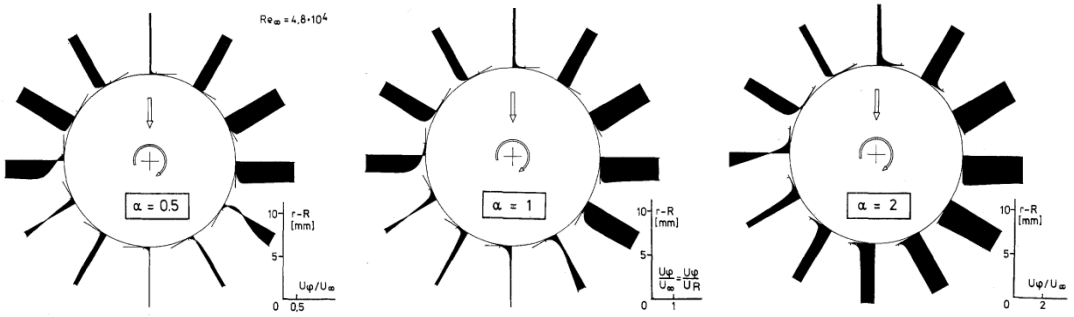

(a) k = 0.5 (b) k = 1.0 (c) k = 2.0

Figure 2.30: Boundary layer mean velocity profiles around a rotating cylinder at varying spin ratios (here α) and Re_D=48000 (Peller, 1986).

Peller (1986) further provided the distribution of the boundary layer thickness around the circular cylinder for the upstream and downstream moving walls at the tested spin ratios, Figure 2.31. From this the concept of boundary layer origin of Swanson (1961) was confirmed, where only at a spin ratio of k = 0 the separation angles measured from the assumed boundary layer origin, indicated by the horizontally written angles, and from the fixed peripheral angle at 0°, indicated by the vertically written angles, coincide. At k = 0.5, the location of zero velocity became 108°- 98°= 10°. Hence confirming the movement of the boundary layer origin towards the retreating side of the cylinder which increases with the increase of spin ratio.

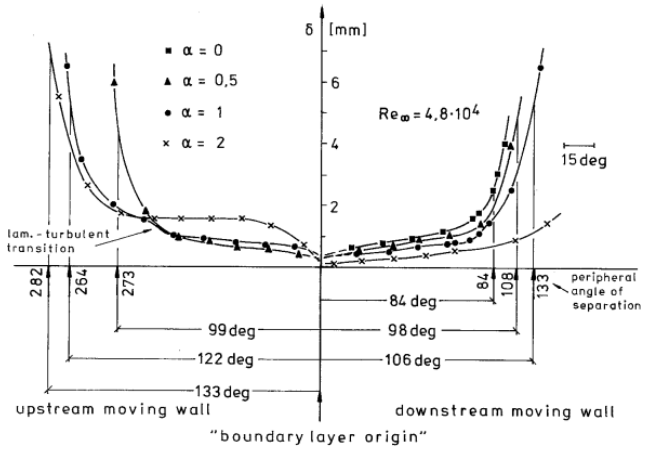

Figure 2.31: Boundary layer thickness distribution around a circular cylinder at various spin ratios and Re_D = 48000 (Peller, 1986).

Peller (1986) at last provided insights on the effects of heating to the boundary layer behavior. It was shown that for a heated cylinder at 100°C compared to one kept at room temperature, T = 21°C, separation of the boundary layer on the retreating side was considerably promoted to a more upstream position. Considering marine scale applications operated on the open sea, heating of the rotor surface is expected to be less of an concern and therefore will not be further addressed in this review.

As stated earlier the aerodynamics around a rotating cylinder is of unsteady nature. These unsteady effects surrounding the rotating cylinder, e.g. periodic vortex shedding, have also an effect on the behaviour of the boundary layer. Tanaka and Nagano (1973) investigated the behaviour of the separation point with the use of a closely placed hot-wire probe at subcritical and critical Reynolds numbers, 48000 < Re_D < 371000 and k < 1.1. They showed the dependency of the fluctuating angular position of the separation points, θ_S, to the spin ratio, and found out that the free shear layer in close proximity to the separation points oscillates in the frequency of the eddy shedding Figure 2.32.

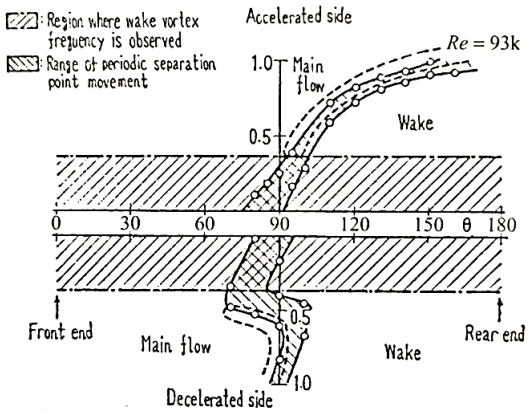

Figure 2.32: Fluctuating angular position of separation points at Re_D = 93000 (Tanaka & Nagano, 1973).

The kink in the figure on the decelerating side of the cylinder is due to boundary layer transition and turbulent re-attachment happening at this side of the cylinder first. This earlier transition on one side of the cylinder will give rise to another phenomenon called the *inverse Magnus effect* and will be covered in more depth in the next subsection 2.2.8.

2.2.8. Inverse Magnus effect

Observations of a lift force opposite to the one expected from the Magnus effect were made already in the early experiments from Lafay (1912a, 1912b). He showed that only for a particular range of Reynolds numbers, later to be found in the TrBL0, TrBL1 and TrBL2 regimes, and at low spin ratios the resultant force initially pointed in the opposite direction. Increase of the spin ratio gradually mitigated this effect and eventually the expected Magnus effect took over once again. Through his measurements of the pressure distribution on the cylinder surface he confirmed the lower pressure on the advancing side compared to the retreating side. This phenomenon is now known as the *inverse Magnus effect*.

Krahn (1956) stated that since the inverse Magnus effect occurs in the lower TrBL regimes, the origin of the inverse Magnus effect was due to the variation of transition points on the sides of the cylinder, where it either separates or turns to turbulent. This hypothesis led to the establishment of the relative Reynolds number concept as described in the previous section. Using the concept, he concluded that the boundary layer on the advancing side becomes transitional first and as a result a postponement of separation and an increase of suction shall be observed, whereas the retreating side boundary layer remains laminar and separates considerably earlier, before also becoming turbulent at higher spin ratios after which the Magnus effect is restored.

First Kelly and Van Aken (1956) partially and later Swanson (1961) proved the statements made by Krahn (1956) of the inverse Magnus effect being confined to the TrBL0, TrBL1 and TrBL2 regimes. In particular Swanson (1961) confirmed, with the use of a cylinder protruding through the wind tunnel walls, which he claimed to be the closest to two-dimensional conditions, the inverse Magnus effect to be present between 99000 < Re_D < 501000 at low spin ratios, Figure 2.33 and Figure 2.34. It was further shown that the largest inverse Magnus effect lift coefficient coincided with the TrBL1 regime, C_L = -0.6 and Re_D = 325000, where the formation of a laminar separation bubble is also present for the non-rotating cylinder case.

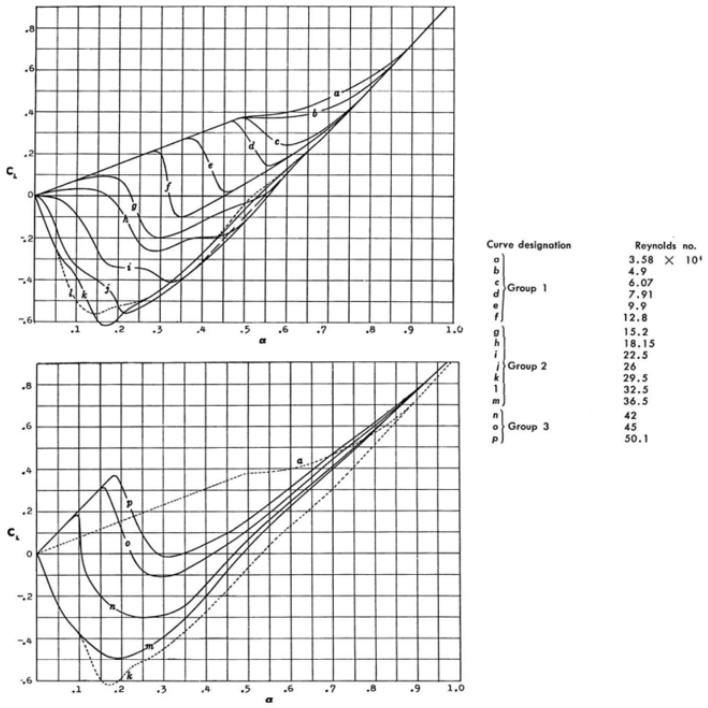

Figure 2.33: Lift coefficient versus spin ratio (here α) within the inverse Magnus effect regime (Swanson, 1961).

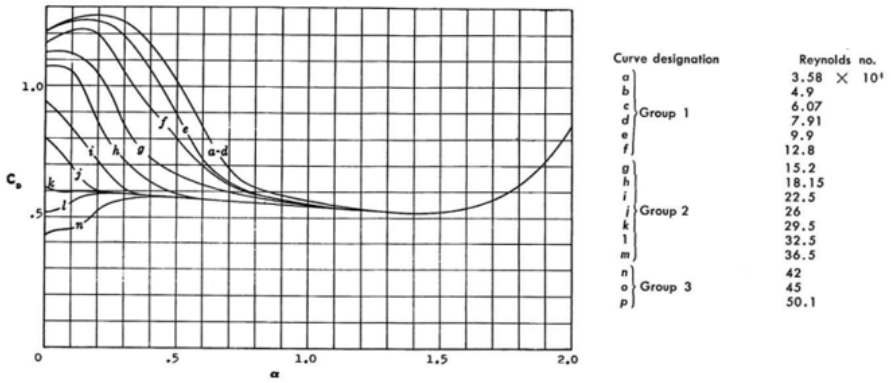

Figure 2.34: Drag coefficient versus spin ratio (here α) within the inverse Magnus effect regime (Swanson, 1961).

Ma et al. (2022) performed experimental research on a rotating cylinder within the inverse Magnus effect regimes at $k < 2$ and for $46000 < Re_D < 510000$. The critical Reynolds number was introduced as the point where after exceeding it a different behavior in mean CL, mean CD and a rapid increase of St is observed, meaning a change in flow regime is also realised. It was stated that the critical Reynolds number at which the LSB on the advancing side forms decreases with the increase of the spin ratio, Figure 2.35, and the strength of the LSB, showing a larger reduction in mean lift coefficient, increases with the increase of Reynolds number. This is in partial agreement with the data from Swanson (1961) where it is instead shown that the LSB becomes weaker again at the largest Reynolds numbers, $Re_D > 450000$. Most likely this is due to the accelerated transition to the turbulent state due to the larger Re_D.

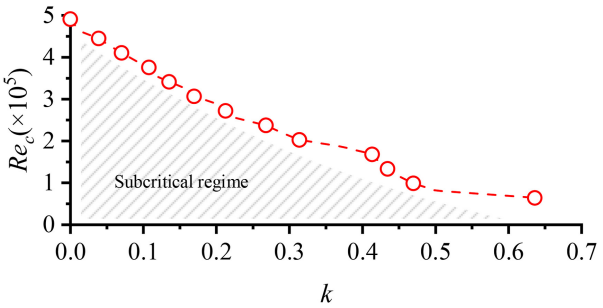

Figure 2.35: Critical Reynolds number relation with varying spin ratio (Ma et al., 2022).

Chopra and Mittal (2023) performed modern day large eddy simulations, LES, on the formation of laminar separation bubbles at the surface of a rotating cylinder in uniform flow. The tested Reynolds numbers were in the high subcritical regimes for Re_D = 60000 and 100000 and spin ratios below two, $k < 2$. The numerical study showed in general the same evolution of the boundary layers as explained by Krahn (1956) and Swanson (1961). However, interestingly it was noted that the boundary layer on the retreating side was said to remain fully laminar for all tested spin ratios. This observation contradicts the statements made earlier by Krahn (1956) and Swanson (1961) of a turbulent one at higher spin ratios, but reinforces the concept of a relative Reynolds number. The same laminar retreating side boundary layer was found by the LES studies of Muto et al. (2012) on a rotating sphere at critical Reynolds numbers.

The study from Chopra and Mittal (2023) further showed the reversal of the Magnus effect at the higher Reynolds number tested and, similarly to Ma et al. (2022), concluded that the critical spin ratio for which transition on the advancing side occurs, decreases with increasing Reynolds number, while an increase of the spin ratio causes the LSB to slowly decrease in size lowering the suction it creates until the regular Magnus effects takes over completely. However, the point at which the regular Magnus effects takes over, does not correspond with the complete disappearance of the LSB, but hence becomes weak enough for the inverse Magnus effect to no longer occur.

2.2.9. Pressure distribution

As earlier stated, the first measurements of the pressure distribution around a rotating cylinder were performed by Lafay (1912a), who used static pressure probes placed close the the surface of the cylinder.

Thom (1926c) designed a special device where a plunger opens the pressure tapping through a cam hitting a fixed stop, which can be placed at any desirable angular position, and a spring closing it shortly after (Zdravkovich, 2003). Using the device he managed to obtain pressure coefficient, C_p, distributions, indicated by the solid line, around the circumference of non-rotating and rotating cylinders at a selection of spin ratios, here V_r/V, and changing Reynolds number in the lower subcritical regimes by adjustments in freestream velocity, here V, Figure 2.36. A comparison is made to the potential flow theory, indicated by the dashed line from which he concluded that at higher spin ratios better agreement is found with the experiments.

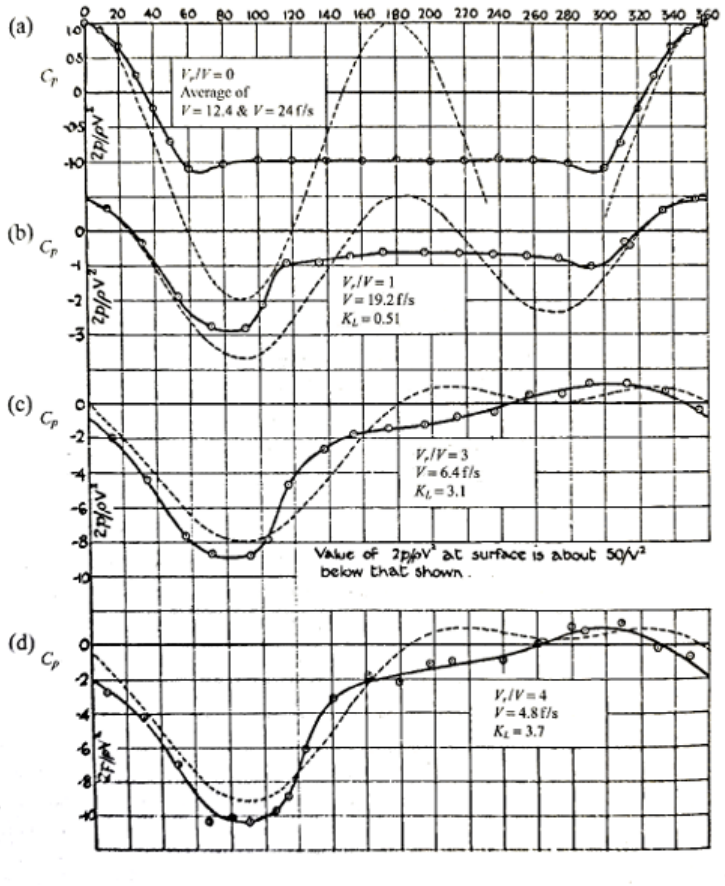

Figure 2.36: Rotating cylinder cross-sectional pressure coefficient distributions at subcritical Reynolds numbers and at (a) k=0, (b) k=1, (c) k=3 and (d) k=4 (Thom, 1926c).

From these pressure distributions with increasing spin ratios, it is shown, as explained before, that the movement of the stagnation point, C_p = 1, is gradually in the direction opposite of the rotation. Furthermore, it can be observed that the minimum pressure coefficient is drastically decreased and the pressure recovery is increased. The result is a greater asymmetry in the pressures between the two sides of the cylinder and hence the Magnus effect is realised. Note K_L is half the coefficient of lift due to the early usage of the dynamic pressure as ρV^2.

The first measurements of the spanwise pressure distribution around a rotating cylinder were also provided in the works from Thom (1926c). The resulting lift and drag coefficient distribution, Figure 2.37, showed only to be uniform in the midspan, with the lift dropping to zero at the ends accompanied by

an increase in drag close to the tip region. He noted that the drop in lift at the tips was not due to the fall of velocity towards zero as only an approximate drop of 10% was seen. Thom further managed with the use of the spanwise lift distribution, to obtain an approximate distribution of the induced drag, shown as k_d', while the solid k_d line is calculated by applying Lock's wall corrections to the obtained results. The distribution shows that the induced drag mainly contributes to the rise of drag near the tips (Zdravkovich, 2003). Tip effects and other three-dimensional effects will be covered in more depth in subsection 2.2.12.

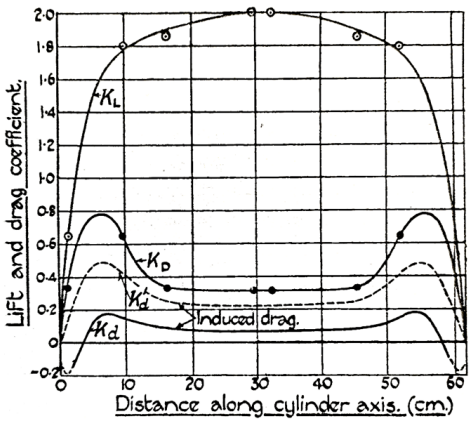

Figure 2.37: Spanwise lift, drag, and induced drag coefficient distribution at Re = 15000 and k = 2 (Thom, 1926c).

Miller (1976) presented a device of his own design for the measurements of pressure distributions around rotating cylinders. He showed the results of using the device at the higher critical Reynolds regime, Re = 224000, 344000, 449000 and spin ratios, k = 0.17, 0.77 and 2.05, Figure 2.38. The force coefficient depicted were deduced from the pressure coefficient values. The distribution at the Re = 344000 and k = 0.17 clearly shows the presence of the inverse Magnus effect as explained before.

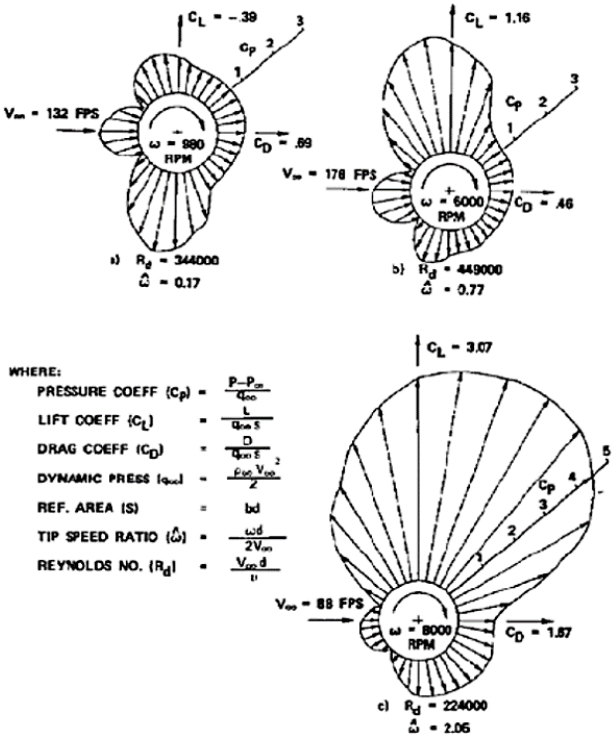

Figure 2.38: Rotating cylinder cross-sectional pressure coefficient distributions at critical Reynolds numbers (here R_d) (Miller, 1976).

Recent experiments on the pressure distribution around rotating cylinders were performed by Bordogna et al. (2019a) covering the critical and supercritical Reynolds number regimes, 180000 < Re_D < 1000000, Figure 2.39. He reported that in the range of 0.5 < k < 2, higher Reynolds numbers led to a more negative Cp_{min} and smaller Cp_{max}. At the tested Reynolds numbers equal to Re_D = 360000 and 1000000, a balanced change between the pressures resulted in a similar lift coefficient for both, while changes between the lower Reynolds numbers saw an increase in the lift coefficient. The drag coefficient within 1< k < 2.5 saw changes across all Reynolds numbers tested and was said to be the cause of the rearward movement of both the stagnation points and suction peaks with increasing Reynolds number. Bordogna et al. (2019a) further showed the changes in the pressure distribution at spin ratio in the range of 2.5 < k < 5 for the critical Reynolds numbers, Re_D = 250000 and 360000. The resulting pressure distributions overlapped showing no variation with Reynolds number, while the absolute C_p values kept increasing with increasing spin ratio.

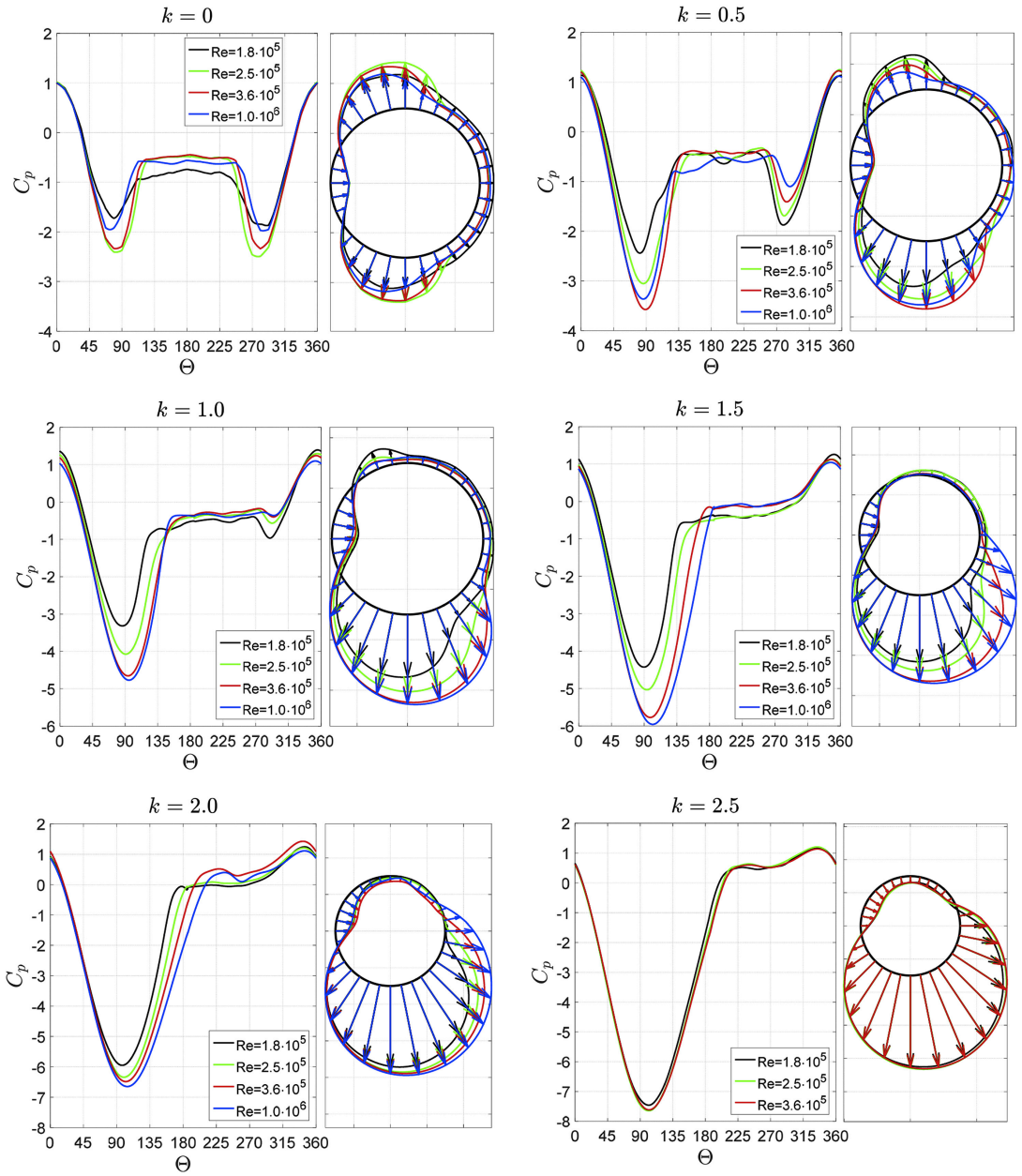

Figure 2.39: Rotating cylinder cross-sectional pressure coefficient distributions at critical and supercritical Reynolds numbers (Bordogna et al., 2019a).

2.2.10. Power consumption

The power consumption of a rotating cylinder, which becomes increasingly important when considering the application of such a device, has been scarcely researched. In the earlier years Reid (1924) was the first to report on such experiments for high subcritical Reynolds numbers. He concluded from his tests that the power consumption is greater for a rotating cylinder in still air compared to when placed in a flow and explained this was due to the rotation causing a smaller relative velocity around most of the circumference when placed in a flow, hence reducing the friction.

During the nineteen-eighties, the second period of particular interest in wind assisted ship propulsion devices, Clayton (1985) tested the aerodynamic performance of a rotating cylinder at subcritical Reynolds numbers, Re = 17100 and 49000, and compared it to similar tests performed with an airfoil. He found that the power absorption by the rotor practically remained the same with a change in Reynolds number.

Badalamenti and Prince (2008a) performed experimental measurements on a rotating cylinder at subcritical Reynolds numbers, 17000 < Re < 96000, for various end conditions and in still air similar to Reid (1924). His results showed, like Clayton (1985), no dependence in the power consumption by varying the Reynolds numbers and in contrast to Reid (1924) no difference for a rotating cylinder placed in either still air or a flow, Figure 2.40.

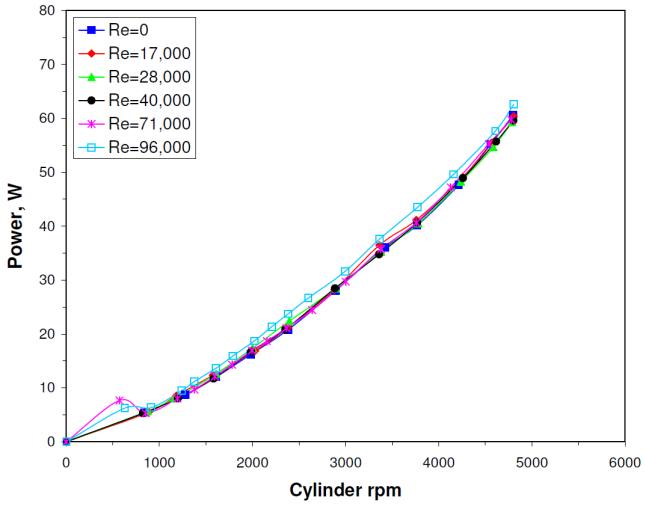

Figure 2.40: Effects of Reynolds number on the power coefficient of a rotating cylinder with two endplates of double the cylinder diameter size (Badalamenti, 2010).

At the critical and supercritical Reynolds numbers, 180000 < Re_D < 1000000, Bordogna et al. (2019a) showed the same independence in power consumption with changes in the Reynolds number, Figure 2.41a, and concluded, by taking measurement uncertainties into consideration, that also no differences are present between a rotating cylinder placed in still air or a flow, Figure 2.41b. However, closer inspection of the figures does seem to indicate that especially at spin ratios above 2.5 an increase in power consumption for the no wind condition occurs. Bordogna et al. (2019a) further showed through comparison with the analytical formula from Subramanya (2005), Equation 2.5, that the power consumption of a Flettner rotor scales with the cube of the tangential velocity, Figure 2.42. Based on the analytical formula, the surface area of the cylinder, $Area_s$, the skin friction coefficient, C_f, and the air density, ρ, further contribute to the power consumption of a rotating cylinder, while it is expected that in reality further contributions are made by any friction caused in the mechanical setup.

$$P = \frac{1}{2} C_f U_r^3 Area_s \tag{2.5}$$

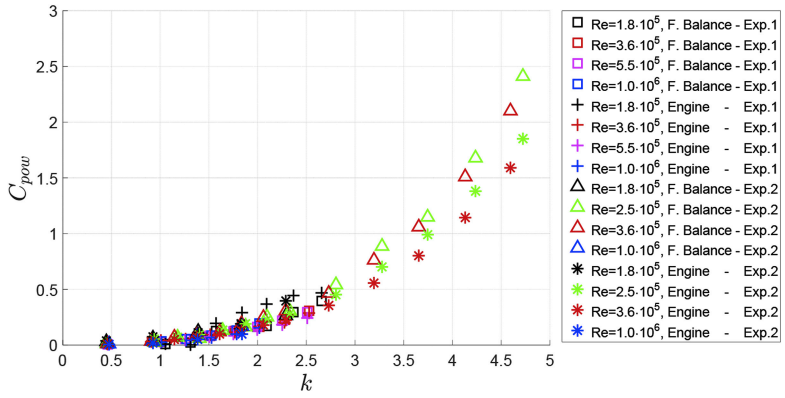

(a) *Wind-on conditions*

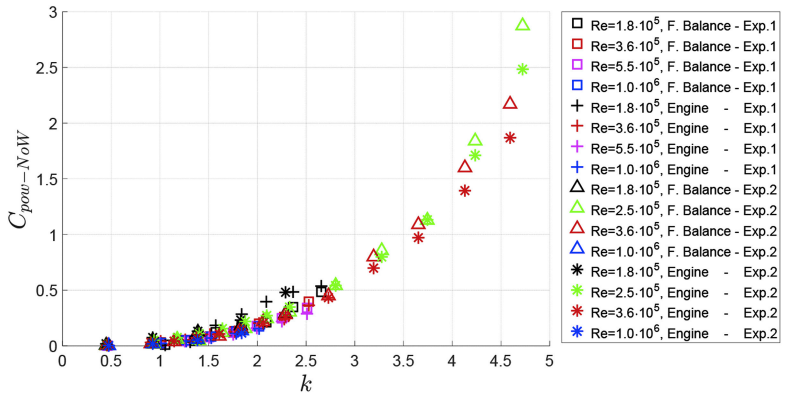

(b) *Wind-off conditions*

Figure 2.41: Effects of Reynolds number on the power coefficient of a rotating cylinder in (a) wind-on conditions and (b) wind-off conditions (Bordogna et al., 2019a).

2.2.11. Compressibility effects

As briefly mentioned before, compressibility effects on rotating cylinders are scarcely investigated in literature. Numerical investigations mainly consider incompressible flow solutions and, due to various testing limitations, experimental studies are more often conducted at lower spin ratios when larger Reynolds numbers are being used. Compressibility effects are however expected to be influential when considering rotating cylinders at large spin ratios, even when the freestream Mach number, M_∞ being the non-dimensional number indicating the extend of compressibility of a flow, is relatively small.

As an example, in case of Flettner rotor investigations this becomes a direct problem. Since the full scale applications operate at low freestream velocities, it is expected that at large spin ratios, the Mach number close to the surface of the cylinder is still small enough such that compressibility effects are considered to be negligible. For wind tunnel testing, most often performed in more readily available non-pressurised wind tunnel facilities with small test sections, an effort to reach flow similarity is realised by an increase of the freestream velocity such that larger Reynolds numbers can be reached. Ideally this results in comparable Reynolds numbers and spin ratios between the model and full scale application. However in such a case the Mach number, including its effects, can then be considerably different between the two.

Zdravkovich (1997) summarised compressibility effects for non-rotating cylinders and showed that the subsonic flow regime ends at a particular freestream Mach number deemed as the critical Mach number, M_{crit}. It has been stated that this value already lies close to 0.4 and therefore far from the sonic Mach number, M = 1. Increasing beyond this critical value of 0.4 will introduce supersonic regions around the point of minimum pressure coefficient, $C_{p_{min}}$, which are abruptly terminated with the occurrence of intermittent shock waves. An overview of the compressible flow regimes for non-rotating cylinders provided by Zdravkovich (1997) is shown below, Figure 2.43.

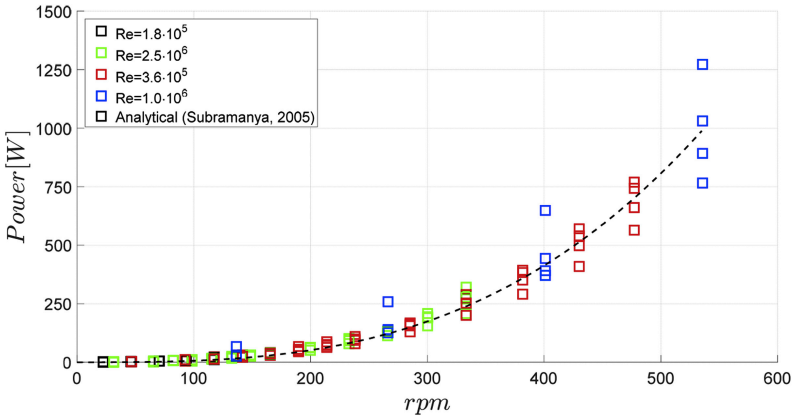

Figure 2.42: Effects of Reynolds number on the power consumption of a rotating cylinder compared to analytical results (Bordogna et al., 2019a).

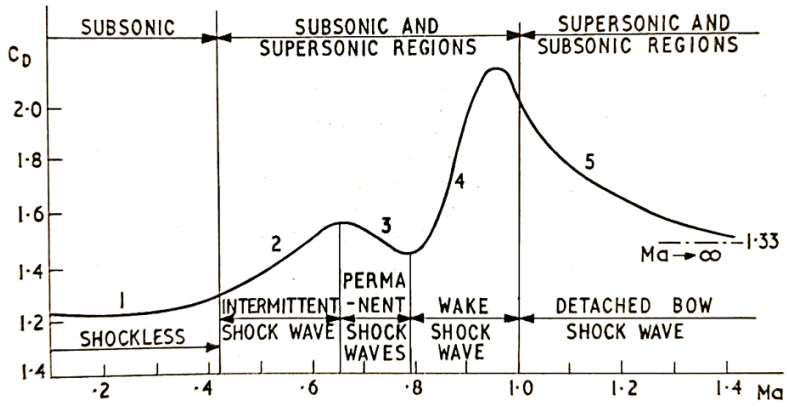

Figure 2.43: Compressible flow regimes classification showing the relation between the drag coefficient, C_D, and Mach number, here Ma, for a stationary cylinder (Zdravkovich, 1997).

The critical Mach number has been experimentally estimated by Naumann and Pfeiffer (1958) at a value of 0.42 for high subcritical Reynolds numbers. The critical Mach number however is not constant and depends on the minimum pressure coefficient. The theoretical critical Mach number can be calculated with the use of the estimated or measured minimum pressure coefficient and the isentropic flow Equation 2.6, with γ being the isentropic expansion ratio, e.g. of air.

$$C_{p_{min}} = \frac{2}{\gamma M_{crit}^2}\left[\left[\frac{\gamma+1}{2+(\gamma-1)M_{crit}^2}\right]^{-\frac{\gamma}{\gamma-1}} - 1\right] \tag{2.6}$$

A decrease in minimum pressure coefficient results in a decrease of critical Mach number. For rotating cylinders, it has been shown that the minimum pressure coefficient can reach values well below -10, (Bordogna et al., 2019a; Thom, 1926a). Making use of this isentropic equation the critical Mach number will then drop to 0.25 at a minimum pressure coefficient of -10. Based on this theoretical calculation it seems more likely for compressibility effects to play a larger role in rotating cylinder flow.

Teymourtasha and Salimipour (2017) did address the importance of compressibility around a rotating cylinder. Numerical simulations were conducted at very low Reynolds numbers, 40 < Re_D < 200, up to high spin ratios, k < 12, and with varying freestream Mach numbers, 0.05 < M_∞ < 0.4. It was shown, but only as an example for Re_D = 200, k = 6 and M_∞ = 0.2, an oscillating normal shock wave does occur, Figure 2.44, and can have a substantial influence on the flow field and force coefficients even at these low freestream Mach numbers.

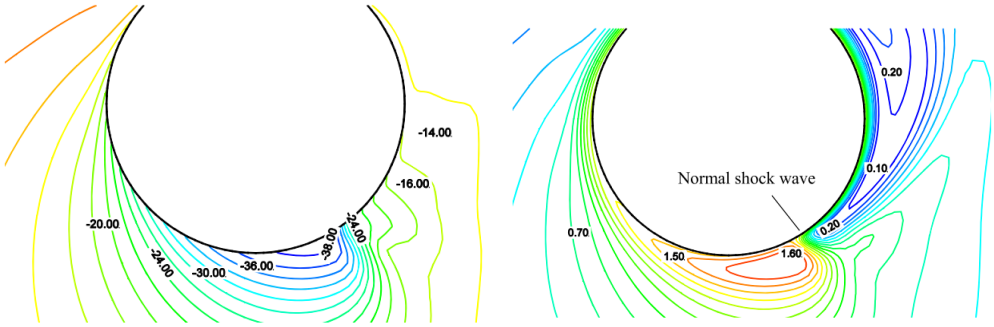

(a) *Pressure coefficient* (b) *Mach number*

Figure 2.44: Rotating cylinder with normal shock wave at Re_D = 200, k = 6 and M_∞ = 0.2 contour plots showing (a) Pressure coefficient and (b) Mach number (Teymourtasha & Salimipour, 2017).

The results at M_∞ = 0.05 showed excellent agreement with the incompressible flow solution from Mittal and Kumar (2003) for spin ratios up to k = 5, Figure 2.45. However, at M_∞ = 0.1 compressibility effects were already considerable at the same high velocity ratios. In general, the lift coefficient experienced plateauing of its mean value which happens at a lower spin ratio and to a lower value with the increase of the freestream Mach number. For the drag coefficient, before first dipping to a lower value, plateauing was also found, which occurs similarly at a lower spin ratio but instead to a higher mean value with the increase of the freestream Mach number. Furthermore, the behaviour of both lift and drag coefficient with M_∞ > 0.2 was found to be independent to changes in the tested Reynolds numbers, while at lower freestream Mach numbers both a decrease in maximum lift coefficient and spin ratio at which plateauing occurs and an increase in drag coefficient and Strouhal number was observed.

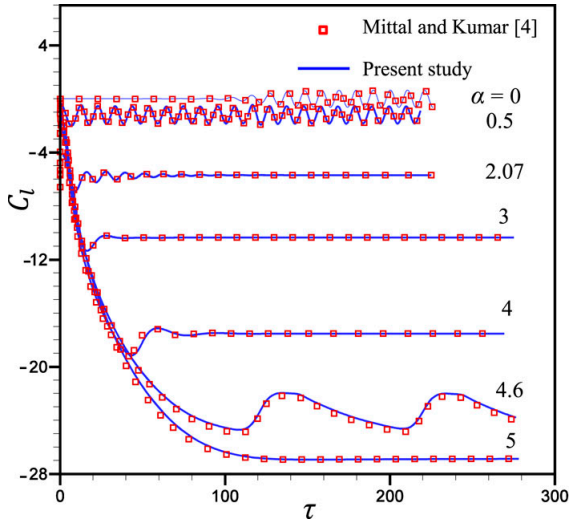

Figure 2.45: Agreement between incompressible and compressible flow simulations of the instantaneous lift coefficient with non-dimensional time τ at Re_D = 200, M_∞ = 0.05 and varying spin ratios (here α) (Teymourtasha & Salimipour, 2017).

The freestream Mach number showed to further have a significant effect on the state of flow. As was discussed in the earlier sections, at low M_∞ < 0.2 and low k, Von Kármán vortex street type shedding occurs and at high k the steady-state flow field solution is reached. However, for M_∞ > 0.2 and high k, the one-sided vortex shedding phenomenon becomes governing, which happens at smaller spin ratios and does not disappear when k is increased further unlike for the incompressible case, Figure 2.46. Additionally, this flow state comes with large fluctuations in the lift coefficient in the order of ΔC_L = 6, especially at the larger freestream Mach numbers. If this one-sided vortex mode is of similar nature as the one discovered by Mittal and Kumar (2003) or different due to formation of shocks is not mentioned.

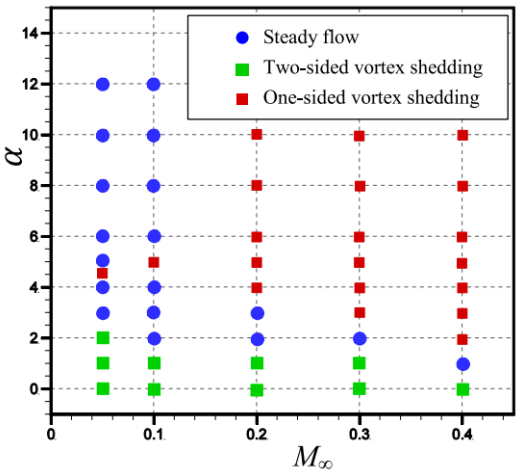

Figure 2.46: Flow states for a rotating cylinder at Re_D = 200 with varying M_∞ and spin ratios (here α) (Teymourtasha & Salimipour, 2017).

Although showing significant compressibility effects, unfortunately the investigation is only considering very low Reynolds numbers, where at the Reynolds number regimes of interest, e.g. subcritical, critical and supercritical, no such studies are performed nor mentioned. The expectation is however that due to the often higher freestream velocities at larger Reynolds numbers, compressibility effects, especially in wind tunnel testing, can not be neglected as has been shown for the low Reynolds numbers. As of now this remains mere speculation and would require further research to show its effects or lack of.

2.2.12. Three-dimensional rotating cylinder in subsonic flow

Although this section only briefly puts the emphasis on the three-dimensional effects around a rotating cylinder placed in a disturbance-free subsonic flow, many of the phenomenon described above are inherently three-dimensional. Eddy shedding, turbulence, the irregular formation and fragmentation of laminar separation bubbles and the occurrence of spanwise toroidal vortices, as shown before, are just a few examples. Additional three-dimensional effects on the applied aerodynamics of a rotating cylinder will be covered throughout section 2.3.

The only geometrical difference between a theoretical two-dimensional rotating cylinder and a three-dimensional rotating cylinder is the finite length with set end conditions. The addition of end conditions allows for additional spanwise effects to occur. The spanwise pressure distribution of such a cylinder has been shown in subsection 2.2.9, Figure 2.37. It was shown that the sectional lift coefficient dropped to zero at the ends. The sectional drag coefficient was at its highest in close proximity to the ends, mainly due to the induced drag, before also dropping to zero. Only for a small portion at midspan the flow was deemed to be approximately two-dimensional.

In terms of absolute force coefficient values, it can be shown that between the quasi-two-dimensional experimental results of Swanson (1961), Figure 2.10, and Bordogna et al. (2019a), Figure 2.13a, and the three-dimensional experimental results of Badalamenti (2010), Figure 2.11a, and Chen and Rheem (2019), Figure 2.12a, that the lift coefficient, in case of a three-dimensional rotating cylinder, will reach a plateau after which it remains constant with an increase of spin ratio. The spin ratio at which this occurs and the height of the the lift coefficient is then depended on the magnitude of the other influencing parameters present. The drag coefficient is seen to keep increasing after the plateauing of the lift coefficient, however at a slower rate as before. Additionally, Badalamenti (2010) showed that the mean drag coefficient of a cylinder at standstill and very low spin ratios was lower compared to the quasi-two-dimensional case. This was deemed to be due to the inflow of air into the wake near the tips of the cylinder, giving a rise in pressure behind the cylinder, and hence reducing the effects of the the bluff body wake on the drag coefficient.

In the earlier studies from Badalamenti and Prince (2008b) experiments on the vortex and wake characteristics of a low aspect ratio three-dimensional rotating cylinder at subcritical Reynolds numbers without endplates were performed. It was found that due to the pressure equalisation at the free ends, a large horseshoe like vortex system of two counter-rotating vortices emerges from the tips of the cylinder that move downstream. It was said that at a spin ratio of k = 1.5, the vortices started to govern the wake and with a further increase of k, the vortices started to move more inboard, towards the midspan, and increase in strength, Figure 2.47. The inwards movement and increased strength might therefore be the cause of the lift coefficient to plateau as this was also found to occur at the same spin ratio, k = 1.5. The drag coefficient keeps increasing, potentially by the influence of the stronger vortex induced low total pressure zone behind the cylinder, and increased tilt of the lift vector, with an increase of the spin ratio. In general it appears however that the drag coefficient is more susceptible to changes in the experimental setup and hence it becomes more difficult to determine any trends (Badalamenti & Prince, 2008a).

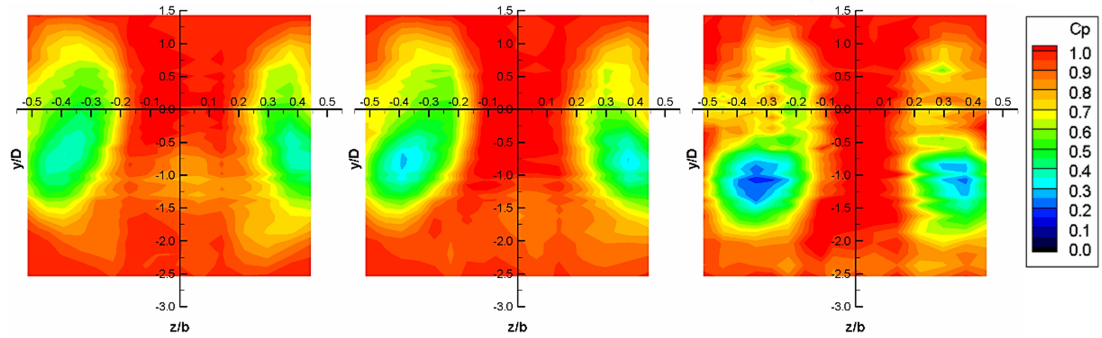

(g) $\Omega = 1.60$ (h) $\Omega = 1.87$ (i) $\Omega = 2.20$

Figure 2.47: Mean spanwise total pressure variation for a three-dimensional rotating cylinder at Re_D = 70000 and various spin ratios (here Ω) (Badalamenti & Prince, 2008b).

2.3. Applied aerodynamics of a rotating cylinder in subsonic flow for thrust producing applications

Fundamental research in terms of aerodynamic force coefficients is often more focused on finding the cause of the changes observed in the mean and fluctuating components with variations in the influencing parameters and to determine their limits. From this it was shown that the rotating cylinder is capable of producing very large lift and drag coefficients as well as large absolute forces for a relatively small surface area. These large force producing capabilities makes the device a promising candidate for real-life applications.

The applications for a rotating cylinder placed in a flow can be divided into two main categories, where it is either used a sole thrust producing device or as a mean of flow control. The focus of this research is in particular on the thrust producing capabilities of the rotating cylinder placed in a subsonic flow, therefore flow control applications, e.g. stall control of an airfoil, will not be further covered here. For the interested reader on flow control using rotating cylinders, the works from Tennant et al. (1976) and Al-Garni et al. (2000) are just two examples of an extensive set of literature available.

Furthermore as there have been many more ideas and attempts on implementing rotating cylinders it will be too much to cover them all. An overview of various ideas and applications surrounding rotating cylinders can be found in the review from Seifert (2012) and the books of Zdravkovich (1997, 2003).

The following section 2.3 builds upon the fundamentals explained in section 2.2 and discusses applied aerodynamics of the thrust producing applications of a rotating cylinder in subsonic flow. The focus will be on thrust producing applications with a particular interest for wind assisted ship propulsion. Important performance characteristics for real life applications of the rotating cylinder will be briefly discussed in subsection 2.3.1 and subsection 2.3.2. Then, some additional external parameters influencing the aerodynamic performance during full scale operations will be covered in subsection 2.3.3. At last for the interested reader, subsection 2.3.4 of this chapter steps shortly away from the main subject of this project, and will give a short summary on flow control methods applied to rotating cylinders.

2.3.1. Lift-to-drag ratio

Recent experimental studies from Chen et al. (2023) showed the aerodynamic performance of Flettner rotors with a focus on marine applications. To determine the aerodynamic performance, the lift-to-drag ratio, C_L/C_D, the resultant force coefficient, C_R, and directionality of the resultant force, θ_R, were investigated for various combinations of influencing parameters as well as for a bare three-dimensional cylinder with one free end and various Reynolds numbers. The lift-to-drag ratio is in particular important for WASP applications as the ship velocity contributes to the apparent wind angle and hence brings the wind angle forward. In operation this means the ship will mostly sail in upwind conditions, where any improvements in the lift-to-drag ratio will yield large benefits (Bordogna et al., 2022).

In case of the unmodified cylinder at Re_D = 233000, Figure 2.48, the resultant force coefficient, and its direction, are showing negative values at first for low spin ratios due to the inverse Magnus effect and is then followed by a steady rise until it plateaus at a specific value. This is in line with the results shown in the section 2.2. The directionality is shown to reach a maximum angle of around 70° between 1.5 < k < 2 after which it slowly decreases again and plateaus around k = 3 just below an angle of 60°. The pressure distributions obtained by Bordogna et al. (2019a), shown in subsection 2.2.9, showed to be in good agreement with the resultant force behaviour, where also the shape of the pressure distribution remains constant at these high spin ratios, where the low pressure zone has moved more to the rear of the cylinder surface. Figure 2.49 shows the lift and drag coefficient behaviour for the same rotor and conditions. The lift-to-drag ratio is also indicated and it is shown that the maximum is obtained for the same range of spin ratios, 1.5 < k < 2, at which unsurprisingly the directionality is at its maximum as well. The effect of the Reynolds number for a three-dimensional rotating cylinder with a small endplate operating within the subcritical and critical regimes on the lift-to-drag ratio is indicated in Figure 2.50. The maximum lift-to-drag ratio appears to occur at slightly higher spin ratio, k = 2, with an increase of Reynolds in the critical regime compared to the subcritical regime where a value of k = 1.5 was found. At Re_D > 187000 the variation in both lift and drag coefficient became almost negligible, which

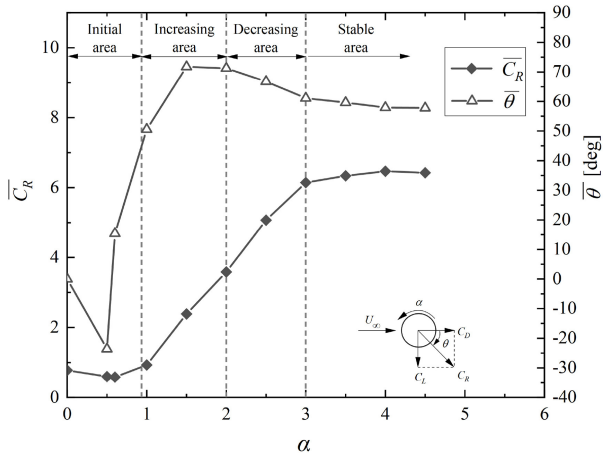

Figure 2.48: Resultant force coefficient (here $\overline{C_R}$) and directionality (here $\overline{\theta}$) behaviour with spin ratio (here α) at Re_D = 233000 (Chen et al., 2023).

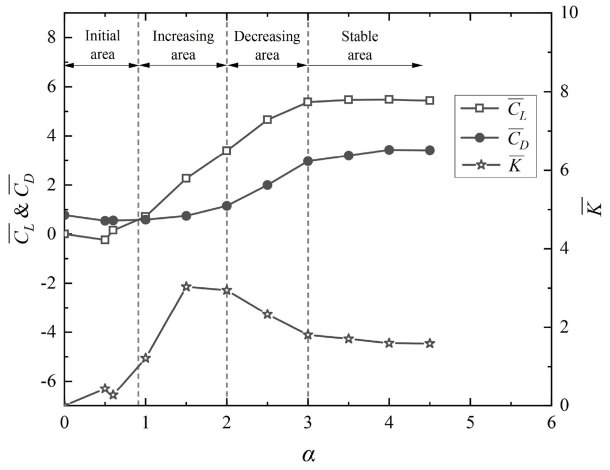

Figure 2.49: Lift and drag coefficient (here $\overline{C_L}$ and $\overline{C_D}$) and lift-to-drag ratio (here $\overline{K}$) behaviour with spin ratio (here α) at Re_D = 233000 (Chen et al., 2023).

is said to be caused by the now stable turbulent boundary layer on the surface of the rotor. From this it was concluded that the results at the larger Reynolds numbers can be scaled towards the real-life applications. However, the results from Bordogna et al. (2019a) indicated the drag coefficient remains dependent on the Reynolds number even in the supercritical regime. A possible explanation might be due to the differences of experimental setup where Bordogna et al. (2019a) is quasi-two-dimensional compared to the three-dimensional setup of Chen et al. (2023). From the results above it is shown that aerodynamically speaking the most efficient spin ratio appears to be in the range of 1.5 < k < 2, where the lift-to-drag ratio is at its highest for the isolated three-dimensional cylinder at the tested conditions and configuration. It was also shown that the resultant force coefficient increases beyond these spin ratios. Based on this it must be noted that it is possible that in real-life marine operations, opposed to aerospace applications, higher spin ratios can yield larger benefits. The wind direction relative to the ships orientation, e.g. tail wind, might result in an optimum directional angle of the resultant force that acts more parallel to the incoming flow, instead of perpendicular when C_L/C_D is at its maximum but not C_R. Therefore, a higher drag coefficient is not always detrimental when considering operational conditions and hence means to control the directionality of the resultant force is much more desired for marine applications.

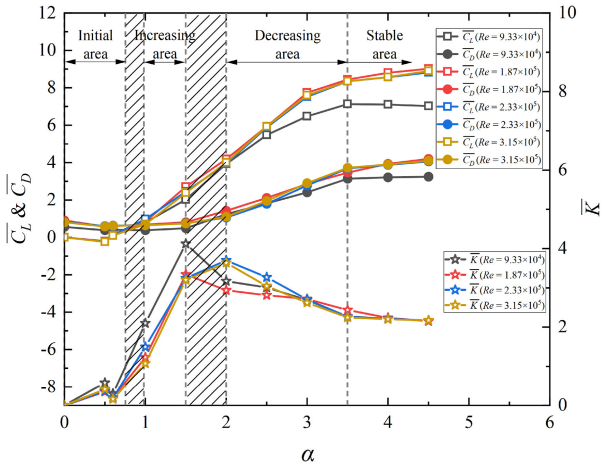

Figure 2.50: Lift and drag coefficient (here $\overline{C_L}$ and $\overline{C_D}$) and lift-to-drag ratio (here $\overline{K}$) behaviour with spin ratio (here α) for subcritical and critical Reynolds numbers (Chen et al., 2023).

2.3.2. Power efficiency

In order to successfully make use out of the large resultant force capabilities of the Flettner rotor in real-life operations, the power necessary to drive the rotor must remain relatively small to make it operationally efficient compared to other thrust producing devices. Badalamenti and Prince (2008a) investigated the power efficiency of various end conditions at subcritical Re_D = 40000. It was shown that for either end condition in terms of power required the lift production is rather costly and quickly plateaus at a value specific to the configuration, where any extra increase of power will yield no additional increase of the lift coefficient, Figure 2.51a. The lift-to-drag ratio rose similarly as the lift coefficient rapidly to a maximum after which it drops off and plateaus at a lower value, Figure 2.51b. The results show similarity to the behaviour of the lift coefficient and lift-to-drag ratio with variation in spin ratio as shown by Chen et al. (2023). This is due to the power consumption mainly being influenced by the tangential velocity as was shown in subsection 2.2.10.

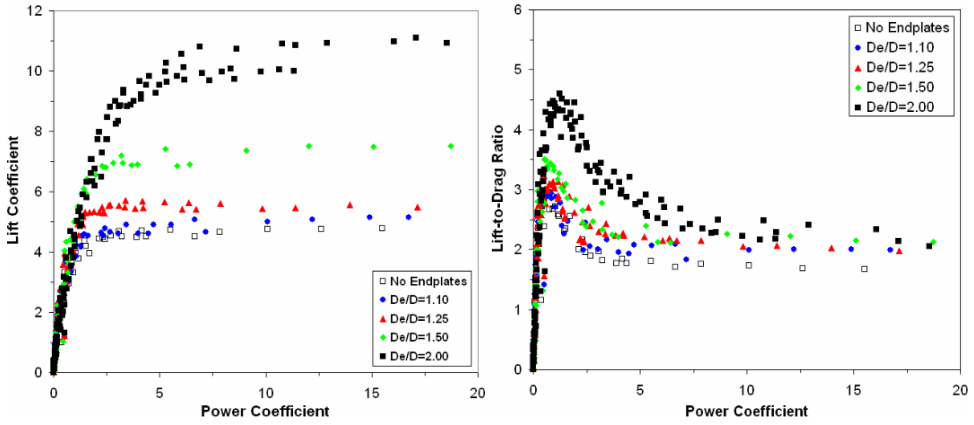

(a) *Lift coefficient efficiency* (b) *Lift-to-drag ratio efficiency*

Figure 2.51: Power efficiency of a three-dimensional rotating cylinder at Re_D = 40000 and various end conditions for (a) Lift coefficient and (b) aerodynamic efficiency (Badalamenti & Prince, 2008a).

Kwon et al. (2022) performed a numerical parametric study using steady RANS simulations for various Flettner rotor configurations at critical and supercritical Reynolds numbers. By analysing the torques generated by the aerodynamic loads, the ratio between the output power of the lift force to the input power to rotate the cylinder was calculated and denoted as the energy efficiency, E. It was found that the energy efficiency drops with an increase of spin ratio and its maximum was found at the lowest spin ratio tested at k = 1, Figure 2.52. The results are inline with the experimental results of Badalamenti and Prince (2008a).

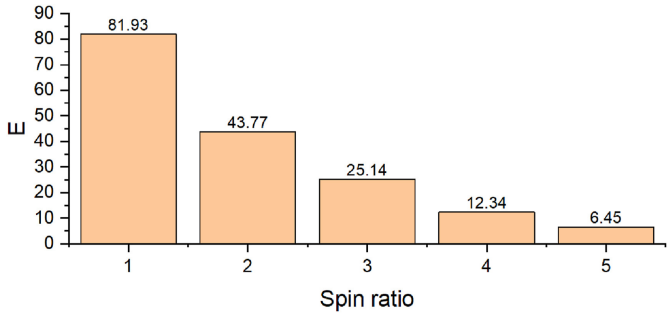

Figure 2.52: Energy efficiency of a three-dimensional rotating cylinder with endplate at Re_D = 766000 and varying spin ratio (Kwon et al., 2022).

2.3.3. External disturbances

This section will cover external disturbances encountered during real-life operations impacting the performance of the Flettner rotor, adding to the list of disturbance parameters outlined in subsection 2.1.3.

When considering real-life applications, variations in wind direction and heeling angles of the mounting platforms, e.g. on a deck of a ship, are causes of a yawed inflow direction of the freestream at the cylinder surface. The effects of a yawed inflow direction on a rotating cylinder has been extensively investigated by Badalamenti (2010). For the lift coefficient, larger angles of yaw meant a loss in maximum obtainable lift coefficient. The shape of the lift curve, between 0.5 < k < 1.5, remained roughly the same and plateauing occurred at lower spin ratios but never lower than k = 1.5 even for large yaw angles and all end conditions. The drag coefficient showed a similar trend as the lift coefficient, where its maximum value gradually lowered, to approximately the same extent, with an increase of yawing angle. For a more detailed explanation, Badalamenti (2010) may be consulted, and further includes the effects of yaw on different end configurations and the moments generated on the cylinder.

Another recent area of active research, which is important to note when considering real-life applications, is on interaction effects. In particular between multiple rotors in close proximity and also with its surroundings, e.g. the hull of the ship. As this would be a completely different field of research and to limit the scope of the current project, also these interaction effects will not be further covered here. Bordogna et al. (2020) and Chen et al. (2023) performed experimental research on the topic and it is advised to consult their works when concerning interaction effects.

When dealing with rotating cylinder applications operating in the atmosphere and in close proximity to the Earth's surface, the atmospheric boundary layer, with a thickness of approximately a couple of tens of meters, will have an effect on the performance of such a device. In particular for large full scale devices reaching heights of several meters, e.g. Flettner rotors on the deck of a ship. As a result of the velocity gradient within the atmospheric boundary layer, the spin ratio across the span of the rotating cylinder will vary. Hence, additional spanwise effects, e.g. differences in pressure distribution, vortex shedding, wake characteristics and boundary layer behaviour, are expected when operating in such conditions. Available research on rotating cylinders operating within the atmospheric boundary layer is scarce, only recently Massaro et al. (2024) conducted such an investigation. The direct numerical simulations, DNS, utilised in the study, showed such spanwise variations and further identified a large scale structure in close proximity to lower wall, which had not been mentioned before.

2.3.4. Means of flow control

For the sake of completeness and curiosity of the reader, this section provides a brief summary on means of flow control applied to a rotating cylinder in past research. The modifications applied are a mix of geometrical modifications, e.g. cross-sectional or spanwise variation in cylinder shape, surface modifications, e.g. rough, porous or structured surfaces, and external, e.g. tip devices, spanwise discs or flaps. Research on the application of active means of flow control, e.g. boundary layer blowing or suction, is believed to have not been published at the time of writing.

Spanwise geometrical modifications have been investigated in the form of a tapered cylinder experimentally by Tanasheva et al. (2020) and numerically by Jiangping et al. (2019), and as a spanwise wavy rotating cylinder numerically by Zhuang et al. (2018). For the tapered cylinder, Tanasheva et al. (2020) stated a decrease in the drag coefficient with the lift coefficient being preserved, whereas Jiangping et al. (2019) showed an increase in aerodynamic performance at high spin ratios, $k > 2$, and a slight deficit at lower spin ratios. The wavy cylinder produced less lift and needed to be spun almost exactly twice as fast to achieve similar levels compared to the circular cylinder, while the majority of the lift was produced on the saddle point between the waves and additional vortices were being shed from the nodes at all spin ratios.

Investigations into a variation of cross-sectional shapes compared to the standard circular cylinder have been performed over the years. Examples of which are; cross shaped (Reid, 1924), elliptic (Lua et al., 2018), multiple sided shapes (Pezzotti et al., 2020), and clover shaped (Huang et al., 2023). It became apparent that any deviations from the unmodified circular cylinder cross-section will result in a reduction of lift coefficient and reduced aerodynamic performance, except for the multiple sided shapes. The multiple sided shapes showed to alter the vortex shedding characteristics drastically, which led to increased lift coefficient at low spin ratios, $k < 1$. However, for all cases at the cost of an large increase in the drag coefficient as well as the power consumption. Nevertheless, as most of the investigations deal with simplifications and non of the cross-sections are shape optimised, it is too early to conclude that no cross-sectional modifications exists that outperform the conventional circular shape.

Surface roughness has been investigated by experimentally by Thom (1926b) and Thom and Sengupta (1932), and numerically by Everts et al. (2014). Both an increase in lift coefficient and drag coefficient had been shown between the studies. Additionally, Thom (1926b) showed a large increase in the torque coefficient, C_T, while Everts et al. (2014) indicated the effects of roughness on the lift-to-drag ratio, where its optimum shifts more towards the higher spin ratios. Furthermore, Thom and Sengupta (1932) found that after the application of roughness no longer the effects of the inverse Magnus effect, described in subsection 2.2.8, are shown. The roughness causes a premature transition of the boundary layer to the turbulent state without the formation of a laminar separation bubble and hence the negative lift typically recorded turns to positive with roughness applied.

The experimental study from Kussaiynov et al. (2015) considered rotating cylinders with porous surfaces at subcritical and critical Reynolds numbers, $40000 < Re_D < 105000$. It was shown that with an increase of porosity the mean lift and drag coefficient are increased, while there is little change in the dependencies to both the Reynolds number at set rotational speed and at set Reynolds number.

Takayama and Aoki (2005) performed experiments on a cylinder with groves of varying depth and a small endplate at subcritical and critical Reynolds numbers, $40000 < Re_D < 180000$ and low spin ratios, $k < 1$. It was shown that the increase of grove depth resulted in a reduction of the critical Reynolds number range and beyond this range the flow would behave in a supercritical sense, meaning the lift coefficient increases monotonically with spin ratio and the drag coefficient remains nearly constant for $k < 1$.

Both the studies from Prince et al. (2016) and Proença et al. (2022) performed experiments on a rotating cylinder with three patterns of structured surfaces at subcritical Reynolds numbers $34000 < Re_D < 60000$. Streamwise, spanwise and diamond shaped protuberances were considered. It was found that the streamwise pattern with rib sizes less than 5% of the cylinder diameter resulted in a large increase of the lift coefficient (Proença et al., 2022). The lift-to-drag ratio was significantly improved between $0.5 < k < 2$, where it reached a slightly higher maximum at a lower spin ratio of $k = 1.5$ compared to the smooth cylinder. The rapid rise in drag coefficient at higher spin ratios resulted in the lower aerodynamic efficiency.

To minimise the negative effects on the aerodynamic performance of the three-dimensional Flettner rotor due to the pressure equalisation at the free ends and the presence of strong tip vortices, many investigations have been performed on altering the end conditions. Thom (1926b) tested the standard square shaped cylinder ends against rounded elliptical ends at $Re_D = 21900$ and $k < 4$ for $A = 3.75$,

4.4. It was shown that the ellipsoid ends produced both less drag and lift, while the reduction in lift was always greater than the drag and appeared sooner (Badalamenti, 2010).

Investigations on tip end devices, e.g. endplates, came from Betz (1925), Badalamenti and Prince (2008a), Thouault et al. (2012), Zhao et al. (2023) and Chen et al. (2023). It was shown that the effects of adding endplates on the aerodynamic forces appear to be similar as an change in the aspect ratio, resulting in a drastic increase of the aerodynamic performance by altering the formation of tip vortices. The best performing endplates in terms of force coefficients were of equal size, rotating and as large as possible placed on the two ends of the cylinder. It was shown that the lift coefficient continued to increase with increasing size, delaying the flatting of the lift curve at high spin ratios, but with an increase in power consumption. For the drag coefficient smaller endplate sizes, D_e/D < 1.5, showed to be beneficial at low spin ratios, k < 0.5, as well as for very high spin ratios, k > 4. While the large endplate sizes provided significant drag reduction at moderate spin ratios, 1 < k < 3.

Another investigation of the many experiments from Thom (1934) was on the effects of spanwise discs placed along the cylinder at two different pitch distances. The addition of spanwise discs showed a drastic increase in the lift coefficient at high spin ratios, k > 4, while the drag coefficient saw a rapid decrease up to a spin ratio of k = 7, before rising again. Surprisingly between the range of 4 < k < 7, a negative drag coefficient was found. Thom (1934) mentioned that a potential cause of this could be due to the wall interference when working in a closed test-section, however Seifert (2012) speculated it to be due to the measurements being taken at the negative peaks of the fluctuating drag coefficient. This is particular pronounced for the one-sided vortex shedding mode that falls within the particular range of spin ratios. It must be noted however that the negative drag was only measured on one set of experiments where also a new force balance was being used and hence could have caused the large differences in results (Badalamenti, 2010).

Thouault et al. (2012) performed fully turbulent unsteady RANS simulations on a three-dimensional rotating cylinder with spanwise discs at a subcritical Reynolds number, Re_D = 29000, and varying spin ratios, 1.9 < k < 3.4. The numerical results on the aerodynamic force coefficients show a different behaviour compared to the results obtained by Thom. Effects on the lift coefficient are already apparent at k > 2.5, opposed to the values of k > 4 in the results from Thom, while the drag coefficient does not reduce at such a rate as before with the curve remaining close in shape to the one considering a bare cylinder. An increase of the streamwise velocity component between the two facing boundary layers on the disc surfaces, a reduction in boundary layer thickness by the influence of the radial flow component towards the discs and the distribution of vortex strength along the span shed at each disc, are the main mechanisms yielding the noted performance increase.

At last, Bordogna et al. (2022) investigated experimentally the effects of a stationary spanwise flap placed on a large scale two-dimensional Flettner rotor. The flap could be fixed at any angular position and was tested at a critical Reynolds number, Re_D = 360000. The main effect of the flap is the capability of setting a fixed separation point at the surface of the cylinder, in turn this would allow for, to a certain extent, the control of the pressure distribution and hence the direction of the resultant force. It has been shown that the aerodynamic performance can be improved by the addition of a spanwise flap, however this added performance comes at a cost. For optimal aerodynamic performance, the Flettner rotor with spanwise flap must be operated at significantly higher spin ratios. From subsection 2.2.10 it was shown that the power consumption of a Flettner rotor scales with the cube of the tangential velocity, hence the power consumption rises significantly. The impact of the added power consumption was however not included in the investigation, allowing for assessing the aerodynamic performance more from a theoretical perspective.

2.4. Research objectives, questions and limitations

As there is a push for reducing greenhouse gas emissions in the shipping industry, aerodynamic research on the promising Flettner Rotor wind assisted ship propulsion device can yield large benefits both environmentally and financially for the shipping industry. Following the literature study, it has been shown that improvements of the aerodynamic performance of such a device can be realised in more than one way. Both the increase of the lift-to-drag ratio, either by increasing the lift coefficient, decreasing the drag coefficient, or a combination of, and the ability of directionality control of the resultant driving force are the main industry level goals. The directionality control in particular can result in the deployment of the device under a wider range of wind conditions, thus providing even greater benefits.

To realise such a large scale investigation on Flettner Rotor design, a suitable and well understood experimental setup is vital to the success of the project. Such a setup is currently not available at the lab where the project will be conducted. Therefore, this section will explain the motivation behind the need of such a setup and presents the topics of the presented research. As the main topic of this project concerns the design and characterisation of a new experimental setup, the presented literature study will be used as a tool of comparison and gaps found will be proposed as recommendations for future research in chapter 7. The specifics on the research topic and its objectives are established in subsection 2.4.1 followed by the research questions in subsection 2.4.2. At last, this section is concluded in subsection 2.4.3 by defining the scope of the project and describing its limitations.

2.4.1. Research topic and objectives

The project will take form as an experimental study on the determination of the aerodynamic performance of a rotating cylinder used as a propulsive device, through the Magnus effect, for wind assisted ship propulsion at subcritical and critical Reynolds numbers. The subcritical, critical or higher Reynolds regimes are of most interest due to the large size of the full scale applications and relatively scarceness of the data available within these regimes. The research objectives are as follows:

1. Development, design and realisation of a suitable experimental setup that can be used as a basis for future research on rotating cylinders up to critical Reynolds numbers.

2. Aerodynamic characterisation of the experimental setup by conducting a series of experiments, from which reference curves will be generated and a general understanding of the setups capabilities established.

To aid in the understanding of the rotating cylinders aerodynamic characteristics and force measurement results, flow visualisations through PIV, which are found to be relatively scarce at the given Reynolds numbers, will be utilised. Comparison with existing data found in literature will then be used to point out any discrepancies and explain known phenomena.

Additionally, an effort will be made to assess the effects of wind tunnel interference. These interference effects are found to be mostly ignored in the body of available rotating cylinder research and will be covered in more detail in section 3.2.

2.4.2. Research questions

This current research will attempt to realise and validate an experimental setup for rotating cylinders by answering the following main research question:

Main research question
"What are the aerodynamic characteristics of a two-dimensional rotating cylinder in uniform subsonic flow at subcritical Reynolds numbers and high blockage ratio?"

The experimental nature of the project allows to deal with the real complex flow phenomena present at the larger Reynolds number regimes as has been discussed throughout the review. The "quasi-two-dimensionality" is chosen, besides structural considerations, such that a larger model diameter could still be selected. The result is an increase in the obtainable Reynolds number range and spin ratios,

while maintaining a reasonable aspect ratio, that is comparable to the full scale applications. Importantly, in this way an attempt to understand the scaling effects of the governing parameters to the full scale can be made. Additionally, the rpm range will be chosen such that the tangential surface Mach number will remain within the ”incompressible” range.

The high blockage ratio is chosen in an attempt to provide insights on wind tunnel interference effects by comparison with existing literature and the employment of flow visualisation techniques. As such the viability of testing at higher Reynolds numbers in small scale wind tunnel facilities can be evaluated and discrepancies found in literature potentially explained.

From the above, to give an answer to the main question effectively and to validate the designed experimental setup, the following list of sub questions are formulated:

- ”What is the effect of the Reynolds number and spin ratio on the aerodynamic force characteristics?”
  - ”What is the effect of the Reynolds number and spin ratio on the aerodynamic force coefficients and their ratios?”
  - ”What is the effect of the Reynolds number and spin ratio on the directionality of the driving force?”
- ”What is the effect of the Reynolds number and spin ratio on the aerodynamic characteristics of the flow field?”
  - “What are the changes in flow features in close proximity to the rotating cylinder by changes in Reynolds number and spin ratio?”
  - “What are the changes in the near-wake structure around the cylinder by changes in Reynolds number and spin ratio?”
- ”What is the effect of high blockage ratio and close nozzle proximity on the aerodynamic performance and flow features of a rotating cylinder in case of open test section testing?”

2.4.3. Research Scope and Limitations

The research concerns a Masters thesis project with limited time and predetermined testing facility. Therefore, the following scope and limitations will hold.

As a completely new setup, including model and support structure design, was a main objective for conducting the project, a large portion of the available time has been spend on the realisation of a working model. As a result, the current project was limited in the amount of time spend doing measurements and new topics being addressed.

The predetermined testing facility dictates the Reynolds regimes at which the experiments can be conducted, and will be explained in section 3.1 in more detail. While full scale marine applications often operates at the higher supercritical Reynolds regimes, for this project only up to the critical Reynolds regimes can be achieved depending on the smoothness of the experimental campaign. Testing at supercritical regimes are therefore out of scope for the current project, but an effort on the scaling effects will be made.

In order to reach these critical Reynolds regimes the model diameter, as well as the tunnel velocity, will be increased up to a point where the aspect ratio remains close to the current full scale applications. The result is a relatively high blockage ratio, which in combination with the lack of wind tunnel corrections for rotating cylinder, results in the uncertainty of experimental results regarding wind tunnel interference effects. Due to time constraints, attempting to establish a suitable wind tunnel correction method is out of the scope, however assessing what the effects of high blockage testing has on the aerodynamic characteristics compared to available data from literature is one of the main topics being addressed.

Furthermore, at the higher Reynolds numbers the model needs to be spun at considerably high rotational speeds to reach the desirable spin ratios. Constraints on this will be the power necessary to run at such rotational speeds, the rated maximum rpm of model components, the possibly disturbing effects of compressibility and vibrational concerns. This means that in case of an severely unbalanced system, a limited value of the spin ratio at each of the Reynolds numbers can be achieved. The combination of very high Reynolds numbers and spin ratios is, as such, out of the scope of this project.

At last, research on a three-dimensional rotating cylinder will not be performed. Reason being that, given the same testing facility, a reduction of cylinder span results in lowering of the aspect ratio, whereas in case of constant aspect ratio the achievable Reynolds number regime decreases. Additionally, structural and safety concerns while running at high rotational speeds become more concerning with a cylinder being fixed at a single end. However, if such an arrangement is desired in the future, the model will be made easily modifiable to cover those needs.

3

Experimental setup and data acquisition

An experimental setup has been designed to fulfil the needs outlined in section 2.4. Before presenting the experimental setup, this chapter first covers the challenges associated with rotating cylinder experiments and in particular the difficulties associated with wind tunnel interference effects. Then a short note will be given on experimental setups from literature to outline how research on rotating cylinder has been performed more recently. Based on the challenges and findings from literature, the development of the experimental setup for the current project will follow.

Development of the experimental setup involved the design and manufacturing of a cylinder model and support structure, the implementation of systems to control and measure its rotation, and means to balance the model to reduce excessive vibrations. An overview of these aspects of the experimental setup, along with a description on the chosen experimental techniques, data acquisition methodologies, facilities, and setup of the used equipment, is provided in the remainder of this chapter.

3.1. Challenges with rotating cylinder flow testing

This section will shortly list some general considerations that need to be taken into account when dealing with rotating cylinders being tested in wind tunnel facilities. The majority of the statements made will be applicable for general wind tunnel testing, however additional difficulties specific to rotating cylinders with a focus on wind assisted ship propulsion are also included. This section does not include details and considerations that come as a result of the current experimental setup, as these will be unique for each setup specifically and will follow in the later sections.

The wind assisted ship propulsion application of rotating cylinders considers a very large full scale. Consequently, the Reynolds number reaches several millions and is often unattainable in wind tunnel testing due to small test sections, model sizes and limited wind tunnel velocities. Considerable differences in the flow features surrounding the cylinder and force coefficient behaviour between the real life application and cylinder model can be the result. The details of these effects between the different Reynolds regimes have been discussed extensively earlier in the report, e.g. for stationary cylinder in section 2.1 and for rotating cylinder throughout section 2.2.

In an attempt to reach flow similarity, changes in the parameters influencing the Reynolds number are often performed. This in turn will introduce additional effects. Increasing the model size diameter to achieve higher Reynolds numbers in relation to the closed cross-sections in which testing is performed, can introduce significant blockage effects for which corrections are necessary, where in open-jet test sections variations in inflow angle poses additional difficulties. In section 3.2 it will be discussed that at present times in case of a rotating cylinder such corrections are not trivial or even well established and hence a large scatter in the available experimental data can be the result. This requires more care when comparing and evaluating between the different data sets.

Besides the necessity to correct for wind tunnel wall effects, the further increase of the model size diameter, while keeping the span the same, will result in a reduction of the aspect ratio. It has been shown in subsection 2.2.4 that the aspect ratio is an important influencing parameter and should not become to small to avoid it becoming governing on the flow phenomena present.

If the tunnel would be able to reach large enough velocities to match the desired Reynolds number, a point will be reached that compressibility effects will almost always play a significant role as well. As discussed in subsection 2.2.11, for rotating cylinders this point will be reached at lower values compared to stationary cylinders and hence this will pose an even larger limiting factor.

Another option will be the use of pressurised wind tunnels, however these are far less common and more expensive to operate compared to standard atmospheric tunnels. Therefore, a balance between the effects of Reynolds number, blockage, aspect ratio and compressibility, by carefully selecting the model size, wind tunnel cross-sectional area, facility and wind tunnel velocities is necessary to arrive at meaningful results that can be translated to the full scale.

In the case of the rotating cylinder, the spin ratio will be another governing parameter to be carefully selected. When considering small model sizes in combination with a relatively large wind tunnel velocity, the maximum obtainable spin ratio will also become limited as the rotational speed needs to be increased significantly to reach a high enough tangential surface velocity. The experimental setup should therefore be designed and its components selected, e.g. bearings, motor, couplings, in such a way that it can cope with these high rotational speeds as well as the centrifugal forces.

The large force producing capabilities of a rotating cylinder placed in a flow, occurring even at small model scale sizes, poses more difficulties. The force balances or sensors should be able to handle these large forces and accurately measure it across a wide range of magnitudes. The combination of large forces and high rotational speeds means enough safety measures should be taken into account and the structure should be strong and stiff enough to endure these loads and limit vibrations.

The vibrations can furthermore be induced from various sources. As with any rotating body, mechanically this means both static and dynamic unbalances and misalignment of components can result in severe vibrations and should be minimised as much as possible. While unsteady aerodynamic phenomena, e.g. periodic vortex shedding, will induce large force fluctuations. In subsection 2.1.3 it was mentioned that longitudinal and lateral oscillations can greatly impact the resulting flow phenomena if sufficiently present and in subsection 2.2.6 it was shown that the mechanical and aerodynamic sources can reinforce each other causing the so called lock-on phenomena. Hence the importance of a stiff structure is emphasized further.

When considering three-dimensional models representing closely the full scale device, e.g. Flettner rotor, even more care should be given into the structural design of the setup as it will no longer be clamped on two sides, especially when running at high rotational speeds is desired.

3.2. Wind tunnel interference and corrections

In any experimental study, knowing what the impact of the wind tunnel walls on the aerodynamic coefficients is, is essential to arrive at accurate and valid results that can be compared to other similar experiments. Corrections for these walls are typically done by using the more common analytical corrections or far less common modern methods like wall static pressure measurements and on-line processing in adaptive wind tunnel working sections. Sadly, for rotating cylinders this has been lacking over the years as there are no such studies and or analytical methods known to exists. In existing literature it is either not mentioned at all or is mentioned but no specifics are given on the methods applied. The result is an increase in the uncertainty of the existing data from literature, where discrepancies between the data sets might be the cause of such wind tunnel wall effects.

Wind tunnel wall effects in closed test sections leads to changes in the freestream velocity due to the constriction of streamlines. Effects are both in longitudinal and normal direction, which can be considered independent when the model is placed in the center of the test section (Badalamenti, 2010). The longitudinal component of the freestream is increased by the blockage interference which consists out of solid blockage, due to the volume of the model, and wake blockage, that is caused by the decreased flow speed in the wake. The wake blockage further impacts the measured drag on the model due to an induced longitudinal static pressure gradient along its surface. The normal component manifest as a change in the local flow direction, which is caused by the circulation around the model and is commonly known as the lift interference.

In general, interference effects in open test sections are smaller compared to closed test section testing, and different correction methods are required to minimise the effects. Firstly, for any open jet wind tunnel an empty tunnel static pressure gradient exist, resulting in an horizontal buoyancy effect which will act upon the model and reduces the drag. A second pressure gradient exist with models placed closely to the nozzle exit plane, where the exit flow velocity profile is modified if the stagnation region of the model is extended into the tunnel nozzle. Furthermore, the exhaust jet of the wind tunnel is no longer constraint and is free to expand and deflect asymmetrically. This causes a reduction of the flow velocity near the model due to over-expansion of the jet, and modifies the forces acting on the body due to deflection. Additional effects arise from the use of a collector at the far end of the test section, where ingestion of the wake of the model also has an influence. The use of wind tunnel corrections for a rotating cylinder in an open jet facility have not been discussed in literature and hence will not be further covered here, however for more general information on open jet wind tunnel interference effects the works from Mercker and Wiedemann (1996), Wickern and Schwartekopp (2004), Wickern (2014), Fischer (2018) and Collin (2019) may be consulted.

The extent of the interference effects depends on a mix of parameters, where the blockage interference is mainly impacted by the blockage ratio, $Area_D/Area_W$, distance to the nozzle exit or collector inlet plane, the freestream Mach number, M_∞, and the type of wind tunnel. The lift interference is mainly impacted by, the lift generation, the tunnel cross-sectional shape, e.g. square or octagonal, and if it is either closed or an open wind tunnel test section (Badalamenti, 2010). This already results in different methods to be applied based on the situation that is applicable, while different methods further exist depending on the model being either streamlined or bluff.

Considering the far more investigated non-lifting static bluff body models, e.g. a non-rotating cylinder, methods do exist and are being employed. However, even for these type of models no clear suitable method for every situation exists nor is it fully understood. This has been mainly a consequence of constraints placed on the separation point locations in existing methods, while in reality uncertainty on the movement of these points do exist. To not go to deep in all the correction methods that do exist, the founding works on bluff body corrections methods in closed section testing are from Maskell (1963), which have been later modified by Hackett (1996), while for open test sections correction methods have been proposed by Mercker and Wiedemann (1996), and can be consulted if further information on the development of bluff body corrections is sought after. For more general information regarding low speed wind tunnel testing correction methods, the book from Pope and Harper (1966) may be consulted.

Shifting the focus now onto rotating cylinders, with keeping the flow regimes from subsection 2.2.5 in mind, it becomes clear why the establishment of such correction methods become more difficult. For low spin ratios the wake of a rotating cylinder resembles the one from a stationary cylinder or bluff body, implying it might be possible to use the same bluff body correction methods. However, in certain Reynolds regimes this bluff body wake, like on other non-rotating bluff body scenarios, further consist out of vortices shed periodically, hence adding an unsteady component. Therefore, it is possibly necessary to use unsteady correction methods instead. But in reality this has been done rarely, also for stationary cylinders where such phenomena exist. The underlying assumption being that the vortices are closely spaced and quickly merge with the wake, steady methods might still be applicable (Badalamenti, 2010).

At high spin ratios the wake becomes steady and reduces more in size with further increase of the spin ratio. At this point the application of streamlined correction methods could possibly be the right method as a result of the lesser influence of the wake on the pressure distribution around the body. However, at this point the circumvolving layer around the body is also formed which effectively changes the cross-sectional area of the rotating cylinder, making it asymmetric and no longer being placed exactly at the centreline of the tunnel. Effects of this are however expected to be small (Badalamenti, 2010). Although the effects have never been quantified.

To complicate things further when placed in a non-uniform freestream flow, e.g. a boundary layer, both steady and unsteady portions of the wake across the span of the cylinder can exists. This is due to the spanwise variation of the spin ratio as has been in shown in the works from Massaro et al. (2024). Effects of corrections for such an arrangement have also not been mentioned in present day literature.

The lift interference is another discussion point for rotating cylinders. The cylinders aerodynamic characteristics as a consequence of its fully symmetric shape depends only, when keeping the other influencing parameters the same, on the spin ratio regardless of what the incidence angle of the flow is. Hence, corrections on the force measurements as a result of lift interference might therefore only require a correction for the rotation of the incoming flow direction (Badalamenti, 2010). However it must also be mentioned that a large deflection of the wake occurs for a rotating cylinder, especially at larger spin ratios. The wake deflection in relation to the proximity of the wind tunnel walls and the interaction between the two is not mentioned in literature and hence its effects are still unknown.

Furthermore, as the flow regimes are further depended on the Reynolds number and as a consequence the behaviour of the boundary layer in the subcritical, critical and supercritical regimes, choosing a suitable correction method is expected to not only vary with the spin ratio but also the Reynolds number. Adding to this the uncertainty on the movement of the separation points with changes in blockage ratio further complicates the matter (Badalamenti, 2010).

Both Thom (1926b) and Peller (1986) were some of the earlier investigators commenting on correction methods applied to their results. However, Thom corrected only for the constriction of the streamlines that closely resembles to later established solid blockage correction methods, while Peller solely used correction methods based on solid blockage without differentiating between stationary and rotating cylinders. In both works the effects of lift interference and wake blockage were not mentioned.

Badalamenti (2010) attempted to assess the effects of existing correction methods by employing one conventional streamlined body correction method against the bluff body correction method from Hackett on the results of a rotating cylinder placed in two separate wind tunnels. The streamline body method was based on Lock (1929) method to correct for the solid blockage, while the correction for the three-dimensional wake blockage was based on a double infinite source-sink image system as outlined in Pope and Harper (1966).

The bluff body correction methods from Hackett concerned both a blockage-induced incremental velocity and drag increment correction from which the blockage correction factor was established. With the use of these methods, the freestream velocity, dynamic pressure, aerodynamic force and moments coefficients, and the spin ratio were corrected.

In Figure 3.1 the results of the two methods applied to the data from each wind tunnel are shown. It was mentioned that the results corresponding to the T2 tunnel had a lower blockage compared to the T3 results. Both the correction methods failed to produce satisfactory results. The conventional method was said to bring the results further away compared to the uncorrected data, while Hackett's method reduced the lift coefficient far below the uncorrected data and showed less similarity to the published data found in literature. This became worse when only the separated drag component was corrected. Hackett's method was said to produce better agreement between the two tunnels in the drag coefficient at high spin ratios, but only when endplate sizes were sufficiently large, $D_e/D > 1.5$. At the end it was concluded to not use any correction methods, due to the good agreement of the uncorrected results for spin ratios below 2 and the uncertainty surrounding the application of correction methods.

However, the good agreement of the uncorrected results might have been due to the low area blockage ratios used for both of the tests, e.g. for T2 equal to 0.08 and for T3 equal to 0.09, and hence wind tunnel interference might have been relatively small from the start. Combining this with a different support structure used for both of the tunnels, discrepancies in the uncorrected data could have potentially come as a result. For a more elaborate explanation of wind tunnel correction methods applied and other related works concerning such methods for rotating cylinders similarly to this section, the work from Badalamenti (2010) is still highly advised.

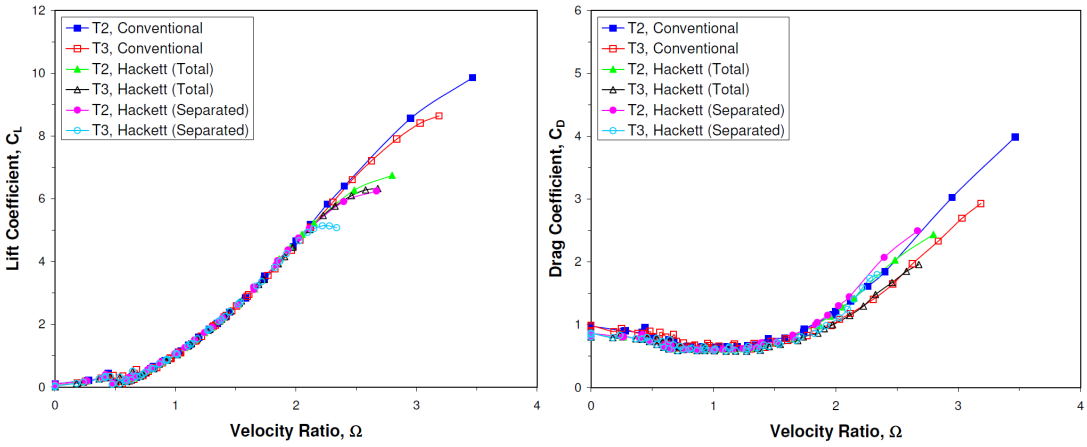

(a) Lift coefficient (b) Drag coefficient

Figure 3.1: Comparison of corrected lift and drag coefficient data between T2 and T3 wind tunnels, using conventional and bluff body correction methods (Badalamenti, 2010).

Although an attempt has been made to assess the more widely used correction methods, none of the proposed hybrid approaches, e.g. varying between methods depending on the flow regime present, have been tried. Therefore, it becomes clear wind tunnel corrections for rotating cylinders is a relatively unexplored area, especially when considering the larger Reynolds number regimes and for open jet facilities.

3.3. Examples of past experimental setups

Although experiments can in reality be performed in full scale directly, it is far more common to perform them in dedicated testing facilities, e.g. wind tunnels. In doing so, it allows for greater control on the testing conditions, which results in better repeatability and comparability of its results. For increased time and cost efficiency, experiments are often performed at smaller model scales. Many types of wind tunnels exists and without going into to much details regarding wind tunnel design it is important to know that the chosen wind tunnel has an effect on the measured results and in general corrections to the results should be made as has been discussed in the previous section 3.2.

Considering the experiment, a distinction can be made between two-dimensional and three-dimensional setups. For which it must be noted that in real life two-dimensional experiments three-dimensional flow phenomena are always present, as has been explained in subsection 2.2.12. In any case, a situation as close to two-dimensional conditions is then the goal. If quasi-two-dimensional conditions are required, it is realised by suppressing the formation of the tip vortices where the model will either extend to the wind tunnel walls with a very small gap, as has been done by Bordogna et al. (2019b), or protruding the tunnel walls completely, similarly to the experiments from Reid (1924) and Swanson (1961). Examples of these type of experimental setups are depicted in Figure 3.2.

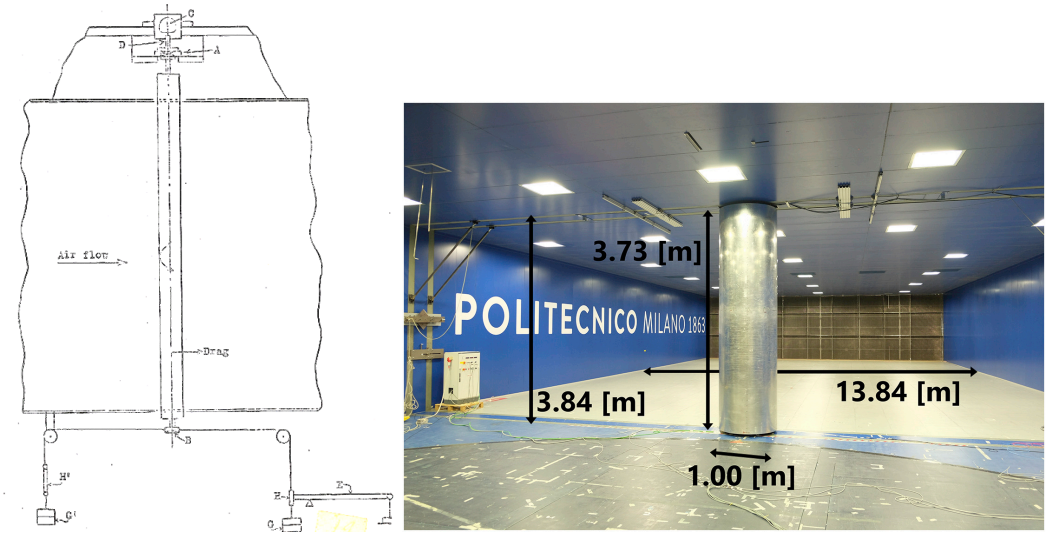

(a) *Protruding rotating cylinder* (b) *Truncated rotating cylinder with small gap*

Figure 3.2: Examples of quasi-two-dimensional rotating cylinder setups with a) protruding wind tunnel walls (Reid, 1924) and b) up to wind tunnel walls with small gap (Bordogna et al., 2019a).

However, with the successful suppression of the tip vortices using the above solutions, it has been shown in the work from Massaro et al. (2024) that formation of vortices close to boundaries due to the presence of a developed boundary layer, e.g. atmospheric or tunnel boundary layer, can still exist. Besides, Swanson (1961) further noted that for his experiments, which are believed to be the closest to the two-dimensional results by making use of two dummy cylinders rotating alongside that both act as the endplates of cylinder, an infinite aspect ratio that results in purely two-dimensional results, can not be considered. Therefore, reaching two-dimensional flow conditions in real-life is practically impossible to achieve.

Three-dimensional experiments can be performed with either one free end, e.g. like Chen et al. (2023), or suspended entirely to a support structure with two free ends, as has been done for example by Badalamenti (2010) and Ma et al. (2022). The one free end setup appears to be particularly suitable for wind assisted ship propulsion as it closely resembles the real life setup, however due to structural and vibrational constraints, such a setup becomes more challenging when running at high rotational speeds and perhaps even limited. Examples of such experimental setups are depicted in Figure 3.3.

(a) *Single free end* (b) *Double free end*

Figure 3.3: Examples of three-dimensional rotating cylinder setups with a) single free end placed on a platform (Chen et al., 2023) and b) double free end suspended by support structure (Badalamenti, 2010).

Modern day rotating cylinder experimental setups can be divided into the following primary components; a rotating assembly, a bearing assembly, a support structure and a drivetrain. For smaller diameter rotating cylinders, the rotating assembly is often a singular shaft driven directly by the motor, e.g like Reid (1924). For larger diameter cylinders it composes typically of a hollow shaft construction where an outer skin is connected to a drive shaft, which can either span the cylinder entirely, as has been done by Bordogna et al. (2019b) or a version where it is splitted in two and connected at either end, e.g. like Badalamenti (2010).

Alignment is often better with the singular shafts, however for modularity and usability, a dual shaft approach can be used in combination with a self-aligning ball bearing setup. The bearing setup can be realised in multiple ways, however limited details on this particular part, although important, are given in literature. In general the ends are placed in bearings of ball or self-aligning type and it is advised to use proper clearances and tolerances based on manufacturer specifications. Ideally, in case force measurements are required, the measuring device should be placed as close as possible to the bearing assembly to limit the effects of the bending moment on the load cells.

The support structure can be realised in multiple ways, depending on the type of experiment, e.g. two-dimensional or three-dimensional, and the testing facility used. To cope with the large forces and vibrations, the support structure should be most importantly strong and stiff enough, while secondary requirements will be on accessibility and ease of use.

In literature the rotation is realised by the use of various types of motors, with the most common being AC or BLDC electrical motors. The specific type of motors are often not mentioned, however for high power and high rpm applications, BLDC RC plane motors are an example of suitable candidates. A common implementation of these motors is done by directly driving the rotating assembly, placing the drive shaft in-line with the axis of rotation, where it is coupled with a flexible shaft or integral clamp style coupling. Such a particular setup has been used by Badalamenti (2010). Another option might be done by placing the drive shaft off-axis with a gearbox assembly, e.g. with pulleys or gears, see for example the work from Yazdi et al. (2019). By utilising either of these options, the rpm is then determined and or controlled with an electrical control unit, encoder or tachometer.

Besides these main components and depending on the objectives of the experiment, more components are often added, which in turn should be taken into consideration during the design phase. Examples of such components are force and moment measuring arrangements, static and or total pressure measurements and flow visualisation techniques.

For the force and moment measurements the most common devices are force balances, that are either smaller external balances, as being used by Chen et al. (2023), or large balances as part of a wind tunnel facility, like the one used by Badalamenti (2010). These balances can have single or multi-axes measuring capabilities where in case of the former multiple devices can be placed to get the desired directions. Custom built force balances by the use of strain gauges give a larger degree of freedom on the implementation of such an arrangement, although they are more difficult to realise. Such a device has been recently done by Bordogna et al. (2019b) on their large scale Flettner rotor experiments. Other techniques to arrive at the forces on the model can be realised by integration of the pressure distribution around the model, while drag measurements can also be obtained through the measurements of the momentum loss in the downstream flow.

Surface pressure measurements as explained in subsection 2.2.9 is not trivial on rotating objects. Thom (1926c) and Miller (1976) presented special devices of their own design capable of measuring such pressures. Nowadays use of pressure taps and pressure scanners is more common. Bordogna et al. (2019b) implemented such an arrangement, where the taps and scanner were mounted on the rotating part, which in combination with a transducer placed on a slip ring that measures the instantaneous velocity and angular position in-phase with the pressure measurements, allowed for determining the pressure distribution around the cylinder. Wake pressure measurements are often performed by placement of a pressure rake consisting of multiple total pressure or multi-directional pressure probes. Examples of experiments using such pressure rakes are from Badalamenti (2010) and Ma et al. (2022).

At last, the deployment of flow visualisation techniques can be done in many different ways depending on the setup and requirements of the research. Some common examples of such techniques are smoke or dye lines, hydrogen bubble and smoke wires, hot-wire anemometry, laser-doppler velocimetry, infrared thermography, schlieren and shadowgraphy for supersonic flow, particle image velocimetry and particle tracking velocimetry. Without going into detail, out of these particle image velocimetry in modern day experiments is most commonly used. Predominantly due to its quantitative analysis capabilities for both two-dimensional slices of the flow field and three-dimensional volumes and will be further covered in section 3.12. Example studies on rotating cylinders using PIV are done by Radi et al. (2013) and Sun et al. (2016).

3.4. Wind tunnel facility

The experimental campaign outlined in this report was performed in the slow low turbulence tunnel, SLT, at the Low Speed Laboratory of the Delft University of Technology. The SLT tunnel was initially designed solely as a boundary layer tunnel, however recently it has been moved and converted to allow for more flexibility in the type of research it can facilitates. As a result, the SLT at the time of the measurements was still under construction with its configuration being of open return and open jet type. A schematic of its used configuration is given in Figure 3.4.

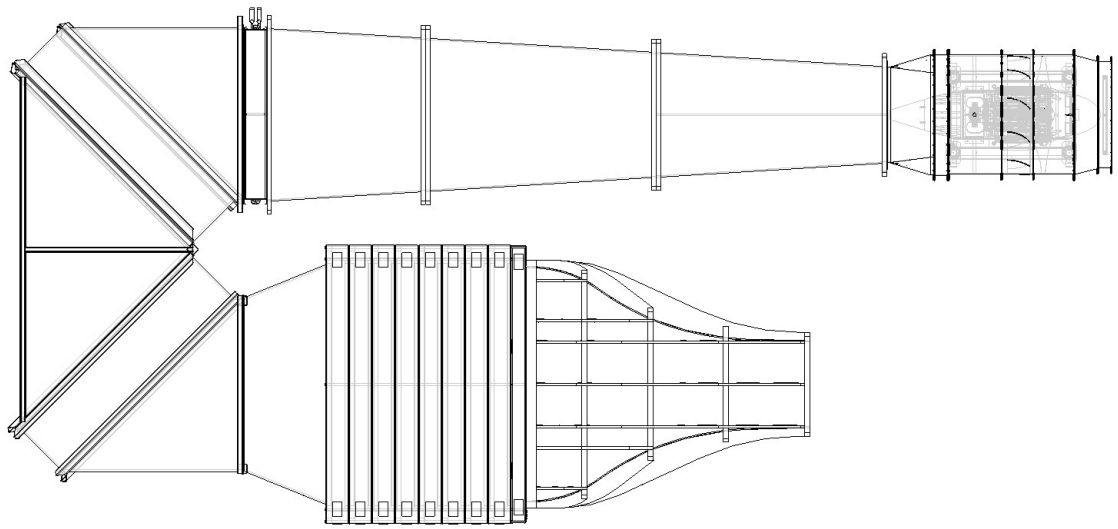

Figure 3.4: Schematic of the SLT wind tunnel in open return and open jet configuration.

The nozzle exit has a rectangular 0.9 m x 0.6 m cross-section, where freestream flow velocities up to approximately 35 m/s can be reached. Consequently, the scale of the experiment is determined from these limits. The tunnel velocity is controlled directly by setting the fan's rotational speed. Delta pressure measurements across the tunnel contraction for determining the exit flow velocities were unavailable, due to ongoing work on the facility, instead exit flow velocity measurements were done through an externally mounted pitot-static probe at the straight part of the nozzle exit outside of the developed tunnel boundary layer, Figure 3.5.

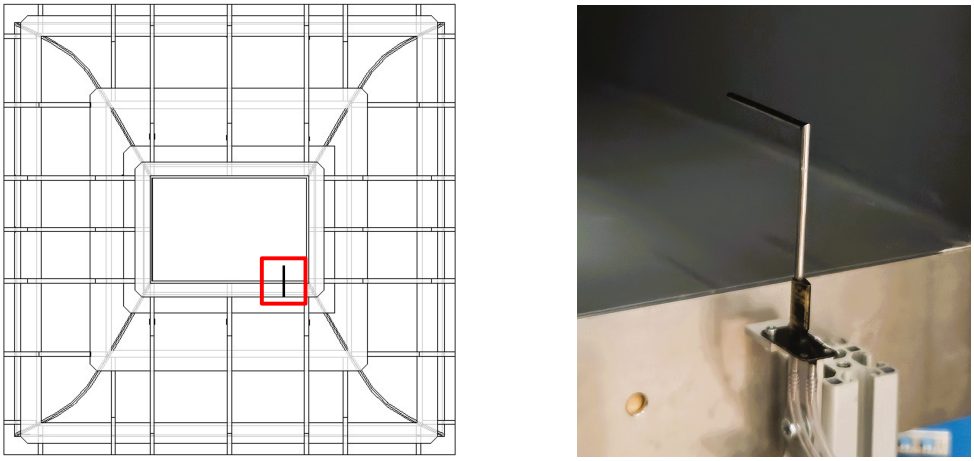

(a) Schematic of pitot-static probe location

(b) Installed pitot-state probe

Figure 3.5: Exit flow velocity measurement through externally mounted pitot-static probe.

Temperature and density of the freestream are taken at the inlet of the contraction, whereas the atmospheric pressure measurements are performed in the plenum. In the enclosed facility, uniformity of these variables is not assured with the absence of any cooling systems. As a result, during prolonged operation the flow tends to heat up, especially at higher tunnel velocities. Additionally, the distance between working section and the measurement location of the freestream parameters, may lead to discrepancies in the flow conditions at the cylinder model from the more upstream recorded values.

Figure 3.6a,b shows the variations in streamwise turbulence intensity, T_i ($U'_{rms}/\bar{U}$), at different pass frequencies, f_p, and its spectral density, ϕ_{uu}, for the full spectrum with varying freestream velocities of the SLT facility based on hot wire anemometry scans at the nozzle exit plane [1]. Freestream turbulence intensity levels, bandpass filtered between 30 Hz to 20000 Hz, are found to be relatively low at the nozzle exit, with T_i values ranging from 0.08% to 0.06% at freestream velocities of 5 m/s to 20 m/s respectively. The strong dependency of the turbulence intensity to the low frequencies is most likely the result of breathing effects of the tunnel.

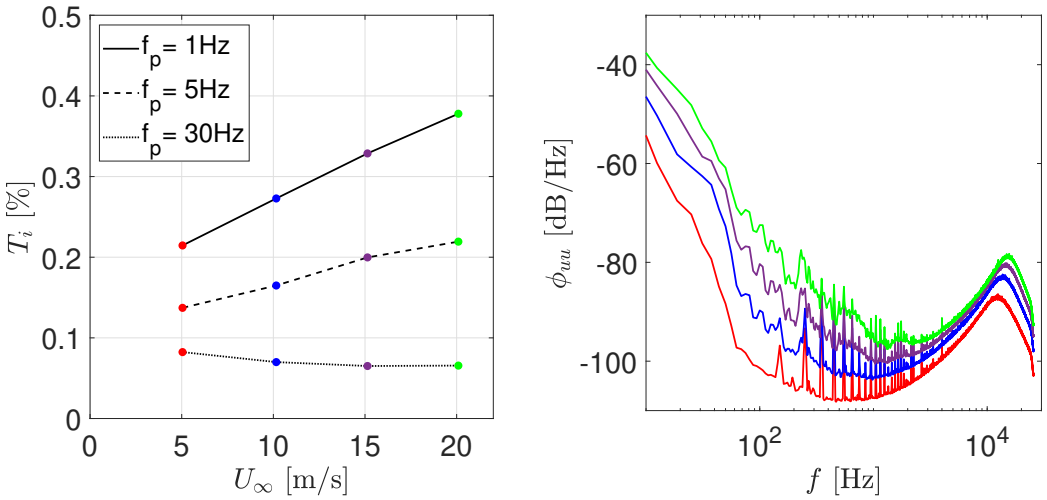

(a) Streamwise turbulence intensity.

(b) Streamwise spectral densities.

Figure 3.6: Streamwise turbulence intensity and spectral densities of the freestream at the nozzle exit. Colours in (a) correspond to the same coloured freestream velocity in (b).

[1] Unpublished data of newly configured tunnel provided by Max knoop

3.5. Model sizing and constraints

The sizing of the cylinder model and systems were greatly influenced by the predetermined wind tunnel facility and industry level WASP applications. This meant model dimensions were sized such that a range close to full scale Reynolds numbers could be achieved along with an aspect ratio similar to the Flettner rotors presently found on ships, and for the sake of comparison, to previous experimental studies. Whilst Reynolds numbers of several millions could not be achieved with the current facility, it was chosen to at least reach up to critical Reynolds numbers, $Re_D > 300000$, such that the transitional state of the boundary layer is reached, and wake characteristics are more representative of large scale applications.

Motor power and rpm characteristics, which importantly determines the achievable spin ratio range, were estimated based on previous experimental results and calculated by Equation 2.5, see subsection 2.2.10. The lowest maximum spin ratio deemed sufficient for set Reynolds numbers, was chosen to be equal to 2, as it was previously found to yield the highest lift-to-drag ratios close to this value, which is important considering its WASP application, see subsection 2.3.1. However, a spin ratio of 3 was preferred as often in operational conditions spin ratios extend to such values. Additionally, based on the findings in subsection 2.2.11, the maximum rpm was bounded by keeping the cylinder surface tangential Mach number, $M_{tan} < 0.3$, low enough such that the effects of compressibility are expected to remain small.

The large critical Reynolds numbers and spin ratios meant the cylinder model was expected to produce significant forces and moments that would be imposed on the force balance system. Estimation of the forces based on large scale Flettner rotor experiments, see subsection 2.2.3, were used in selecting a suitable force balance system.

As there is little available information on the blockage effects of rotating cylinders, see section 3.2, the model blockage is deliberately allowed to become much larger as what is typically considered to be acceptable for bluff body testing. By comparison with existing experimental data at lower blockage ratios within the same Reynolds number and spin ratio range, valuable insights on this topic can then be obtained. Keeping these constraints in mind, a parametric study followed between these conflicting requirements and as a result a suitable experimental setup has been designed and manufactured.

3.6. Cylinder model

The cylinder model consists out of a single piece extruded aluminium hollow tube, a steel drive shaft, four aluminium ribs and modified shaft clamp couplings to connect drive shaft and rib components, see Figure 3.7a. The outer tube has dimensions of length B = 890 mm with a 5 mm clearance to the wind tunnel walls on each side, an external diameter D = 200 mm, and wall thickness of t_w = 5 mm. As a result the obtainable Reynolds number range equals to 62500 < Re_D < 437500 for 5 m/s < U_∞ < 35 m/s, respectively. The aspect ratio, $A\ (B/D)$, is equal to 4.5 and the blockage ratio, $Area_s/Area_w$, a large 33%. In case different model dimensions are desired, the outer tube with internal ribs can be swapped out for a different model.

The manufacturing process of the external outer tube can lead to variations in wall thickness along the circumference, which are commonly found to be in the order of a few percent of the specified wall thickness. To reduce unwanted excitation of the boundary layer, close to perfect roundness of the external diameter must be ensured. Therefore, machining of the surface is advised and often needed.

Unfortunately, as a consequence of several delays during the manufacturing process of the cylinder model and support structure, planned final refinements to the cylinder surface were postponed for later iterations of the experimental setup. Therefore, the results presented in this report are obtained with the non-machined outer surface of the cylinder model, for which it was found that the variation in wall thickness was approximately 1 mm at the mid-span section.

The cylinder surface has been lightly sanded to remove any imperfections, screw holes were taped off, and before each measurement set the model was cleaned to remove oxidation and dirt buildup.

Additionally, at the mid-span section, matte black vinyl sheets ensured a smooth and low reflective surface needed to perform the employed flow measurement techniques, see section 3.12.

The cylinder ribs had been laser cut, where small imperfections meant the cylinder skin was able to move with tightening of the bolts and resulted in assembly difficulties as well as small alignment variations. Although proper tightening proved to be tedious, with proper care the variations were reduced to a minimum.

The 32 mm diameter steel drive shaft with tight tolerance specifications spanned the entire cylinder such that misalignment concerns were kept to a minimum. The drive shaft ends were machined to fit into bearings with a bore of 25 mm, where on one side its fixed with an additional set screw type shaft clamp, and on other other side remains free to move axially to allow for thermal expansion in case of prolonged operation. For more details on bearing housing setup see section 3.8. Bordering the locations of the internal ribs, slits were machined into the steel drive shaft to allow for the installation of shaft clamps. These clamps were in turn bolted to the internal ribs, and as a result prevents the outer tube from any axial movement and rotational slippage, Figure 3.7b.

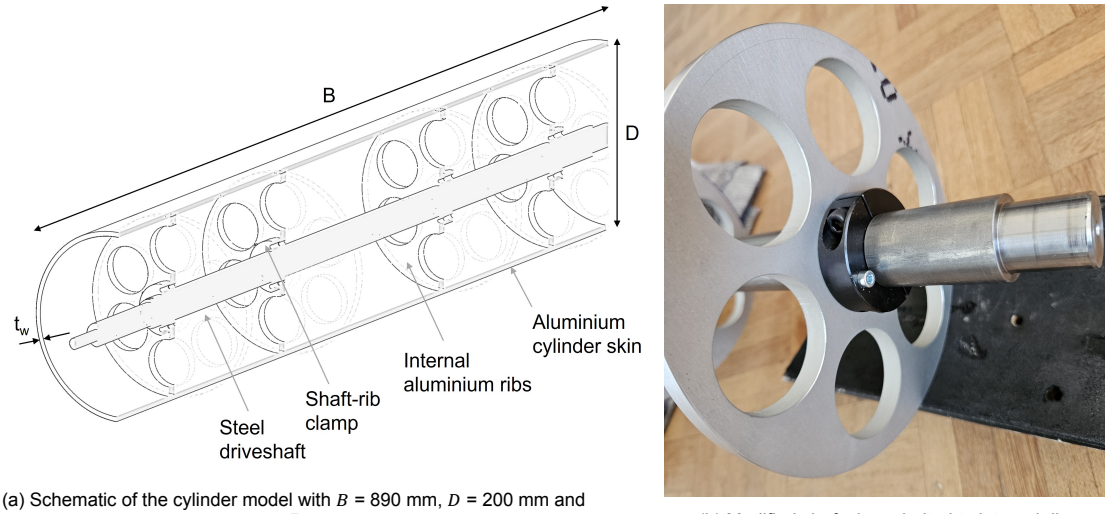

(a) Schematic of the cylinder model with B = 890 mm, D = 200 mm and t_w = 5 mm.

(b) Modified shaft clamp bolted to internal rib.

Figure 3.7: Cylinder model schematic and internal structure.

3.7. Cylinder rotation and control

Following the parametric study, an maximum rpm of 9835 is desired such that a spin ratio of 3 is reached at the highest Reynolds number, $Re_D = 437500$, whilst the compressibility constraint is still satisfied. The power necessary to allow for such operations with the presented cylinder model was estimated by using the analytical formula, Equation 2.5.

An industrial LMT Torquestar3 variable speed BLDC electric motor had been selected due its ability of delivering the desired power and rpm output as well as its availability. The motor shaft was directly mounted to the drive shaft through a NBK® MST-32 set screw type flexible shaft coupling rated for high rpm's, which allows for a small misalignment between motor shaft and drive shaft. Power to the motor was provided by a three-phase power socket, allowing for delivery of the large power requirements while running at high rpm.

For the determination of the cylinders rpm, an US Digital® E6 optical hollow shaft encoder was utilised. This particular model has been selected due to its compatibility with the facilities equipment, its small size, and rpm capabilities. A cycles per revolution, CPR, rating of 512 was chosen such that both the maximum rpm and pulse frequency constraints are satisfied when running at the maximum rpm of 10000. In Figure 3.8 motor and encoder setup is shown.

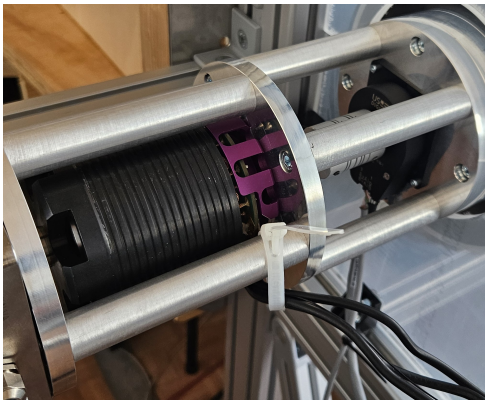

Figure 3.8: Motor and encoder setup within the fully assembled experimental setup.

Speed control has been performed through an in-house custom made hardware and software setup, originally designed for propeller research, that uses the rpm value of the encoder directly. By varying the applied motor voltage, the rotational speed of the cylinder is controlled. As a result a minimum angular frequency, ω_f, of approximately 2.7 Hz, corresponding to a value of roughly 160 rpm, could be achieved with its maximum well above the desired 10000 rpm. In the full range of rotational frequencies, stability could be achieved in the order of $<10^{-1}$ Hz with better results at higher rpm, however some time is needed before the rotational frequency is fully stabilised and thus ready for performing any measurements.

For safety considerations, the model was only spun at the lowest rotational frequencies, accompanied by blast shields, when people were present in the room. Therefore, all speed control has been performed from a different room with a live camera feed for inspection of the setup during operation. To reduce stress on the components and motor from the initial startup torque, a small rotation before turning on the motor was induced before each operation.

3.8. Bearing setup

The steel drive shaft is supported by three SKF® 6205-2RSL sealed ball bearings, which are capable of taking loads in both radial and axial direction. The sizing of the bearings was done by taking the maximum bore size such that a thicker drive shaft could be used, whilst also being capable of operating in the desired rpm range. Three bearings are chosen to prevent the drive shaft of bending under load and to ensure proper alignment throughout. The fixed end ensures that axial movement of the cylinder model is halted, which is realised by enclosing the bearings with a set screw shaft clamp on one end and drive shaft abutment on the other. The free end is to allow for thermal expansion of the drive shaft. A schematic overview of the bearing setup and drive shaft is depicted in Figure 3.9.

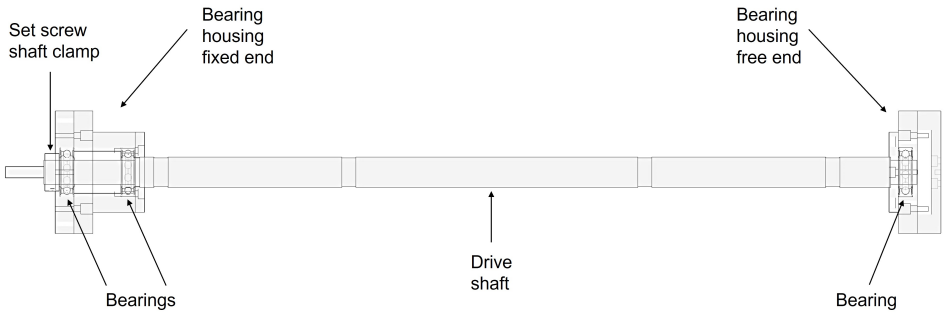

Figure 3.9: Schematic of bearing housing setup.

3.9. Force measurement system

The force measurement system is a vital component in the characterisation of the experimental setup. The data obtained through the force measurements will be used to establish reference curves for the experimental setup, allowing for a data set to compare to with future work on this particular setup. Furthermore as there is an extensive set of force measurement data available in literature, the data can be validated by comparison, and discrepancies, e.g. potential sensitivity to the higher blockage ratio, can be further investigated.

Both force and bending moment limit constraints were considered in the selection of the force measurement system. To ease the requirements on the the system a reduction of model assembly weight and length was aimed for during its design. However, as it was opted for an direct drive approach with all components placed concentric with the axis of rotation, it meant the moment arm on one side was significantly increased. Consequently, out of two, the bending moment constraint was most limiting.

The experimental results of Swanson (1961) and Bordogna et al. (2019a) were used to give an initial estimate of the expected loads on the cylinder, since the setups being similarly quasi-two-dimensional and operated at close to the same spin ratios and Reynolds numbers. Based on the findings, two ME-Meßsysteme K3D120 2kN/VA 3-axis force sensors were installed on both ends of the model. The sensors are capable of measuring up to 2kN of force in all directions with an ISO 376 accuracy class rating of 0.5, whilst the bending moment limit is sufficiently high at 250 Nm. Additionally, due to its small size, the side-view remained unobstructed, which was an additional requirement set necessary for the employed flow measurement technique, see section 3.12. A schematic of the full model assembly, including force sensors is shown in Figure 3.10.

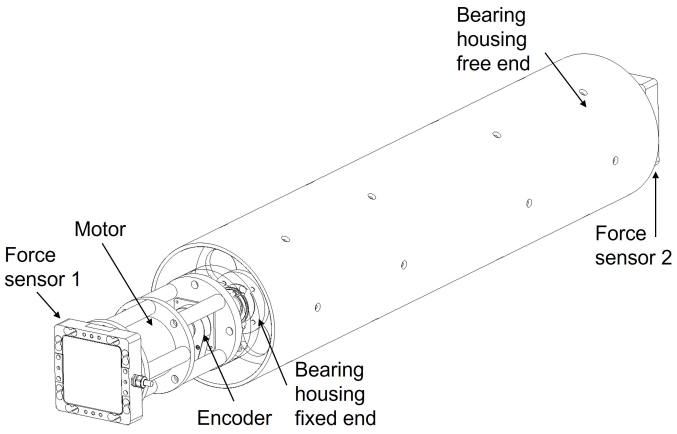

Figure 3.10: Schematic of full model assembly.

The data acquisition system composes out of a *National instruments cDAQ-9174* chassis with two *NI-9237* strain/bridge input modules for the force measurement readouts, a single *NI-9401* digital I/O interface for encoder data, and a *NI-9234* sound and vibration module providing the encoder signal necessary for the balancing software, see section 3.11. As a result, data acquisition is performed at a maximum sampling frequency, f_a, of 51.2 kHz.

3.10. Support structure

With the absence of an universal test section to mount the model assembly, a new support structure has been developed. The design of this support structure ensures a rigid base and could be directly attached to the wind tunnel contraction or other test sections, which helps in preventing any unwanted vibrations. The structure is composed out of multiple aluminium profile beams and can be easily secured by extending the lower legs or moved away on its attached wheels, Figure 3.11a.

The sides of the support structure additionally serve as the side walls of the wind tunnel, whilst top and bottom can be closed off in case closed test section testing is desired. The side walls are made of highly transparent acrylic glass, giving excellent optical access for the employment of flow measurement techniques, e.g. particle image velocimetry. For installment of the cylinder model, a removable and separable wind tunnel wall is located on one side of the structure, whilst the other side remains as a single piece for earlier mentioned optical access. A through hole in the walls with a smaller diameter than the outer diameter of the cylinder ensures for minimal spillage effects on the aerodynamic performance. The overall design installed in the SLT facility can be viewed in Figure 3.11b below, where the center spanwise beam was moved to a lower position during the experiment.

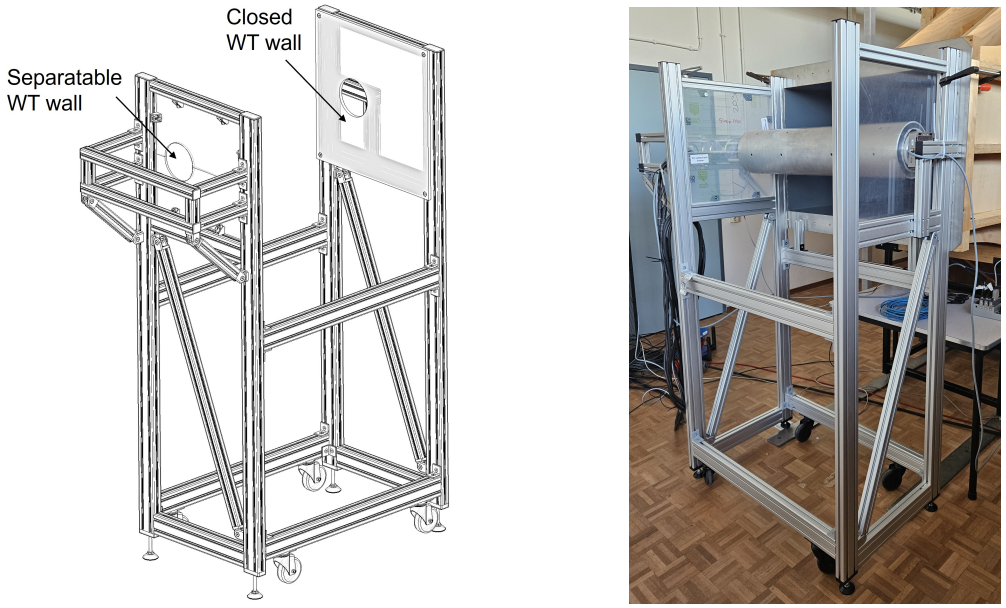

(a) Schematic of support structure.

(b) Installed model and supports in the SLT facility.

Figure 3.11: Model support structure and installment.

3.11. Cylinder balancing

Unbalance is the most common source of vibrations in any rotating model, which becomes especially noticeable for objects spinning at high rpm. As such for the cylinder model of the current experiment, if left uncorrected, detrimental effects on the measurements, alterations in the state of the flow and the risk of structural failures can be the result. For rigid rotors, different balancing techniques exist and for extra information on each of the methods the reader is referred to the document of MacCamhaoil (2016) on which this section is based.

The vibration due to an unbalance, is the result of interaction between an uneven weight distribution and the radial acceleration of the spinning object. By balancing the model, the unevenness in the weight distribution is counteracted by the placement of correction weights or removal of material at specific locations. With the use of accelerometers or force sensors, the unbalance can be sensed, once each revolution, at any fixed location on the bearings. Therefore, through frequency spectrum analysis of the filtered vibration signal, the magnitude of the unbalance can be identified as an peak close to the rotational frequency of the object. The phase of the unbalance can be determined by calculating the difference in phase between the filtered vibration signal and a reference signal provided by a tachometer or encoder. It must be noted that if no dominant peak is present close to the rotational frequency in the filtered vibration signal, the cause of vibrations might not be the result of an unbalance, but rather misalignment, bent components or some other fault, and as such balancing can not provide the desired outcome.

There are three types of unbalance, namely, static, couple and dynamic unbalance, Figure 3.12. Static unbalance is the eccentricity of the center of gravity, shifting the inertia axis away parallel to the axis of rotation such that it is no longer concentric. Couple unbalance is a shift in the inertia axis, while there is no eccentricity of the center of gravity. Dynamic unbalance is the combination of both static and couple unbalance. For rotating objects with its width much larger compared to its diameter, e.g. a cylinder, dynamic balancing is almost always necessary and hence needed for the current experiment.

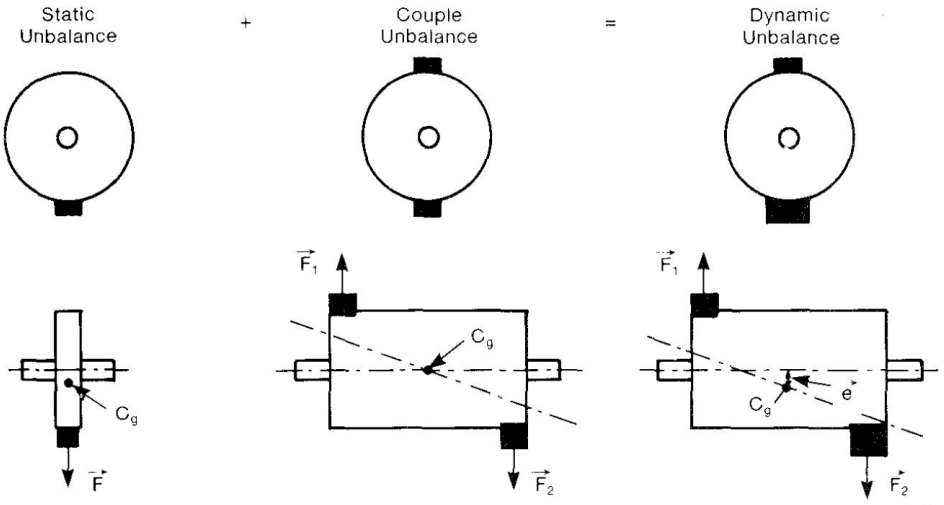

Figure 3.12: Overview of types of unbalances encountered on rigid rotors, with C_g being the center of gravity, e the eccentricity, and F_1 and F_2 the forces due to the weight imbalances indicated as black blocks (MacCamhaoil, 2016).

Dynamic balancing of rigid object is done through a two-plane balancing technique. Two accelerometers or force sensors are needed for this procedure. In the light of the current experiment, this can be done by the two 3-axis force sensors on either side of the model, as the forces on the bearing housing are directly measured here. The encoder data is then used for the determination of the phase angles, Figure 3.13a. This type of balancing is called field balancing, as the model will be balanced within its own support structure and bearing setup without the use of a balancing machine. Ideally, the balancing is performed directly on the maximum operating speed, however as the maximum operating speed is high and the weight of the cylinder model relatively large, at approximately 15 kg, it was chosen to do the balancing procedure multiple times at increasing rotational speeds for each attempt.

Before balancing, a trial weight, m_T, needs to be selected. The trial weight is needed to make temporary alterations to the weight distribution, such that the response of the vibrations based on the added unbalance can be determined. The selection of the trial weight follows from the calculation of the maximum allowable residual weight, m_{res}, Equation 3.1, where m_{su} $[gmm/kg]$ is the specific unbalance requirement based on the maximum rpm and chosen balance quality grade, m_R $[kg]$ the weight of the rotor, and r_c $[mm]$ the correction radius at which the weights are placed. The trial weight is then around 5 to 10 times that of the maximum residual weight (MacCamhaoil, 2016).

$$m_{res} = \frac{m_{su} m_R}{r_c} \tag{3.1}$$

Having chosen a balance quality grade of 6.8 due to given geometry and application, the specific unbalance was estimated at a value of 15 $g\ mm/kg$ based on the table provided in MacCamhaoil (2016). With this requirement and the cylinder models weight, diameter, and wall thickness in mind, a 20 g trial weight had been selected.

The procedure starts with the measurement of the initial vibration level and phase angle on both planes at the chosen rotational speed as described above. Then, the trial weight is added on plane 1 at a known but arbitrary angular position, θ. The magnitude and phase measurements are repeated on both planes with the trial weight in place. Next, the trial weight is removed and placed on plane 2 at

the marked location and measurements are again repeated. Based on these three measurements, the correction weights, m_C, and correction angles are calculated. For the calculation, multiple methods exists and are outlined in the document from MacCamhaoil (2016). The balancing calculations were performed in a modified version of the "Two Plane Balancing Example with DAQmx" program run in LabVIEW™ software (ExamplePrograms, 2023, November 27th), such that it could be used with the setups equipment. After the correction weights are mounted, the procedure can be repeated for further reductions at the same or higher rotational speeds, see for an example Figure 3.13b.

(a) Schematic of two-plane balancing setup.

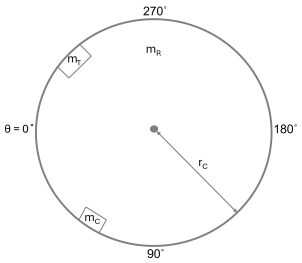

(b) Schematic example of correction weight, m_C, and trial weight, m_T, addition at an arbitrary plane.

Figure 3.13: Two-plane balancing setup and equipment.

Following the procedure described above, balancing of the cylinder model was performed. As noted before, to minimise the risk of structural failure due to potentially larger than expected vibrations, and to gain confidence in the experimental setup and balancing technique, the procedure was performed at increasing rotational speeds and redone multiple times to arrive at a satisfactory level of unbalance. As the balancing procedure, in combination with the installment of the experimental setup, took a considerable amount of the available time, it was cut short, to allow enough time for the force and flow visualisation measurements. Consequently, the maximum achievable rpm was lowered to a value of 3820 rpm, or 63.6 Hz, down from the originally planned 10000 rpm, with the final balancing performed at an angular frequency of 36 Hz. An overview of the final balancing procedure weight additions is depicted in Table 3.1.

Table 3.1: Final balancing procedure weight additions.

$Balancing\ attempt\ [-]$	$Trial\ weight,\ m_T\ [g]$	$Angular\ frequency,\ \omega_f\ [Hz]$	$Correction\ weight\ 1,\ m_C\ [g]$	$Correction\ weight\ 2,\ m_c\ [g]$	$Angular\ position\ 1,\ \theta\ [deg]$	$Angular\ position\ 2,\ \theta\ [deg]$
1	20	10	36.5	30.5	328	298
2	10.51	27	6.86	6.66	218	26
3	4.89	36	2.17	0.81	162	92

As a result of the lower maximum rpm, the achievable range of spin ratios for each of the Reynolds numbers decreased. Therefore, it was decided to run the experiment at lower Reynolds numbers, such that at least a spin ratio of 2 could still be achieved at the highest Reynolds number. Three subcritical Reynolds number at Re_D = 62500, Re_D = 125000 and Re_D = 250000 for spin ratios equal to $0 \leq k \leq 8$, $0 \leq k \leq 4$ and $0 \leq k \leq 2$ respectively, were selected.

3.12. Particle Image Velocimetry

The purpose of employing flow visualisation techniques in the light of the experiment are twofold, one to understand the underlying flow phenomena, which have been scarcely visualised at current Reynolds numbers in the past, from which a better understanding of the results obtained through the force measurements can established, and second to allow for direct comparison between the different Reynolds numbers tested and to what has been noted in literature. In this way the newly designed experimental setup can be characterised and the obtained data validated.

Particle Image Velocimetry, PIV, is one of the most extensively utilised and validated techniques in modern day experimental aerodynamics. PIV allows for obtaining quantitative flow velocity data at high spatial resolution and as such can be used to visualise complex flow phenomena, in the comparison of separate measurements, or to validate numerical simulations. The strengths of the PIV technique are that it is considered to be non-intrusive, as it is purely optical, and that it can measure hundreds of instantaneous two-dimensional (planar or stereographic PIV) or three-dimensional (tomographic PIV) velocity vector data from a single measurement. The recent works from Raffel et al. (2018) and Scharnowski and Kähler (2020) provide excellent overviews and may be consulted for detailed explanations and applications of PIV techniques.

The foundation of the PIV technique lies in the introduction of seeding particles, which can effectively be considered as a representation of fluid elements of the flow, and the determination of the average velocity of seeding particles ensembles within interrogation windows over a small interval of time. The quality of the seeding is the most important factor in the success of the measurements (Scharnowski & Kähler, 2020). Seeding particles should remain small enough to faithfully follow the flow, without disturbing the flows natural development and properties, whilst large enough to scatter enough light, such that they can be identified by the means of digital cameras. The mass density of the seeding particles should be close to that of the fluid in question, which becomes more important the larger the particle diameter is. The distribution of seeding particles should be dense, up to a limit for high spatial resolution, and homogeneous over the entire measurement region without areas becoming overly dense or too sparse. In case of low speed aerodynamics, e.g. current experiment, water glycol vapor is most commonly used with a particle diameter of approximately 1 μm.

The seeding particles in the measurement region are made visible with the use of high powered double pulsed laser systems. Green light of wavelength equal to 532 nm is emitted and formed into a thin laser sheet of approximately 1 mm thickness (planar PIV) or laser volume (tomographic PIV) by the use of cylindrical and or spherical lenses. The short pulse durations of the lasers, and consequently the exposure time of the camera, results in the seeding particles to appear to be frozen in time. The particles can then be clearly identified, opposed to when the pulse duration becomes too long, as then the particles will be smeared out and individual particles will be harder to detect. For a single measurement two instances of illumination in rapid succession are required, such that the displacement of the particles between the two instances can be determined. Illumination intensity should be homogeneous and the same between the two laser pulses. The scattered light of the particles for each instance is then recorded by means of specialised digital camera(s), which can, unlike more standard camera systems, cope with the extremely small pulse separation times, Δt, between the two recordings.

Recordings can be performed in low speed, high speed or time-resolved manner, where in the latter repetition rates in range of kHz, and even MHz with pulse burst lasers, can be achieved such that the relevant features of the flow are temporally well resolved. Today however, low speed planar PIV remains to be an highly popular technique, mostly because of its relative simplicity in operation and robust data processing as well as its capabilities of already providing the necessary data for many types of research (Scharnowski & Kähler, 2020).

Therefore, as an initial characterisation of the newly developed experimental setup is required over a large variety of spin ratios and Reynolds numbers, PIV is well suited and will be used throughout the present work. Furthermore, as quasi-two-dimensional conditions are expected and with a focus on general flow characteristics over a large area, low speed planar PIV has been chosen opposed to more elaborate and advanced PIV techniques.

3.12.1. Low speed planar PIV

As described previously, planar PIV setups require the dual laser beams to be shaped into thin sheets of approximately 1 mm thickness through the use of both cylindrical and spherical lenses. An example of which is being shown in Figure 3.14a where a laser sheet is formed and redirected by the use of a mirror to the desired measurement location. The light sheet of each laser head should be perfectly aligned to, and homogeneous in intensity across, both laser sheets and the desired measurement plane.
A single camera is placed to be normal to, and focused on, the illuminated measurement plane. With a single camera two out of three components of the velocity vector can be determined, with a second camera needed for the third, e.g. stereoscopic PIV. Spatial calibration of the setup is done with the use of an calibration target, that depicts a set of markers at known locations from which the optical magnification factor, M_f, and the dimensions of the field of view, FOV, relative to the pixel size is determined. After proper calibration is performed, seeding particles can be introduced to the flow and recordings of the image pairs where the seeding particles show as pixels of high intensity, like depicted in Figure 3.14b, can be performed.

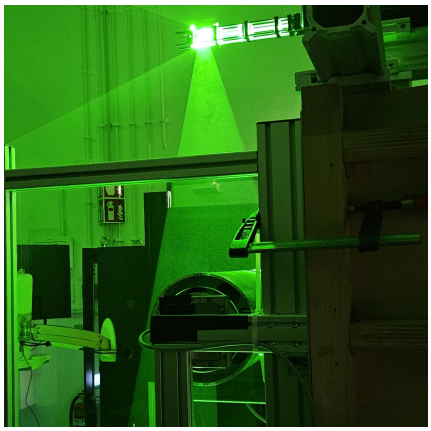

(a) Example of illuminated seeding particles in planar PIV configuration.

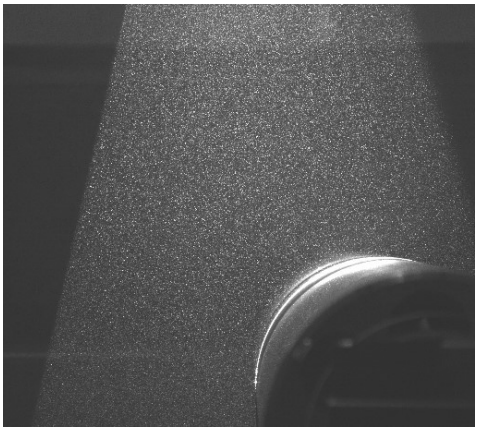

(b) Example of a raw PIV image recording.

Figure 3.14: Illumination and recording of seeding particles in planar PIV configuration.

Setup of all aforementioned components should be done with utmost care, where in the case of misalignment between laser sheets, laser sheet to measurement plane, camera to laser sheet or camera to the calibration target as well as differences in laser light intensities, systematic errors are introduced into the system which can no longer be corrected for during post-processing of the results (Scharnowski & Kähler, 2020).

The pulse separation time of the recordings should be significantly smaller than the time scales in the flow in order to successfully capture the true displacement in good approximation of the paired particles between the two recordings. Too long separation times might result in bias errors due to curved streamlines or convective accelerations in the flow (Scharnowski & Kähler, 2020). As such, depending on the flow conditions, e.g. Reynolds number, pulse separation times should be adapted accordingly. From the particle image displacement, $\Delta\vec{x}$, the pulse separation time, Δt, and the optical magnification factor, M_f, the particle image flow velocity, $\Delta\vec{v}$, can be determined with the use of Equation 3.2.

$$\Delta\vec{v} = \frac{1}{M_f}\frac{\Delta\vec{x}}{\Delta t} \tag{3.2}$$

The particle image displacement between each recordings at t and $t + \Delta t$ is estimated through a statistical process. The measurement domain is subdivided into a large number of interrogation windows of size m x n pixels. Each corresponding image pair within the interrogation window, has an intensity value, I_1 and I_2 respectively, of which I_2 is then used as a sliding window, over distances Δx and Δy, for the estimation of the normalised cross-correlation with I_1 by using Equation 3.3. The interpolated combination of Δx and Δy that results in the maximum value of the cross-correlation coefficient, C,

then determines the average particle displacement within that interrogation window. Obtaining the results of all interrogation windows, yields the velocity vector data across the full measurement domain. By performing the cross-correlation within the frequency domain using fast fourier transformation, the computational efficiency can be significantly improved (Willert & Gharib, 1991).

$$C(\Delta x, \Delta y) = \sum_{\Delta x=1}^{m} \sum_{\Delta y=1}^{n} \frac{[I_1(x,y) - \bar{I}_1(x,y)] \cdot [I_2(x+\Delta x, y+\Delta y) - \bar{I}_2(x,y)]}{\sqrt{[I_1(x,y) - \bar{I}_1(x,y)]^2} \cdot \sqrt{[I_2(x,y) - \bar{I}_2(x,y)]^2}}$$
$$= \sum_{\Delta x=1}^{m} \sum_{\Delta y=1}^{n} \frac{I_1'(x,y) \cdot I_2'(x+\Delta x, y+\Delta y)}{\sigma_{I_1(x,y)} \cdot \sigma_{I_2(x,y)}} \tag{3.3}$$

3.12.2. PIV equipment and setup

The current research involves a low speed planar PIV setup for the investigation of the flow field's general characteristics on the $x - y$ plane at the centreline of the rotating cylinder by obtaining two component velocity data, Figure 3.15a,b. Particle seeding is provided by the *SAFEX FOG 2010*, using a mixture of water and glycol, which once vaporized results in droplets with an diameter of approximately 1 μm, Figure 3.16a. The droplets are illuminated by an *Quantel Evergreen EV00200 series* Double-pulse Nd:YAG laser system at a wavelength of 532 nm, with a maximum repetition rate of 15 Hz and 200 mJ pulse energy, Figure 3.16b. The collimated laser beam, at 65% power for current measurements, is shaped into a thin laser sheet of approximately 1 mm thickness with the use of an array of spherical and cylindrical lenses. The formed laser sheet is redirected by a specialised mirror, that is treated with a protective coating, to reach the desired measurement location.

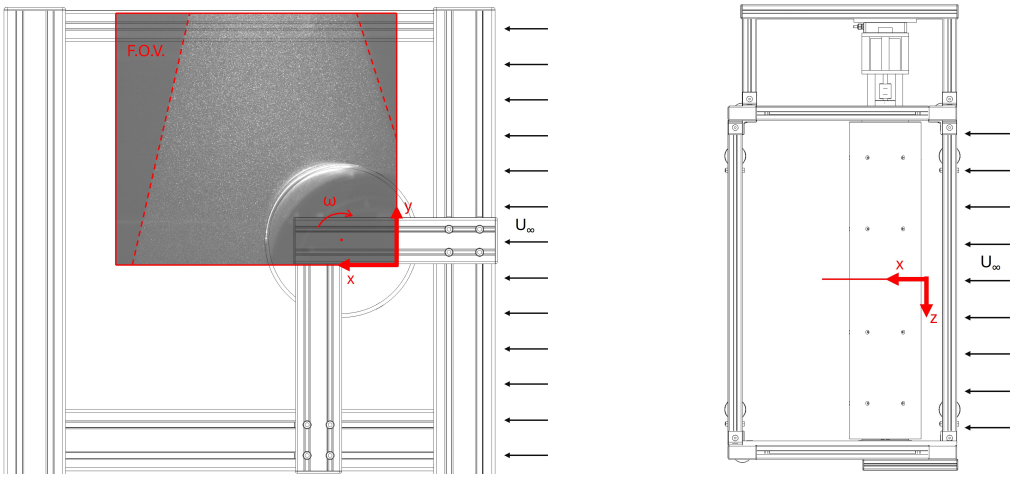

(a) Side view. (b) Top view.

Figure 3.15: Schematic illustration of the PIV measurement plane and FOV.

The illuminated particles are captured by a single 16-bit *LaVision Imager sCMOS CLHS* camera with a sensor size of 2560 x 2160 pixels, placed normal to the measurement plane at a distance of approximately 2 m, Figure 3.16c. The camera is equipped with a 60 mm *Laowa* macro lens, set at an aperture of f/5.6. The field of view, FOV, is cropped to 404.3 x 364.2 mm, yielding a magnification factor of M_f = 0.035 and resolution of 5.32 px/mm. To limit light reflection of the surrounding metallic surfaces, the cylinders centre section and image background are covered with matte black vinyl sheets, Figure 3.16b. The acquisition rate is limited by the maximum repetition rate of the double pulse laser system, and thus for obtaining statistics, 500 image pairs at a rate of 15 Hz are recorded for each measurements. Recording time took 33.3 s for each measurement. The pulse separation time is adjusted accordingly for each Reynolds number tested at Δt = 300 μm for Re = 62500, Δt = 210 μm for Re = 125000, and Δt = 100 μm for Re = 250000. Synchronisation of the laser and camera systems is done digitally, where the reference time is set at the moment the system is actuated.

(a) *Smoker setup*

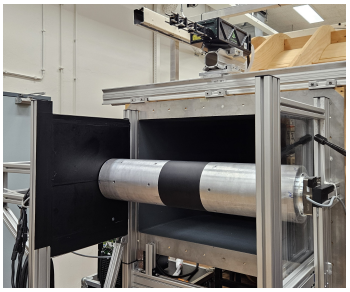

(b) *Laser setup*

(c) *Camera setup*

Figure 3.16: Smoker, laser and camera setup for low speed planar PIV measurements.

4

Data processing

The data obtained through the experimental setup and data acquisition techniques explained in chapter 3 has undergone various post-processing treatments to arrive at the results outlined in chapter 5. An overview of the relevant post-processing methodologies and uncertainty quantification for the force measurement and PIV data is given below.

4.1. Post-processing methodologies

To arrive at meaningful conclusions, further analysis on the acquired data is often necessary. Thereby, a selection of the most relevant post-processing methodologies used for the current research are presented here. Each of the methods applied helps in the understanding of the data by extracting different information and as such new insights on the results are found.

4.1.1. Post-processing of force measurement data

The acquired force measurement data composes out of large time signals for each of the force components, $F_{x,1}(t)$, $F_{y,1}(t)$ and $F_{x,2}(t)$, $F_{y,2}(t)$, and encoder voltage reference pulse data from each of the two sensors respectively. Data acquisition is performed at a sampling frequency, f_a, of 51.2 kHz for a duration of approximately, t_a, 15 s, yielding roughly 768000 data samples, N, for each measurement. The post-processing procedure applied on the force measurement data, yielding the performance characteristics, e.g. C_L/C_D, and reference curves, e.g. C_L vs. k, of the rotating cylinder, is outlined in Figure 4.1.

The raw data is cleaned from any NaN readouts and passed through a low-pass filter at a cutoff frequency of 1000 Hz to remove any high frequency noise, and smoothen the data. The cleaned force signals are then added appropriately to obtain the total combined force readouts, corresponding to the total forces acting in the direction of the lift, $F_y(t)$, and drag, $F_x(t)$, on the cylinder over time. Measured flow properties, rotational control settings, and cylinder dimensions are then given to non-dimensionalise the data, yielding the determination of the Reynolds number, Re_D (Equation 2.1), spin ratio, k (Equation 2.3), and force coefficients, $C_L(t)$ (Equation 4.1) and $C_D(t)$ (Equation 4.2) for each measurement. More specifically, lengths are non-dimensionalised by the cylinder diameter, D, whereas for velocities the freestream, U_∞, is used.

Statistics are performed on the calculated quantities by time-averaging to obtain, F_x, F_y, C_L, C_D, and through calculating the standard deviations, σ_{F_x}, σ_{F_y}, σ_{C_L}, σ_{C_D}, respectively. Uncertainties are determined and can be found in section 4.2. These quantities are then used to extract the performance characteristics of, and reference curves for, the rotating cylinder setup. At last, the resultant force coefficient, C_R, and its direction, θ, are calculated with Equation 4.3 and Equation 4.4. The results and analysis of the post-processed force measurement data is treated in section 5.1.

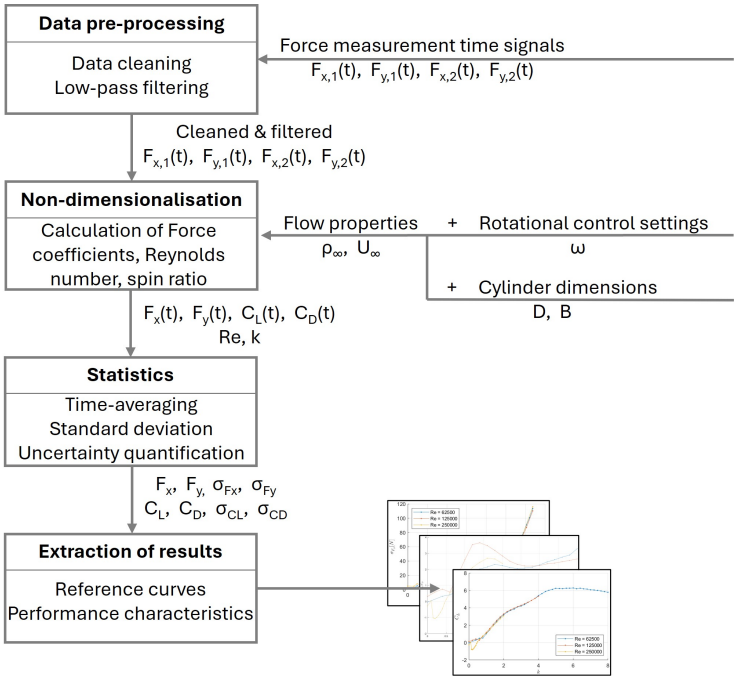

Figure 4.1: Schematic of the force measurement data post-processing procedure.

$$C_L(t) = \frac{F_{y,1}(t) + F_{y,2}(t)}{\frac{1}{2}\rho_\infty U_\infty^2 BD} \tag{4.1}$$

$$C_D(t) = \frac{F_{x,1}(t) + F_{x,2}(t)}{\frac{1}{2}\rho_\infty U_\infty^2 BD} \tag{4.2}$$

$$C_R = \sqrt{C_L^2 + C_D^2} \tag{4.3}$$

$$\theta = \arccos\left(\frac{C_D}{C_R}\right) \cdot \frac{C_L}{|C_L|} \tag{4.4}$$

4.1.2. Post-processing of PIV data

The calibration, acquisition and processing of the 500 double frame image pairs for each measurement point is done with the LaVision Davis 10.2.1 software. The recorded raw images are first shift corrected relative to the first image, to improve alignment between the images as it is necessary due to cylinder model imperfections, see section 3.6. Image pre-processing is then performed by applying spatial and temporal minimum subtraction and normalisation with the local average, to remove background noise and achieve more uniform particle pixel light intensities, respectively. Pre-processing is concluded by masking the images from unwanted objects outside of the measurement domain, as they would otherwise falsely contribute to the cross-correlation and hence introduce errors in the velocity estimation.

Calculation of the particle image displacements, $\Delta\vec{x}$, is performed with the multi-pass interrogation window algorithm (Scarano & Riethmuller, 2000). Window sizes are reduced from an initial 64 x 64 pixels to 16 x 16 pixels with two passes each and a 0% overlap. Selection of windows sizes and overlap are the result of an iterative process, where the initial window size is the result of the maximum particle shift in pixels, and the final window size chosen up to the limit of spatial resolution. The result is a vector spacing of 3mm in both x and y directions.

The 0% overlap is selected since the current research is only looking at general flow characteristics, where accuracy in the determination of the flow field's velocity derivatives is less critical. Additionally, tests with higher values of overlap appeared to present similar results as with no overlap on the current data set, as such, with an overlap of 0%, a reduction in overall computation time and storage space is achieved.

For the multi-pass procedure a round weighting factor that assumes a Gaussian weighting function is used (Astarita, 2007). Consequently, centrally located pixel information is higher weighted and hence the local particle image displacement is better represented, at the cost of slightly longer simulation time.

As there is a particular interest in the general flow characteristics, potentially spurious vectors are removed during the multi-pass window procedure, whenever the peak ratio, Q, relative to the minimum value of the correlation plane between the two highest peaks drops below a value of 1.2. By doing so, a more accurate time-average and standard deviation can be calculated, whereas the value of 1.2 ensures not too many vectors are discarded. Similarly, a median filter with universal outlier detection, suitable for a large variety of flows (Westerweel & Scarano, 2005), is applied to reject and replace spurious vectors. An example of the PIV image processing and velocity vector calculation results of a single double frame pair is shown in Figure 4.2.

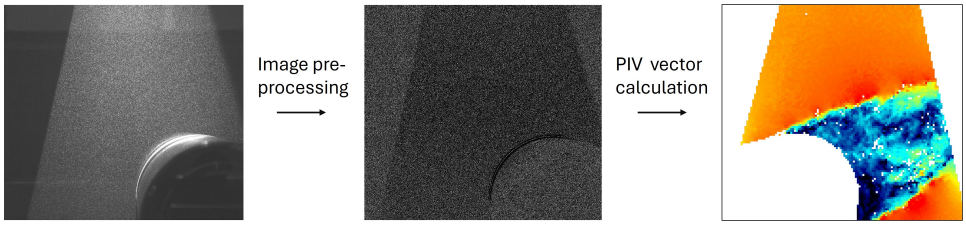

Figure 4.2: Example of PIV processing from raw image to velocity vector data.

Further post-processing of the PIV results starting from the determined velocity vector and coordinate system data is done with a self-developed code. A mask is created to clean up boundary data by setting values outside of the domain to NaN and erode a small edge surrounding the measurement domain. Statistics are determined, yielding time-averaged velocity data and standard deviations of the velocity components, u and v in x and y direction respectively. Time-averaged quantities are denoted with an overline, e.g. $\bar{u}$, temporal fluctuations with an apostrophe, e.g. u', and directions with their respective velocity component, e.g. standard deviation of the u-component of the velocity vector is denoted as σ_u. These quantities are then further used to calculate other quantities of interest, e.g. velocity magnitude $|U|$ and vorticity on the x - y plane ω_z. At last, results are non-dimensionalised with the use of the cylinder diameter, D, for lengths and the freestream velocity, U_∞ for velocities. A schematic of the PIV process is outlined in Figure 4.3.

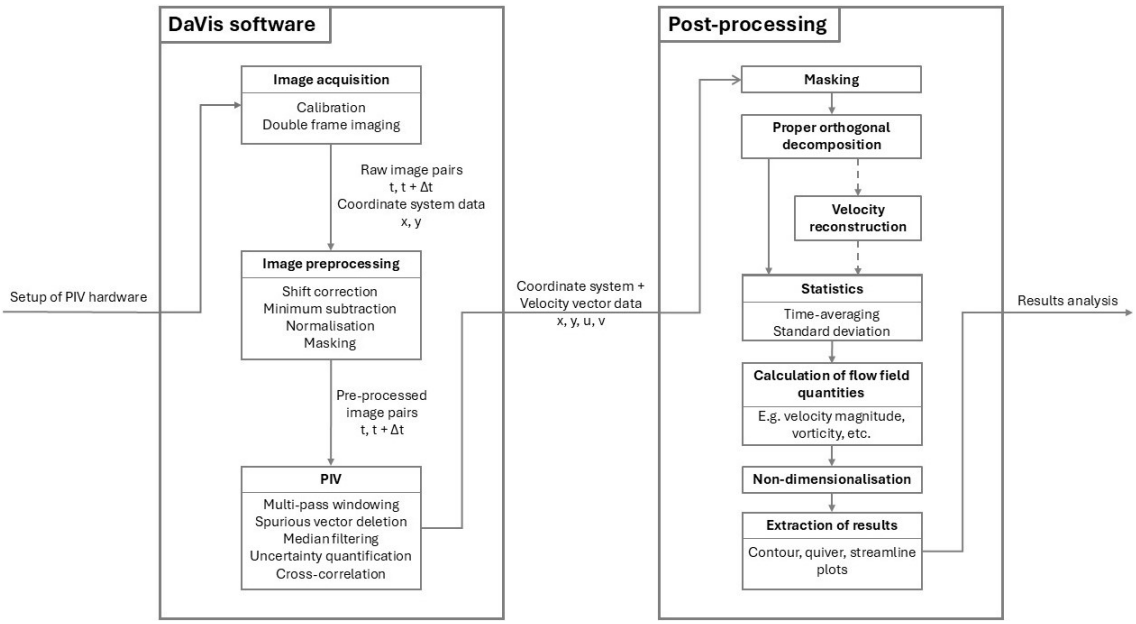

Figure 4.3: Schematic of post-processing procedure for the PIV data.

4.1.3. Proper Orthogonal Decomposition

Proper Orthogonal Decomposition, POD, is utilised for the identification of coherent structures and data order reduction. This statistical method was first introduced by Pearson (1901) as the Principal Component Analysis, PCA, and has been later introduced for fluid dynamics purposes by Lumley (1967) as the classical direct POD method, and by Sirovich (1987) as the snapshot POD method. The methods rely on the proper, or optimal, decomposition of a vector field into an orthogonal set of deterministic eigenfunctions, called POD modes, each representing a small portion of the total fluctuating kinetic energy and are ordered by their contribution to the total energy. Analysis of the dominant modes could then provide information about the flow's organisation, and reveal coherent structures that are otherwise difficult to identify. The method has been successfully applied for numerous flow field investigations such as from Berkooz et al. (1993) and Q. Zhang et al. (2014), while recent comprehensive overviews of POD and other modal decomposition techniques are provided by Taira et al. (2017) and Rowley and Dawson (2017).

For a reduction of computational time, the snapshot POD method is often the preferred method for data sets with large numbers of spatial measurement points, as is the case for most PIV and CFD data, whereas the direct method is more suitable for data obtained at a limited number of point-wise measurements that have higher temporal resolution (Weiss, 2019). Furthermore, as current PIV data is not time-resolved, the employed method can only provide modes that are spatially coherent. This form of POD is called space-only POD as each snapshot of the flow is treated as an independent realisation of a random process, and hence loses its dynamical information, whereas spectral POD could retain both (Towne et al., 2018). As the current project is dealing with low speed planar PIV data, the (snapshot) space-only POD method will be utilised and its current form as presented by Michelis (2017) will be further explained below.

First, the fluctuating velocity field, $U'(x_i, y_j, t_k) = [u'(x_i, y_j, t_k)\ v'(x_i, y_j, t_k)]^T$, is obtained by subtracting the time-averaged velocity, $\bar{U}(x_i, y_j)$, from the velocity vector, $U(x_i, y_j, t_k) = [u(x_i, y_j, t_k)\ v(x_i, y_j, t_k)]^T$. Each spatial fluctuating velocity field is ordered into a single column at each time instant, or snapshot. The result is a m x n matrix of snapshots, **S** (Equation 4.5), where m is the number of spatial measurement locations, $m = N_x \times N_y$, and n the corresponding time instances, $n = N_t$.

$$\mathbf{S} = \begin{bmatrix} U'(x_1, y_1, t_1) & U'(x_1, y_1, t_2) & U'(x_1, y_1, t_3) & \dots & U'(x_1, y_1, t_{N_t}) \\ \vdots & \vdots & \vdots & \ddots & \vdots \\ U'(x_{N_x}, y_{N_y}, t_1) & U'(x_{N_x}, y_{N_y}, t_2) & U'(x_{N_x}, y_{N_y}, t_3) & \dots & U'(x_{N_x}, y_{N_y}, t_{N_t}) \end{bmatrix} \tag{4.5}$$

From the snapshot matrix, the autocovariance matrix, $\mathbf{R} = \mathbf{S}^T\mathbf{S}$ is calculated and introduced to the following eigenvalue problem Equation 4.6, where Λ is an diagonal matrix of eigenvalues λ^m, and **a** the matrix of temporal eigenfunctions, $a^n(t)$.

$$\mathbf{R}\,\mathbf{a} = \mathbf{S}^T\mathbf{S}\,\mathbf{a} = \Lambda\,\mathbf{a} \quad \text{with,}$$

$$\Lambda = \begin{bmatrix} \lambda^1 & 0 & 0 & 0 \\ 0 & \lambda^2 & 0 & 0 \\ 0 & 0 & \ddots & 0 \\ 0 & 0 & 0 & \lambda^m \end{bmatrix} \text{ and, } \mathbf{a} = \begin{bmatrix} a^1(t_1) & a^2(t_1) & \dots & a^{N_t}(t_1) \\ a^1(t_2) & a^2(t_2) & \dots & a^{N_t}(t_2) \\ \vdots & \vdots & \ddots & \vdots \\ a^1(t_{N_t}) & a^2(t_{N_t}) & \dots & a^{N_t}(t_{N_t}) \end{bmatrix} \tag{4.6}$$

As such, a proper orthogonal basis of eigenvectors is established to project the variances of the data onto. Consequently, the projected variables are uncorrelated, and thus, each correspond to variations of one independent spatial mode of the fluctuating velocity field, Φ^n. The spatial modes can be expressed as follows,

$$\Phi^n(x,y) = \sum_{k=1}^{N_t} a^n(t_k)\ U'(x,y,t_k) \tag{4.7}$$

whereas energy contribution of each spatial mode to the total fluctuating energy may be indicated by the corresponding eigenvalue, or variance, as

$$E = \frac{\lambda^m}{\sum_{i=1}^{m} \lambda_i}. \tag{4.8}$$

By ordering the spatial modes based on their energy contribution, starting from the most energetic, e.g. largest eigenvalue, the most dominant features of the flow can be determined and coherent structures may be identified. However, as it is a statistical method, the resulting relative energy of each mode is depended on the FOV, therefore care must be taken, such that all relevant modes are identified (Michelis, 2017).

Besides flow structure identification by analysis of the individual POD modes, the modes can also be used to reconstruct a reduced order representation of the velocity field, U_{POD}. A selection of POD modes can be chosen to account for the fluctuating component of the velocity field, where the velocity field can then be reconstructed by summing with the time-averaged velocity field Equation 4.9. In doing so further analysis can be performed to identify the underlying phenomena, however it must be noted that the resulting flow field is no longer physical.

$$U_{POD}(x,y,t) = \bar{U}(x,y) + U'(x,y,t) = \bar{U}(x,y) + \sum_{i=1}^{\Phi^\#} a^i(t)\ \Phi^i(x,y) \tag{4.9}$$

4.2. Uncertainty quantification

Error sources in experimental measurements causes uncertainties in the obtained results. Whereas the error is the difference between the measured value and the actual value, uncertainty used in this section, and throughout the report, is a range of values that can occur for a measurement with high probability in which the true value lies with said confidence, e.g. 95%. For an comprehensive overview on uncertainty quantification in experiments the reader may consult the work from Coleman and Steele (2009).

In the light of the current experiment, uncertainties in the determination of the force coefficients through the force measurements, and velocity estimations in the PIV measurements are present. The nature of error sources are either systematic or random and will be covered in the subsequent sections below.

4.2.1. Uncertainty in the freestream velocity

The unavailability of the delta pressure measurements at the SLT facility during the time of the experiment meant freestream velocity data has been obtained through an externally mounted pitot-static probe, section 3.4. The pitot-static probe was mounted on the lower side of the nozzle and consequently in the vicinity of the cylinder model. The tunnel fan rpm was set to reach the desired freestream velocity as indicated by the pitot-static probe, $U_{pitot,0} \approx U_\infty$. As the rotational speed of the cylinder was slowly increased, the accelerated flow region was sensed by the probe in the full range of rotational frequencies. The measured velocity, U_{pitot}, started to increase for all initial freestream velocities at a similar rate with increasing spin ratio, whereas the tunnel fan rpm remained constant at its set value, Figure 4.4. Therefore, it remains unclear if the same freestream velocity at zero rotation is kept throughout the measurement set and unfortunately the uncertainty remains unquantified.

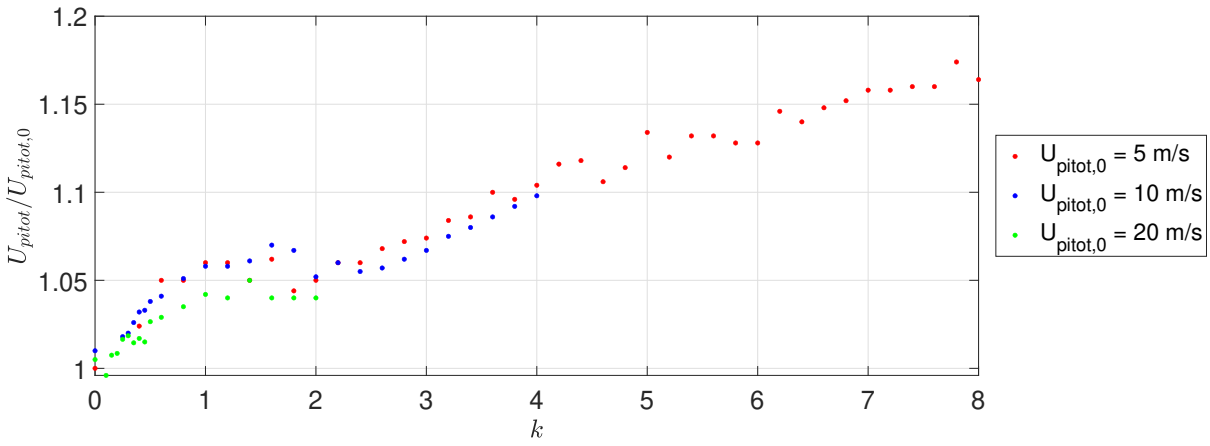

Figure 4.4: Variation in Pitot-static probe velocity measurements with increasing spin ratio for all set freestream velocities.

Additionally, further uncertainty regarding the determination of the freestream velocity arises following concerns on the extent of wind tunnel interference effects for rotating cylinders, section 3.2. As the setup is designed with a high blockage ratio and close proximity of the model to the nozzle exit plane in mind, these interference effects are expected to play a role. Hence, the pitot-static measurements are not used in the remainder of the report for determining other quantities of interest, e.g. the lift coefficient. Therefore, the freestream velocity values are assumed to be equal to the set values of U_∞ = 5, 10 and 20 m/s and Reynolds numbers equal to Re_D = 62500, 125000 and 250000 respectively.

4.2.2. Force measurement uncertainties

Uncertainties in the force measurement data presented in this work are expected to be mainly the result of errors due to potential misalignment of the model, model imperfections, unbalance, determination of the freestream velocity, and force sensor accuracy. Although care has been taken to minimise the effects of the aforementioned error sources, peculiarities associated with the initial experimental campaign of the new setup meant quantification of the uncertainty is difficult to determine and errors are expected to be relatively large.

The bias errors of the used measurement equipment follow from the ISO 376 standardised calibration procedure, to which the sensors are rated in accuracy class 0.5. Within this accuracy class the worst case combined relative standard uncertainty, u_{bias}, equals to 0.008% full scale (Aydemir et al., 2022). As such, for each of the 2 kN force sensors, a maximum relative standard bias uncertainty of 1.6 N is assumed. Although, 1.6 N is small in the scale of the experiment, at the lower Reynolds numbers and spin ratios, 1.6 N is still significant. However, do note this assumes a worst case, based on the ISO calibration standards, while in reality the sensors are expected to perform better.

Furthermore, although zeroing before each session was performed, it must be noted some drift, $F_x < 2\ N$ and $F_y < 0.5\ N$, in the force readouts was observed between the start and end of the measurement session in no wind and no spin conditions.

In an ideal case of proper installment and calibration of equipment, which results in negligible effects due to systematic errors, the standard measurement uncertainty, u_m, is mainly the result of the random maximum and statistical errors. When the systems used are highly sensitive with minimal internal friction and high bit-depth, random statical errors dominate and the resultant standard measurement uncertainty for the force measurements is then given by;

$$u_m = \frac{\sigma}{\sqrt{N}}\,, \tag{4.10}$$

with σ the standard deviation of the measured quantity, and N the number of samples. Combining both the standard measurement and bias uncertainties, the total expanded uncertainty with a confidence interval of 95% can be calculated as follows;

$$u_{95} = t_s \sqrt{u_m^2 + 2u_{bias}^2}\,, \tag{4.11}$$

where t_s is the coverage factor to provide a confidence level of 95%, u_m the standard measurement uncertainty of the force measurement data and u_{bias} the standard uncertainty of the bias errors for each of the force sensors. The uncertainty of the measured forces, e.g. $F_{x_{uncertainty}}$, is then given by;

$$F_{x_{uncertainty}} = \bar{F}_x \pm u_{95}\,, \tag{4.12}$$

and is propagated to further derived quantities, e.g. C_D.

Figure 4.5 depicts the calculated force measurement uncertainties given the standard measurement and bias uncertainties described above. Do note this does not include the unquantified uncertainties, e.g. within the determination of the freestream velocity and density, and hence true expected uncertainty is expected to be larger.

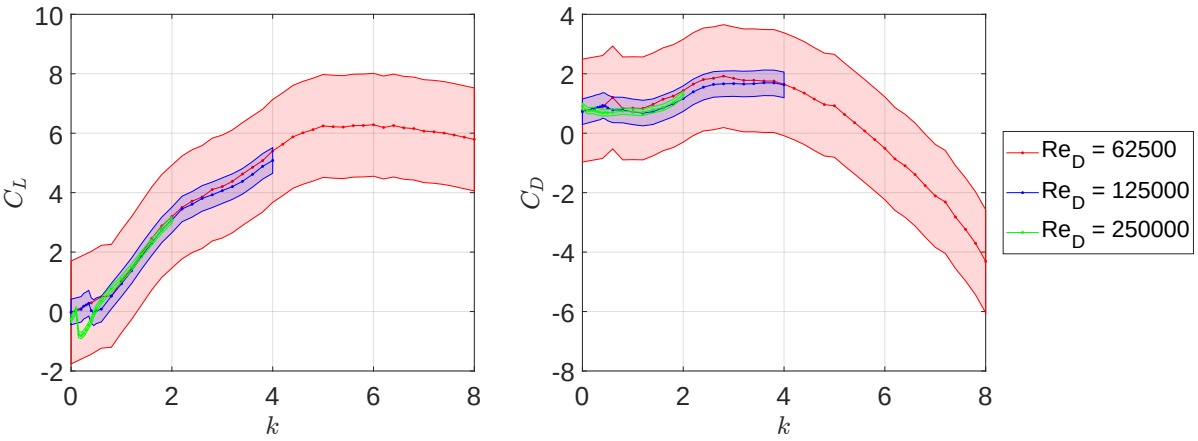

Figure 4.5: Measurement uncertainty, u_{95}, with 95% confidence level versus spin ratio, k, for left; total lift coefficient, C_L, and right; total drag coefficient, C_D.

As noted down earlier, the highest uncertainty is associated with the lowest Reynolds number as a consequence of the bias uncertainty dominating with the lower forces recorded, e.g. 1.6 N makes a relatively larger contribution at the lower Reynolds numbers. Therefore, when the force increases, a gradual decrease in uncertainty towards the higher spin ratios is noticeable. However, the decrease of the bias uncertainty is counteracted by the growth of the standard measurement uncertainty, since at the highest spin ratios the effects of unbalances in the system will become more visible. This will be covered in more detail in subsection 5.1.4. At the larger Reynolds numbers, for which the experimental setup was originally designed for, the uncertainty is considerably lower and the effect of the bias uncertainty is less noticeable.

4.2.3. PIV measurement uncertainties

When considering low speed planar PIV measurements, where the choice and introduction of seeding particles is done correctly, proper alignment of equipment is ensured and the pulse separation time is selected appropriately, the uncertainties in the velocity estimation are mainly a result of errors in the particle image displacement, $\Delta\vec{x}$, e.g due to in-plane motion, peak locking, out-of-plane motion and image noise effects. To determine the uncertainty in the particle image displacement many methods nowadays exist. For an extensive review on such methods the work from Sciacchitano (2019) may be consulted.

The uncertainty in the velocity estimation for the current PIV data set is determined with the use of the correlation statistics method (Wieneke, 2015) on the time-averaged velocity fields. The method relies on quantifying differences in particle image displacement by mapping the two image pairs onto each other with the use of the calculated displacement vector. From this, positional disparity can be

determined based on the amount of asymmetry in the correlation peak. As such, through a statistical analysis, the uncertainty in the displacement vector is estimated by checking the contribution of each pixel to the shape of the correlation peak across each interrogation window for each image pair, yielding the total uncertainty over the full vector field.

Maximum uncertainties in the time-averaged velocity fields are found to be the largest at the lower spin ratios, $k < 1.5$, near the point of separation and further downstream where the shear layers tend to breakdown and come closer together. Along the rest of the visible shear layer, uncertainties drop by an order of 10, whereas in the freestream a further reduction in uncertainty is observed. Table 4.1 gives an indication of the maximum estimated uncertainties for each Reynolds number and all spin ratios in the freestream, shear layers and near the separation points. Uncertainties are found to be smaller at the same locations for all other spin ratios tested.

Table 4.1: Estimated maximum uncertainties in the particle image displacements.

$Re_D[-]$	$Location$	$\lvert U_{uncertainty}\rvert[m/s]$	$\lvert U_{uncertainty}\rvert[\%]$
62500	FreeStream Shear Layer Separation Point	≈ 0.005 ≈ 0.10 ≈ 0.30	$\approx 0.08\%\lvert\bar{U}\rvert$ $\approx 2.77\%\lvert\bar{U}\rvert$ $\approx 6.43\%\lvert\bar{U}\rvert$
125000	FreeStream Shear Layer Separation Point	≈ 0.012 ≈ 0.22 ≈ 0.55	$\approx 0.12\%\lvert\bar{U}\rvert$ $\approx 3.30\%\lvert\bar{U}\rvert$ $\approx 4.90\%\lvert\bar{U}\rvert$
250000	FreeStream Shear Layer Separation Point	≈ 0.02 ≈ 0.45 ≈ 0.92	$\approx 0.08\%\lvert\bar{U}\rvert$ $\approx 3.60\%\lvert\bar{U}\rvert$ $\approx 3.95\%\lvert\bar{U}\rvert$

5

Results and analysis

In this chapter, the results obtained from the data of the experimental campaign are presented and analysed. In section 5.1, the outcomes of the force measurements are discussed and the force characteristics of this particular setup are presented. Based on the force characteristics, section 5.2 aims to show the different states of the flow and to explain the underlying physics behind the force measurement behaviour.

Before continuing, Figure 5.1 first depicts the coordinate system definition, rotation direction of the cylinder model, and conventions used throughout the remainder of the report, to gain a better understanding of the shown results. As such it must be noted that, for safety and tunnel jet deflection considerations, an rotation in anti-clockwise direction has been chosen such that the lift force, F_y, is acting, for the majority of the spin ratios tested, downwards into the ground. Therefore, positive lift values in this report are pointing in the negative y-direction, whereas positive drag, F_x, points in the positive x-direction. To stay consistent with the positive directions of both the lift and drag forces, the angular position, θ, is positive in the clockwise direction. Additionally, following the limit set on the maximum rpm after the performed balancing procedure, see section 3.11, an overview of the performed measurements, for which results will be shown, is indicated in Table 5.1 below.

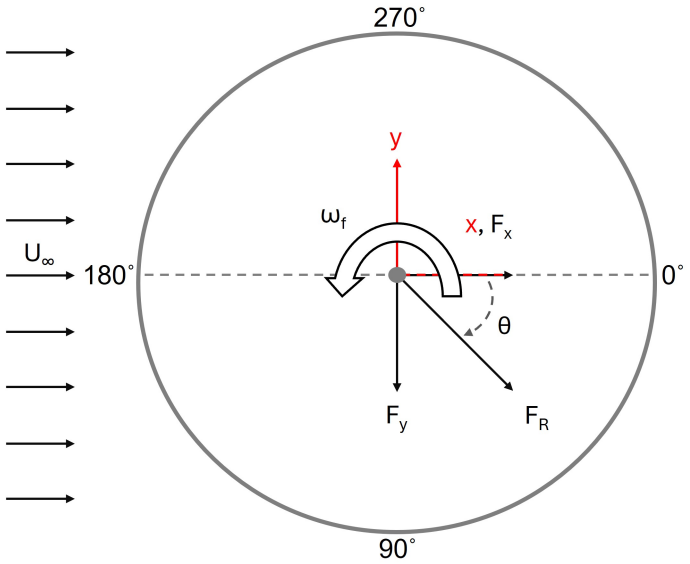

Figure 5.1: Coordinate system definitions and direction of rotation of the cylinder model.

Table 5.1: Summary of performed measurements and conditions.

$Data\ set$	$Freestream\ velocity,\ U_\infty\ [m/s]$	$Reynolds\ number,\ Re_D\ [-]$	$Aspect\ Ratio,\ A\ [-]$	$Blockage\ ratio,\ Area_D/Area_W\ [\%]$	$Spin\ ratio,\ k\ [-]$
●	5	62500	4.5	33.3	$0,$ $0.4 \leq k \leq 8,\ \Delta k = 0.2$
●	10	125000	4.5	33.3	$0,$ $0.2 \leq k \leq 0.5,\ \Delta k = 0.05$ $0.6 \leq k \leq 4,\ \Delta k = 0.2$
●	20	250000	4.5	33.3	$0,$ $0.1 \leq k \leq 0.5,\ \Delta k = 0.05$ $0.6 \leq k \leq 2,\ \Delta k = 0.2$

Furthermore, in Table 5.2 an overview is given of the most relevant and recent experimental research on rotating cylinder flow to be used for the comparison with the current research. This set of literature will be primarily, but not exclusively, used in the discussion presented in the subsequent sections.

Table 5.2: Summary of comparable experimental rotating cylinder research.

$Author(s)$	$Facility$	$Type$	$Reynolds\ number,\ Re_D \cdot 10^4\ [-]$	$Spin\ ratio,\ k\ [-]$	$Aspect\ Ratio,\ A\ [-]$	$Blockage\ ratio,\ Area_D/Area_W\ [\%]$	$Endplate\ size,\ D_e/D\ [-]$
Swanson (1961)	Closed section - wind tunnel	2D	3.58 - 50.1	0 - 17	∞	?	N.A.
Badalamenti (2010)	Closed section - wind tunnel(s)	3D - two free ends	1.6 - 9.5	0 - 8	5.1	8 - 9 (incl. support)	1 - 3
Chen and Rheem (2019)	Water tunnel	3D - two free ends	3.06 - 22.3	0 - 8	1.85 - 5.78	5.7 - 12.3 (approx. from given data)	4.90 - 1.57
Bordogna et al. (2019a)	Closed section - wind tunnel	quasi 2D	18.0 - 100.0	0 - 5	3.73	7	N.A.
Ma et al. (2022)	Closed section - wind tunnel	3D - two stationary endplates of different size	4.6 - 51.0	0 - 2	10	5.1	3.33 (side 1), 2 (side 2)
Chen et al. (2023)	Closed section - wind tunnel	3D - one endplate	9.33 - 31.5	0 - 4.5	3.5 - 6	3.4 - 5.8 (approx. from cylinder dimensions)	1 - 2

5.1. Force characteristics

In this section the results acquired from the force measurement data, following the methodology described in subsection 4.1.1, are presented and compared to literature. First, in subsection 5.1.1 and subsection 5.1.2, lift and drag coefficient data as a result of the increase in spin ratio and Reynolds number are covered. Then similarly, in subsection 5.1.3 the resultant force coefficient and its directionality are shown. At last, fluctuations in the force coefficient data are discussed in subsection 5.1.4. For clarity, each of the quantities shown in these sections are time-averaged and the colours used throughout stay consistent and correspond to the Reynolds numbers tested. The underlying mechanisms as a cause of the force coefficient behaviours will be addressed in more detail in section 5.2.

5.1.1. Lift coefficient

The total lift coefficients, C_L, as a result of the increase in spin ratio are deduced from the force measurements over the entire cylinder, at each of the Reynolds number tested, and are shown in Figure 5.2. Within the current range of Reynolds numbers, lift coefficient behaviour can be categorised in a number of distinct ranges of spin ratio. Namely, first the range of $0 < k < 1$ shows a larger dependency on the Reynolds number, which is followed by a regime of steady increase in the lift coefficient independent of the Reynolds number between $1 < k < 2.2$, then for $2.2 < k < 5$ a reduced rate at which the lift coefficient increases is observed, before plateauing and eventually decreasing of the lift coefficient occurs for $k > 5$. Each of the regimes will be addressed in more detail below and throughout section 5.2.

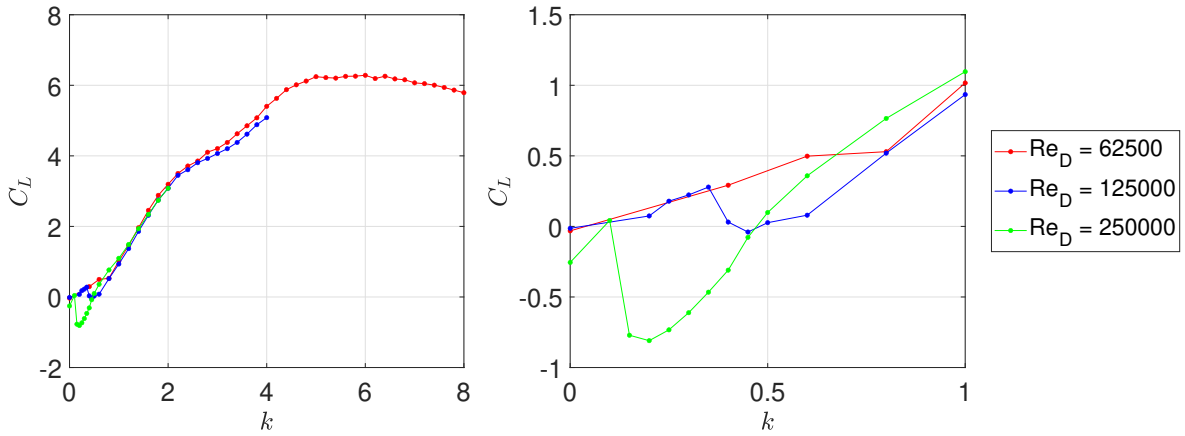

Figure 5.2: Total lift coefficient, C_L, versus spin ratio, k, for left; $0 \leq k \leq 8$, and right; $0 \leq k \leq 1$.

At k = 0, it is expected for a cylinder at the tested Reynolds numbers to produce mean zero lift coefficients, see Figure 2.5. This is the case for the two lowest Reynolds numbers. However, at Re_D = 250000 a negative lift coefficient was recorded for multiple instances. According to Table 2.1, the one-bubble TrBL1 regime is not reached for Re_D < 300000, and hence within a disturbance-free flow no such force should be present. Therefore, in subsection 5.2.1 this discrepancy will be further covered.

The initial rise in lift coefficient is the result of the regular Magnus effect, where due to the moving wall effect, asymmetries in the pressure distribution between the upper and lower surface results in the lifting force, as has been explained in subsection 2.2.2 in more detail. The remainder of the regime for k < 1 shows a large dependency of the lift coefficient on the Reynolds number. It has been previously discussed by Krahn (1956), Swanson (1961), Ma et al. (2022) and throughout chapter 2 that the transitional state of the boundary layer, the formation of laminar separation bubbles and movement of the separation points in combination with the influence of the moving wall effect are the main mechanisms causing the dependency at this particular range of Reynolds numbers. Most notably, a drop or temporarily plateauing of the lift coefficient is visible. The critical spin number at which this change occurs has been shown to decrease with an increase of the Reynolds number (Ma et al., 2022). For the two largest Reynolds numbers tested, the drop is large enough such that negative values of the lift coefficient are obtained. This is in accordance with the expected regime of the inverse Magnus effect as explained by Swanson (1961) and the statements made by Ma et al. (2022) on the growing strength of the laminar separation bubble with an increase of Reynolds number, see subsection 2.2.8.

Comparing with similar quasi-two-dimensional experimental data of Figure 2.33 from Swanson (1961), the results at Re_D = 62500 and 125000 of the current experiment, shows similarity in both shape and magnitude to the results at lower Re_D = 49000 and 99000, respectively. A potential cause might be found in the large nozzle blockage, reducing the flow velocity at the model, and hence lowering the Reynolds number which in turn increases the spin ratio as the rotational frequency is kept the same. However, the results shown for Re_D = 250000 show an opposite effect, where it appears to have a closer resemblance in shape to the larger Re_D = 420000 for 0 < k < 0.15 and k > 0.4, whereas the magnitude and sharpness of the peak is closer to Re_D = 260000 and 295000. Additionally, the results for the smooth cylinder in the quasi-two-dimensional experiments of Takayama and Aoki (2005) show good similarity for both shape and magnitude at Re_D = 62500 and 125000, eventhough the aspect ratio is significantly lower with A = 2.15 compared to the current A = 4.5.

The lowest lift coefficient recorded reached a value of C_L = -0.8, which is substantially lower compared to the minimum value from the experiments of Swanson (1961), C_L = -0.6. Possibly the discrepancies found for the stationary case at this Reynolds number plays a role in the different behaviour, while wind tunnel interference effects and different tunnel configuration, e.g. open-return, are other factors of uncertainty. However, the results from Ma et al. (2022) do indicate such low values, C_L = -1.16, at higher critical Reynolds numbers, Re_D = 490000.

The quasi-two-dimensional data from Bordogna et al. (2019a), Figure 2.13a, shows overall higher lift coefficients and higher values of the lift coefficient with increasing Reynolds number. Do note results for k < 0.4 are not shown and hence the regime of the inverse Magnus effect is not visible in the data. Instead, in terms of shape and magnitude of the lift coefficient curve, more similarity is found with the three-dimensional studies from Badalamenti (2010), Figure 2.11a, Chen and Rheem (2019), Figure 2.12a, and Ma et al. (2022) in the range of 0 < k < 1. The closer resemblance to the three-dimensional data, especially with the tests from Badalamenti (2010) using two stationary endplates and Ma et al. (2022), can be the result of the side walls potentially acting in the same way as having two large stationary endplates.

Between 1 < k < 2.2, the Reynolds number appears less influential and a steady increase of the lift coefficient with spin ratio is shown at an increased rate compared to before the drop in the lift coefficient occurred. The change in gradient, dC_L/dk, was previously noted down by Kelly and Van Aken (1956) and Swanson (1961). The shallower slope at the larger Re_D = 250000 is also depicted in the data from Chen and Rheem (2019) and Bordogna et al. (2019a), whereas the slope and absolute differences in lift coefficient between Reynolds numbers at the same spin ratio is more similar to the three-dimensional and lower Reynolds number results from Badalamenti (2010) and Ma et al. (2022). Bordogna et al. (2019a) indicated the lift coefficient to be influenced by the Reynolds number up to k = 2.5, whereas in the current experiment and in the data from Chen and Rheem (2019) independency to the Reynolds numbers appears at much lower spin ratios with the curves being much closer together.

The knee in the lift coefficient curve is according to Swanson (1961) a result of the coming together of the separation points and the formation of closed streamlines around the cylinder. This has been covered in more detail in subsection 2.2.5. The knee occurs at k = 2.2 for the current results, which is substantially different compared to the results from Swanson (1961), k = 3, and in the averaged sectional lift coefficient data from Bordogna et al. (2019a), k = 2.5.

The three-dimensional studies from Badalamenti (2010) and Chen et al. (2023) do not show a knee in the lift coefficient curve, but rather plateauing at similar spin ratios. The point at which plateauing occurs, is dependent on the aspect ratio, see subsection 2.2.4, and is caused by the presence of tip vortices, subsection 2.2.12. In contrast, the quasi-two-dimensional data from Swanson (1961) and Bordogna et al. (2019a), and the three-dimensional results from Badalamenti (2010) and Chen et al. (2023) with the addition of endplates, shows a steady increase of the lift coefficient beyond this point, and is related to the growing of the circumvolving layer formed around the cylinder, see subsection 2.2.5. Interestingly to note is that the slope of the lift coefficient curve is now similar to what has been found before the drop in lift coefficient at low spin ratios.

The plateauing for the current results occurs at a much higher spin ratio of k = 5 for a value of C_L = 6.25, which is much lower compared to what has been found by Swanson (1961), C_L = 9, and Bordogna et al. (2019a), $C_L \approx 9$ at k = 5. It is unlikely to be the cause of the formation of tip vortices due to the small gap between model and wind tunnel walls suppressing the formation. Therefore, a possible explanation lies in the change of incoming flow direction due to the large blockage ratio, close proximity to the nozzle exit and large amount of lift interference at these spin ratios. As a consequence, the lift vector might get tilted and a reduction in the lift coefficient follows. Furthermore, within this range of spin ratios the circumvolving layer is formed and increases in size with spin ratio. The result is a change in cylinder shape and consequently a growth in blockage ratio. Therefore, it is expected that the lift coefficient is in reality still growing and behaving similarly as for Swanson (1961) and Bordogna et al. (2019a). The same effect can be seen in the drag coefficient and will be discussed in more detail in subsection 5.1.2.

5.1.2. Drag coefficient

The total drag coefficients, C_D, resulting from the increase of the spin ratio are deduced from the force measurements over the entire cylinder, at each of the Reynolds number tested, and are shown in Figure 5.3. In the same fashion as for the lift coefficient, the following ranges of spin ratio of distinct coefficient behaviour will be covered to aid in the discussion; 0 < k < 1, 1 < k < 2.4 and k > 2.4.

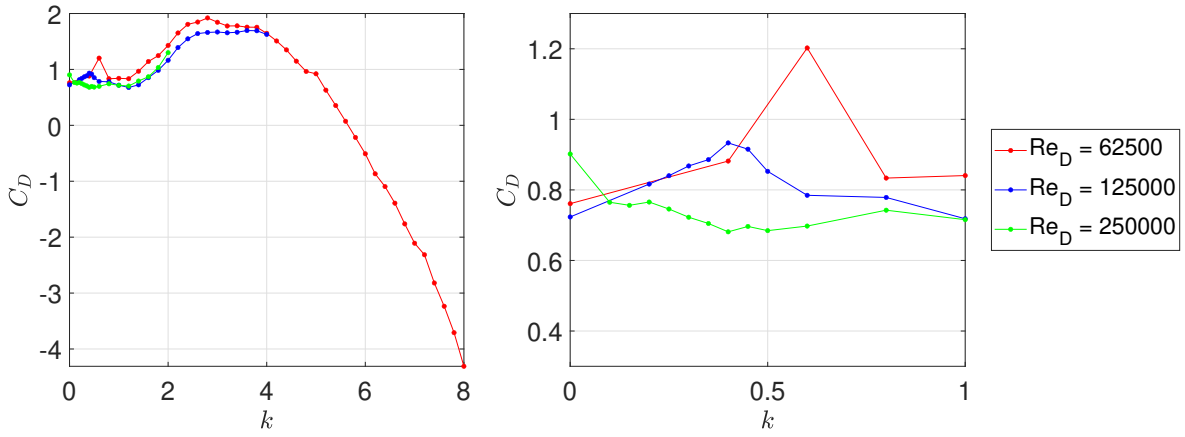

Figure 5.3: Total drag coefficient, C_D, versus spin ratio, k, for left; $0 \leq k \leq 8$, and right; $0 \leq k \leq 1$.

For the current experiment, noticeable differences are already observed at the stationary case, k = 0. Earlier it was shown in Figure 2.5 that, for a stationary cylinder in disturbance-free flow at subcritical Re_D, the drag coefficients are reported to be $C_D \approx 1.15$, whereas for the critical Reynolds a sharp drop means C_D values as low as 0.4 can be the result (Zdravkovich, 1997). While it is true in Figure 5.3 that a slight drop in drag coefficient occurs when increasing Re_D within the subcritical regime from 62500 to 125000 with C_D = 0.76 and 0.72 respectively, the magnitude of the drop and drag coefficient values are lower than anticipated. Nevertheless, the same low drag coefficient as the current experiment at similar Reynolds numbers are recorded in both the three-dimensional data from Badalamenti (2010) and Ma et al. (2022) as well as for the quasi-two-dimensional data from Bordogna et al. (2019a).

The opposite occurs when considering the largest Reynolds numbers tested, Re_D = 250000. The recorded value of the drag coefficient, C_D = 0.9, is now similar to the expected quasi-two-dimensional values presented by Swanson (1961) and Zdravkovich (1997), but surprisingly larger than the recorded values for the subcritical Re_D = 62500 and 125000. Furthermore, in contrast both the quasi-two-dimensional results from Bordogna et al. (2019a) and three-dimensional results from Chen and Rheem (2019) already showed the drag reduction properties of the TrBL2 regime at this Reynolds number, and hence much lower drag coefficients, $C_D \approx 0.4$.

Badalamenti and Prince (2008a) indicated that the drag coefficient is more sensitive to the experimental setup, whereas Bordogna et al. (2019a) further noted that any changes to the pressure distribution of the cylinder has a greater effect on the drag coefficient compared to the lift coefficient. A small change in flow direction or movement of the suction peak leads to a greater response in the drag coefficient and as such a larger scatter of the results in the experimental data is found. Therefore, as the current experiment is dealing with a far less common large blockage ratio and open-return tunnel configuration, discrepancies are expected to be most notable in the drag coefficient.

Wickern and Schwartekopp (2004), Wickern (2014) and Collin (2019) described the effects of open test section wind tunnel interference effects, which become more potent with an increase of the blockage ratio. In particular, the balance between an increase in the drag coefficient due to nozzle blockage and nozzle gradient effects, and drag reducing effects of the jet expansion due to solid model blockage, are expected to play an important role in the determination of the measured forces for the current experiment. It can be speculated that the increase of the drag coefficient at the largest Reynolds number is the result of an increased pressure built up in front of the model, and as such extending into the nozzle further. For the lowest Reynolds number, the nozzle blockage and gradient effects, if present, might be less pronounced and as such the lower than expected drag coefficient is mainly the result of the jet expansion. The smaller than anticipated drop in drag coefficient between Re_D = 62500 and 125000 can then be explained by the growing, but yet not overly present, effects of the nozzle interference effects.

Another influencing effect might come from the open test section configuration with finite side walls of the current experiment. The data of stationary three-dimensional cylinders with two free ends from Zdravkovich et al. (1989) was similarly used by Badalamenti (2010) to explain the differences in C_D at k = 0. From Zdravkovich et al. (1989) it was shown that for a moderately low and similar aspect ratio to the current experiment, A = 5, at subcritical Re_D between 13300 and 88000 and k = 0, C_D values were in the range of 0.75 to 0.82. The three-dimensional data from Badalamenti (2010) also recorded these lower values, compared to the results for the two-dimensional case. As has been explained in subsection 2.2.12, it was mentioned that the inflow from the sides causes a reduction of the pressure differential over the cylinder and has a reducing effect on the drag coefficient that becomes greater at lower aspect ratios. It was also shown that the addition of endplates of increasing size brings the C_D values closer to the two-dimensional case, but still only up to a value of approximately 0.9. However, as the current experiment considers much larger side walls, in comparison to the endplates used by Badalamenti (2010), and the wind tunnel boundary layer is present in this region, it is most likely only a minor influence to the results. Perhaps in this case due to the presence of the tunnel boundary layer on the sides, a similar vortex system is developed as for the rotating cylinder in the presence of the Earths boundary layer as has been shown by Massaro et al. (2024), which then could provide the drag coefficient reducing pressure equalisation on the sides.

Additionally, the non-zero lift coefficient at Re_D = 250000 must be noted as the drag coefficient might as well be influenced by some other effect. However, continuing to speculate further, the increased dynamic pressure at the model, due to larger nozzle blockage and gradient effects, increases locally the Reynolds number and as such the one-bubble TrBL1, Re_D > 300000, could potentially be initiated. This would explain the non-zero lift coefficient, whereas the increased drag is mainly due to the interference effects. This would also explain the closer resemblance of the lift coefficient curve to the results of Swanson (1961) at higher Re_D. But, by investigation of the flow field, no sign of boundary layer transition is visible and hence the negative lift is unlikely to be the cause of the aforementioned wind tunnel interference effects. In subsection 5.2.1 this will be covered further.

As mentioned earlier in subsection 2.2.5, the flow field around a rotating cylinder at k < 1 behaves similarly as for the stationary case. Therefore, aerodynamic features of the Reynolds regimes for a stationary cylinder, as has been outlined in subsection 2.1.1, will be present and the regime will change depending on the relative Reynolds number induced by the rotation. For the two subcritical Re_D = 62500 and 125000 between 0 < k < 1, a peak in the drag coefficient is recorded. This peak occurs at lower spin ratios and to a lesser extend with an increase of the Reynolds number. This initial rise in the drag coefficient is expected to be partially the result of the TrSL3 regime. Transition eddies form along the shear layers, which induce a low pressure zone on the backside of the cylinder as they move

closer with an increase of Reynolds number. After the peak, the transition in boundary layer regime is initiated and the eddies move further away again, which in combination with the delayed boundary layer separation, reduces the drag coefficient. At the higher Re_D = 250000, the TrSL3 is potentially already reached at k = 0, and hence starts from this elevated value.

Comparing the results for the range 0 < k < 1 with Figure 2.34 (Swanson, 1961), the magnitudes are noticeably different, yet the trends of the drag coefficient show good similarity for all tested Reynolds numbers and an even better match to the three-dimensional results from Badalamenti (2010) with stationary endplates at slightly lower subcritical Reynolds numbers. However, as the data from Badalamenti (2010), Chen and Rheem (2019) and Bordogna et al. (2019a) is limited in the range of 0 < k < 1 and the drag peak appears to be confined to a small range of spin ratios, it is unclear if the magnitude of the drag peak, if present at all, extents to similar values as for the current results. The results from Swanson (1961) does indicate a small rise of drag coefficient for the subcritical Reynolds numbers, but at much lower spin ratios k < 0.2, whereas Ma et al. (2022) does not show such a peak and resembles closer to Badalamenti (2010). The large rise in drag might be the result of current high blockage ratio as well as the features of the TrSL3 regime.

Within 1 < k < 2.4, as for the lift coefficient, the drag coefficient between the Reynolds numbers starts to behave similarly. The drag coefficient rises more quickly with each increase of the spin ratio and this effect appears to be more prominent at larger Reynolds numbers. The trends in literature mostly agree with these observations, however some variations are recorded. For instance, the two-dimensional results from Swanson (1961) show that all drag coefficient curves coincide at a spin ratio of k = 1.2, after which, unlike for the current data, the drag coefficient becomes invariant of the Reynolds number. While the three-dimensional data from Badalamenti (2010) comes close to the two-dimensional results, higher subcritical Reynolds numbers show a slight reduction of the drag coefficient within this range of spin ratios and Reynolds number. The reduction in the current data set is much larger between Re_D = 62500 and 125000. The larger drag coefficients at Re_D = 62500 are unexpected and might be a consequence of wind tunnel interference effects. The data at higher Reynolds numbers from Bordogna et al. (2019a) shows an increasing rate of the drag coefficient with spin ratio for larger Reynolds number. The same trend is visible in the current data set, although at a lesser degree.

Shortly after the knee in the lift coefficient curve, the drag coefficient reaches a plateau at slightly higher $k \approx 2.4$. In subsection 2.2.5 it was explained with increasing spin ratio that first due to prolonged attachment of the boundary layer on the rear side of the cylinder the drag coefficient increases, after which it eventually decreases again and converges to a set value due to movement of the near-wake to the front of the cylinder (Swanson, 1961). As a result of these effects, a peak in the drag coefficient curve for two-dimensional rotating cylinders occur at larger $k \approx 4$. Three-dimensional results, e.g. Badalamenti (2010) with stationary endplates, often see flattening of the curve at much lower k and drag coefficients remain to increase beyond k = 4 without dropping to a lower value. The development of tip vortices, the aspect ratio and treatment of the end conditions play an important role in the differences between the two-dimensional and three-dimensional curves.

The earlier flattening and eventual decrease in drag coefficient of the current results is likely to be the consequence of the additional wind tunnel interference effects. It is speculated, that the large lift production at the higher spin ratios is modifying the conditions at the outlet considerably and has been briefly addressed in the previous section. At k = 3.8, the gradient of the lift coefficient curve starts to decline, whereas at the same spin ratio the drag coefficient starts to decrease at an increasing rate. The decrease in the drag coefficient does not stop and even becomes negative for k > 5.6 and eventually reaches a C_D = -4.3 at k = 8. Thom (1934) tested a rotating cylinder with spanwise discs in a closed test section. This type of arrangement showed to produce large lift coefficients and interestingly negative drag values at similar spin ratios of the current experiment. Perhaps the interference effects played an important role as he mentioned himself, however it was also mentioned the results were only measured once and after a new balance was installed. Nevertheless, with the drag coefficient reaching such low values and the lift coefficient no longer rising against expectation, a change in the inflow conditions and a tilt of the force system is likely to be the cause of such behaviour. In subsection 5.2.4 and subsection 5.2.5 more details will be given on this particular behaviour of the force coefficients.

5.1.3. Resultant force coefficient magnitude and direction

The resultant force coefficients, C_R, deduced from combination of the lift and drag coefficient, is illustrated in Figure 5.4, whereas its direction, θ, it makes with the horizontal as outlined by Figure 5.1, are depicted in Figure 5.5. For 0 < k < 1, the step-like behaviour follows from moving through the various Reynolds regimes encountered by increase of the spin ratio as has been previously explained. At Re_D = 62500 and 125000, the lift coefficient is small relative to the drag coefficient at low spin ratios such that the resultant force coefficient follows closely the curve of the drag coefficient. This is further indicated by the fact that the angle stays close to the horizontal axis at 0 degrees, where deflection in positive direction is due to the growth in the lift coefficient as a consequence of the Magnus effect. For Re_D = 250000 this does not hold for k < 0.5 due to the stronger effects of the TrBL1 and TrBL2 regimes at this Reynolds number, e.g a possibly stronger laminar separation bubble. Only within 0 < k < 1 shows the resultant force coefficient to experience a drop in its magnitude, which follows from both the drop in positive lift and drag. At Re_D = 250000, the angle becomes briefly negative, with its maximum reaching θ = -46.6°, clearly indicating the inverse Magnus regime. The three-dimensional data from Chen et al. (2023) at Re_D = 250000, A = 5 and no endplate, does not show k < 0.5, but at k = 0.5 a drop in the resultant force coefficient was also shown.

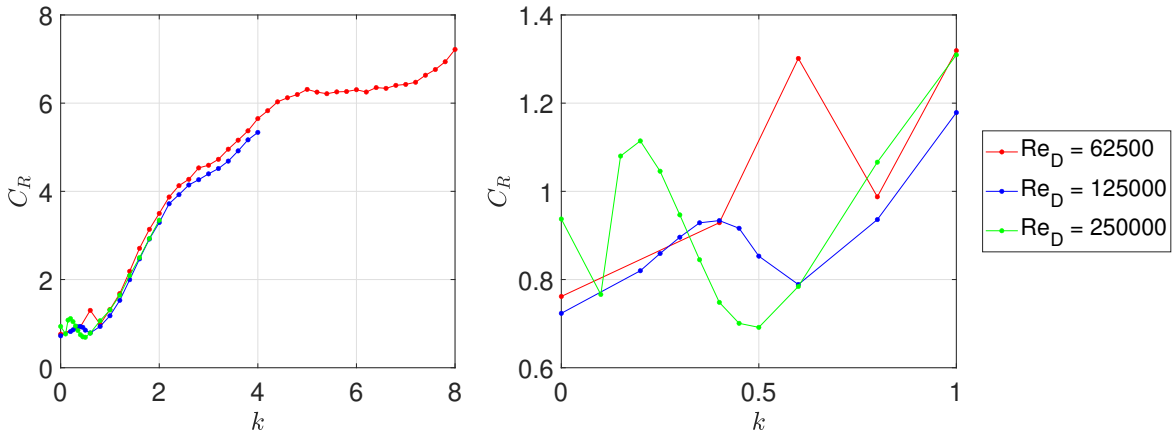

Figure 5.4: Resultant force coefficient, C_R, versus spin ratio, k for left; $0 \leq k \leq 8$, and right; $0 \leq k \leq 1$.

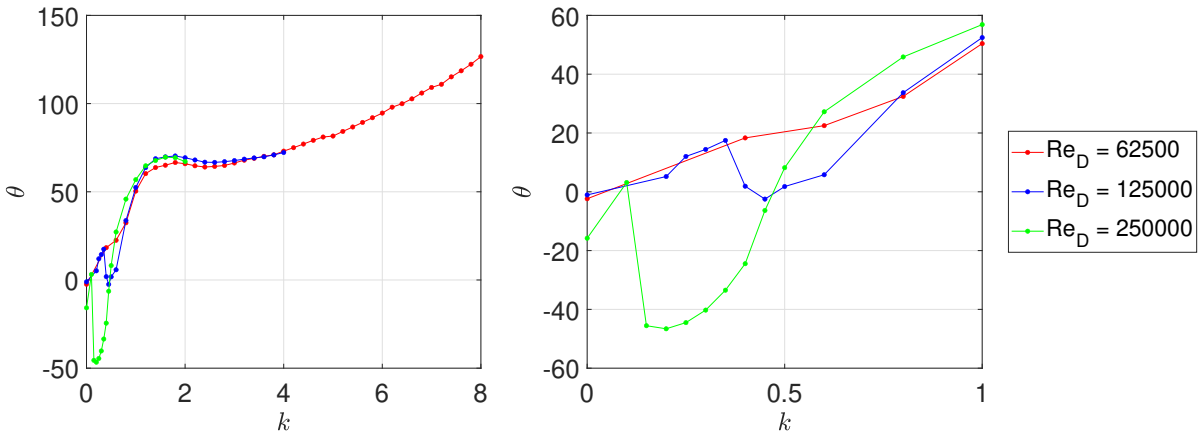

Figure 5.5: Direction, θ, of the resultant force versus spin ratio, k, w.r.t. x-axis, U_∞ for left; $0 \leq k \leq 8$, and right; $0 \leq k \leq 1$.

Between 1 < k < 2.4 owing to the regular Magnus effect, an increase of the spin ratio causes a rapid rise in the resultant force coefficient magnitude. With the rapid rise of the lift coefficient, the resultant force coefficient starts to follow the trend of the lift coefficient at higher spin ratios. For k > 2.4 following the knee in the lift and drag coefficient curves, the resultant force coefficient increases at a reduced rate. The knee is not visible in the data from Chen et al. (2023), which instead plateaus at a value of k = 3 as it has likely been a result of three-dimensional effects, e.g. tip vortex formation of increased strength.

The angle rapidly rises to an angular position of approximately 67° at k = 1.2, peaks at k = 1.6 - 1.8 to a value of θ = 69° and slowly decreases up to k = 2.8, before starting to rise again. The general trend and values up to k = 2.8 are similar to the data from Chen et al. (2023), however the current data does not show settling at a specific position. The angle for k > 2.8 starts to increase and does not show any convergence to a set value for the current range of spin ratios. Furthermore, as the angle is closely related to the lift-to-drag ratio of the rotating cylinder, a first maximum is found at the same k = 1.6 - 1.8, see Figure 5.6, but then keeps on rising for k > 2.8. The first maximum agrees well with Chen et al. (2023), especially for Re_D = 250000 at similar aspect ratio and without endplate. However, in contrast to Chen et al. (2023), lower Reynolds numbers show its maximum to occur at higher spin ratios.

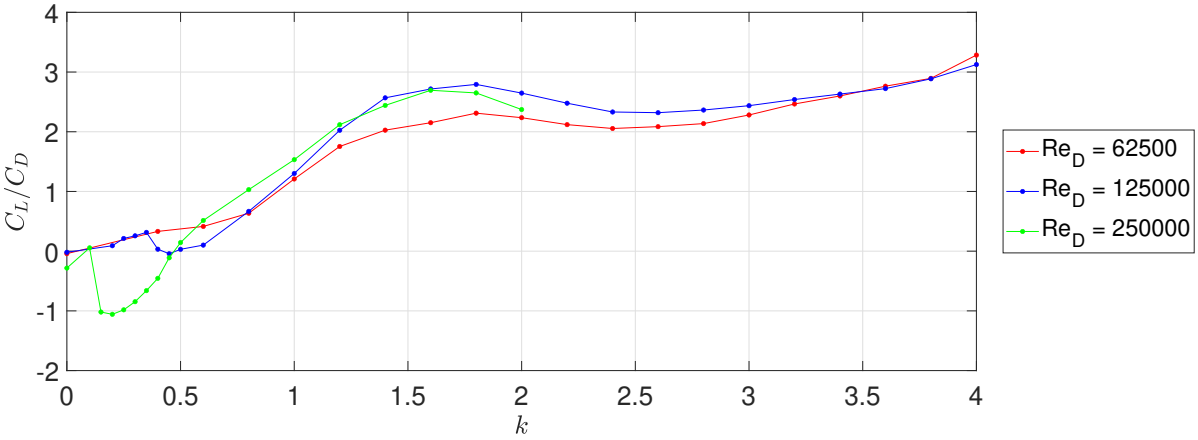

Figure 5.6: Lift-to-drag ratio, C_L/C_D, versus spin ratio, k.

In the range 4.8 < k < 6.8, following the plateauing of the lift coefficient and the relative small values of the drag coefficient, the resultant force coefficient remains constant at a value of $C_R \approx 6.3$. This appears to be similar to the plateau found by Chen et al. (2023) of $C_R \approx 6.5$, however it was obtained at a significantly lower spin ratio, k = 3, which would imply it to be more of a coincidence and rather the result of three-dimensional nature.

The three-dimensional results from Badalamenti (2010), Chen and Rheem (2019) and Chen et al. (2023) all show plateauing of the lift coefficient at this range of spin ratios, with the drag coefficient rising slightly with an increase of spin ratio. The quasi-two-dimensional data from Bordogna et al. (2019a) shows that the drag coefficient slowly flattens between 3 < k < 5, whereas the lift coefficient remains to rise. This follows the general trend of the two-dimensional result from Swanson (1961), where the drag coefficient reaches a peak at approximately k = 4.2 and the lift coefficient increases steadily.

In the data from Swanson (1961) $dC_D/dk \approx$ -0.3 and $dC_L/dk \approx 0.47$ between 4.2 < k < 6.8. The current results shows a plateau, with $dC_L/dk \approx 0$ and $dC_D/dk \approx$ -1.5. As the drag coefficient switches sign over this range of spin ratios, the resultant force coefficient remains close to a constant, since it mainly depends on the relative larger lift coefficient. With the drag coefficient rapidly decreasing, its influence becomes more visible in the resultant and from k > 6.8, C_R starts to grow again. At k = 6.8, dC_D/dk increases to approximately -2.5, dC_L/k decreases to approximately -0.3 and $d\theta/dk \approx 15°$. Interestingly at the same k = 6.8 in the data from Swanson (1961), the magnitude of dC_D/dk begins to decrease and slowly starts to flatten, a consequence of the near-wake slowly settling at a fixed position. The same mechanism might be the cause of changes in the slopes of the current results. However, the vastly different coefficient behaviour is most likely the result of the interference effects and tilting of the force system. For instance, how the flow reacts between model and nozzle geometries, as well as on how the near-wake interacts within this region at high spin ratios, e.g. with a the potential of blocking off one side, is yet to be explained. The flow visualisations presented throughout section 5.2 are aimed to provide further insights on this matter.

5.1.4. Force fluctuations

It has been shown in subsection 2.2.5 and subsection 2.2.6, that the aerodynamics of a rotating cylinder can be of unsteady nature, e.g. due to the presence of vortex shedding and wake fluctuations. As such the instantaneous force measurements can vary considerably in the presence of such phenomena. In case of experimental investigations, further sources of variations in the force measurements can be the result of the experimental setup, e.g. vibrations, resonance and residual unbalance of the system.

The fluctuations in the force coefficients from the determined mean with the increase of the spin ratio is depicted as the standard deviation and shown in Figure 5.7. From the figure, it becomes immediately apparent that variations grow rapidly with the spin ratio and to large magnitudes. The fluctuations are of an order greater than the resultant force coefficient acting on the cylinder at high spin ratio. Swanson (1961) and Badalamenti (2010) reported that in case of the lift force the fluctuations can be of the same order of its mean value, while for the drag force such variations are smaller. At $k < 4$ this seems to be similarly the case for the current data, however in contrast, both the lift and drag coefficient recorded similar levels of fluctuation. Furthermore, various spikes are present that do not seem to present a common pattern with the spin ratio and fluctuations remain large even beyond $k > 2$, for which a steady regime should be obtained and fluctuations should reduce to values close to zero, see subsection 2.2.5.

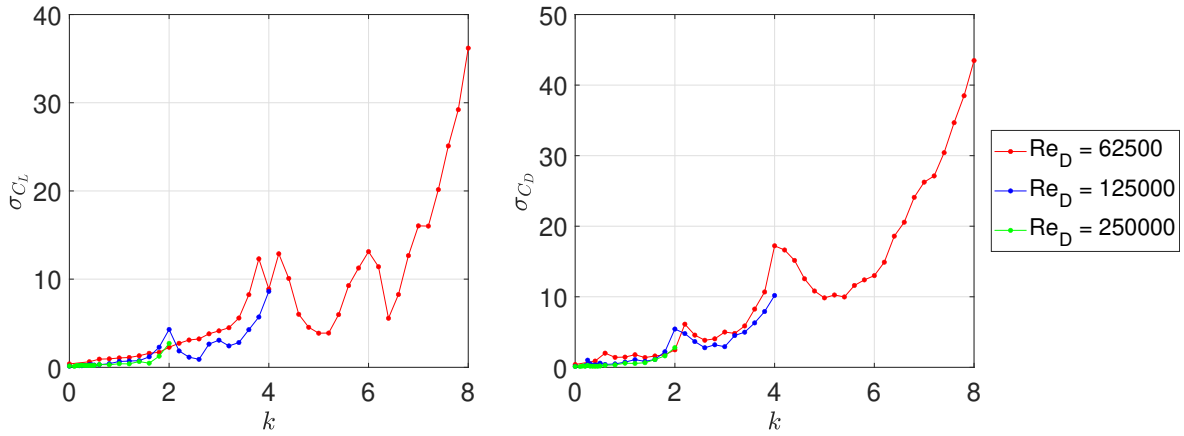

Figure 5.7: Force coefficient fluctuations indicated by the standard deviation, σ_{C_L} and σ_{C_D}, versus spin ratio, k.

Following the concerns of residual unbalances in the system section 3.11, and force sensor uncertainty at the lower Reynolds numbers tested section 4.2, the presented fluctuating force coefficient behaviour is likely not of aerodynamic nature (unless the large blockage ratio causes another phenomenon to occur), but rather an artifact of the experimental setup. This becomes more visible when looking at the force coefficients and force measurements in relation to the rotational frequency, Figure 5.8 and Figure 5.9 respectively.

Figure 5.8 and Figure 5.9 show similar trends between the different Reynolds numbers tested and in contrast to Figure 5.7 the peaks correspond, although less visible at Re_D = 250000, to the same specific rotational frequencies. During the experiment resonance of the experimental setup was observed at these rotational frequencies, especially at $\omega_f \approx 32$ and 48 Hz, and hence explains the various peaks in the figures.

From Figure 5.9 it is seen that the fluctuations are close in magnitude between the different Reynolds numbers. This can be explained by the residual unbalance of the rotating model, as this will not change with a difference in the Reynolds number. The centrifugal force as a result of the residual unbalance will be shown in the fluctuations and grows exponentially with an increase of the rotational frequency. The rapid growth above $\omega_f \approx 50$ hz is then explained by the last balancing attempt which had been performed at only ω_f = 36 hz, see section 3.11. However, a possible aerodynamic cause of the rapid rise in fluctuations following from the large blockage ratio and nozzle proximity is not excluded and will be further covered in subsection 5.2.5.

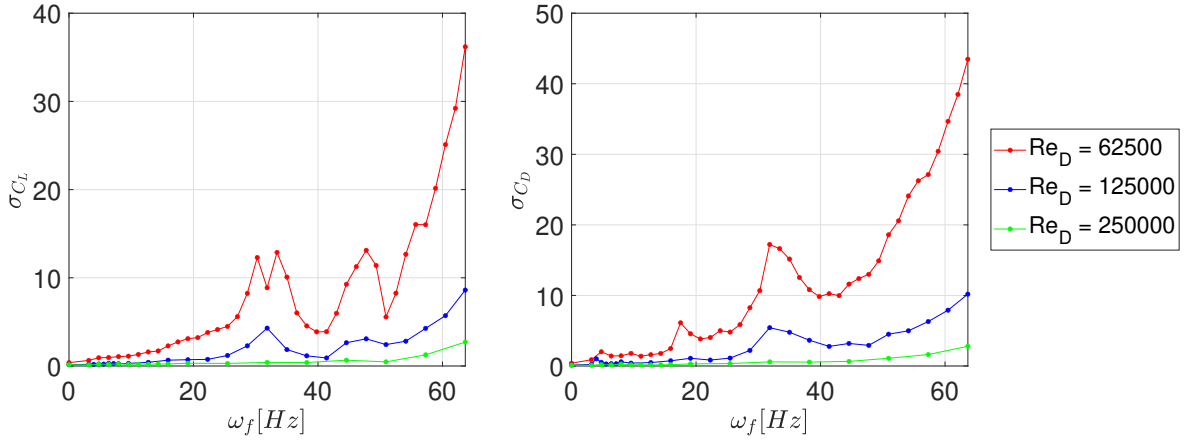

Figure 5.8: Force coefficient fluctuations indicated by the standard deviation, σ_{C_L} and σ_{C_D}, versus rotational frequency, ω_f.

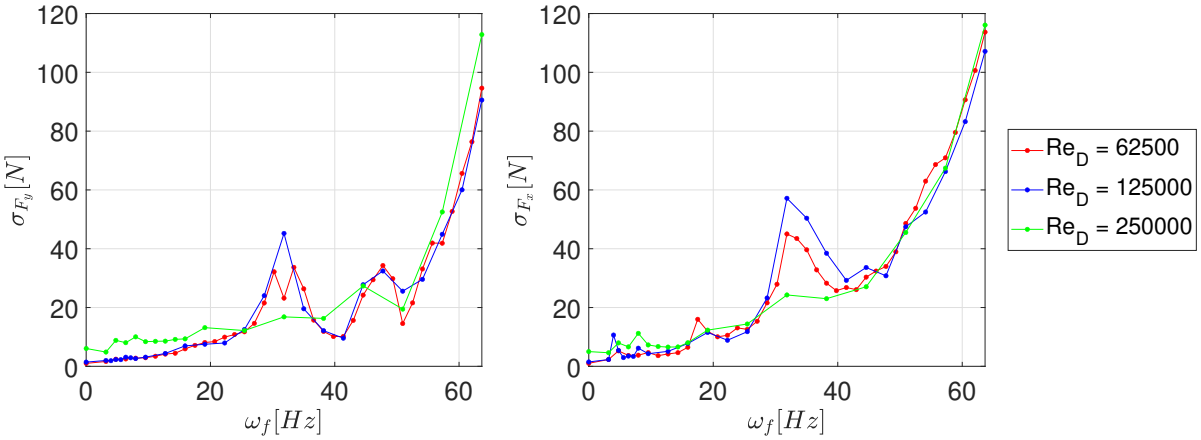

Figure 5.9: Force fluctuations indicated by the standard deviation, σ_{F_x} and σ_{F_y}, versus rotational frequency, ω_f.

With the force fluctuations being similar in magnitude for the different Reynolds numbers, a relatively larger influence and thus larger fluctuations in the force coefficients is shown, Figure 5.8. This is similarly as for the force sensor uncertainty explained earlier in subsection 4.2.2. Additionally, as the standard deviation grows, the standard measurement uncertainty, see subsection 4.2.2, grows with it and becomes thus more pronounced at the larger spin ratios.

5.2. Flow field characteristics

In an attempt to discover the underlying physics of the force coefficients behaviors, this section, following the methodology described in subsection 4.1.2, presents and analyses the results of the PIV measurements at the given Reynolds numbers. First, in subsection 5.2.1 the stationary case will be covered with a particular focus on the lifting force measured for Re_D = 250000. Next, in subsection 5.2.2 the regime for k < 1.0, with a strong dependency on the Reynolds number that has been linked to the transition between various Reynolds regimes, is discussed. Then in subsection 5.2.3, the regular Magnus effect regime with a reduced influence of the Reynolds number between $0.8 \leq k \leq 2.2$ is covered. The regime of the knee in the coefficient curves at spin ratios $2.2 \leq k \leq 2.6$ is investigated in subsection 5.2.4 and the analysis is concluded in subsection 5.2.5 showing the phenomena at spin ratios in excess of k > 3.0.

5.2.1. Stationary cylinder case

The force measurements results, outlined in subsection 5.1.1 and subsection 5.1.2, revealed inconsistencies with the available data found in literature. At k = 0, the magnitudes of the drag coefficient are lower than anticipated, but as there is a large scatter in drag coefficient data across different experi-

ments, the lower values are probably a result of the specific peculiarities of this experimental setup. The most notable inconsistency however are the recorded values at Re_D = 250000. For one, the mean lift coefficient indicates the presence of a negative lift force (in positive y-direction). Normally, this should only occur for a cylinder in disturbance-free flow, due to the formation of a single laminar separation bubble within the TrBL one-bubble regime, 300000 < Re_D < 400000. Secondly, drag coefficient values should drop with an increase of the Re_D within the subcritical and lower critical regimes, especially when entering the aforementioned one-bubble or two-bubble regimes by delayed turbulent boundary layer separation. In case of the current experiment the opposite is true, where the drag coefficient is larger at Re_D = 250000 compared to Re_D = 62500 and 125000.

Figure 5.10 shows the non-dimensionalised mean velocity components $\bar{u}/U_\infty$ and $\bar{v}/U_\infty$ and velocity magnitude $\bar{U}/U_\infty$ for Re_D = 62500, 125000 and 250000 at k = 0. As expected a thick bluff body wake is visible for all three Reynolds numbers reminiscent of laminar boundary layer separation. The separation points of the upper boundary layer are at an angular position of approximately 261°, 262° and 267° for Re_D = 62500, 125000 and 250000 respectively, which compares well with the values noted in Figure 2.3 of laminar boundary layer separation. Thus, it is unlikely that the lift force at Re_D = 250000 is the result of the TrBL one-bubble regime, since in case of a turbulent boundary layer, separation occurs much later between approximately 300° - 340° at given Re_D.

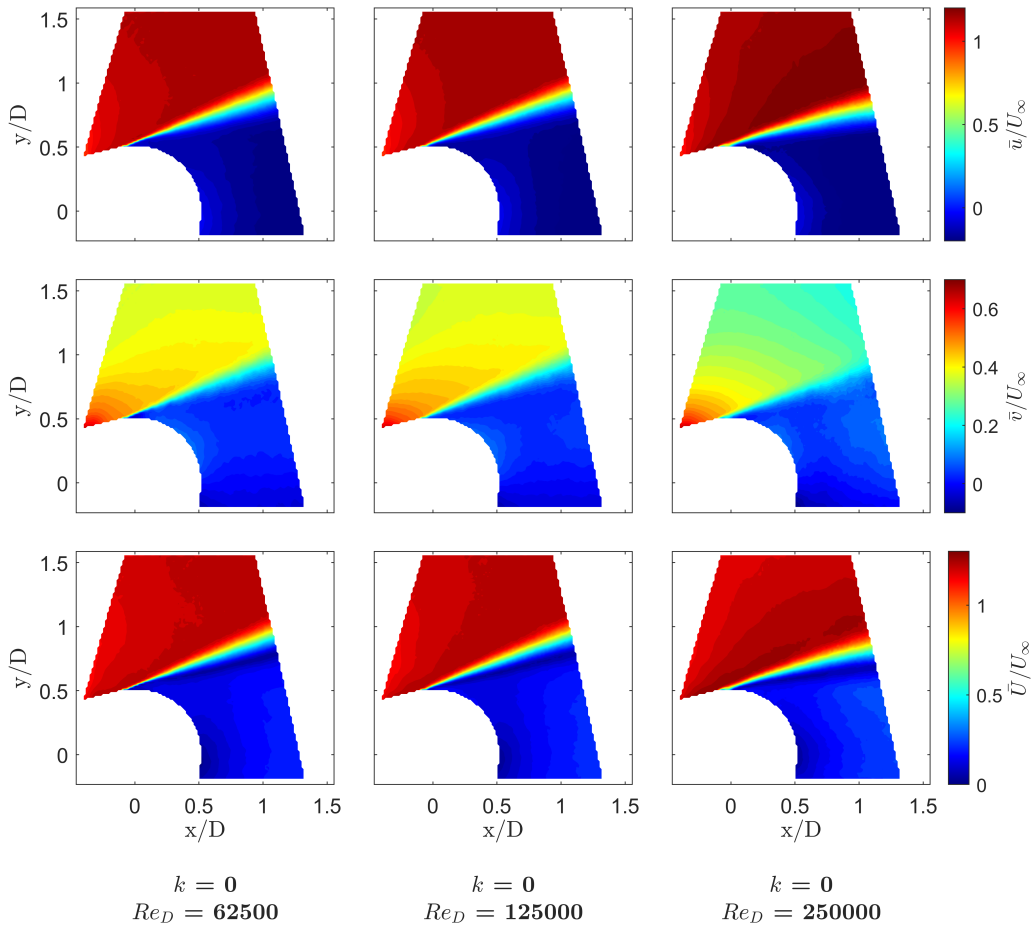

Figure 5.10: Non-dimensionalised mean velocity components $\bar{u}/U_\infty$ and $\bar{v}/U_\infty$ and velocity magnitude $\bar{U}/U_\infty$ for Re_D = 62500, 125000 and 250000 at k = 0.

Instead, all velocity fields between the different numbers do not differ substantially, however some variation is observed. At Re_D = 250000, the shear layer of the velocity magnitude is curving downwards and a potential decrease in size of the near-wake is realised. The lesser growth of the near-wake is clearly visible from the reduction in the vertical velocity component in comparison to the lower Reynolds numbers tested. A possible explanation can be found in the characteristics of the TrSL3 regime, namely

an increase in Reynolds number results in transition eddies within the shear layer being formed closer to backside of the cylinder in combination with the narrowing of the near-wake, see section 2.1.

Proper Orthogonal Decomposition, POD, analysis is utilised in order to identify dominant structures in the flow and in particular to show if variations in the formation of such transitional eddies are present between the different Reynolds numbers. Figure 5.11 shows the energy contents of the 20 most energetic modes. For Re_D = 250000, a different distribution of energies is shown with distinct mode pairs appearing as dominant features of the flow, e.g. ϕ^3 and ϕ^4. These mode pairs are typically associated with convective phenomena, like vortex shedding, and will thus be further investigated.

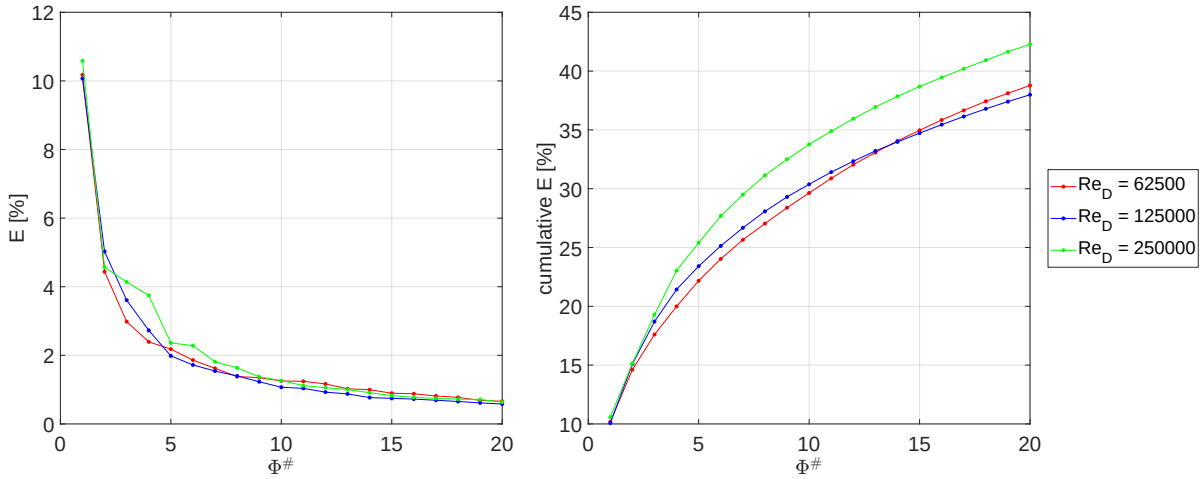

Figure 5.11: Energy distribution of the 20 most energetic spatial POD modes ϕ^n for Re_D = 62500, 125000 and 250000 at k = 0.

For the identification of vortices in the shear layer of an incompressible fluid, the Q-criterion is widely utilised (Hunt et al., 1988; Kolář, 2007; Y. Zhang et al., 2018). The Q-criterion states that vortices are identified as regions where the second invariant of the velocity gradient tensor is positive. This means that within these regions the magnitude of the vorticity is dominant compared to the magnitude of the strain-rate. Direction of rotation of the individual vortices is determined by first calculating the vorticity, ω_z, after which its sign is applied to the regions of $Q_{crit} > 0$, (Michelis, 2017). The expression of Q-criterion used in this report reads;

$$Q_{crit} = -\frac{1}{2}\left((\frac{\partial u}{\partial x})^2 + 2\frac{\partial u}{\partial y}\frac{\partial v}{\partial x} + (\frac{\partial v}{\partial y})^2\right), \tag{5.1}$$

$$Q_\omega = (Q_{crit} > 0)\frac{\omega_z}{|\omega_z|}, \tag{5.2}$$

where $Q_\omega > 0$ indicates counterclockwise rotation and $Q_\omega < 0$ clockwise rotation. The values of Q_ω are then non-dimensionalised with the cylinder diameter and freestream velocity.

The higher order spatial POD modes are mostly related to random fluctuations of small scale turbulence and PIV noise as well as harmonics of the low order modes. By selecting the six most energetic POD modes, a reconstructed velocity field is created such that the dominant features of the flow are more easily identifiable. Figure 5.12 shows a sequence of instantaneous Q_ω at $\Delta t = 6.67 \times 10^{-2} s$ with number of isosurfaces equal to 20. As predicted from the characteristics of the TrSL3 regime, regions of clockwise Q_ω appear to be more coherent, of larger size, and develop earlier at Re_D = 250000. However, it must be noted that the shown data is not time-resolved and thus not deterministic, as such the sequence shown are random instances of time and therefore only show the existence of structures but not their individual development. Additionally, as the far wake and the lower side of the cylinder are not captured in the FOV, it is uncertain if the vortices are of Von Karman type, typical for a stationary cylinder at given Reynolds numbers, or if they are solely associated with the transition of the shear layer from laminar to turbulent.

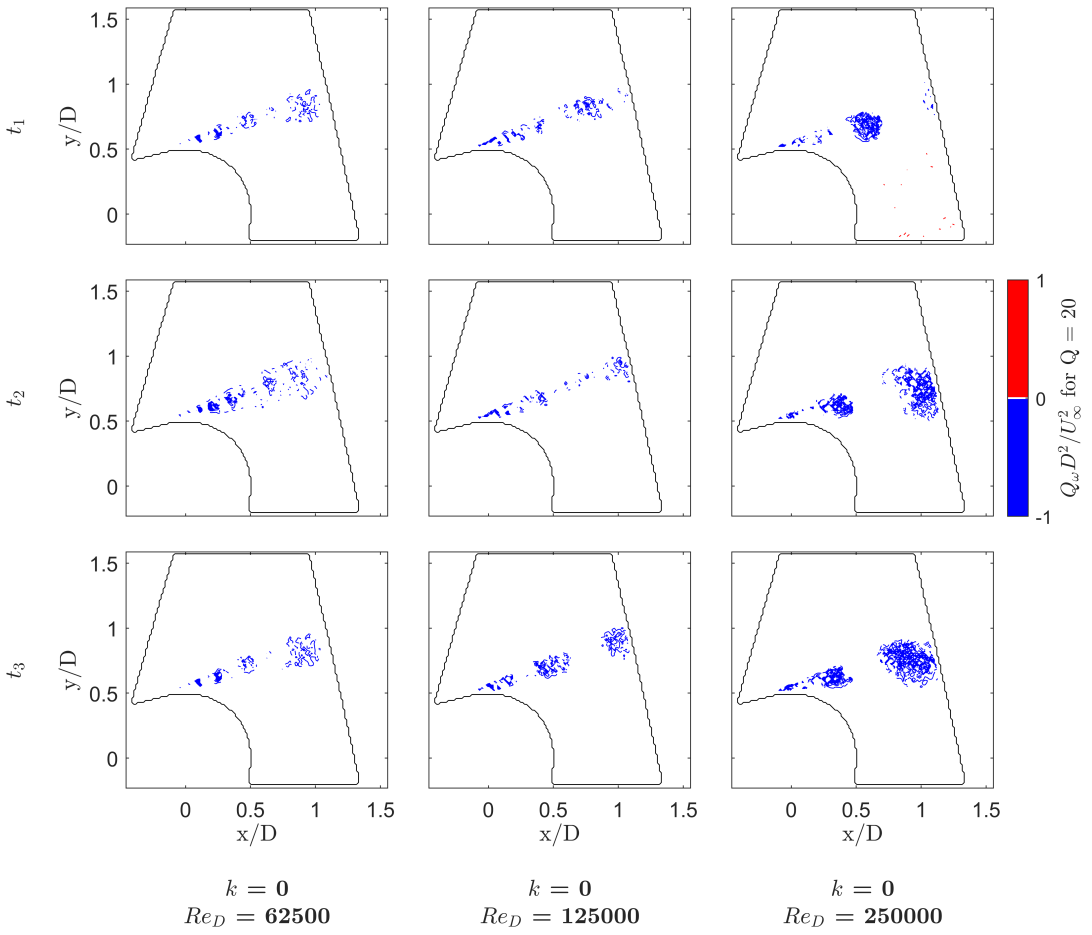

Figure 5.12: Sequence of instantaneous Q_ω at $\Delta t = 6.67 \times 10^{-2} s$ of the reconstructed flow field using the six most energetic POD modes at Re_D = 62500, 125000 and 250000.

As slight differences in vortex shedding behaviour are observed that correspond well with the TrSL3 regime, it can not provide an explanation for the relatively large mean lift coefficient, C_L = -0.26. A closer inspection of the near-wake behind the cylinder does show a slight downwards deflection at Re_D = 250000 on the rear part of the wake, whereas the rear stagnation point moves counterclockwise, see Figure 5.13. The upwards shift of the rear stagnation point, which in combination with the more aft upper separation point, indicates the wake could have shrunk in size at Re_D = 250000 and thus has been rotated in counterclockwise direction. As such the overall size of the wake has most likely reduced, which is in agreement to the characteristics of the upper TrSL3 regime. If true, the rise in drag coefficient at Re_D = 250000 is then possibly the result of the increased pressure built up in front of the cylinder at the highest Re_D, which then extends into the nozzle further and causing larger wind tunnel interference effects. It must also be noted that the rear stagnation point for Re_D = 62500 and Re_D = 125000 do not lie exactly on y = 0, eventhough zeroing had been performed with no-wind conditions, and checked after turning the tunnel on that no lift forces for these cases were recorded.

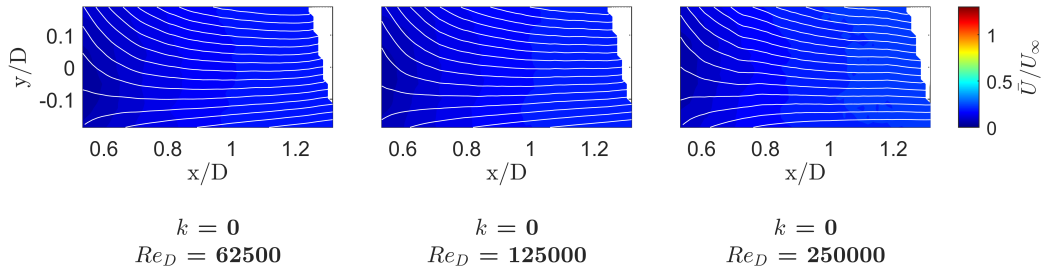

Figure 5.13: Streamlines representation in the near-wake for Re_D = 62500, 125000 and 250000 at k = 0.

Speculating further, a potential cause of the negative lift coefficient and tilt of the system might be related to an unfavorable interaction of the tunnel shear layer and the support structure. In particular the center spanwise beam shown in Figure 3.11b, could be interacting differently at the larger Re_D, due to altered outflow conditions and or the largely increased momentum in the tunnel jet. As such, the support beam is potentially either impinged by the tunnel shear layer or fully submerged in the jet. The resulting support beam wake then deflects the tunnel jet such that the cylinder wake and stagnation points move counterclockwise on its surface, as shown in Figure 5.14.

Another possible theory could be found in the effects of wind tunnel interference, where due to the increased pressure built up in front of the cylinder at the largest Re_D, the tunnel conditions at the outlet potentially settles asymmetrically either naturally or due to the support beam interference. As such the force vector tilts, and therefore the drag force points slightly in the direction of the lift, which would result in a similar situation as depicted in Figure 5.14.

In both cases, or a combination of, it is expected that the wake deflects upwards, the drag coefficient reduces as lift becomes non zero and the flow field surrounding the cylinder remains symmetric. Neither of these conditions can be confirmed. However, this can still be true if the drag is larger as a consequence of the increased nozzle blockage and interference effects. Unfortunately, none of this can be confirmed as the lower side is missing from the FOV. Thus, the force measurement results at k = 0 remain uncertain, but the PIV measurements do not present major divergence from the expectations of a stationary cylinder flow field at given Re_D.

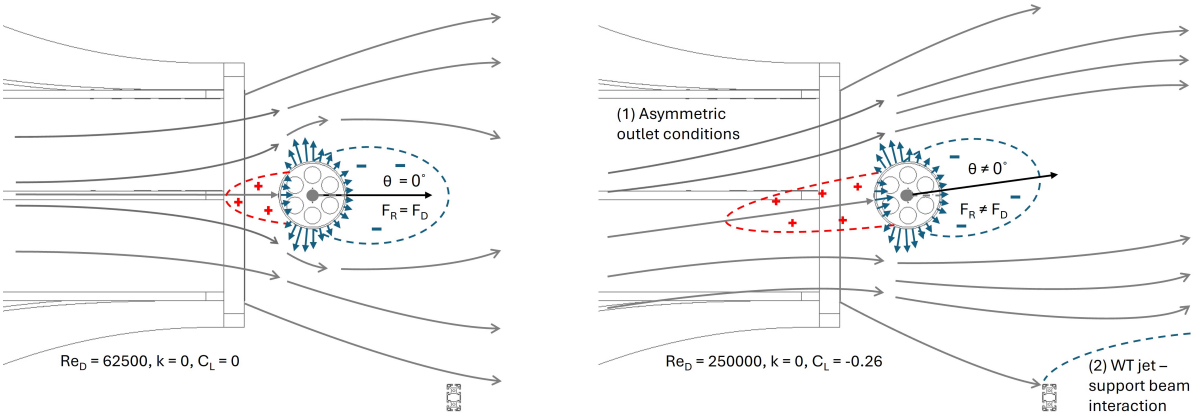

Figure 5.14: Speculative schematic of asymmetric pressure built and support structure interference at Re_D = 250000, resulting in an larger drag coefficient and negative lift coefficient. Note for the purpose of explaining, effects are exaggerated.

5.2.2. Regime of Reynolds number dependency

The results of the force measurements for k < 1, indicates large differences between each of the Reynolds numbers tested, which has been linked with the transition between the various Reynolds regimes (Badalamenti, 2010; Ma et al., 2022; Swanson, 1961). The flow field of a rotating cylinder at low spin ratios is expected to behave similar to the stationary case, see subsection 2.2.5, where based on the concept of a relative Reynolds number, the local Reynolds number changes with an increase of the spin ratio. In the current FOV, the advancing side (acting against the freestream) is visible, and thus experiences a larger relative Reynolds number when rotation is added. As such, flow phenomena associated with transition are expected to be captured and will be analysed in the coming sections.

Starting with Re_D = 62500, Figure 5.15 depicts sequences of non-dimensionalised mean velocity magnitude, $\bar{U}/U_\infty$, and mean turbulent kinetic energy, TKE_U/U_∞^2, with increasing spin ratio in the range of $0 < k < 1$. The mean turbulent kinetic energy, TKE, is an important quantity for measuring turbulence intensity, and is defined as the kinetic energy per unit mass of the turbulent velocity fluctuations,(Stull, 1988). TKE can be calculated as follows;

$$TKE_U = \frac{1}{2}\overline{u_i' u_i'} = \frac{1}{2}(\sigma_u^2 + \sigma_v^2), \tag{5.3}$$

where σ_u^2 and σ_v^2 are the variances of the velocity components.

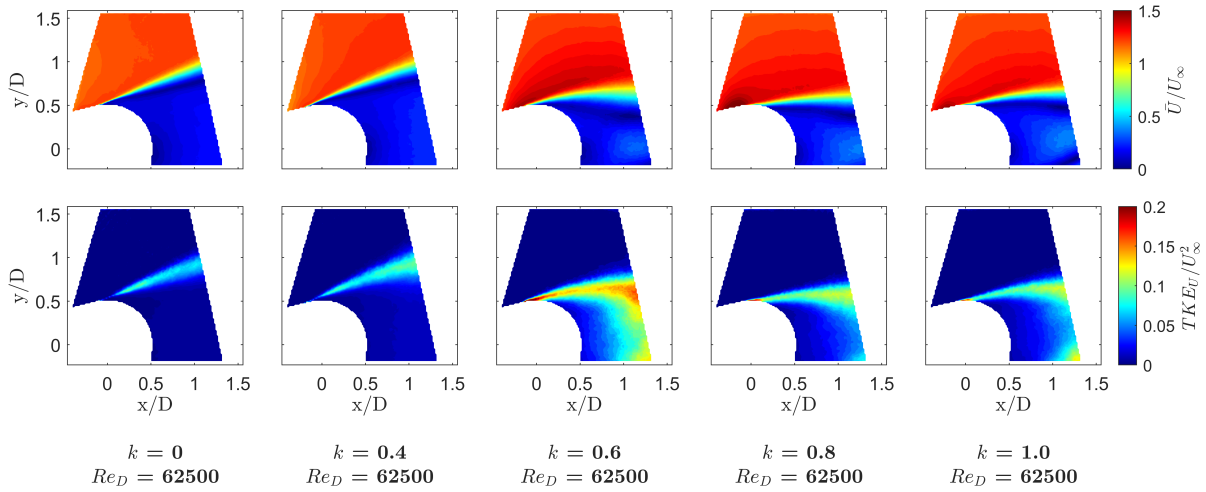

Figure 5.15: Development of the non-dimensionalised mean velocity magnitude, $\bar{U}/U_\infty$ (top), and non-dimensionalised mean Turbulent Kinetic Energy, TKE_U/U_∞^2 (bottom), at Re_D = 62500 and $0 \leq k \leq 1.0$.

The bluff body wake and laminar separation at k = 0, reminiscent of the TrSL3 regime, does not vary significantly when a spin ratio of k = 0.4 is reached. The separation point moves upstream with the direction of rotation, from an angular position of approximately 261° to 255°, and the wake deflects in the same direction as indicated by the upwards shift of the rear stagnation point. TKE values rise slightly along the shear layer, partially as a result of the larger relative Reynolds number at the separation point, but also due to the FOV showing a larger portion of the shear layer as separation shifted more upstream. The asymmetry of the flow field as a result of the low spin ratio at this Reynolds number is expected to be solely the result of the Magnus effect.

At k = 0.6, the flow field shows a different state. The separation and rear stagnation points move clockwise, eventhough the cylinder is spinning at a higher rate. The rear stagnation point is again at a similar angular position when comparing to k = 0, indicating that the size of the near-wake has reduced. Flow velocity increased over the top side of the cylinder, but the slope of the lift coefficient did not yet reduce. TKE values are elevated, especially near the separation point and the rear portion of the visible shear layer.

Two possible scenarios could explain the changes in flow state. Firstly, the reduced size of the near-wake, increased turbulence intensity in close vicinity to the backside of the cylinder and elevated drag coefficient values, hint to the characteristics of the upper bound of the TrSL3 regime, as explained in subsection 2.1.1. Whereas, the second scenario is the formation of a weak laminar separation bubble, which according to Ma et al. (2022) appear when starting from a lower subcritical Reynolds number, and follows from the clockwise movement of the separation point and increased velocity in front of it. However, even for a weak LSB a reduction in both lift and drag coefficient is expected, mainly as a consequence of delayed turbulent boundary layer separation, and thus appears to be the less likely scenario here. It must be noted that the rapid increase in drag coefficient to the extent shown in the current results has not been recorded in literature and appears to be related to vortex induced suction, but perhaps the higher blockage ratio could play a role as well.

The situation at k = 0.8 does resemble more that of a formed laminar separation bubble or fully developed turbulent boundary layer. Both the separation and rear stagnation points moved clockwise again and velocity increased on the top side of the cylinder in a concentrated area in close vicinity of the separation point. TKE now reduced in the visible near-wake, indicating vortices have moved further away. The lift coefficient increased at a reduced rate showing a relative weak transition effect. The drag coefficient does show a large drop in magnitude, owing to the vortices greater distance and delayed boundary layer separation reminiscent of the TrBL regimes.

To confirm the state of the flow follows the characteristics of the TrSL3 and TrBL regimes at k = 0.6 and k = 0.8 respectively, POD is utilised. Figure 5.16 shows the relative and cumulative energies of the POD modes at each of the shown spin ratios. The larger contribution of the first two modes does seem to indicate a significant change occurs at k = 0.6. However, as POD is dependent only on the information that is contained within the FOV, this redistribution of energy does not tell a new mechanism is at hand or that existing structures have moved into the FOV and thus appear as more dominant. Furthermore, the energy distributions of k = 0.4, 0.8 and 1.0 are close in shape, indicating the structures responsible for the velocity fluctuations are similar, even when by inspection of the time-averaged velocity fields in Figure 5.15 clear differences in flow state are shown, especially between k = 0.4 and 0.8.

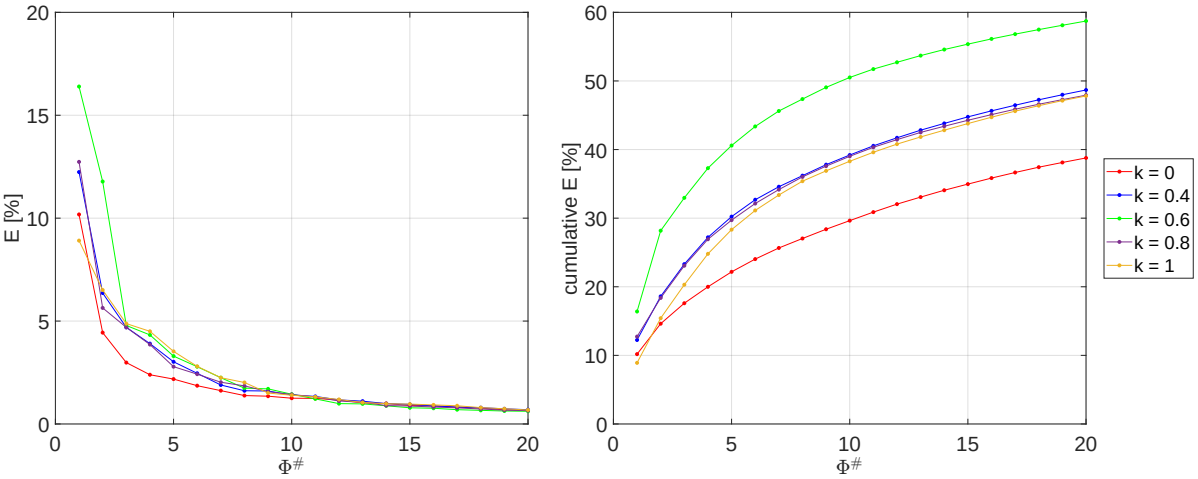

Figure 5.16: Energy distribution of the 20 most energetic spatial POD modes ϕ^n for $Re_D = 62500$ and various k.

By reconstructing the velocity field using the six most energetic modes, Q-criterion isosurfaces are shown to reveal the vortical structures in the flow, see Figure 5.17. At k = 0.4, structures appear more coherent and closer to the results shown for the stationary cylinder at k = 0 and Re_D = 250000. This process continues for k = 0.6, where vortices appear much larger and are formed close to the backside of the cylinder. Combining this with the near-wake reduced size and counterclockwise deflection, vortical structures coming from the lower shear layer of opposite direction are also detected. The relative size of these structures in comparison to the cylinder and alternating shedding behaviour does now resemble more that of Von Karman type shedding, typically present for stationary and rotating cylinders at these Reynolds numbers and spin ratios.

These vortices are most likely different compared to the ones shown for k = 0 and 0.4, for which it is expected that the Von Karman type vortices are instead formed outside of the FOV and are thus not detected. Furthermore, the formation of large vortices in close proximity to the backside of the cylinder provides more evidence in favour of the upper TrSL3 regime and could explain the spike in the drag coefficient by vortex induced suction.

For k = 0.8 growth of the vortical structures appear to be delayed. This is a consequence of the clockwise movement of the separation point, such that the vortices are pushed further away from the backside of the cylinder. The combination of delayed turbulent boundary layer separation and the vortices greater distance to the backside of the cylinder allows for the drag coefficient to reduce by a significant margin, and thus provides more evidence that the TrBL regime is now reached.

Although comparisons are made to the Reynolds regimes of a stationary cylinder, it must be noted that at the spin ratio of k = 0.8, the relative Reynolds number is only $Re_{rel} \approx 62500 \times 1.8 = 125000$. This is in fact far below the Reynolds number at which a LSB naturally forms on a stationary cylinder in a disturbance-free flow, $Re_D \approx 300000$. Thus, the comparisons to the stationary regimes and the usage of the relative Reynolds number concept are only made to aid in the explanation of possible phenomena occurring on a rotating cylinder, but can not be interchanged one to one.

At k = 1.0, the flow field reacts to a change in spin ratio similar as before the change in flow regime occurred, e.g. k < 0.6. The separation and rear stagnation points move in counterclockwise direction, showing the near-wake has deflected upwards. The velocity peak in front of the separation point has shrunk either by decreasing strength of the LSB or due to it moving out of the FOV, The TKE shows similar results, where, due to the deflection, the lower side shear layer starts to appear in the FOV and TKE magnitudes do not change significantly. The vortical structures present a similar picture as for k = 0.8, but due to the counterclockwise rotation of the wake, the vortical structures of opposite sign appear again and remain to develop further away compared to the situation at k = 0.6. At this point the effects of the spin ratio and hence the Magnus effect are most dominant.

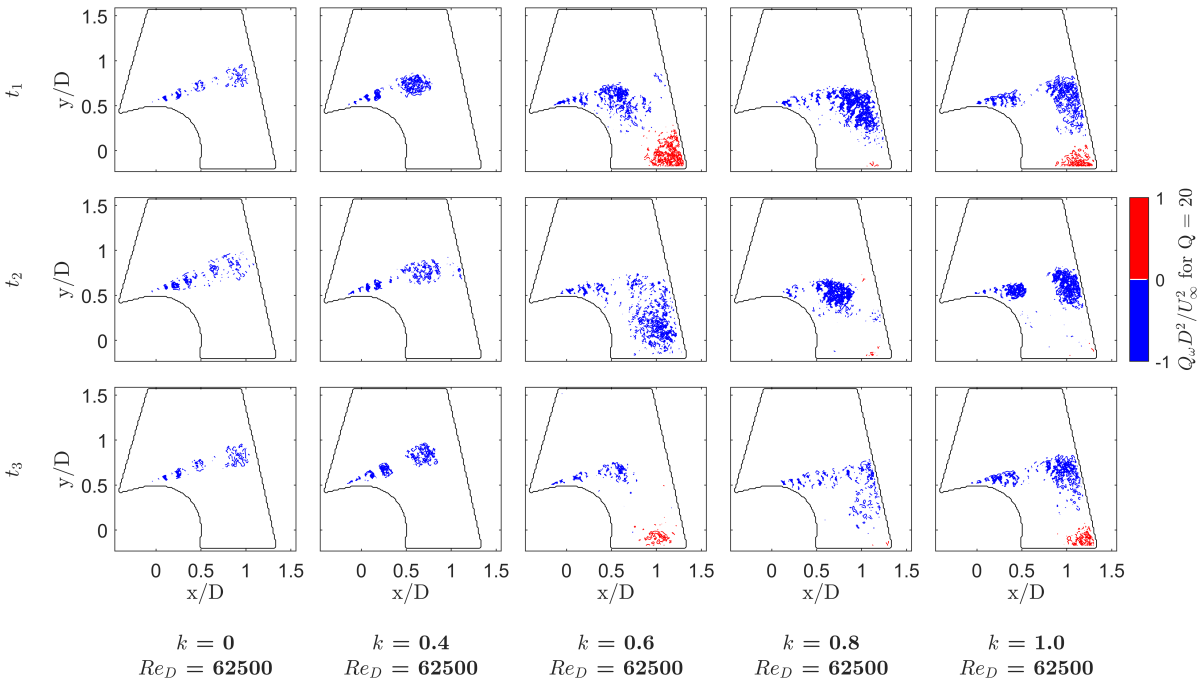

Figure 5.17: Sequence of instantaneous Q_ω at $\Delta t = 6.67 \times 10^{-2} s$ of the reconstructed flow field using the six most energetic POD modes for Re_D = 62500 at 0 ≤ k ≤ 1.0.

The flow fields between Re_D = 62500, 125000 and 250000 for 0 < k < 1 show great similarity, except transition occurs at a lower spin ratios and the effects of the transition are greater with an increase of Reynolds number. This trend is in line with the findings from Ma et al. (2022) and Chopra and Mittal (2023). As Re_D = 125000 is an intermediate step where much of the same as for Re_D = 62500 can be said, the discussion will continue to show the results for Re_D = 250000 instead.

As for Re_D = 62500, Figure 5.18 depicts sequences of non-dimensionalised mean velocity magnitude, $\bar{U}/U_\infty$, and mean turbulent kinetic energy, TKE_U/U_∞^2, with increasing spin ratio in the range of 0 < k < 1 for Re_D = 250000. Do note the specific spin ratios shown here are now much smaller, since significant changes in the flow field occur at lower spin ratios with higher Reynolds numbers.

It has been shown in subsection 5.2.1 that the flow field at k = 0 in the current FOV does not show any major discrepancies that would explain the relatively large negative lift coefficient to be present. At k = 0.1, the lift coefficient disappeared and instead a value in line with the other Reynolds numbers was realised. As expected, the separation point moved counterclockwise with the direction of rotation, however the rear stagnation point moved in opposite direction, which would imply the wake to have grown. At the same time the drag coefficient reduced from C_D = 0.9 to 0.76, which is again more in line with the other Reynolds numbers, but is a surprising result if the wake has grown or at the very least remained similar in size.

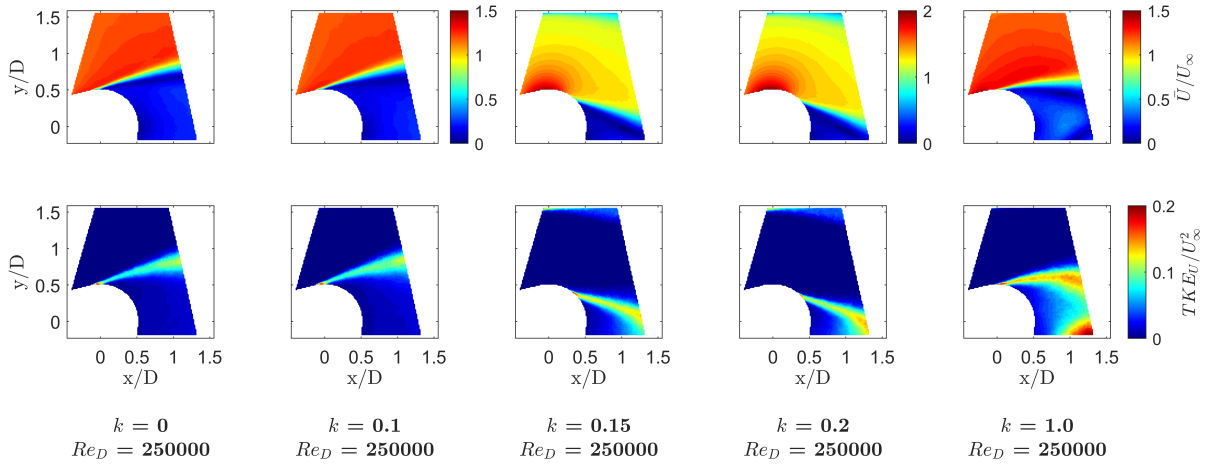

Figure 5.18: Development of the non-dimensionalised mean velocity magnitude, $\bar{U}/U_\infty$ (top), and non-dimensionalised mean Turbulent Kinetic Energy, TKE_U/U_∞^2 (bottom), at Re_D = 250000 and 0 ≤ k ≤ 1.0.

A possible explanation can found in the earlier speculation about an unfavourable interaction of the lower tunnel jet shear layer and support structure, see Figure 5.14. For instance the added rotation might be enough to deflect the lower tunnel shear layer to no longer interact, such that flow conditions similar as for the other Reynolds numbers is restored. While another possibility might still be found in the second speculation on the outflow conditions settling asymmetrically. As the near-wake appears to be thinner, this tilt in flow field system seems more plausible, especially since expectations are that the forward stagnation point moves clockwise against the direction of rotation, see subsection 2.2.5, and hence tilting the system in opposite direction. In reality a combination of both and/or other effects might be at hand, but unfortunately none can be confirmed.

The inverse Magnus effect is captured at k = 0.15 and 0.2 in Figure 5.18. The upper boundary layer appears to have undergone transition between 0.1 < k < 0.15. At k = 0.15, the separation point moves to an angular position of approximately 306°, which falls within the expected range of turbulent BL separation for a stationary cylinder, see Figure 2.3. The effects of transition are stronger compared to the lower Reynolds numbers tested, especially with Re_D = 62500. Velocity increases to approximately two times the freestream velocity in front of the separation point, owing to the delayed turbulent boundary separation and potential existence of a LSB. TKE values are raised in the now fully turbulent shear layer.

Signs of the upper TrSL3 regime, with vortical structures being formed in close proximity to the backside of the cylinder have not been recorded for Re_D = 250000. The abrupt nature of the transition at Re_D = 250000 might be an indication this regime is skipped entirely or is only confined to a very small range of spin ratios and Reynolds numbers. Thus, perhaps some luck is required to capture it fully. If the latter is the case, it might also explain why in literature this spike in the drag coefficient is not shown. Besides with the strong deflection of the tunnel jet, the support beam will most likely be fully submerged and could cause some interference effects as well.

The inverse Magnus effect reaches maximum strength at k = 0.2 with $C_L \approx$ -0.81. Compared to k = 0.15, the separation point moves in clockwise direction and velocity increases further on the top side of the cylinder. Since the boundary layer already underwent transition and the spin ratio increased, the clockwise movement suggests the growing of an LSB as the cause of the movement and increased negative lift coefficient. This agrees well with the results from Ma et al. (2022) and Chopra and Mittal (2023). Additionally, the increased negative vertical velocity in front of the separation point is an strong indication of the presence of an LSB that growths in strength between k = 0.15 and 0.2, see Figure 5.19

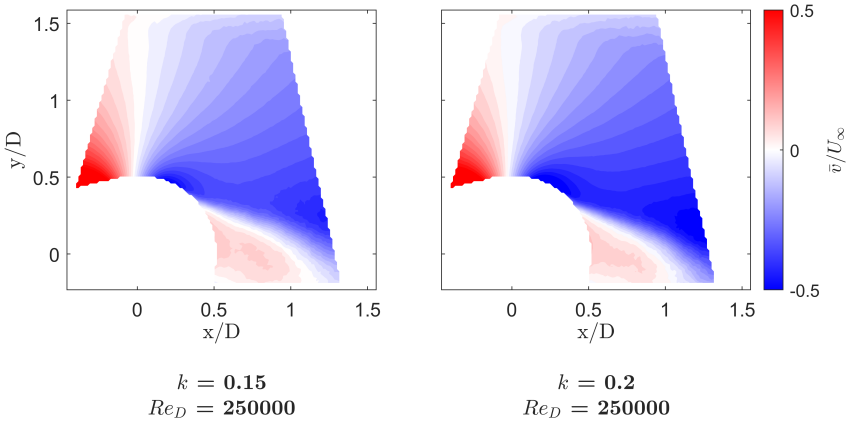

Figure 5.19: Non-dimensionalised mean vertical velocity component, $\bar{v}/U_\infty$ (top) at Re_D = 250000 for k = 0.15 and 0.2.

As a consequence of the strong inverse Magnus effect and large blockage ratio, the first signs of the effectiveness of the rotating cylinder in deflecting the tunnel jet, and thus altering the outflow conditions, becomes visible. For k = 0.15 and 0.2, the tunnel shear layer appears at the top boundary of the FOV Given the extent of the deflection at these conditions, the situation on the opposite side of the cylinder is expected to be much more extreme when the regular Magnus effect dominates, especially at high spin ratios. This will be covered further in subsection 5.2.4 and subsection 5.2.5.

For 0.2 < k < 1, the lift coefficient rises and switches sign at $k \approx$ 0.47. The separation points moves in counterclockwise direction and the velocity on the top side of the cylinder decreases gradually in the same way as for Re_D = 62500 and 125000 between 0.8 < k < 1.0 and 0.6 < k < 1.0 respectively. After transition, the flow fields between the different Reynolds numbers show great similarity in both shape and magnitude, e.g. Re_D = 62500 and 250000 at k = 1.0. Only for Re_D = 250000 are TKE magnitudes higher, possibly owing to the larger Reynolds number.

The energy distribution of the most energetic modes at Re_D = 250000 is depicted in Figure 5.20. The distributions for k = 0 and 0.1 are similar, where the small differences are most likely the result of the slightly more upstream separation and shear layer visibility. Likewise, for k = 0.15 and 0.2 energy distributions only differ slightly, owing to the movement of the separation point and shear layer as well as the greater visibility of the tunnel jet shear layer for k = 0.2. The distribution at k = 1.0 for Re_D = 250000 compares well to Re_D = 62500 at the same spin ratio, which follows closely the statements made on flow field similarity after transition of the boundary layers.

Using the reconstructed velocity field from the ten most energetic modes, Q-criterion isosurfaces are shown to reveal the vortical structures in the flow, see Figure 5.17. The flow structures do not vary considerably from k = 0 to 0.1, as was the case for Re_D = 62500 between k = 0 and 0.4. After transition for k = 0.15 and 0.2, structures remain to be shed, which due to the inclination of the shear layer and delayed turbulent separation are close to the backside of the cylinder. This could be an indication why there is not a drop in the drag coefficient, see Figure 5.3, eventhough the delayed separation would typically result in reduced drag coefficients.

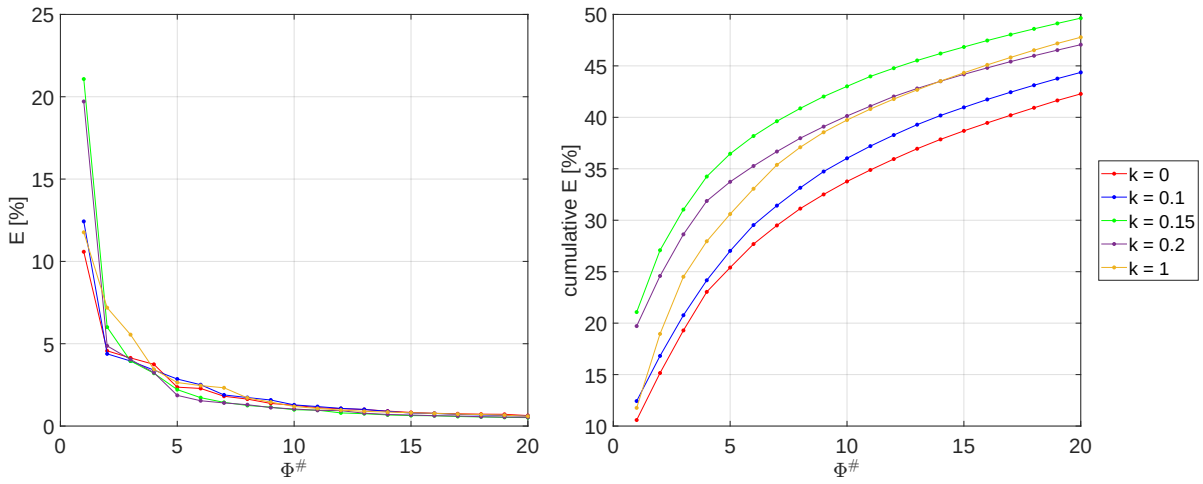

Figure 5.20: Energy distribution of the 20 most energetic spatial POD modes ϕ^n for $Re_D = 250000$ and $0 \leq k \leq 1.0$.

Earlier speculations on a tilt of the force system by the influence of wind tunnel interference effects could make it so that the negative lift force is partly acting in the direction of the drag. However, since the maximum velocity is still in front of the centreline of the cylinder, Figure 5.18, which is associated with the point of minimum pressure, it is unlikely, but not fully proven, that the negative lift force is contributing to the drag and might therefore be excluded as a possible cause. However, the support structure beam is now most likely fully submerged in the tunnel jet, and thus a possible interaction with its wake could result in changes in the drag coefficient as well.

The structures on the upper boundary are the result of the tunnel shear layer and disappear again from the FOV when the spin ratio is further increased, e.g. at k = 1. At a spin ratio of 1, the lower side vortices reemerge in the FOV and flow structures similar to the ones shown for Re_D = 62500 at k = 1 are presented.

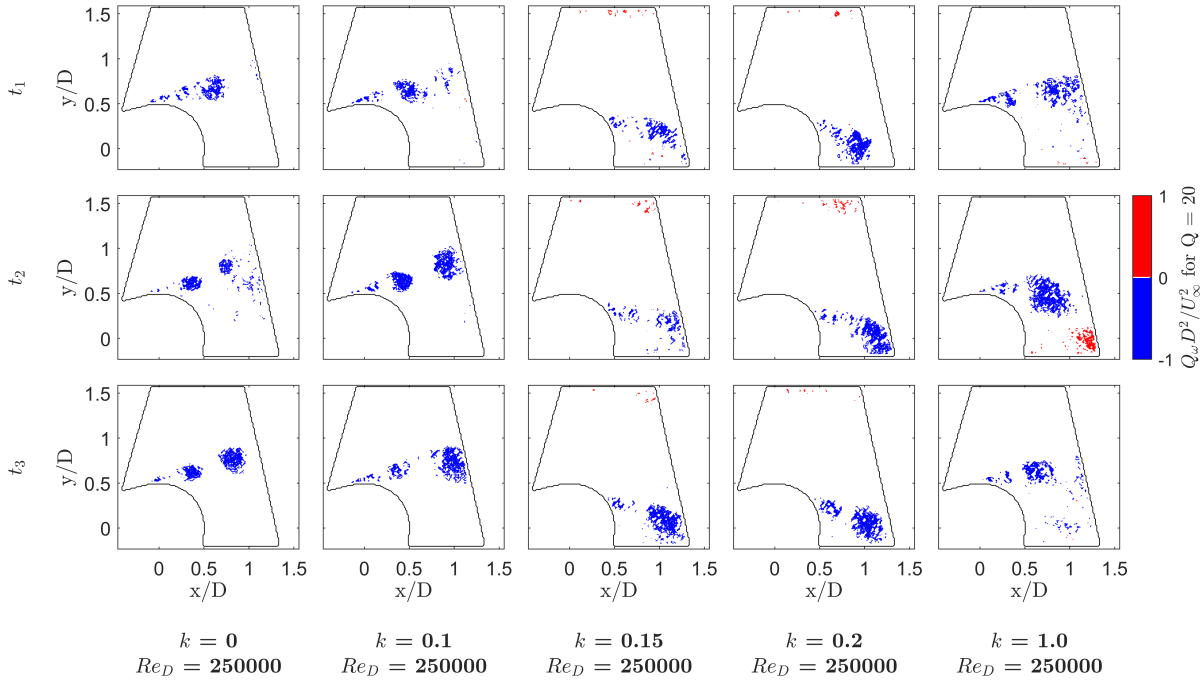

Figure 5.21: Sequence of instantaneous Q_ω at $\Delta t = 6.67 \times 10^{-2} s$ of the reconstructed flow field using the ten most energetic POD modes for Re_D = 250000 at $0 \leq k \leq 1.0$.

5.2.3. Regime of regular Magnus effect

The force measurement results, presented in section 5.1, showed for k > 1 no considerable differences in the coefficient behaviour with an increase of the spin ratio between the different Reynolds numbers. In the previous subsection 5.2.2, it was shown this particular behaviour was initiated after transition to the TrBL regimes was realised for all tested Reynolds numbers at approximately a spin ratio of k = 0.8. The flow fields at spin ratios beyond the transition point showed great similarity between the different Reynolds numbers at the same spin ratio, e.g. for Re_D = 62500, 125000 and 250000 at k = 1.

In the current experiment, the regime starting from the aforementioned TrBL regime extending up to the knee in the lift curve covers the range 1.0 < k < 2.2, which has been shown in subsection 5.1.1 and subsection 5.1.2 to be significantly smaller compared to the two-dimensional results from Swanson (1961), k < 3. Within this range, the change in force coefficients with an increase of the spin ratio do not present significant variations between the different Reynolds numbers tested. This compares well with most experimental literature at similar Reynolds numbers, e.g. Badalamenti (2010), Chen and Rheem (2019), and Ma et al. (2022), expect for Bordogna et al. (2019a) where some variations are visible.

Flow visualisations within this range of spin ratios are depicted in Figure 5.22, Figure 5.23 and Figure 5.24 for Re_D = 62500, 125000 and 250000 respectively. Sequences of non-dimensionalised mean velocity magnitude, $\bar{U}/U_\infty$, and mean turbulent kinetic energy, TKE_U/U_∞^2, with increasing spin ratio in the range of 1.2 < k < 2.0 are utilised in the comparison. Do note the change in colour scale at k = 2.0 as a result of the increased velocity and reduced TKE at the backside of the cylinder following the added rotation.

In general the flow fields appear to present a similar picture between the different Reynolds numbers. With an increase of the spin ratio, separation points move counterclockwise such that the wake deflects in the direction of rotation and its size reduces. At k = 2.0, the wake has reduced significantly and is now fully captured in the FOV. The maximum velocity in the FOV reaches two times the freestream velocity and occurs at the backside of the cylinder.

Slight differences in wake sizes and external velocities outside of the shear layer are observed between the Reynolds numbers. The external velocities on both sides of the wake are relatively larger, at smaller Re_D for all spin ratios shown. If this is the result of the Reynolds number or some other effect regarding tunnel interference, e.g. larger jet expansion at highest Re_D, is unclear. For the wake sizes, at k = 1.2, 1.4 and 1.6, the wake for Re_D = 125000 is largest in comparison, with Re_D = 250000 having the smallest wake followed by Re_D = 62500. At k = 1.8 and 2.0 this changes, where the largest wake in comparison belongs to the lowest Reynolds number Re_D = 62500 and the smallest to Re_D = 250000. However, as there is also additional uncertainty in the determination of the freestream velocity and thus the spin ratio, both of these small differences, e.g. in wake sizes and non-dimensionalised external velocities, could be the result of a slight deviation in actual spin ratio between each case.

Although the non-dimensionalised mean velocity magnitude fields are similar between the different Reynolds numbers, an interesting observation regarding the lower shear layer can be made when investigating the non-dimensionalised mean TKE fields. At k = 1.2, TKE values increase with an increase of the Reynolds number where a similar portion of the shear layer is visible between each case. At k = 1.4, TKE reduces for Re_D = 125000 and 250000 with the latter showing a larger reduction, whereas for Re_D = 62500 an increase is observed, bringing the results between the Re_D closer together.

The TKE values continue to grow for Re_D = 62500 and peak at k = 1.6, which in comparison to the larger Re_D are now distinctly larger. The lower shear layer at 1.2 $\leq k \leq$ < 1.8 and Re_D = 62500 is also more inclined into the direction of rotation, whereas the upper shear layer does not present such a difference between the different Reynolds numbers. At k = 1.8, TKE has reduced again and the inclination of the shear layer changes such that the similarity between the different cases is restored. For k = 2.0, no major deviations are observed, although TKE is slightly elevated at Re_D = 125000.

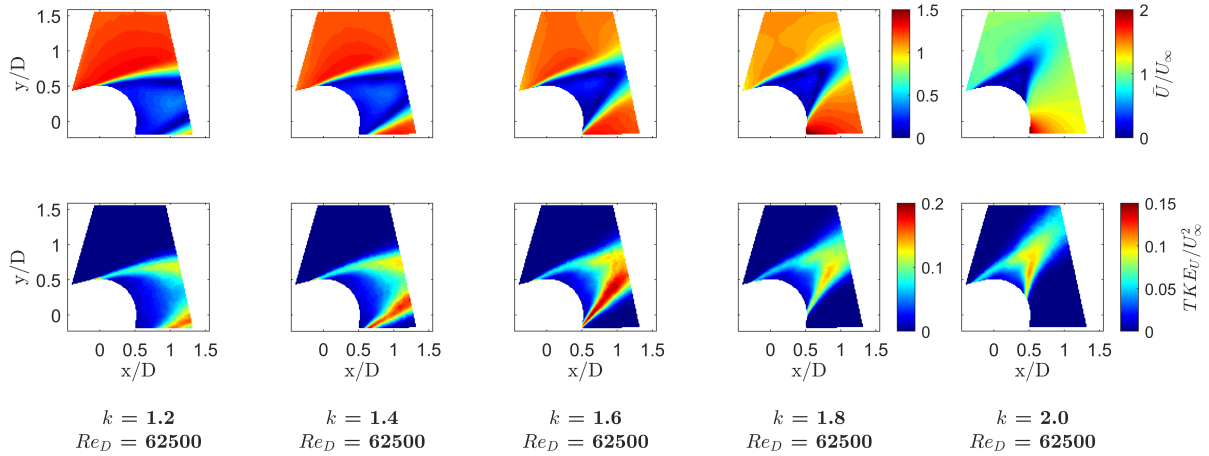

Figure 5.22: Development of the non-dimensionalised mean velocity magnitude, $\bar{U}/U_\infty$ (top), and non-dimensionalised mean Turbulent Kinetic Energy, TKE_U/U_∞^2 (bottom), at Re_D = 62500 and 1.2 ≤ k ≤ 2.0.

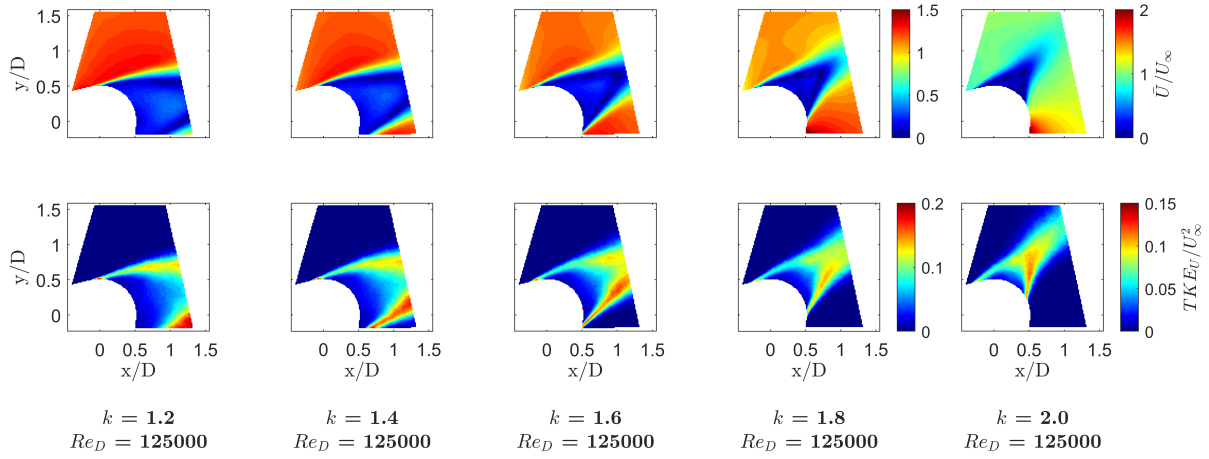

Figure 5.23: Development of the non-dimensionalised mean velocity magnitude, $\bar{U}/U_\infty$ (top), and non-dimensionalised mean Turbulent Kinetic Energy, TKE_U/U_∞^2 (bottom), at Re_D = 125000 and 1.2 ≤ k ≤ 2.0.

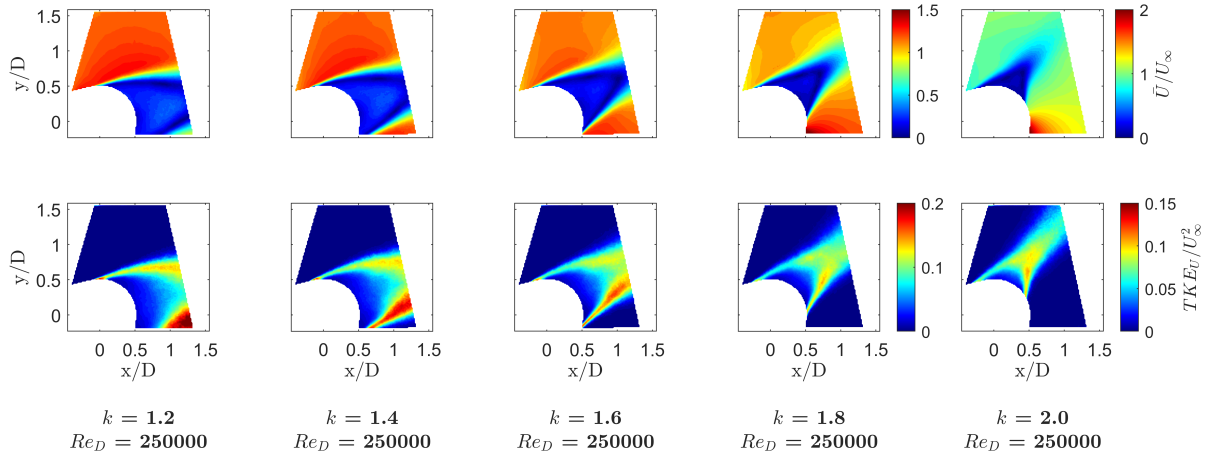

Figure 5.24: Development of the non-dimensionalised mean velocity magnitude, $\bar{U}/U_\infty$ (top), and non-dimensionalised mean Turbulent Kinetic Energy, TKE_U/U_∞^2 (bottom), at Re_D = 250000 and 1.2 ≤ k ≤ 2.0.

Speculating on a possible explanation of the behaviour at the retreating side of the cylinder could be related to boundary layer transition. At subcritical, critical and supercritical Reynolds numbers, the state of the boundary layer on the retreating side of a rotating cylinder has been scarcely researched. Both Krahn (1956) and Swanson (1961) argued in favour of a turbulent boundary layer due to the large absolute velocity, regardless of the low relative Reynolds number. In contrast, Chopra and Mittal (2023) showed by the use of modern LES simulations a laminar state of the boundary layer, even at large spin ratios and subcritical Reynolds numbers. Experimentally this has not been proven and thus uncertainty on the state of the retreating side boundary layer at these Reynolds numbers and spin ratios remains.

The changes in TKE, shear layer inclination and wake size by varying the spin ratio can be the result of boundary layer transition, much like what has been shown on the advancing side. When moving along with a point on the surface of the cylinder in the direction of rotation, the lower half (between 0° and 90°) will act to a lesser degree with the incoming flow and as such is expected to increase the relative Reynolds number which in turn promotes boundary layer transition to a turbulent state. Since Re_D = 250000 is closer to the point of natural transition for a stationary cylinder in a disturbance-free flow, transition occurs at a lower spin ratio, e.g. k < 1.4, whereas for Re_D = 62500 it occurs later, e.g. k < 1.8. The more energised turbulent boundary layer in combination with the moving wall then allows for the boundary layer to remain attached on the backside of the cylinder.

The relative larger size of the wake at Re_D = 62500 for k > 1.6 and change in shear layer inclination are in favour of the opposite, where due to the increased momentum of the moving wall a possible relaminarisation occurs. However, for this to be possible, the retreating side boundary layer must have transitioned to the turbulent state at lower spin ratios, eventhough relative Reynolds numbers are expected to reduce on the retreating side. The force coefficient results do not present a clear sign of a change in flow regime and the current FOV does not show this particular area to prove such a statement.

With the lack of information on the state of the retreating side boundary layer from the results of the current setup and in literature, the above remains to be speculation. However, the results do indicate differences to be present within this range of Reynolds numbers and spin ratios, which could be an interesting direction to pursue in fundamental rotating cylinder research in the future.

POD analysis further indicates a clear difference at Re_D = 62500 in the energy distribution at k = 1.6, see Figure 5.25. The energy content of the first mode is considerably larger at Re_D = 62500, whereas the other modes do not present such a difference to the same modes of the other Reynolds numbers. As the visible wake in the FOV is of similar size between the Reynolds number, such a strong difference might not be the result of the limited size of the FOV. Besides for all other spin ratios, the energy distributions do not present as large of a difference in mode energies between the Reynolds numbers.

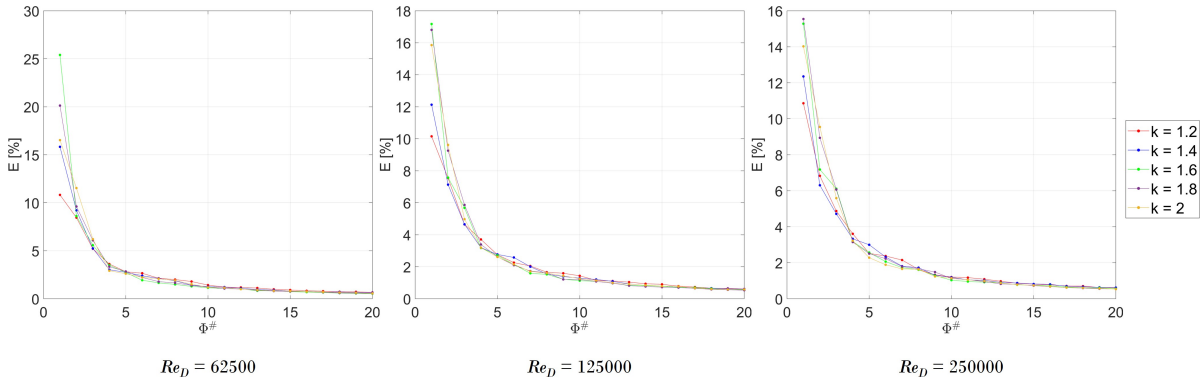

Figure 5.25: Energy distribution of the 20 most energetic spatial POD modes ϕ^n for Re_D = 62500, 125000 and 250000 at 1.2 ≤ k ≤ 2.0.

Figure 5.26 illustrates the normalised velocity components of the first POD mode at k = 1.6 and Re_D = 62500, 125000 and 250000. The first modes present a similar structure across the three cases, whereas the magnitudes in the normalised velocity components vary. The change in energy of the first mode is therefore not the result of a change in dominant flow structure. Do note the flipped magnitudes at Re_D = 250000, which for the purpose of comparing the underlying mechanisms can be ignored as it is solely the result of the sign of the temporal coefficients.

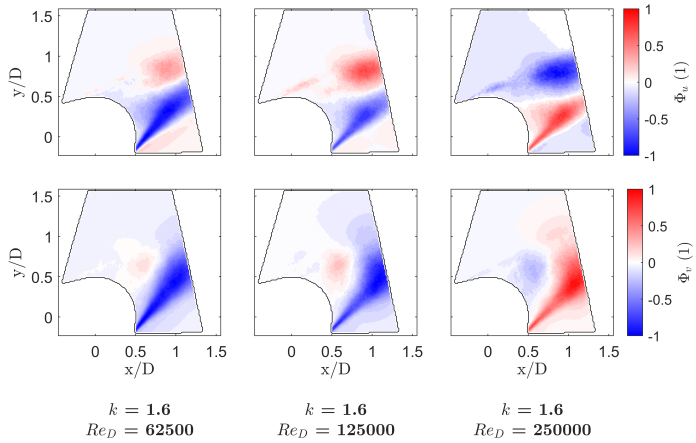

Figure 5.26: Normalised velocity components of the first POD mode, $\phi_u(1)$ (top) and $\phi_v(1)$ (bottom), at k = 1.6 and Re_D = 62500, 125000 and 250000.

Identification of vortical structures is once more done by utilising Q-criterion isosurfaces of the reconstructed velocity field containing the ten most energetic modes. The results for Re_D = 62500 are depicted in Figure 5.27. Periodic shedding of structures remains to be present for all shown spin ratios, where at k = 2.0, due to the shear layers being captured entirely in the FOV, propagation of vortical structures is more clearly visible. Overall size of the vortical structures appear to decrease with an increase of the spin ratio, but do not disappear as has been stated in various sources at k = 2.0, e.g. Prandtl and Tietjens (1934), Aljure et al. (2015) and Ma et al. (2022). For Re_D = 125000 and 250000 similar shedding behaviour is found and will thus not be shown below.

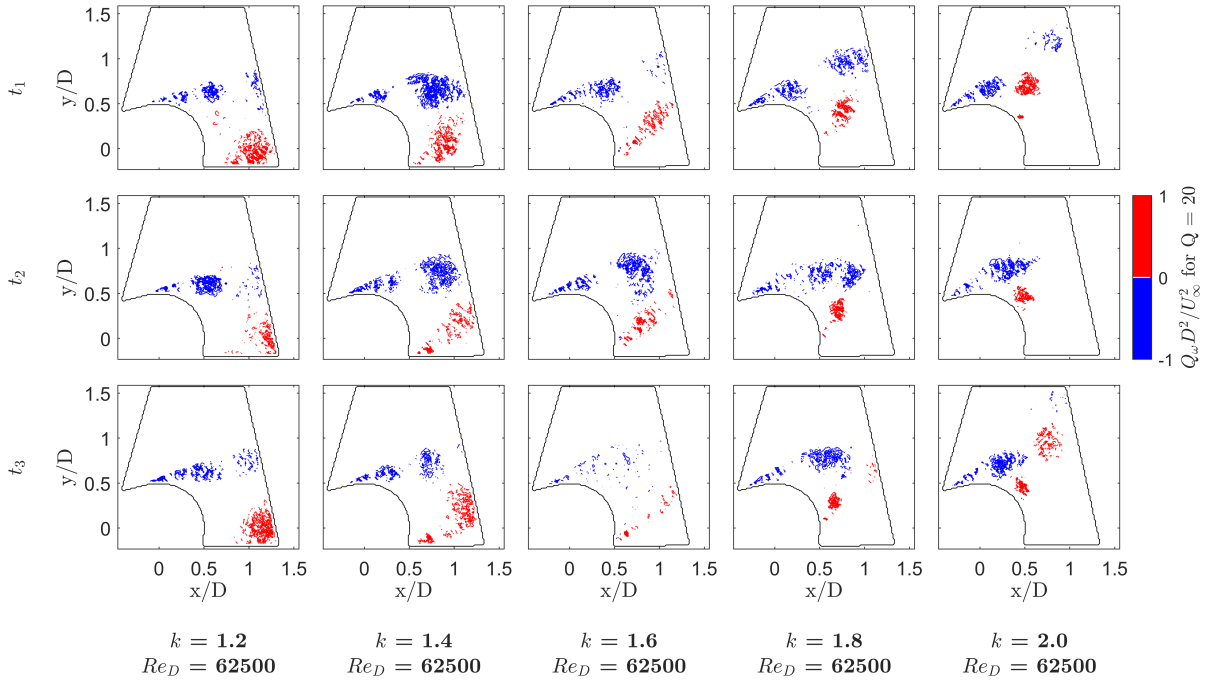

Figure 5.27: Sequence of instantaneous Q_ω at $\Delta t = 6.67 \times 10^{-2} s$ of the reconstructed flow field using the ten most energetic POD modes for Re_D = 62500 at 1.2 ≤ k ≤ 2.0.

5.2.4. Regime of rotating boundary layer formation

Within the range $2.2 \leq k \leq 2.6$ a kink in the lift and drag coefficients curves is observed, after which the coefficient behaviour changes with a further increase of the spin ratio , see subsection 5.1.1 and subsection 5.1.2. Swanson (1961) mentioned this change in force coefficient behaviour to be the result of the formation of closed streamlines around the cylinder surface, see subsection 2.2.5. Earlier investigations have shown closing of the streamlines to occur at spin ratios $k \geq 3$, e.g. Swanson (1961) Karabelas et al. (2012) and Aljure et al. (2015). As such to confirm the same mechanism is causing the difference in coeffficient behavior, Figure 5.28 and Figure 5.29 presents sequences of non-dimensionalised mean velocity magnitude and non-dimensionalised mean TKE at Re_D = 62500 and 125000 in the range of $2.2 \leq k \leq 2.6$ respectively.

The general characteristics of the flow field between the two Reynolds numbers remain similar and the same trend in the velocity magnitude fields for the range $1.0 \leq k \leq 2.0$ continues with an increase of the spin ratio. Namely, by increasing the spin ratio, the added momentum causes the retreating side boundary layer to remain attached for longer, the wake moves in counterclockwise direction and reduces in size due to the separation points moving closer together, and the maximum velocity increases at the backside of the cylinder, e.g. $\bar{U}_{max}/U_\infty \approx 2.7$ at k = 3.0. At approximately k > 2.6, the separation points coincide, marking the beginning of the formation of the closed streamlines around the cylinder surface and the end of the knee in the force coefficient curves.

In contrast to the velocity magnitude fields, for k > 2.2 mean TKE fields show a gradual decrease in magnitude with an increase of the spin ratio. At $k \approx 2.6$, TKE values are reduced significantly, whereas for k = 3.0 TKE starts to grow again but now in the high velocity region near the backside of the cylinder.

The growing region of high velocity at the backside of the cylinder and its associated suction is likely the cause of the rise in drag between $1.0 \leq k \leq 2.2$, whereas for $2.4 \leq k \leq 2.8$ the wake starts to move to a more upstream position of the cylinder, causing the drag coefficient to drop again. Both of these phenomena have been similarly stated by Swanson (1961). It must also be noted that due to the movement of the wake over the top side of the cylinder, the rate of change of the lift coefficient with the spin ratio is expected to reduce by the influence of the lower pressure in the wake. Thus, the knee in the lift coefficient curve is potentially also linked to this effect, but likely not the sole reason it occurs.

Comparing the flow fields between Re_D = 62500 and 125000 the following can be observed. At k = 2.2 and 2.4, the angular position of the wake matches closely between the two cases, with the wake being slightly larger for Re_D = 62500. At k = 2.6, wakes are closer in size and the angular position of the wakes remain to be similar in comparison. However, for k > 2.6, the flow field starts to deviate to a larger extent, where the wake is increasingly more deflected at k = 2.8 and 3.0 for Re_D= 62500 compared to Re_D = 125000, which in turn could explain the difference in force coefficients at higher spin ratios.

A possible explanation can be found in the ability of the wake to block of one side of the nozzle as a consequence of the large blockage ratio. As the energy of tunnel jet is lower at the smaller Reynolds number, it might be possible that the deflection is strong enough to block a larger portion of upper part of the tunnel jet and thus allows the wake to settle at a more upstream angular position. This potential cause of discrepancies will be addressed further in the coming subsection 5.2.5. Additionally, it must also be noted that the deflection is already more than expected, see subsection 2.2.5, which reinforces the idea of blockage effects to play a significant role in the shown phenomena.

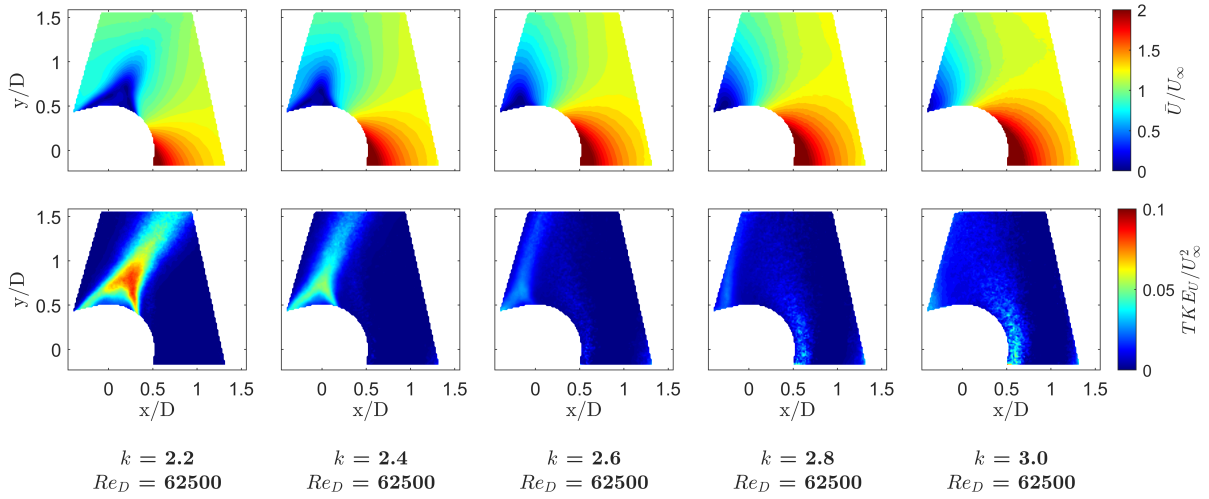

Figure 5.28: Development of the non-dimensionalised mean velocity magnitude, $\bar{U}/U_\infty$ (top), and non-dimensionalised mean Turbulent Kinetic Energy, TKE_U/U_∞^2 (bottom), at Re_D = 62500 and 2.2 ≤ k ≤ 3.0.

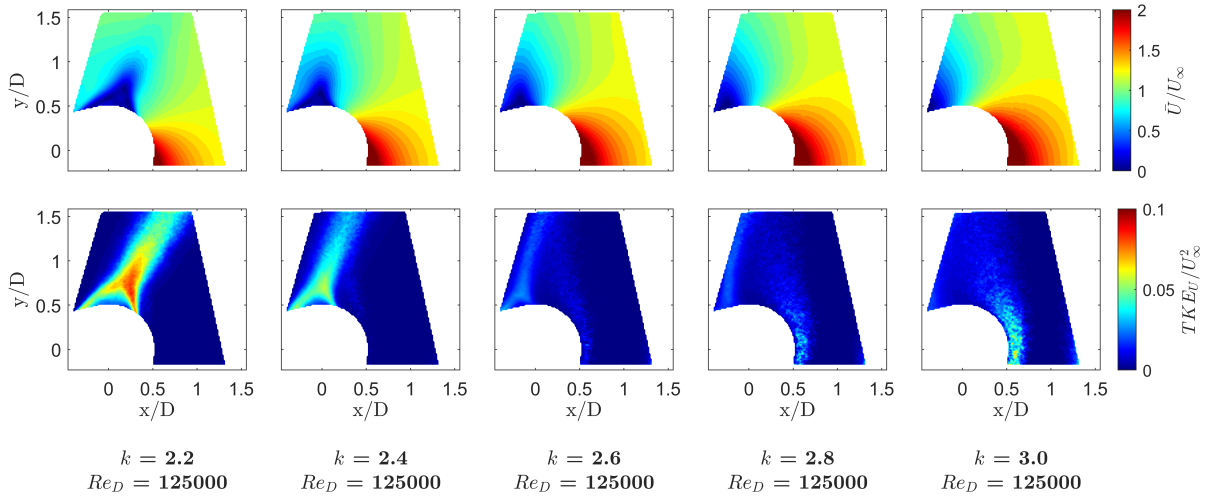

Figure 5.29: Development of the non-dimensionalised mean velocity magnitude, $\bar{U}/U_\infty$ (top), and non-dimensionalised mean Turbulent Kinetic Energy, TKE_U/U_∞^2 (bottom), at Re_D = 125000 and 2.2 ≤ k ≤ 3.0.

The energy distribution of the 20 most energetic spatial POD modes for Re_D = 62500 and 125000 at 2.2 ≤ k ≤ 3.0 is shown in Figure 5.30. As expected from the flow field similarities between the two cases, the energy distributions do not present vastly different outcomes. The largest variation can be found for the first POD mode at k = 3, where at Re_D = 62500 it contains 8.8% more energy compared to the first POD mode of Re_D = 125000, e.g. 17.1% versus 8.3%. However, in both cases the first POD is mostly dominant as the second and third modes only contain approximately 3% and 1.5% respectively, whereas the variation in energy of the modes is predominantly the result of the variation in wake deflection out of the FOV.

With the increase of the spin ratio, a gradual decrease of relative energy between the first and subsequent modes, e.g. ϕ^1 versus $\phi^n > \phi^1$, can be observed at both Reynolds numbers. In particular the mode pairs ϕ^4, ϕ^5 and ϕ^6, ϕ^7 at k = 2.2 disappear at the larger spin ratios. As stated earlier, these mode pairs are typical for convection of coherent structures in the flow, e.g. periodic vortex shedding, which would thus indicate a gradual decrease is taking place of vortex strength before eventually ceasing to exist. The gradual shift of energy from the dominant vortices into smaller ones at subcritical Reynolds numbers has previously been observed by Liu et al. (2023), where although at lower spin ratios 1 < k < 2, the same could be taking place here.

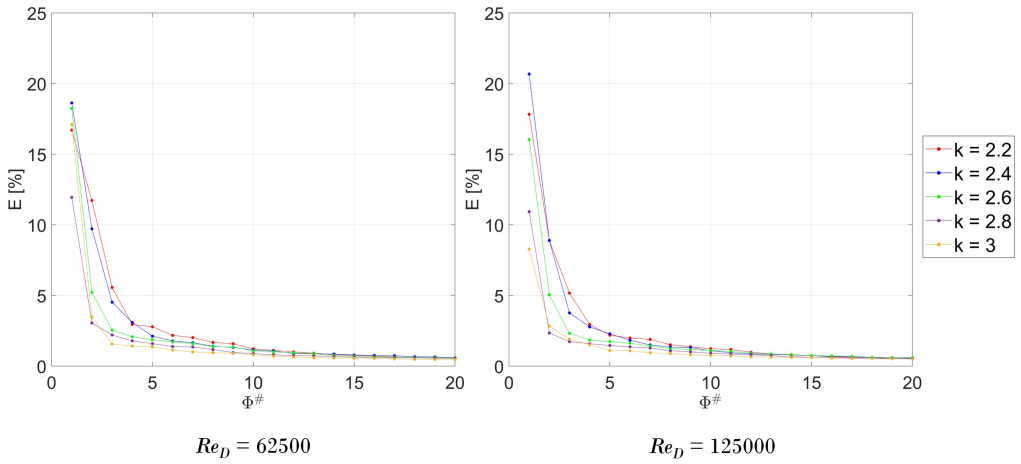

Figure 5.30: Energy distribution of the 20 most energetic spatial POD modes ϕ^n for Re_D = 62500 and 125000 at 2.2 ≤ k ≤ 3.0.

By reconstructing the velocity fields containing the first ten most energetic POD modes and showing Q-criterion isosurfaces, the change in vortical structures with the increase of the spin ratio is revealed. Figure 5.31 shows the results for Re_D = 62500, whereas for Re_D = 125000 presents a similar behaviour and is thus not shown here. At k = 2.2 vortical structures remain to be formed in close proximity to the cylinder surface. However unlike for k = 2.0, shown in Figure 5.27, structures do not appear to propagate into the flow at these three particular snapshots in time. As such, periodic vortex shedding, as has been discussed in subsection 2.2.5, might have stopped between 2.0 < k < 2.2 for the current experiment, which is similar to the often reported k = 2.0 and could also explain the drop in TKE in the wake region at these spin ratios. Tunnel interference and uncertainty in the determination of the freestream velocity are most likely causing the slight deviation.

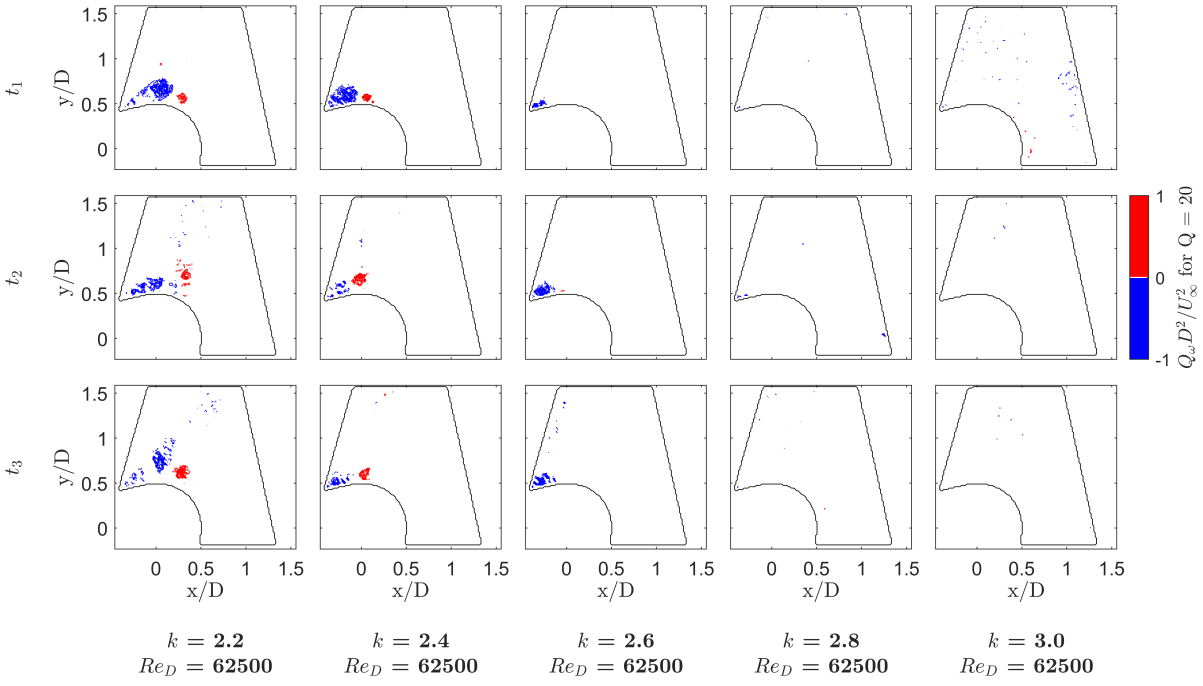

Figure 5.31: Sequence of instantaneous Q_ω at $\Delta t = 6.67 \times 10^{-2} s$ of the reconstructed flow field using the ten most energetic POD modes for Re_D = 62500 at 2.2 ≤ k ≤ 3.0.

The gradual decrease in size of the dominant vortical structures is clearly shown, where the ones originating from the retreating side boundary layer completely disappear at k = 2.6. From this point on, only clockwise vorticity remains to be present in the region of separated flow, which has been linked to the coming together of the separation points (Swanson, 1961). The complete disappearance of vorticity built up near the separated flow region or the continuation of shedding of vortices from the advancing side cannot be confirmed, due to the partial movement of the wake outside of the FOV. However, although no large scale structures are identified for $2.6 \leq k \leq 8$, at higher spin ratios the one sided vortex mode might still occur (Mittal & Kumar, 2003; Stojković et al., 2003). Additionally at k = 2.6 the knee in the force coefficient curves ends, indicating that indeed some relationship with the coming together of the separation points and the change in force coefficient curves is taken place.

Between k = 3.0 and 4.0, the separation point region remains to be more deflected for the lower Reynolds number and changes in the flow field follow a similar trend between the two cases, see Figure 5.32. The increase of the spin ratio enlarges the region of high velocity on the backside of the cylinder, where the maximum velocity has now reached approximately 2.85 times the freestream velocity. With this added momentum, the separation point region now starts to lift off from the surface of the cylinder, where it appears to have either rotated slightly in a clockwise direction or became thicker as whole.

The works of Matsui (1981), Mittal and Kumar (2003) and Aljure et al. (2015), although at much lower Re_D < 5000, argued in favour of the widening of the wake at larger spin ratios $k \geq 4$, and linked it with the slow vorticity built up in the region near the separation point and shedding of vortices in the direction of rotation. If this same phenomena is occurring at current Reynolds numbers can not be confirmed due to FOV limitations. However, some increase of TKE in this region is observed, as TKE values remain to increase in the region close to the cylinder surface and near the separation point.

Additionally, Aljure et al. (2015) showed that when the circumvolving layer is formed, the appearance and growing of TG vortices on the surface of the cylinder across the full span with an increase of the spin ratio, is also taking place. The planar PIV of the current experiment does not allow to identify such vortices fully, however the growing turbulence intensity close to the cylinder surface does hint to such behaviour.

Based on speculation, another possible explanation or factor in favour of clockwise movement of the separation point region might be caused by the increased blockage of the rotating boundary layer. As the rotating boundary layer grows, blockage ratio increases, the gap between nozzle and model is squeezed more, which in turn increases the tunnel jet velocity in between the smaller gap allowing for the wake to be blown downstream.

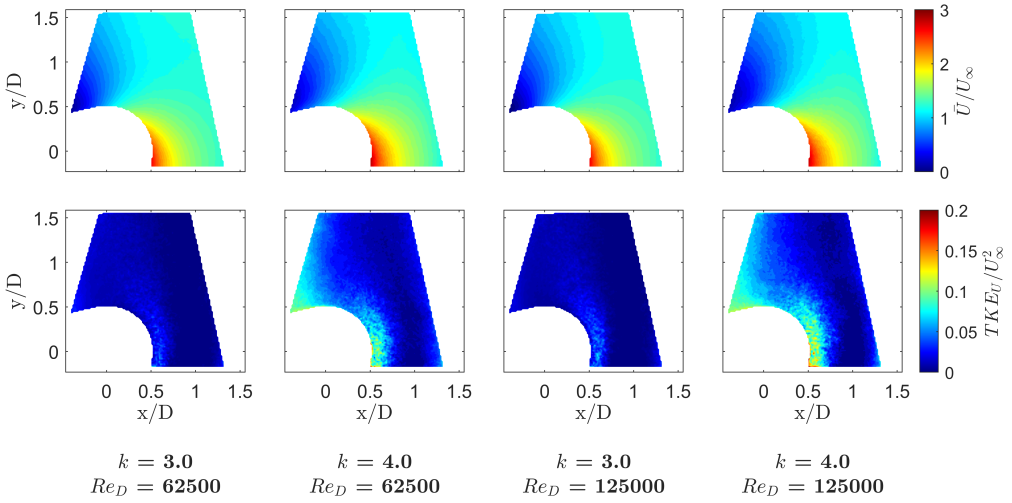

Figure 5.32: Comparison of non-dimensionalised mean velocity magnitude, $\bar{U}/U_\infty$ (top), and non-dimensionalised mean Turbulent Kinetic Energy, TKE_U/U_∞^2 (bottom), between Re_D = 62500 and 125000 for k = 3.0 and 4.0.

5.2.5. Regime of nozzle-model gap interference

The same trend as for 3.0 ≤ k ≤ 4.0 continues when increasing the spin ratio further. Figure 5.33 shows sequences of non-dimensionalised mean velocity magnitude and non-dimensionalised mean TKE at Re_D = 62500 in the range of 4.0 ≤ k ≤ 8.0. At these spin ratios the visible flow field has been turned completely, where the majority of the flow field is going into a near vertical and negative x-direction against the direction of the incoming flow, see Figure 5.34. The separation point region slowly disappears away from the surface of the cylinder and the FOV, indicating the rotating region around the cylinder is growing in size with the increase of the spin ratio, which has been similarly stated by Badalamenti (2010).

Within the rotating region, TKE values show an intense turbulent region in close proximity to the cylinder surface, which grows rapidly with the increase of the spin ratio and is possibly linked with the growth of TG vortices as stated before. At k = 8.0, non-dimensionalised mean TKE values in excess of 1.0 have been recorded, which is approximately 4 times larger than the maximum recorded values of TKE before k < 4. However, the slight variation in wall thickness of the cylinder skin and increasing strength of the residual unbalance at high spin ratios could be an factor in the growth of the TKE near the cylinder surface as well.

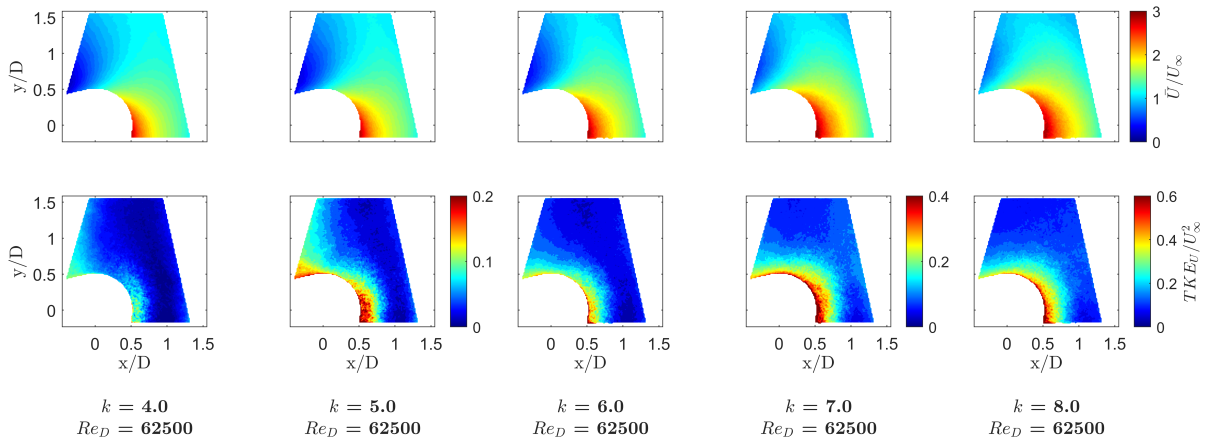

Figure 5.33: Development of the non-dimensionalised mean velocity magnitude, $\bar{U}/U_\infty$ (top), and non-dimensionalised mean Turbulent Kinetic Energy, TKE_U/U_∞^2 (bottom), at Re_D = 62500 and 4.0 ≤ k ≤ 8.0. Note the change in colourbar limits.

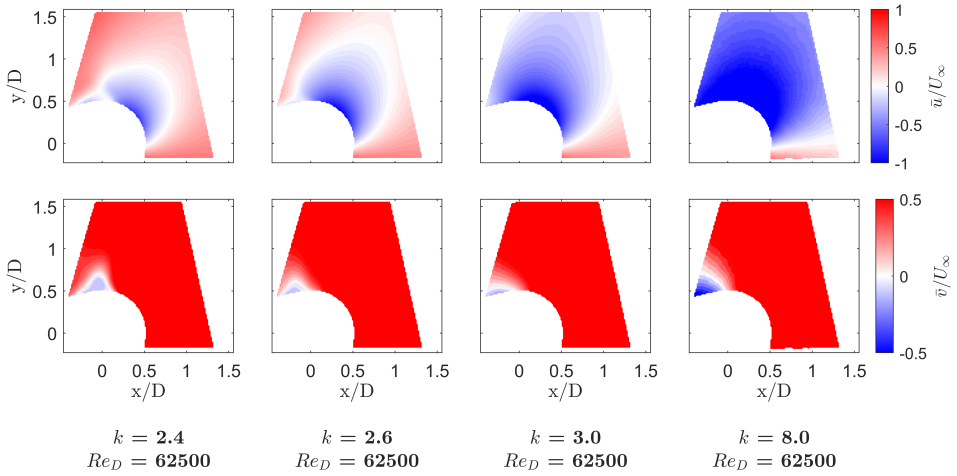

Figure 5.34: Development of the non-dimensionalised mean velocity components, $\bar{u}/U_\infty$ (top) and $\bar{v}/U_\infty$ (bottom), at Re_D = 62500 and 2.4 ≤ k ≤ 8.0. Note the colourbar limits are set to allow for qualitative comparison.

The high velocity region on the backside of the cylinder increases in size with the increase of the spin ratio, however interestingly the maximum velocity for $k \geq 5$ only increases slightly or even decreases, e.g. $\bar{U}/U_\infty$ = 2.85, 2.87, 2.94, 3.01, 2.96 for k = 4.0, 5.0, 6.0, 7.0, 8.0 respectively. At the same k = 5 the lift coefficient curve also plateaus before starting to decrease, whereas the drag coefficient starts to decrease more rapidly. Perhaps the point of absolute maximum velocity on the bottom side of the cylinder, located outside of the FOV, which is associated with the point of lowest pressure, moves to a more clockwise position. If true, the forward stagnation point is also likely to have moved in clockwise direction, tilting the system clockwise and in turn results in the lift force to act more in the positive x-direction.

Speculating on a possible cause, the large blockage ratio and subsequent interference effects might facilitate such behaviour. The separated flow region is located in close proximity to the upper side of the nozzle exit and the rotating boundary layer grows asymmetrically in size, where it pushes the separation point further away from the surface at high spin ratios. As such the blockage ratio increases in particular on the upper side of the cylinder, which in turn increases its ability to block of the upper part of the nozzle. Consequently, the flow in front of the cylinder is turned to a larger extent towards the lower side of the cylinder and guided through the lower nozzle-model gap, where flow velocity increases rapidly and pressure drops. As a result a tilt of the force system is realised. Figure 5.35 present a schematic of this situation, where the rotating boundary layer and separated region block off the upper nozzle-model gap, shifting the forward stagnation point clockwise, which results in a tilt of the force system. The vector plot shows the extent of the flow deflection at the largest k = 8.0.

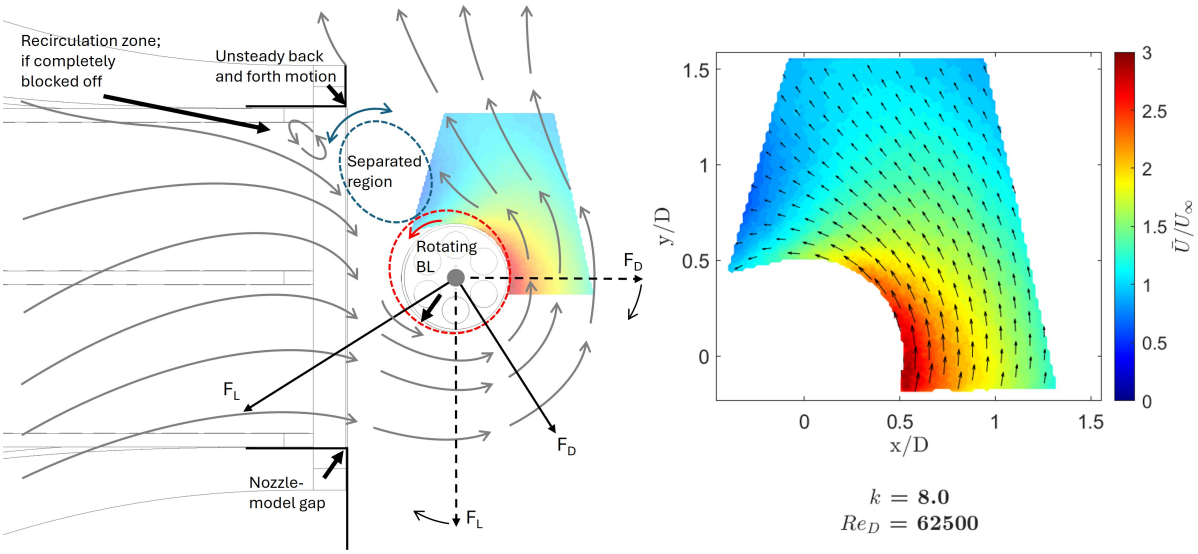

Figure 5.35: Schematic of flow deflection and force vector tilt at Re_D = 62500 and k > 3.0, including velocity vector plot on mean velocity magnitude contours at Re_D = 62500 and k = 8.0. The rotating boundary layer is indicated in red and the separated region in blue. Note for the purpose of explaining, effects are exaggerated and at its most extreme.

Further reinforcement of these statements follows from the measurements by the pitot-static probe near the lower nozzle-model gap, see Figure 4.4. After an initial increase between $0 \leq k \leq 1.0$, the measured velocity plateaued for approximately $1.0 \leq k \leq 2.4$ and then started to rise again for $k >$ 2.4. This coincides with the formation of the rotating boundary layer and the mean wake settling to a position in close proximity of the upper nozzle-model gap. If this theory is proven to be true, it will most likely be also present for closed wind tunnel testing at high blockage ratio. As such, the negative drag forces measured by Thom (1934) on his high lift configuration might be coming from the same effects.

The energy distributions of the first 20 spatial POD modes ϕ^n for Re_D = 62500 at $4.0 \leq k \leq 8.0$ are depicted in Figure 5.36. With an increase of the spin ratio, the energy distribution slowly flattens out, where the relative energies of the dominant modes are reducing. As such, the velocity fluctuations at high spin ratios consists solely out of random fluctuations in the current FOV. Consequently, coherent vortical structures as shown for k < 2.6 do no longer appear as was similarly the case for k = 3.0.

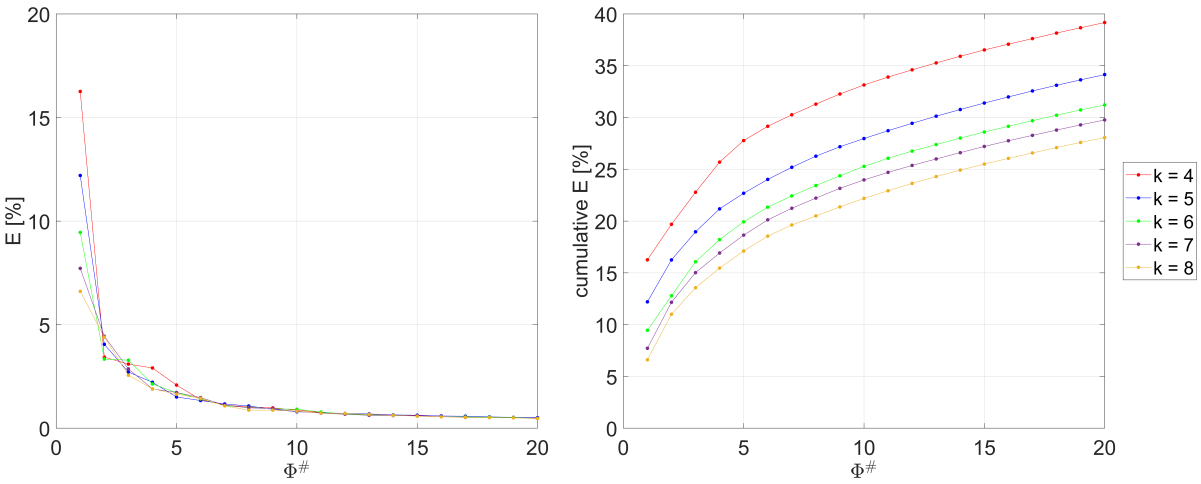

Figure 5.36: Energy distribution of the 20 most energetic spatial POD modes ϕ^n for Re_D = 62500 at 4.0 ≤ k ≤ 8.0.

Although coherent structures disappear, the flow field is not steady and the wake does not settle at a fixed position. By reconstructing the velocity field using the six most energetic modes, the main fluctuations outside of the rotating boundary layer in the flow field can be investigated by the reconstructed velocity components standard deviations, see Figure 5.37. If the actual velocity field is being used, the large amount of small random fluctuations in the rotating boundary layer, e.g. due to TG vortices, the higher order modes and the additional noise, causes the fluctuations outside of this layer to be hidden from the shown fields. Especially at high spin ratios as a result of the large growth of unsteadiness near the cylinder surface.

From Figure 5.37, a constant back and forth motion of the separated region into the FOV is observed, where the flow displaced by the rotation of the cylinder is working against the tunnel jet. This effect appears stronger with the increase of the spin ratio, as the cylinder becomes more effective in deflecting the flow field towards the upper nozzle-model gap. As the motion appears to be random, this would explain the flattening energy distributions of the fluctuating velocity field.

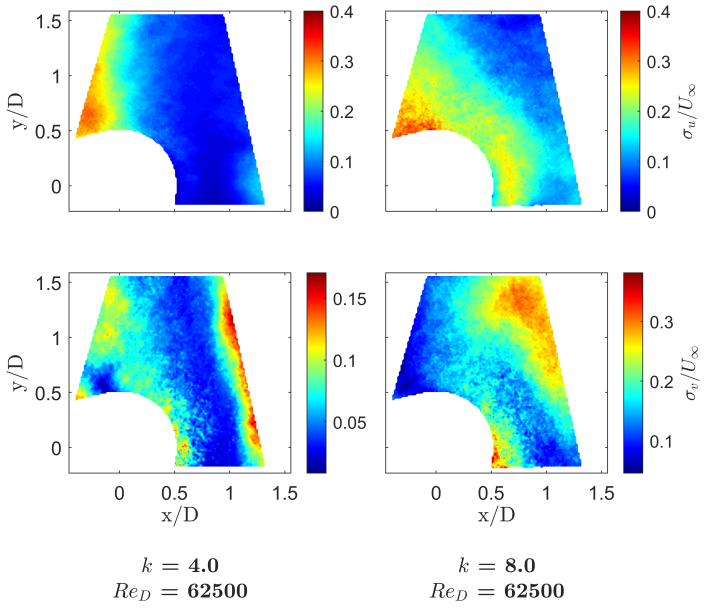

Figure 5.37: Development of the non-dimensionalised reconstructed velocity components standard deviations, σ_u/U_∞ (top) and σ_v/U_∞ (bottom), at Re_D = 62500 and k = 3.0 and 8.0 using the first six POD modes.

On the right and upper right regions of the FOV another area of elevated velocity fluctuations is shown. These fluctuations could be related to the deflection of the lower tunnel shear layer. In subsection 5.2.2 the upper tunnel shear layer appeared under the influence of the inverse Magnus effect in the FOV. Since at the current spin ratios force coefficients magnitudes are much larger, expectations are that the lower tunnel shear layer is deflected to an larger extent. Therefore, it is plausible that the lower tunnel shear layer is located in close proximity to the right boundary of the FOV. However, the tunnel shear layer does not yet appear in the mean velocity magnitude as has been shown before in Figure 5.33.

The large unsteadiness in close proximity to the cylinder surface and back and forth motion of the separated region is another cause of fluctuations in the force coefficients. As these velocity fluctuations become large with the increase of the spin ratio, the fluctuations in the force coefficients are expected to rise as well. In subsection 5.1.4, it was shown the standard deviation of the measured forces to rise rapidly at high rotational frequencies, similarly between the different Reynolds numbers, regardless of the spin ratio. As such the cause of the large fluctuations in the forces are likely the result of the residual unbalance in the system. Perhaps, the unbalance and variation in wall thickness of the cylinder surface are then the main reason of why the flow becomes unsteady and large standard deviations are shown near the cylinder surface.

However, at k = 4.0 the standard deviations of the velocity components between Re_D = 62500 and 125000 as illustrated in Figure 5.38 does not show significant difference, eventhough the rotation frequency at Re_D = 125000 in comparison is twice as large. As such the largely increased standard deviations in close proximity to the cylinder surface are still expected to be the result of the formation and growing of TG vortices. Whereas, the back and forth motion of the flow field outside of the rotating boundary is potentially the combined result of the residual unbalance and tunnel interference effects.

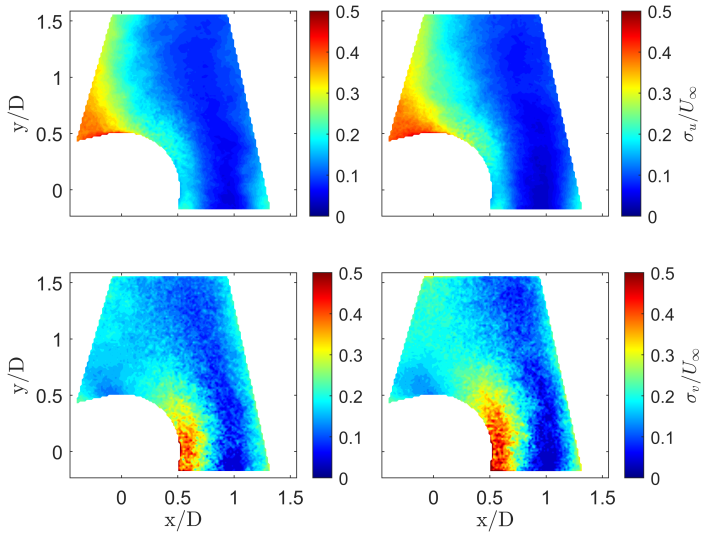

Figure 5.38: Development of the non-dimensionalised velocity components standard deviations, σ_u/U_∞ (top) and σ_v/U_∞ (bottom), for Re_D = 62500 and 125000 at k = 4.0.

6

Conclusion

This report concerned the development, realisation and characterisation of an experimental setup to allow testing of rotating cylinders in the SLT wind tunnel facility up to critical Reynolds numbers. In particular, large scale wind assisted ship propulsion design constraints were considered for the development of the setup. An initial experimental campaign has been performed, using the new experimental setup, to characterise the aerodynamics of a two-dimensional rotating cylinder, such that reference data is generated for future comparisons. Alongside, the viability of high blockage ratio testing of rotating cylinders has been evaluated to enable high Reynolds number testing in smaller scale wind tunnel facilities. The following main research question stood central in the presented report;

Main research question

"What are the aerodynamic characteristics of a two-dimensional rotating cylinder in uniform subsonic flow at subcritical Reynolds numbers and high blockage ratio?"

The aerodynamic characteristics are obtained by the utilisation of force measurements, encoder rpm readouts, and low speed planar PIV flow visualisation. By comparison with available data in literature, the existence of known aerodynamic characteristics of a rotating cylinder were tested and discrepancies were analysed. POD analysis enabled the visualisation of the flow fields dominant characteristics, where a particular focus was put on the identification of vortical structures.

The experiment has been performed in the newly configured open-return low turbulence SLT wind tunnel facility for subcritical Re_D = 62500, 125000 and 250000 at spin ratio ranges equal to $0 \leq k \leq 8$, $0 \leq k \leq 4$ and $0 \leq k \leq 2$ respectively. Comparable to full scale WASP applications and existing literature, an aspect ratio of the cylinder model equal to 4.5 was chosen. As a result, the area blockage ratio reached an unconventional high 33%.

In general, the aerodynamic characteristics followed the known experimental trends up to spin ratios of 2.5, with the exception of the differences in the force coefficient magnitudes, owing to the peculiarities of the experimental setup and wind tunnel interference effects, as has been shown throughout section 5.1. The open test section with side walls installed, resulted in a force coefficient behaviour that resembles closest to the three-dimensional cylinder with stationary endplates at subcritical Reynolds numbers up to k = 2.5.

The stationary cylinder case, see subsection 5.2.1, presented lower than anticipated drag coefficients for Re_D = 62500 and 125000 at C_D = 0.76 and 0.72 respectively. The results for Re_D = 250000 being an outlier with C_D = 0.9 and C_L = -0.26, which is speculated to be a consequence of wind tunnel shear layer interaction with the support structure, deflecting the flow field around the cylinder, and causing the drag force to act slightly in the direction of the lift as the force measurement system remains fixed in place. The increased drag coefficient is speculated to be the result of increased nozzle interference due to larger pressure built up in front of the cylinder that extends into the nozzle. The flow fields showed

large bluff body wakes with laminar separation for all tested Reynolds numbers, with in comparison a slight deflection of the near-wake for Re_D = 250000. Additionally, vortical structures are present in the shear layer and are shown to be more coherent and larger in size for Re_D = 250000.

In the range $0 \leq k \leq 0.8$, the Reynolds number is influential to the aerodynamic characteristics, see subsection 5.2.2. At low spin ratios, depending on the Reynolds number, the regular Magnus effect dominates the flow field. A large bluff body wake and shedding of vortices persist, where the separation points and near-wake are deflected in the direction of rotation. As a result, both the lift and drag coefficient increases. With an increase of the spin ratio vortices form, and turbulent kinetic energy increases, in close proximity to the back side of the cylinder. Consequently, the drag coefficient rises rapidly within a confined range of spin ratios, as has been captured at k = 0.6 and Re_D = 62500, where C_D = 1.2. A further increase of the spin ratio results in the advancing side boundary layer to transition to the turbulent state with strong indications of the presence of a laminar separation bubble. The transition effects results in a drop in the lift and drag coefficients, with the former owing to prolonged boundary layer attachment and laminar separation bubble formation on the advancing side, and the latter due to reduction of the near-wake size and delayed vortex formation. With an increase of the Reynolds number, the transition effects are stronger and occur at lower spin ratios. As such, negative lift coefficients can be obtained at the larger subcritical Reynolds numbers. Additionally, with strong negative lift coefficients, the tunnel shear layer appears in the FOV. This showed the ability of the rotating cylinder to substantially deflect the tunnel jet when operating at such large blockage ratios.

Beyond k > 0.8, advancing side boundary layer transition has taken place for all Re_D. The force coefficient behaviour and flow field topology showed great similarities with a further increase of the spin ratio between the different Reynolds numbers, see subsection 5.2.3. Between $0.8 \leq k \leq 2.2$, the regular Magnus effect causes the lift and drag coefficients to increase with an increase of the spin ratio, where flow velocity increases on the backside of the cylinder, separation points move towards each other and wake deflects with the direction of rotation. Periodic shedding of vortical structures becomes weaker and remains up to k = 2.0. The retreating side boundary layer shows signs of transition with increased turbulent kinetic energy in the shear layer and changes in its inclination after a certain spin ratio is reached. This burst of turbulent kinetic energy occurs, as for the advancing side boundary layer, at lower spin ratios with an increase of the Reynolds number. After occurrence of this phenomenon, for all tested Reynolds number, even greater similarity between the flow fields is achieved.

In the range $2.2 \leq k \leq 2.6$, a knee in the lift and drag coefficient curves is recorded, which is at lower spin ratios compared to previous similar experiments, e.g. $k \approx 3$. The flow fields showed this to be the result of the mean wake settling to a position at the front of the cylinder in proximity to the upper nozzle-model gap, the coming together of the separation points and creation of the rotating boundary layer around the circumference of the cylinder, see subsection 5.2.4. Propagation of periodically shed vortical structures is no longer present at k = 2.2, and for k = 2.6 vortical structures in the sense of cylinder rotation cease. This coincides with the coming together of the separation points and marks the end of the knee in the force coefficient curves.

For k > 2.6 flow fields between Re_D = 62500 and 125000 start to deviate, where the former showed a larger deflection of the separated region, see subsection 5.2.4 and subsection 5.2.5. It is speculated that the lower energy of the tunnel jet at Re_D = 62500 is less effective in preventing the separated region to block off the upper nozzle-model gap, causing the deviation between the two cases. In close proximity to cylinder surface the rotating boundary layer grows with the increase of the spin ratio. This region has shown to contain high values of turbulent kinetic energy and has been linked with the formation of spanwise Taylor-Görtler vortices. As a result, the blockage ratio increases and the rotating cylinder becomes more effective in deflecting and working against the tunnel jet.

At last, the captured flow field for k > 3 is fully moving in the opposite direction of the tunnel jet. Large negative mean drag coefficients were recorded and is speculated to be the result of a tilt in the force system, owing to the large blockage ratio and close nozzle proximity. Namely, unsteady nozzle-model gap interactions with the cylinder wake results in blocking of the upper gap, whereas on the other side an increasingly large volume of air is accelerated through the lower gap. Consequently, the outflow

conditions are changed and results in tilting of the system, where the large lift force is partially acting in the negative x-direction. The unsteady nature of this phenomenon results in large fluctuations in the instantaneous force coefficients. It is expected that similar interference effects occur for closed section testing at high spin ratios and the extent of its influence to be dictated by the blockage ratio.

7

Recommendations

The presented research concerned the design of an experimental setup and initial experimental campaign of a two-dimensional rotating cylinder at high blockage ratio, this chapter will provide recommendations on both topics separately in section 7.1 and section 7.2 respectively.

7.1. Recommendations on the experimental setup

As discussed, during the course of the project and the initial experimental campaign, various inconveniences were encountered that altered the quality and contents of the research performed. The following list of recommendations on the improvements of the experimental setup and its operation procedure is presented below.

- **Machining of cylinder surface**; As a consequence of multiple delays in the manufacturing process of the cylinder model, the imperfect cylinder skin showed to have an approximate 1mm variation of thickness at the centre plane. To prevent unwanted excitation of the boundary layer and improve balancing performance, machining of the cylinder surface on the current or future models is highly advised.

- **Reduce cylinder surface light reflections**; Although the centre section was covered with low reflective black matte vinyl, some reflections were still captured on the PIV recordings. Extending the coverage with additional vinyl or applying low reflective paint on the surface would improve PIV image quality.

- **Reduce support structure interference**; As the experimental setup proved to be sufficiently stiff, the additional spanwise support beam could be lowered or removed fully to prevent potentially unwanted interference effects. As such the discrepancies at the stationary case might be resolved.

- **Internal ribs fitting**; In case a new cylinder model of different dimensions is desired, it is advised to ensure the internal ribs are of equal size with as little imperfections as possible, e.g. opting for CNCed components instead of laser cutting. Adjustability as well as spanwise outer cylinder alignment will be improved.

- **Balancing at max rpm**; As the balancing procedure is now fully established and understood, see section 3.11, final balancing should be performed at the maximum rpm of the given experiment. As such, the design Reynolds number and spin ratios ranges can be achieved in the future.

- **Test at higher Reynolds numbers**; In case of a properly balanced cylinder, the full range of design Reynolds numbers up to the maximum critical Re_D = 437500 can be achieved for spin ratios of $k \leq 3$. At the highest Reynolds numbers the uncertainty in the force coefficient results are reduced significantly, which makes it more suitable for investigating instantaneous effects.

- **Increase nozzle outlet proximity**; To reduce the effects of nozzle interference, it is advised to increase the distance of the model to the nozzle exit plane. A few example solutions are as follows in order of increasing effort; turn the setup 180° around, place the cylinder more central in the setup by manufacturing new windows, or extend the sidewalls to place the setup more downstream.
- **Determination of the freestream velocity**; When available it is advised to use the SLT wind tunnel facility built in delta pressure measurements for the determination of the freestream velocity. The actual test Reynolds numbers can then be more accurately defined.

Furthermore, it is ill-advised to increase the blockage ratio any further. Especially, when opting for adding additional flow control devices. If such an experiment is desired, it is advised to install a smaller scale cylinder. However, given the same Reynolds number, with a smaller cylinder diameter the rotational frequency must be increased to obtain sufficiently large spin ratios. In such a case, and after ensuring a properly balanced system, the maximum rpm should not exceed 10000 due to component limitations.

7.2. Recommendations for future research

Following the general aerodynamic characterisation of the experimental setup and the analysis of the results as outlined in chapter 5, a selection of speculative theories were established. As a consequence of the limitations in the FOV, which could be enlarged or altered depending on future research, these theories bring further questions along and are yet to be proven. Recommendations for future research on rotating cylinders thus follow from these theories and are listed below.

- **Investigation into retreating side boundary layer state**; The sudden increase in turbulent kinetic energy and change in inclination of the retreating side shear layer between a spin ratio of $1.0 \leq k < 1.8$ depending on the Reynolds number, strongly hints to a change in state of the retreating side boundary layer. Whether a possible relaminarisation occurs or transition to the turbulent state is reached is unclear. Additional flow field measurements in close proximity to the cylinder surface would be required to proof the state and mechanisms involved.
- **Investigation into nozzle-model gap interaction**; It was speculated that significant nozzle interference effects started to develop at large enough spin ratios, where the wake of the cylinder has moved in close proximity to the nozzle-model gap. The blocking off one side and increased flow acceleration on the other side, is believed to result in a tilt of the force system and altered outflow conditions. Visualising these areas through additional PIV measurements could provide more insights into this particular phenomena.
- **Investigation into the rotating boundary layer**; The rotating boundary layer with the current experiment and FOV is not sufficiently explored. The large turbulent kinetic energy within this region is believed to be the result of Taylor-Görtler vortex formation and could be investigated further. Furthermore, the region within the rotating boundary layer in close proximity to the separation point is another area of interest. The complete disappearance of vortex shedding as well as the potential presence of the one-sided vortex mode at high spin ratios could not be confirmed due to the FOV limitations.
- **Investigation into cylinder-wall junction**; The effects of the stationary side wall junction, spillage and wind tunnel boundary layer interaction on the flow topology and force coefficient is unclear. These investigations could be extended to the influence of larger boundary layers and applied aerodynamic topics, e.g. effects of the Earths boundary layer when placed on the deck of a ship. Furthermore, the potential presence of a wall bounded vortex system or complete suppression of the tip vortex could then be confirmed.
- **Blockage ratio sensitivity**; Testing at various blockage ratios, while keeping the range of Reynolds numbers and spin ratios the same provides further insights on the extend of its effects. Ideally, the aspect ratio should remain the same, which would imply a change in the span of the cylinder. The sensitivity of the blockage ratio on the flow topology and force coefficient magnitudes could then be determined. Additionally, the blockage ratio and nozzle proximity interaction is an important factor to consider.

- **Nozzle proximity sensitivity**; Testing at various distances to the nozzle outlet, while keeping the range of the Reynolds number and spin ratio as well as the aspect ratio the same. The sensitivity of the nozzle-model gap interaction can then be tested. Additionally, the blockage ratio and nozzle proximity interaction is an important factor to consider.
- **Effects of open and closed section testing**; The effects of blockage ratio on closed and open section testing is a further step in the investigation on interference effects for rotating cylinders. In a closed section the gap between wind tunnel wall and model could react in a similar manner or worse as has been speculated for the nozzle-model gap interaction. By performing the same tests with open and closed sections this could be easily confirmed.

Finally, additional scarcely investigated topics, following the information presented in chapter 2, that are not directly related to the performed research, but are of importance to the aerodynamics of a rotating cylinder, are;

- **Compressibility effects**; The effects of compressibility are mostly untouched in rotating cylinder research as was discussed in subsection 2.2.11. Only at the lower Reynolds regimes Teymourtasha and Salimipour (2017) showed numerically that these effects cannot be ignored. At the higher Reynolds regimes these effects have not been quantified nor mentioned. As Flettner rotors are becoming larger in size while also running at spin ratios of up to 5, this topic is expected to grow in importance, especially when considering model scale testing. Therefore, experimental studies at high spin ratios and freestream velocity can potentially be a good direction to go in for future research.
- **Freestream turbulence effects**; Effects of freestream turbulence on non-rotating cylinders have been briefly discussed in subsection 2.1.3, however for rotating cylinders it is believed no such studies have been performed at present day. As freestream turbulence in the Earths boundary layer is for certain a factor in real life WASP applications, and depending on the magnitude of its effects also a potential source of scatter in existing experimental data, further investigations on this topic could be of great value.

Bibliography

Al-Garni, A. Z., Al-Garni, A. M., Ahmed, S. A., & Sahin, A. Z. (2000). Flow control for an airfoil with leading-edge rotation: An experimental study. *Journal of Aircraft*, *37*(4), 617–622. https://doi.org/10.2514/2.2673

Aljure, D., Rodríguez, I., Lehmkuhl, O., Pérez-Segarra, C., & Oliva, A. (2015). Influence of rotation on the flow over a cylinder at re=5000 [Special Issue devoted to the 10th Int. Symposium on Engineering Turbulence Modelling and Measurements (ETMM10) held in Marbella, Spain on September 17-19, 2014]. *International Journal of Heat and Fluid Flow*, *55*, 76–90. https://doi.org/https://doi.org/10.1016/j.ijheatfluidflow.2015.07.015

Anderson, K., & Bows, A. (2012). Executing a scharnow turn: Reconciling shipping emissions with international commitments on climate change. *Carbon Management*, *3*(6), 615–628. https://doi.org/10.4155/cmt.12.63

Astarita, T. (2007). Analysis of weighting windows for image deformation methods in piv. *Experiments in Fluids*, *43*, 859–872. https://doi.org/10.1007/s00348-007-0314-2

Aydemir, B., Knott, A., Altintas, A., Arrhén, F., Averlant, P., Germak, A., Hiti, M., Kumme, R., Malengo, A., Martín, M., Röske, D., & Vavrecka, L. (2022, March). *Guidelines on the uncertainty of force measurements euramet calibration guide no. 4 version 3.0 (02/2022)*. EURAMET.

Badalamenti, C. (2010). *On the application of rotating cylinders to micro air vehicles* [Unpublished], City University London. https://openaccess.city.ac.uk/id/eprint/8693/

Badalamenti, C., & Prince, S. (2008a). The effects of endplates on a rotating cylinder in crossflow. *Collection of Technical Papers - AIAA Applied Aerodynamics Conference*. https://doi.org/10.2514/6.2008-7063

Badalamenti, C., & Prince, S. (2008b). Vortex shedding from a rotating circular cylinder at moderate sub-critical reynolds numbers and high velocity ratio. *ICAS Secretariat - 26th Congress of International Council of the Aeronautical Sciences 2008, ICAS 2008*, *6*, 404–414. https://www.scopus.com/inward/record.uri?eid=2-s2.0-84878452017&partnerID=40&md5=72b24e2acba381c6b65759a55a4315ad

Bain News Service. (n.d.). Buckau [Retrieved from the Library of Congress]. https://www.loc.gov/item/2014717912/

Basu, R. (1985). Aerodynamic forces on structures of circular cross-section. part 1. model-scale data obtained under two-dimensional conditions in low-turbulence streams. *Journal of Wind Engineering and Industrial Aerodynamics*, *21*(3), 273–294. https://doi.org/https://doi.org/10.1016/0167-6105(85)90040-6

Bearman, P. (1969). On vortex shedding from a circular cylinder in the critical reynolds number region. *Journal Fluid Mechanics*, *37*, 577–87. 1, 4, 5, 6, 7.

Bearman, P., & Morel, T. (1983). Effect of free stream turbulence on the flow around bluff bodies. *Progress Aerospace Sciences*, *20*, 97–123. 14.

Bergeson, L., & Greenwald, C. (1985). Sail assist developments 1979–1985. *Journal of wind engineering and industrial aerodynamics*, *19*(1-3), 45–114.

Berkooz, G., Holmes, P., & Lumley, J. (1993). The proper orthogonal decomposition in the analysis of turbulent flows. *Annual Review of Fluid Mechanics*, *25*, 539–575. https://doi.org/10.1146/annurev.fl.25.010193.002543

Bérnard, H. (1908a). A 'cinematographic' study of eddies and ripples produced by towed obstacle (in french). *Comptes Rendus Academie des Sciences*, *147*, 970–2. 1, 3, 5.

Bérnard, H. (1908b). Formation of centres of circulation behind a moving obstacle (in french). *Comptes Rendus Academie des Sciences*, *147*, 839–42. 1, 3, 5.

Betz, A. (1925). *The "magnus effect," the principle of the flettner rotor* (tech. rep.).

Bordogna, G., Muggiasca, S., Giappino, S., Belloli, M., Keuning, J., & Huijsmans, R. (2020). The effects of the aerodynamic interaction on the performance of two flettner rotors. *Journal of Wind Engineering and Industrial Aerodynamics*, *196*. https://doi.org/10.1016/j.jweia.2019.104024

Bordogna, G., Muggiasca, S., Giappino, S., Belloli, M., Keuning, J., Huijsmans, R., & Van t Veer, A. (2019a). Experiments on a flettner rotor at critical and supercritical reynolds numbers. *Journal of Wind Engineering and Industrial Aerodynamics*, *188*, 19–29. https://doi.org/10.1016/j.jweia.2019.02.006

Bordogna, G., Muggiasca, S., Giappino, S., Belloli, M., Keuning, J., Huijsmans, R., & Van t Veer, A. (2019b). Wind-tunnel experiments on a large-scale flettner rotor. *Lecture Notes in Civil Engineering*, *27*, 110–123. https://doi.org/10.1007/978-3-030-12815-9_9

Bordogna, G., Rijkens, A., & Van der Kolk, N. (2022). Performance evaluation of a flettner rotor with a flap. *27th International HISWA Symposium, Amsterdam, The Netherlands*.

Bozhkov, V., Vasilev, L., & Zhigulev, S. (1980). Features of subsonic cross flow past a circular cylinder. *Izvestiya Akademii Nauk SSSR Mekhanika Zhidkostii Gaza*, *2*, 154–9. 6.

Busemann, A. (1932). Messungen an rotierenden zylindern. In *Lfg. 4* (pp. 101–105). Oldenbourg Wissenschaftsverlag. https://doi.org/10.1515/9783486764406-018

Chen, W., & Rheem, C. (2019). Experimental investigation of rotating cylinders in flow. *Journal of Marine Science and Technology (Japan)*, *24*(1), 111–122. https://doi.org/10.1007/s00773-018-0535-5

Chen, W., Wang, H., & Liu, X. (2023). Experimental investigation of the aerodynamic performance of flettner rotors for marine applications. *Ocean Engineering*, *281*, 115006. https://doi.org/https://doi.org/10.1016/j.oceaneng.2023.115006

Chopra, G., & Mittal, S. (2023). Laminar separation bubble on a rotating cylinder in uniform flow. *Physics of Fluids*, *35*(4). https://doi.org/10.1063/5.0141336

Clayton, B. (1985). Bwea initiative on wind assisted ship propulsion (wasp). *Journal of Wind Engineering and Industrial Aerodynamics*, *19*(1), 251–276. https://doi.org/https://doi.org/10.1016/0167-6105(85)90064-9

Coleman, H., & Steele, W. (2009). *Experimentation, validation, and uncertainty analysis for engineers, 3rd ed.* John Wiley Sons. https://doi.org/10.1002/9780470485682

Collin, C. (2019). *Interference effects in automotive, open jet wind tunnels*. Technische Universität München. https://books.google.nl/books?id=RU5y0AEACAAJ

Coutanceau, M., & Menard, C. (1981). Visualisation of the flow development around a circular cylinder impulsively subjected to a combined motion of rotation and translation. *Flow visualisation III*, *ed. Yang*, 54–58.

Diaz, F., Gavalda, J., Kawall, J. G., Keffer, J. F., & Giralt, F. (1985). Asymmetrical wake generated by a spinning cylinder. *AIAA Journal*, *23*(1), 49–54. https://doi.org/10.2514/3.8870

Diaz, F., Gavaldà, J., Kawall, J. G., Keffer, J. F., & Giralt, F. (1983). Vortex shedding from a spinning cylinder. *The Physics of Fluids*, *26*(12), 3454–3460. https://doi.org/10.1063/1.864127

Ericsson, L. (1988). Moving wall effects in unsteady flow. *Journal of Aircraft*, *25*(11), 977–990. https://doi.org/10.2514/3.45691

Everts, M., Ebrahim, R., Kruger, J., Miles, E., Sharifpur, M., & Meyer, J. (2014). Turbulent flow across a rotating cylinder with surface roughness. *International Conference on Heat Transfer, Fluid Mechanics and Thermodynamics*.

ExamplePrograms. (2023, November 27th). Two plane balancing example with daqmx [online forum post]. https://forums.ni.com/t5/Example-Code/Two-Plane-Balancing-Example-with-DAQmx/ta-p/3996066

Fischer, O. (2018). *Investigation of correction methods for interference effects in open-jet wind tunnels* (1st ed.). Springer Vieweg Wiesbaden. https://doi.org/10.1007/978-3-658-21379-4

Hackett, J. (1996). Tunnel-induced gradients and their effect on drag. *AIAA Journal*, *34*, 2575–2581.

Huang, L., Song, Q., Zhang, R., Wang, K., & Ma, R. (2023). Study of the influence of rotor shape on the aerodynamic characteristics of flettner rotor. *Advances in Transdisciplinary Engineering*, *40*, 798–804. https://doi.org/10.3233/ATDE230543

Hunt, J., Wray, A., & Moin, P. (1988). Eddies, streams, and convergence zones in turbulent flows. *Studying Turbulence Using Numerical Simulation Databases*, *1*, 193–208.

International Chamber of Shipping. (2014). Shipping, world trade and the reduction of co2 emissions [Accessed on February 22th, 2024].

International Chamber of Shipping. (2024a). Advantages of a global maritime ghg pricing mechanism covering all ghg emissions as part of a basket of measures [Accessed on February 22th, 2024]. https://www.ics-shipping.org/search/GHG

International Chamber of Shipping. (2024b). Zero emission shipping fund proposal submitted to un to deliver on shipping's net zero targets [Accessed on February 22th, 2024]. https://www.ics-shipping.org/press-release/zero-emission-shipping-fund-proposal-submitted-to-un-to-deliver-on-shippings-net-zero-targets/

International Maritime Organization. (2020). Fourth greenhouse gas study [Accessed on March 20th, 2024]. https://www.imo.org/en/ourwork/Environment/Pages/Fourth-IMO-Greenhouse-Gas-Study-2020.aspx

International Maritime Organization. (2023). Imo's work to cut ghg emissions from ships [Accessed on February 22th, 2024]. https://www.imo.org/en/MediaCentre/HotTopics/Pages/Cutting-GHG-emissions.aspx

Jaminet, J., & Van Atta, C. (1969). Experiments on vortex shedding from rotating circular cylinders. *AIAA Journal*, *7*(9), 1817–1819. https://doi.org/10.2514/3.5407

Jiangping, H., Yanxia, W., Jinfang, W., & Jingpu, C. (2019, May). The dynamic performance of a rotating frustum of a cone. In M. Felli & C. Leotardi (Eds.), *Proceedings of the sixth international symposium on marine propulsors - smp'19* (pp. I–192). National Research Council of Italy.

Karabelas, S., Koumroglou, B., Argyropoulos, C., & Markatos, N. (2012). High reynolds number turbulent flow past a rotating cylinder. *Applied Mathematical Modelling*, *36*(1), 379–398. https://doi.org/10.1016/j.apm.2011.07.032

Kaushik, M. (2019). Potential flow theory. In *Theoretical and experimental aerodynamics* (pp. 107–126). Springer Singapore. https://doi.org/10.1007/978-981-13-1678-4_4

Kelly, H., & Van Aken, R. (1956). The magnus effect at high reynolds numbers. *Journal of the Aeronautical Sciences*, *23*, 1053–1054.

Kolář, V. (2007). Vortex identification: New requirements and limitations [Including Special Issue of Conference on Modelling Fluid Flow, Budapest]. *International Journal of Heat and Fluid Flow*, *28*(4), 638–652. https://doi.org/https://doi.org/10.1016/j.ijheatfluidflow.2007.03.004

Krahn, E. (1956). Negative magnus force. *Journal of the Aeronautical Sciences*, *23*, 377–378.

Kumar, S., Cantu, C., & Gonzalez, B. (2011). Flow past a rotating cylinder at low and high rotation rates. *Journal of Fluids Engineering, Transactions of the ASME*, *133*(4), 41201–1–41201–9. https://doi.org/10.1115/1.4003984

Kussaiynov, K., Tanasheva, N., Turgunov, M., Shaimerdenova, G., & Alibekova, A. (2015). The effect of porosity on the aerodynamic characteristics of a rotating cylinder. *Modern Applied Science*, *9*(2), 215–222. https://doi.org/10.5539/mas.v9n2p215

Kwok, K. (1986). Turbulence effect on flow around circular cylinder. *Journal of Engineering Mechanics*, *112*(11). https://doi.org/10.1061/(ASCE)0733-9399(1986)112:11(1181)

Kwon, C., Yeon, S., Kim, Y., Kim, Y., Kim, Y., & Kang, J. (2022). A parametric study for a flettner rotor in standalone condition using cfd. *International Journal of Naval Architecture and Ocean Engineering*, *14*, 100493. https://doi.org/https://doi.org/10.1016/j.ijnaoe.2022.100493

Lafay, A. (1912a). Contribution expérimentale à l'aérodynamique du cylindre et á l'étude du phénomène de magnus. *Revue de Méchanique*, *30*, 417–42.

Lafay, A. (1912b). Sur 1'inversion du phenomene de magnus. *Comptes Rendus*, *151*, 61.

Lienhard, J. (1966). *Synopsis of lift, drag, and vortex frequency data for rigid circular cylinders*. Technical Extension Service, Washington State University. https://books.google.nl/books?id=qSlQGgAACAAJ

Liu, J., Ma, W., Jin, L., Liu, X., & Li, T. (2023). Experimental and numerical investigation on the wake flow and vortex shedding of a rotating circular cylinder. *Physics of Fluids*, *35*(7). https://doi.org/10.1063/5.0157682

Lock, C. (1929). The interference of a wind tunnel on a symmetrical body. *Aeronautical Research Council*, *Reports and Memoranda*(1275).

Lua, K., Lu, H., & Lim, T. (2018). Rotating elliptic cylinders in a uniform cross flow. *Journal of Fluids and Structures*, *78*, 36–51. https://doi.org/https://doi.org/10.1016/j.jfluidstructs.2017.12.023

Lumley, J. (1967). The structure of inhomogeneous turbulent flows. *Atmospheric Turbulence and Radio Wave Propagation*. https://cir.nii.ac.jp/crid/1571980075051475712

Ma, W., Liu, J., Jia, Y., Jin, L., & Ma, X. (2022). The aerodynamic forces and wake flow of a rotating circular cylinder under various flow regimes. *Journal of Wind Engineering and Industrial Aerodynamics*, *224*, 104977. https://doi.org/https://doi.org/10.1016/j.jweia.2022.104977

MacCamhaoil, M. (2016). Static and dynamic balancing of rigid rotors. *Bruel & Kjaer application notes, BO*, 0276–12.

Magnus, G. (1853). Ueber die abweichung der geschosse, und: Ueber eine auffallende erscheinung bei rotirenden körpern. *Annalen der physik*, *164*(1), 1–29.

Maskell, E. (1963). A theory of the blockage effects on bluff bodies and stalled wings in a closed wind tunnel. *Aeronautical Research Council*, *Reports and Memoranda*(3400).

Massaro, D., Karp, M., Jansson, N., Markidis, S., & Schlatter, P. (2024). Direct numerical simulation of the turbulent flow around a flettner rotor. *Scientific Reports*, *14*(1). https://doi.org/10.1038/s41598-024-53194-x

Matsui, T. (1981). Flow visualization studies of vortices. *Proceedings of the Indian Academy of Sciences Section C: Engineering Sciences*, *4*, 239–257.

Mercker, E., & Wiedemann, J. (1996). On the correction of interference effects in open jet wind tunnels. *SAE Technical Paper 960671*. https://doi.org/10.4271/960671

Michelis, T. (2017). Boundary layer separation: Diagnostics and control. *[Dissertation (TU Delft), Delft University of Technology]*. https://doi.org/10.4233/uuid:f5ecca35-71f6-4c99-92e8-a3004113fa53

Miller, M. (1976). Surface pressure measurements on a spinning wind tunnel model. *AIAA Journal*, *14*(12), 1669–1670. https://doi.org/10.2514/3.61510

Mittal, S., & Kumar, B. (2003). Flow past a rotating cylinder. *Journal of Fluid Mechanics*, *476*, 303–334. https://doi.org/10.1017/S0022112002002938

Muto, M., Tsubokura, M., & Oshima, N. (2012). Negative Magnus lift on a rotating sphere at around the critical Reynolds number. *Physics of Fluids*, *24*(1), 014102. https://doi.org/10.1063/1.3673571

Naumann, A., Morsbach, M., & Kramer, C. (1966). The conditions of separation and vortex formation past cylinders. *AGARD CP*, *4*, 539–574.

Naumann, A., & Pfeiffer, H. (1958). Investigation of vortex streets behind cylinders at high velocities. *Forschungsberichte Nord Rhein Westfalen*, *493*, 16.

Pearson, K. (1901). Liii. on lines and planes of closest fit to systems of points in space. *Philosophical Magazine Series 1*, *2*, 559–572. https://api.semanticscholar.org/CorpusID:125037489

Peller, H. (1986). Thermalfluid dynamic experiments with a heated and rotating circular cylinder in cross-flow. part 2.1, boundary layer profiles and location of separation points. *Experiments in Fluids*, *4*(4), 222–231. https://doi.org/https://doi.org/10.1007/BF00717818

Pezzotti, S., Nadal Mora, V., Sanz AndrÃ©s, A., & Franchini, S. (2020). Experimental study of the magnus effect in cylindrical bodies with 4, 6, 8 and 10 sides. *Journal of Wind Engineering and Industrial Aerodynamics*, *197*, 104065. https://doi.org/https://doi.org/10.1016/j.jweia.2019.104065

Pope, A., & Harper, J. (1966). *Low Speed Wind Tunnel Testing*. John Wiley & Sons, Inc., New York, NY.

Prandtl, L. (1925). Magnuseffekt und windkraftschiff. *Naturwissenschaften*, *13*, 93–108. https://doi.org/https://doi.org/10.1007/BF01585456

Prandtl, L., & Tietjens, O. (1934). *Applied hydro- & aeromechanics (translated in english by j.p. den hartog)*. Dover Publications Inc.

Prince, S., Holt, J., & Episkopou, P. (2016). Geometric roughness effects on the aerodynamic characteristics of a spinning cylinder in crossflow. https://api.semanticscholar.org/CorpusID:201919887

Proença, A., Gerhard, K., Prince, S., Garry, K., & Tragin, T. (2022). Roughness effects on the aerodynamic forces and wake flowfield of spinning cylinders. https://doi.org/10.2514/6.2022-4021

Radi, A., Thompson, M. C., Rao, A., Hourigan, K., & Sheridan, J. (2013). Experimental evidence of new three-dimensional modes in the wake of a rotating cylinder. *Journal of Fluid Mechanics*, *734*, 567–594. https://doi.org/10.1017/jfm.2013.486

Raffel, M., Kähler, C., Willert, C., Wereley, S. T., Scarano, F., & Kompenhans, J. (2018). *Particle image velocimetry: A practical guide* (3rd). Springer. https://doi.org/10.1007/978-3-319-68852-7

Rayleigh, J. (1877). On the irregular flight of a tennis ball. *Messenger of Mathematics*, *7*, 14–16.

Rayleigh, J. (1896). *The theory of sound. 2nd ed.* (Vol. 2). Dover.

Reid, E. (1924). *Tests of rotating cylinders* (tech. rep.).

Reynolds, O. (1883). An experimental investigation of the circumstances which determine whether the motion of water shall be direct or sinuous, and the law of resistance in parallel channels. *Philosophical Transactions*, *174*, 935–82.

Robins, B. (1805). *New principles of gunnery*. F. Wingrave, in the Strand. London.

Roshko, A. (1954). On the development of turbulent wakes from vortex streets. *National Advisory Committee for Aeronautics*, *NACA TR 1191*, 1, 3, 4, 5.

Roshko, A. (1961). Experiments on the flow past a circular cylinder at very high reynolds numbers. *Journal Fluid Mechanics*, *10*, 345–56. 1, 6, 7.

Rowley, C., & Dawson, S. (2017). Model reduction for flow analysis and control. *Annual Review of Fluid Mechanics*, *49*(Volume 49, 2017), 387–417. https://doi.org/https://doi.org/10.1146/annurev-fluid-010816-060042

Scarano, F., & Riethmuller, M. (2000). Advances in iterative multigrid piv image processing. *Experiments in fluids*, *29*(Suppl 1), S051–S060.

Schäfer, M., Turek, S., Durst, F., Krause, E., & Rannacher, R. (1996). Benchmark computations of laminar flow around a cylinder. In E. H. Hirschel (Ed.), *Flow simulation with high-performance computers ii: Dfg priority research programme results 1993–1995* (pp. 547–566). Vieweg+Teubner Verlag. https://doi.org/10.1007/978-3-322-89849-4_39

Scharnowski, S., & Kähler, C. (2020). Particle image velocimetry - classical operating rules from today's perspective. *Optics and Lasers in Engineering*, *135*, 106185. https://doi.org/https://doi.org/10.1016/j.optlaseng.2020.106185

Sciacchitano, A. (2019). Uncertainty quantification in particle image velocimetry. *Measurement Science and Technology*, *30*(9), 092001.

Seifert, J. (2012). A review of the magnus effect in aeronautics. *Progress in Aerospace Sciences*, *55*, 17–45. https://doi.org/10.1016/j.paerosci.2012.07.001

Sirovich, L. (1987). Turbulence and the dynamics of coherent structures. i - coherent structures. *Quarterly of Applied Mathematics*, *45(3)*, 561–571. https://doi.org/10.1090/qam/910463

Stojković, D., Schön, P., Breuer, M., & Durst, F. (2003). On the new vortex shedding mode past a rotating circular cylinder. *Physics of Fluids*, *15*(5), 1257–1260. https://doi.org/10.1063/1.1562940

Strouhal, V. (1878). Ueber eine besondere art der tonerregung (on an unusual sort of sound excitation). *Annalen der Physik und Chemie*, *3*(5(10)), 216–251.

Stull, R. (1988). *Turbulence kinetic energy, stability and scaling* (R. Stull, Ed.). Springer Netherlands. https://doi.org/10.1007/978-94-009-3027-8_5

Subramanya, K. (2005). *1000 solved problems in fluid mechanics (includes hydraulic machines)* (second ed.). Tata McGraw-Hill Education.

Sun, J., Zhang, B., Tang, Z., & Chen, W. (2016). Experimental study on the flow past a rotating cylinder with piv. *Shiyan Liuti Lixue/Journal of Experiments in Fluid Mechanics*, *30*(1), 81–90. https://doi.org/10.11729/syltlx20150037

Swanson, W. (1961). The magnus effect: A summary of investigations to date. *Journal of Basic Engineering*, *83*(3), 461–470. https://doi.org/10.1115/1.3659004

Taira, K., Brunton, S., Dawson, S., Rowley, C., Colonius, T., McKeon, B., Schmidt, O., Gordeyev, S., Theofilis, V., & Ukeiley, L. (2017). Modal analysis of fluid flows: An overview. *AIAA Journal*, *55*(12), 4013–4041. https://doi.org/10.2514/1.J056060

Takayama, S., & Aoki, K. (2005). Flow characteristics around a rotating grooved circular cylinder with grooved of different depths. *Journal of Visualization*, *8*, 295–303. https://doi.org/10.1007/BF03181548

Talluri, L., Nalianda, D., & Giuliani, E. (2018). Techno economic and environmental assessment of flettner rotors for marine propulsion. *Ocean Engineering*, *154*, 1–15. https://doi.org/https://doi.org/10.1016/j.oceaneng.2018.02.020

Tanaka, H., & Nagano, S. (1973). Study of flow around a rotating circular cylinder. bull. *Transactions of the Japan Society of Mechanical Engineers*, *16*, 234–43.

Tanasheva, N., Chirkova, L., Dyusembaeva, A., & Sadenova, K. (2020). Aerodynamic characteristics of a rotating cylinder in the form of a truncated cone. *Journal of Engineering Physics and Thermophysics*, *93*(3), 551–555. https://doi.org/10.1007/s10891-020-02152-1

Taneda, S. (1980). Visualisation of steady flows induced by a circular cylinder performing a rotary oscillation about an eccentric axis. *Journal Physics Society Japan*, *46*, 1935–1940.

Tennant, J. S., Johnson, W. S., & Krothapalli, A. (1976). Rotating cylinder for circulation control on an airfoil. *Journal of Hydronautics*, *10*(3), 102–105. https://doi.org/10.2514/3.48147

Teymourtasha, A., & Salimipour, S. (2017). Compressibility effects on the flow past a rotating cylinder. *Physics of Fluids*, *29*(1). https://doi.org/10.1063/1.4973564

Thangadurai, M., Singh, M., Kumar, V., & Chatterjee, P. K. (2017, September). Effect of free stream turbulence on flow over a circular cylinder in the sub-critical regime: An experimental investigation. https://doi.org/10.1007/978-81-322-2743-4_119

Thom, A. (1926a). The aerodynamics of a rotating cylinder [dissertation]. *University of Glasgow*.

Thom, A. (1926b). Experiments on the air forces on rotating cylinders. *Aeronautical Research Council*, *Reports and Memoranda*, 1018.

Thom, A. (1926c). The pressure round a cylinder rotating in an air current. *Aeronautical Research Council*, *Reports and Memoranda*(1410), 66–73.

Thom, A. (1931). *Experiments on the flow past a rotating cylinder* (tech. rep.). https://reports.aerade.cranfield.ac.uk/handle/1826.2/1419

Thom, A. (1934). *Effects of discs on the air forces on a rotating cylinder* (tech. rep.). https://reports.aerade.cranfield.ac.uk/handle/1826.2/1421

Thom, A., & Sengupta, S. (1932). *Air torque on a cylinder rotating in an air stream*. HM Stationery Office.

Thouault, N., Breitsamter, C., Adams, N., Seifert, J., Badalamenti, C., & Prince, S. (2012). Numerical analysis of a rotating cylinder with spanwise disks. *AIAA Journal*, *50*(2), 271–283. https://doi.org/10.2514/1.J050856

Towne, A., Schmidt, O., & Colonius, T. (2018). Spectral proper orthogonal decomposition and its relationship to dynamic mode decomposition and resolvent analysis. *Journal of Fluid Mechanics*, *847*, 821–867. https://doi.org/10.1017/jfm.2018.283

United Nations Conference on Trade and Development. (2023). *Review of maritime transport 2023* (2023rd ed.). United Nations. https://www.un-ilibrary.org/content/books/9789213584569

Von Kármán, T. (1911). On the mechanism of resistance produced by moving body in liquid (in german). *Nachrichtungen des Gesellshaft Wissenshaft*, 509-17 and 547–56.

Von Kármán, T., & Rubach, H. (1912). On the mechanism of resistance in fluids (in german). *Physikalische Zeitschrift*, *13*.

Weiss, J. (2019). A tutorial on the proper orthogonal decomposition. *AIAA Aviation 2019 Forum*. https://doi.org/10.2514/6.2019-3333

Westerweel, J., & Scarano, F. (2005). Universal outlier detection for piv data. *Experiments in Fluids: experimental methods and their applications to fluid flow*, *39*(6), 1096–1100. https://doi.org/10.1007/s00348-005-0016-6

Wickern, G. (2014). A theoretical approach towards the self-correcting open jet wind tunnel. *SAE Technical Paper 2014-01-0579*. https://doi.org/10.4271/2014-01-0579

Wickern, G., & Schwartekopp, B. (2004). Correction of nozzle gradient effects in open jet wind tunnels. *SAE Technical Paper 2004-01-0669*. https://doi.org/10.4271/2004-01-0669

Wieneke, B. (2015). Piv uncertainty quantification from correlation statistics. *Measurement Science and Technology*, *26*(7), 074002. https://doi.org/10.1088/0957-0233/26/7/074002

Willert, C., & Gharib, M. (1991). Digital particle image velocimetry. *Experiments in fluids*, *10*(4), 181–193.

Yazdi, E., Javad, M., Rad, A., & Khoshnevis, A. (2019). Features of the flow over a rotating circular cylinder at different spin ratios and reynolds numbers: Experimental and numerical study. *European Physical Journal Plus*, *134*(5). https://doi.org/10.1140/epjp/i2019-12508-3

Ye, H., & Wan, D. (2017). Benchmark computations for flows around a stationary cylinder with high reynolds numbers by rans-overset grid approach. *Applied Ocean Research*, *65*, 315–326. https://doi.org/https://doi.org/10.1016/j.apor.2016.10.010

Yin, D., Passano, E., Jiang, F., Lie, H., Wu, J., Ye, N., Sævik, S., & Leira, B. (2022). State-of-the-art review of vortex-induced motions of floating offshore wind turbine structures. *Journal of Marine Science and Engineering*, *10*(8). https://doi.org/10.3390/jmse10081021

Zdravkovich, M. M., Brand, V. P., Mathew, G., & Weston, A. (1989). Flow past short circular cylinders with two free ends. *Journal of Fluid Mechanics*, *203*, 557–575. https://doi.org/10.1017/S002211208900159X

Zdravkovich, M. (1997). *Flow around circular cylinders Vol 1: Fundamentals*. Oxford University Press.

Zdravkovich, M. (2003). *Flow around circular cylinders Vol 2: Applications*. Oxford University Press.

Zhang, Q., Liu, Y., & Wang, S. (2014). The identification of coherent structures using proper orthogonal decomposition and dynamic mode decomposition. *Journal of Fluids and Structures*, *49*, 53–72. https://doi.org/https://doi.org/10.1016/j.jfluidstructs.2014.04.002

Zhang, Y., Liu, K., Xian, H., & Du, X. (2018). A review of methods for vortex identification in hydroturbines. *Renewable and Sustainable Energy Reviews*, *81*, 1269–1285. https://doi.org/https://doi.org/10.1016/j.rser.2017.05.058

Zhao, D., Zhang, Y., Bi, M., Zheng, X., Zhong, X., & Zhang, S. (2023). The aerodynamic characteristics of a rotating cylinder based on large-eddy simulations. *Journal of Marine Science and Engineering*, *11*(6). https://doi.org/10.3390/jmse11061162

Zhuang, Y., Sun, X., & Huang, D. (2018). Numerical study of unsteady flows past a rotating wavy cylinder. *European Journal of Mechanics - B/Fluids*, *72*, 538–544. https://doi.org/https://doi.org/10.1016/j.euromechflu.2018.07.017